High temperature turbulence

Coupling of radiative and convective heat transfer in turbulent flows

Silvestri, S.

DOI
10.4233/uuid:8d149766-f4b1-4b6c-b73e-faadfd5deae6

Publication date
2021

Document Version
Final published version

Citation (APA)
Silvestri, S. (2021). *High temperature turbulence: Coupling of radiative and convective heat transfer in turbulent flows* . [Dissertation (TU Delft), Delft University of Technology].
https://doi.org/10.4233/uuid:8d149766-f4b1-4b6c-b73e-faadfd5deae6

Important note
To cite this publication, please use the final published version (if applicable).
Please check the document version above.

HIGH TEMPERATURE TURBULENCE

COUPLING OF RADIATIVE AND CONVECTIVE HEAT TRANSFER IN TURBULENT FLOWS

HIGH TEMPERATURE TURBULENCE

COUPLING OF RADIATIVE AND CONVECTIVE HEAT TRANSFER IN TURBULENT FLOWS

Proefschrift

ter verkrijging van de graad van doctor
aan de Technische Universiteit Delft,
op gezag van de Rector Magnificus Prof.dr.ir. T.H.J.J. van der Hagen,
voorzitter van het College voor Promoties,
in het openbaar te verdedigen op mandaag 14 juni 2021 om 17:30 uur

door

Simone SILVESTRI

Werktuigkundig ingenieur,
Technische Universiteit Delft, Nederland,
geboren te Milaan, Italië.

Dit proefschrift is goedgekeurd door de

promotor: Prof.dr. D.J.E.M. Roekaerts
promotor: Dr.ir. R. Pecnik

Samenstelling promotiecommissie:

Rector Magnificus	voorzitter
Prof.dr. D.J.E.M. Roekaerts	Technische Universiteit Delft, promotor
Dr.ir. R. Pecnik	Technische Universiteit Delft, promotor

Onafhankelijke leden:

Prof.dr. P. Coelho	Universidade de Lisboa, Portugal
Prof. G. Iaccarino	Stanford University, Verenigde Staten van Amerika
Prof.dr.ir. J.A. van Oijen	Technische Universiteit Eindhoven
Prof.dr. S. Hickel	Technische Universiteit Delft
Prof.dr.ir C. Vuik	Technische Universiteit Delft
Prof.dr.ir. B.J. Boersma	Technische Universiteit Delft, reservelid

Keywords: Turbulence, Heat transfer, Radiation

Printed by: Ridderprint

ISBN 000-00-0000-000-0

An electronic version of this dissertation is available at
http://repository.tudelft.nl/.

[1]Author e-mail address: silvestri.simone0@gmail.com

Dedicated to my sister and my parents...

CONTENTS

SUMMARY

Radiative heat transfer has a large influence in engineering systems, especially when the temperature involved is elevated. For this reason a correct assessment of heat transfer in presence of radiation is of great importance in high temperature and pressure equipment such as combustion chambers, heat exchangers as well as reentry vehicles and rockets. This thesis presents the results of innovative coupled radiative heat transfer and turbulence simulations, which aim at investigating turbulence-radiation interactions and the effect of radiation in the turbulent heat transfer process. The simulations are performed employing heterogeneous high performance computing systems in which the radiative heat transfer is solved on graphical processing units while the fluid flow is solved on CPUs. The conclusions can be summarized as follows.

Initially, the effect of radiation on the turbulent temperature field and the heat transfer process has been studied. Due to radiation new terms appear in the energy equation which are dependent on the "optical thickness" (τ) of the flow, or the ability of the medium to absorb incoming radiation. We used this last parameter to categorize the effects of radiation on the turbulent heat transfer process by highlighting the contrasting effects of radiative emission and absorption.

For a low optical thickness ($\tau = 0.1$) the role of absorption is limited to the modification of mean profiles since incident radiation (G) is not influenced by local thermal fluctuations. On the other hand, emission affects the whole temperature spectrum, stabilizing temperature and reducing thermal fluctuations caused by velocity. For an intermediate case ($\tau = 1$) the effects are amplified and a strong depletion of the thermal fluctuation field is noticed because of emission. When increasing the optical depth to moderately optically thick levels ($\tau = 10$), the effect of a larger absorption fluctuation field is then translated in a modification of TRI. Radiative fluctuations are not only restricted to dissipating temperature fluctuations, but also cause a redistribution of fluctuations over the temperature scales. This results in larger and more isotropic temperature structures which are decoupled from the velocity field. The direct analogy between velocity and temperature turbulence (constant turbulent Prandtl number) therefore, breaks down completely.

The effect of anisotropic turbulence results in a reduction of the aforementioned TRI transition where the thin streaky structures are not able to retain the emitted thermal radiation. Furthermore, a study of the budgets of temperature variance shows that with an increase in the optical thickness, the direct effect of radiation on temperature statistics grows drastically, replacing the role of molecular terms in dissipating and redistributing temperature fluctuations. The radiative term ($\mathscr{R}_\theta$) has been investigated, in analogy with molecular terms, by decomposition in two quantities, namely radiative diffusion ϕ_r and radiative dissipation ϵ_r. As the optical thickness is increased, we observed a similarity between the behaviour of radiative and molecular terms. Finally, we proved that, due to the non-local effect of long range heat transfer, encompassed in the incident radiation

fluctuations, a collapsing of mean profiles via direct scaling is not possible, irrespective of the scaling chosen.

Following this analysis, we investigated the effect of a variable absorption coefficient, showing that, in non-reactive flows, TRI can be usually accounted for by the variations of the mean absorption coefficient alone. On the other hand, the presence of a wavelength-dependent absorption coefficient complicates the description of TRI as the behaviour of the latter disconnects from the value of optical thickness. In particular, the variability of the absorption spectrum itself impacts the interactions between temperature and radiative field. Therefore, we derived a new spectrally averaged absorption coefficient that includes a turbulent quantity (the average length of the energy-containing temperature structure). This new turbulence based mean absorption coefficient κ_g proves to effectively predict TRI in non-gray gas turbulent flows. In addition, κ_g provides the base for the definition of a new optical thickness τ_g which allows a conclusive comparison among flows with and without wavelength-dependent absorption coefficient. This τ_g is not useful only in the context of turbulent flows but allows additional insight in media at rest also.

Finally, based on the physical description of TRI provided we proposed a model which allows a coupling of radiative heat transfer and turbulence in a Reynolds averaged Navier-Stokes (RANS) framework. The model consists of a first order approximation of the fluctuating radiative field which is expressed as a linear function of temperature fluctuations. This TRI closure model is then applied to a two-equation turbulent heat flux model which evaluates temperature variance and scalar dissipation rate. The improved model has been tested on several cases in comparison with the available DNS data to prove its validity. The results show that in case of a radiatively participating flow, the proposed model is always capable to improve the results when compared to the standard models available.

1

INTRODUCTION

When I meet God, I am going to ask him two questions. Why relativity? And why turbulence? I really believe he will have an answer for the first.

Werner Heisenberg

1.1. RADIATION

We tend to think of radiation as a complex phenomena occurring in stars and celestial bodies in far away galaxies. In reality, literally everything in our universe is constantly radiating thermal energy, from the above mentioned stars to the cup of tea which is cooling on the coffee table. This is caused by the constant vibrations and rotation of molecules, undergoing rapid state transitions, releasing and capturing one or several photons in the process. As such radiation (or, better defined, thermal radiation) modifies the energy content of the molecules, participating in the heat transfer process. Despite thermal radiation being continuosly emitted by every object, the impact of radiative heat transfer is noticeable (on earth) mainly in high temperature systems.

As an example, radiative heat transfer is the dominant heat transfer mode in combustion systems, where temperatures usually exceed 1500 K [1], especially in furnaces, but also in small combustors [2, 3]. For this reason, many crucial design choices are linked to the correct prediction of radiative fluxes. Some of them include (1) the material of the casing, (2) the dimension of the combustor and (3) the injected fuel ratio which influences the injector design. In addition, the pollution from combustion systems such as gas turbine combustors and boilers, are heavily influenced by the temperature of the flow, and neglecting radiative heat transfer can lead to a underprediction of pollutant emission of up to 50% [4]. A proper understanding of radiative heat transfer is, therefore, necessary, to assess and design more efficient combustors and air pollution control devices in large process and power plants. On the other hand, radiation is also influencial when dealing with long distance heat transfer, as, contrarily to conduction, radiative heat transfer can potentially occur at an infinite range. An example are planetary boundary layers and atmospheric flows. Here, radiation is responsible for cloud formation and cooling of the atmospheric boundary layer [5–8], while the absorption of infrared radiation from CO_2 and H_2O molecules is at the base of the well-known green-house effect.

Unfortunately, radiative heat transfer constitutes a formidable problem to investigate. This is because it is intrinsically non-local and multidimensional, i.e., it depends on space, time and propagation direction. Additionally, the absorption coefficient (which quantifies the amount of emitted and absorbed radiation from the medium) depends on the energy transitions that a molecule undergoes (i.e., changes in the rotational and vibrational frequencies or changes in electron's orbitals). Due to the quantization of energies associated with these transitions, the emitted/absorbed photons are characterized by distinct frequencies, which result in an absorption spectrum composed of discrete spectral lines. A clear example is the radation that reaches earth's surface from the sun. As shown in figure 1.1, the solar irradiance spans over a spectrum comprised of multiple wavelengths. The atmosphere, through water vapour and carbon dioxide, absorbs energy at different rates depending on the considered wavelength, shaping the incoming energy in the characteristic solar spectrum which reaches the surface of the earth. The presence of a spectral nature thus adds complexity to the solution of radiative heat transfer. In addition, the absorption coefficient's strength depends on the number of molecules which are able to interact with thermal radiation in a given volume (i.e., density of the gas). Futhermore, the numerous molecule collisions occurring in high-pressure gases cause a spectral broadening effect which extends absorption over

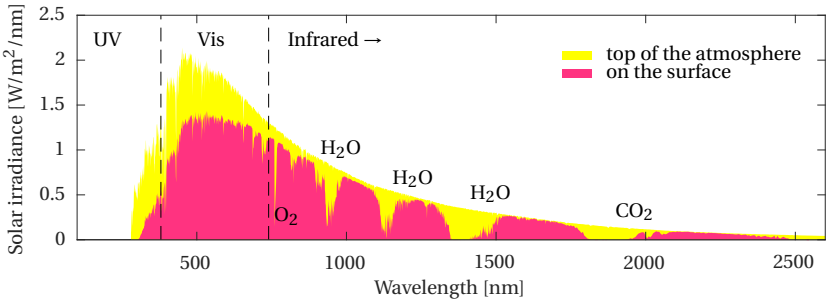

Figure 1.1: Solar irradiance dependency on wavelength at the top of the atmosphere and at the earth's surface. Data source: [10]

previously transparent parts of the spectrum. For this reason, at high pressure, the total absorption increases drastically rising the optical density of a gas. Therefore, in the current energy scenario, in which a constant increase in pressure and temperature is required to achieve a higher conversion efficiency, the knowledge of radiative heat transfer is crucial in order to design performing equipment [4, 9].

An example are new supercritical CO_2 Brayton cycles which aim to increase the efficiency of current power production systems. In these innovative thermodynamic cycles, CO_2 at a supercritical pressure is employed to decrease the compression power required while maintaining a high specific work in the turbine [11–13]. By increasing the pressure from 1 to 250 bar, the total transmissivity of CO_2 at 700°C decreases from 89.7 to 32.9% [14], leading to an optically dense fluid which is largely influenced by radiative heat transfer.

1.2. RADIATION IN TURBULENT FLOWS

A common occurrence for all the scenarios presented in the previous section is the presence of a turbulent flow. Turbulence is defined as the chaotic motion of a fluid and is characterized by a multitude of "eddies" and vortices of multiple scale. As a consequence, a turbulent flow experiences a strong momentum and energy mixing. An example of the temperature field in a turbulent flow on top of a heated plate is shown in figure 1.2.

Many theoretical analysis and experimental investigations have shown the appearance of interactions between radiation and turbulence when these occur simultaneously, mainly due to the non-linearity between radiative heat transfer and temperature. Consequently, the coupling between turbulence and radiation can lead to a difference in the emitted power source of up to 100% when compared to laminar flows [15]. These interactions are crucial in a wide range of applications that include radiative and convective heat transfer, from turbulent combustion and flames [3], to harvesting solar energy for solar thermal power applications [16]. Turbulence radiation interaction (TRI) can be classified in two main phenomena, namely: (1) the appearance of a fluctuating radiative field produced by turbulent motion and (2) the modification of turbulence structures

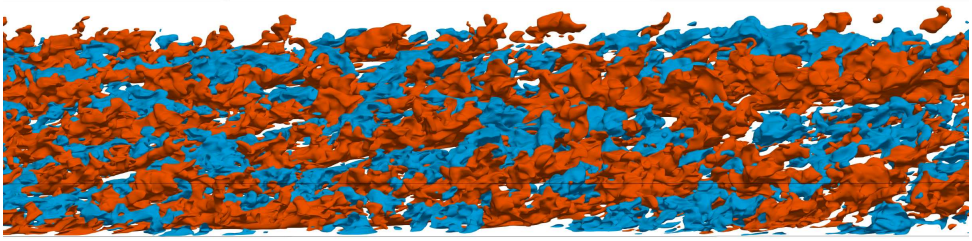

Figure 1.2: Snapshots showing the typical temperature field in a turbulent flow. Blue surfaces show low temperature zones while red surfaces highlight a high temperature zone. These isocontours are representative of "temperature structures", or flow patches with a consistent temperature which fluctuates around a mean value.

due to the action of radiative heat transfer.

A large amount of open literature on radiation, turbulence coupling is available mainly in the field of combustion science. In particular [17], [18], [19], [20], [21] and [22], studied the influence of turbulence on thermal radiation for non reactive and reactive flows in different conditions. The common conclusion is that the impact of the fluctuations of the radiative field on the mean radiative power are mainly negligible for non reactive flows, whereas they largely affect reactive flows, in which the high temperature gradients produce large temperature fluctuations. This results in a highly fluctuating radiative field that can increase the medium transmissivity and the heat losses by up to 30%.

On the other hand, the effect of radiative heat transfer on the modification of the turbulence field has received much less attention. The first theoretical studies have been performed in the field of atmospheric science, since, due to the presence of highly absorbing H_2O and CO_2, infrared radiation plays a large role in heating and cooling the atmosphere (see figure 1.1). In his pioneering work, Townsend [23] observed the influence of TRI on the temperature variance in a turbulent flow. He identified the role of radiation in the destruction of temperature fluctuations and derived an expression for new appearing dissipation. Coantic et al [24] investigated the impact of radiative cooling on the planetary boundary layer. They noticed that the dissipation produced by the action of radiation is proportional to the ratio of the Planck mean absorption coefficient κ_p to the Kolmogorov wavenumber ω_K. Thus it decreases for highly turbulent flows and increases for highly absorbing flows. The impact of radiation on turbulent atmospheres was further analysed by [25] using the assumption of homogeneous isotropic turbulence. They focused on the spectral budget of the temperature variance and defined the relative spectral damping rate, which is spectral counterpart of the radiative dissipation introduced by [23]. They observed that for weak radiative effects, radiative cooling has only a slight perturbation on the turbulent temperature spectra, while for large radiative effects the turbulent temperature spectrum is strongly modified. The theory developed in the field of atmospheric science has been extended by [26] to high-temperature radiating gases in homogeneous isotropic turbulence. Investigating the spectral radiative dissipation term in H_2O and CO_2, he concluded that, at high temperatures, radiation modifies the turbulent temperature spectrum mainly in the high frequency region.

More recently, detailed numerical studies to investigate the effect of the TRI on tur-

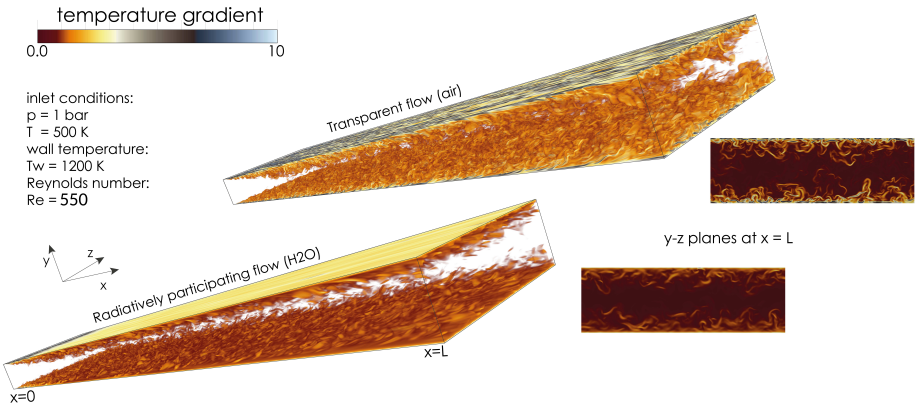

Figure 1.3: Temperature and wall-normal velocity on a wall normal plane confronted for a trasparent and radiative developing channel flow. Both flows have entrance temperature of 500 K and isothermal walls at 1200 K. Properties (both thermophysical and radiative) are the ones of water vapour. The shows the results between 0.2L and L where L is the total length of the channel. It is visible the homogenization of the temperature field due to the action of radiative heat transfer (top contours). This leads to the reduction in turbulence intensity as visible on the bottom contour.

bulence have been performed with the aid of large-eddy simulation (LES) and direct numerical simulation (DNS). Sakurai et al [27] investigated the effect of TRI on buoyant turbulent motions in a horizontal plane channel flow using the optically thin approximation. The results showed that radiation causes a break up of the organized large scale vortices, resulting in a reduction of the turbulent heat flux with the increase of the optical thickness. They explained this decrease with the modification of mean gradients rather than through direct dissipative action of radiation. Zhang et al [28] performed a DNS of a channel flow with low Mach number approximation. They studied the role of gas to gas and gas to wall radiative heat transfer in the modification of the mean temperature profile with an optimized reciprocity emission based Monte Carlo method. Follwing on the work of Zhang et al, Viquelin et al [29] calculated the radiative term in the enthalpy variance and the turbulent heat flux transport equation. Based on their results they proposed a “radiation scaling” to scale all radiation affected quantities. LES of a supersonic channel and pipe flow in conjunction with discrete ordinates method (DOM) for radiative transport was performed [30, 31] to study the influence of radiation in turbulent supersonic flows. Turbulence-radiation itneractions, in this case, acted mainly on the mean temperature and density, modifying the work done by mean flow and pressure distribution. The effect of radiative dissipation was not observed. Finally, Ghosh et al [32] investigated the influence of radiative heat transfer in inert and reactive mixing layers with coupled LES and DOM. Again, the direct influence of radiation on the temperature variance was found to be negligible when compared to the other budgets of temperature variance.

1.3. MOTIVATION

The coupling between turbulence and radiation is highly non-linear and hard to predict. The main reasons is that analytical representations are inaccessible, experimental investigations are difficult, and detailed numerical simulations are "simply" computationally unfeasible with conventional codes. For this reason, While some effort has been spent in the theoretical analysis of radiation-turbulence coupling, all the numerical investigations have been performed with low to intermediate values of optical thickness. Therefore, an identification and categorization of the effect of radiative heat transfer in turbulent flows is clearly lacking, particularly for complex problems involving non-gray radiative heat transfer or high optical thickness flows. As a consequence, the current state-of-the-art does not allow the correct coupling of radiative heat transfer and turbulence in the absence of a huge (in most cases prohibitive) amount of computational resources. Thus, the objective of this research is to

1. Develop an optimized tool to allow the full coupling of radiative heat transfer and turbulence

2. Perform high-fidelity direct numerical simulations (DNS) that give access to a complete description of TRI.

3. Provide a clear characterization of the coupling between turbulence and radiation, for different optical thicknesses, variable and spectral radiative properties and including the effects of anisotropic turbulent structures.

4. Reconcile the effect of radiation on temperature by providing scaling relations, which are able to describe the turbulence-radiation coupling independently of the above specified parameters

5. Develop a simplified model which allows the calculation of high-temperature turbulent participating flows without the necessity of performing heavy duty simulations.

1.4. THESIS OUTLINE

Following the above declared objectives, the thesis comprises of seven chapters.

Chapter 2 presents the simulation setup and the innovative numerical implementation which allows a full one-to-one coupling of turbulence and radiative heat transfer. A particular focus is given to the GPU implementation of the quasi-Monte Carlo radiation solver.

Chapter 3 investigates turbulence-radiation interaction with the use of the gray gas approximation. The radiative field and its impact on temperature and heat transfer is analysed thoroughly. The optically thin, intermediate and thick categorization for radiative

heat transfer is extended to TRI by providing a phenomenological explanation of the TRI mechanism.

Chapter 4 introduces a linear approximation of TRI which relates the fluctuations of radiative quantities to the temperature field. This approximation is validated using the gray gas cases.

Chapter 5 investigates the effects of variable radiative properties and, in particular, the impact of a spectral varying absorption coefficient.

Chapter 6 summarizes the theoretical findings in a TRI closure which can be implemented in a standard turbulent heat flux model applied to the solution of the RANS equations.

Chapter 7 provides a summary of the present study and an outlook for future studies.

2

RESEARCH METHODS AND ALGORITHMS

Coupling radiative heat transfer and turbulent flows in numerical simulations is a challenging task due to the computational expenses involved. More so if an in-depth analysis of turbulence-radiation interactions is required. In this chapter a complete decription of the state-of-the-art methodologies and numerical schemes is provided. Additionally, as the radiative heat transfer solution is the bottleneck of the numerical experiments, a particular emphasis is given to the development of an innovative GPU implementation for a Quasi-Monte Carlo radiative solver, which enables the coupling of a fully resolved turbulent flow simulations with a complete spectral radiative heat transfer solver.

Part of the contents of this chapter appeared in the following pubblications, Silvestri & Pecnik, A fast GPU Monte Carlo radiative heat transfer implementation for coupling with direct numerical simulation, J. Comp. Phys. X, **3** (2019), 100032. [33]

2.1. INTRODUCTION

In order to access the complete physics of turbulence radiation interactions, better than state-of-the-art methods must be employed. This means, using a "Direct Numerical Simulation" (DNS) approach to solve the motion of the fluid. DNS consists in the direct solution of the Navier-Stokes equations which describe the fluid flow and are introduced later in this chapter. Turbulent flows are characterized by a multitude of temporal and spatial scales that must be fully resolved. For this reason the Navier-Stokes equations are usually discretized on a fine spatial grid and evolved in time with small steps to capture the smallest spatial and temporal features of the flow. As such, this approach demands the use of High Performance Computing (HPC) centers to meet both the computational and memory requirements.

On the other hand, modelling the radiative heat transfer with an accuracy comparable to DNS is challenging due to the numerical complexity and the associated computational costs [34]. In particular, while for a turbulent flow the main issue is the requirement of a fine spatial grid to resolve all scales involved in momentum and energy transfer, for radiative heat transfer the computational challenges are exacerbated by the presence of multiple propagation directions and a (usually complicated) wavelength spectrum. For this reason, while the DNS approach has been largely established in the past three decades, and implementation details are widely available and documented, the modelling of radiative heat transfer is significantly lagging behind. A common approach to tackle the computational requirement is to reduce the dimensionality of the radiative heat transfer with the aid of simplifying assumptions to ease the computational burden.

In particular, two widely adopted approximations are the Optically Thin Approximation (OTA) [27, 35] and the gray gas assumption [20, 21, 30, 31]. The OTA neglects self-absorption from the participating medium, leading to a constant incident radiation throughout the domain. This assumption greatly simplifies the description of radiative heat transfer. However, it does not allow the evaluation of incident radiation fluctuations and is, therefore, restricted to low values of the absorption coefficient, κ, as demonstrated in Ref. [17]. The gray gas assumption, on the other hand, does not simplify the Radiative Transfer Equation (RTE) itself (eq. 2.1f) but neglects the dependency of the absorption coefficient on wavelength, assuming a constant κ throughout the spectrum. Despite being highly idealized – real fluids are intrinsically non-gray – this approximation allows a complete description of turbulence-radiation interactions. The advantage of the gray assumption is that fairly simple methods can be used for the solution of the Radiative Transfer Equation (RTE, equation (2.1f)), such as the Discrete Ordinates Method (DOM) or the Finite Volume Method (FVM).

If a spectral description of radiative heat transfer is considered, the state of art is to use a Monte Carlo (MC) method. Compared to the above mentioned RTE solution methods, the Monte Carlo method can be considered the most accurate and flexible approach. Its solution time only slowly increases with the complexity of the problem. This allows a detailed spectral description or the simulations of complex geometries, which is precluded with other methods such as DOM. Despite these desirable characteristics, a standard MC implementation is still extremely demanding and not suited for coupling with a DNS solver which requires the solution over a very fine grid. However, since the

Monte Carlo method is inherently "embarassingly parallelizable" (i.e., can be divided into a number of completely independent computations), it greatly benefits from the use of parallel architectures and in particular from the use of general purpose graphical processing units (GPGPU).

The use of GPUs in computational science has significantly increased, especially for large parallelizable problems that are more efficiently mapped on many GPU parallel multiprocessors [36]. The development of NVIDIA CUDA, a versatile GPU programming language, has further popularized GPUs as accelerators alongside CPUs in HPC systems [37]. Several examples of GPU codes are available, ranging from machine learning [38] to imaging [39] and computational biology [40].

Likewise, in the field of fluid mechanics, Khajeh et al. [41] and Salvadore et al. [42] have implemented a Navier-Stokes solver on GPUs obtaining speedups up to 22×. Additionally, many Monte Carlo codes have been developed on graphical processing units for many diverse fields and applications such as finance [43] and molecular dynamics [44]. The only MC method for solving thermal radiation on GPUs were developed independently by Humphrey et al. [45] for gray gas applications and by Heymann and Siebenmorgen [46] for dust radiation around active galactic nuclei. The code of the former showed excellent scaling capabilities up to 16834 GPUs, proving the feasibility of the GPU MC concept for thermal radiation. The latter focused on the optimization of the MC procedure, reaching a speed up of around 100×.

The following chapter will present the governing equations and the numerical methods adopted to solve the coupled turbulence – radiative heat transfer problem. Since one of the novelties of this thesis is the development of a fast Monte Carlo solver, which allows a one-to-one coupling with the fluid flow solution, most of the chapter will be dedicated to the implementation and the benchmarking of the GPU Monte Carlo radiative solver.

2.2. GOVERNING EQUATION AND NUMERICAL SETUP

To study the interaction between turbulence and radiation in high temperature participating flows we use state-of-the-art methods, such that all physical phenomena are captured for the investigation.

In this work we make use of a canonical geometry which allows a detailed study of TRI. The setup, shown in figure 2.1, consists in a statistically one dimensional channel flow, periodic in the streamwise and spanwise direction and bounded by a hot and a cold isothermal wall. A participating turbulent flow is simultaneously heated by the hot wall and cooled by the cold wall. The participating fluid is also capable of absorbing radiation from the hot wall and emitting towards the cold wall. In addition, fluid-to-fluid radiative heat transfer modifies the redistribution of the energy within the channel. The scattering from the medium is neglected, which is a reasonable assumption for molecular gases. In addition, the flow is assumed to be considerably slower than the speed of sound, such that we can make use of the low Mach number approximation of the Navier Stokes equations. This assumption is realistic in case of high temperatures and atmospheric pressures, like the flows under investigation. Under these assumptions, the

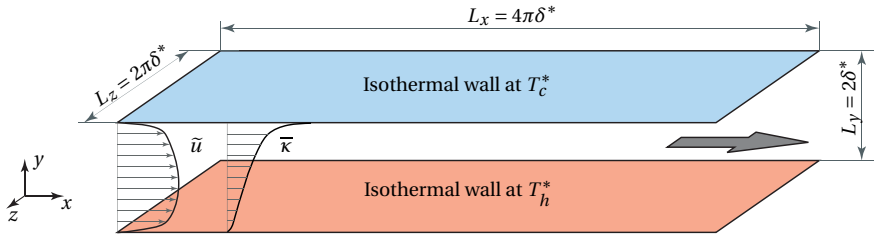

Figure 2.1: Schematic displaying the computational domain. The profiles shown are the Favre averaged streamwise velocity ($\widetilde{u}$) and Reynolds averaged Planck-mean absorption coefficient ($\overline{\kappa}$) for case H.

governing equations read

$$\frac{\partial \rho}{\partial t} + \frac{\partial \rho u_j}{\partial x_j} = 0\,, \tag{2.1a}$$

$$\frac{\partial \rho u_i}{\partial t} + \frac{\partial \rho u_j u_i}{\partial x_j} = -\frac{\partial p}{\partial x_i} + \frac{1}{Re}\frac{\partial \tau_{ij}}{\partial x_j}\,, \tag{2.1b}$$

$$\text{with} \quad \tau_{ij} = 2\mu S_{ij} \quad \text{and} \quad S_{ij} = \frac{1}{2}\left(\frac{\partial u_i}{\partial x_j} + \frac{\partial u_j}{\partial x_i}\right) - \frac{1}{3}\frac{\partial u_k}{\partial x_k}\delta_{ij}\,, \tag{2.1c}$$

$$\frac{\partial \rho\theta}{\partial t} + \frac{\partial \rho u_j \theta}{\partial x_j} = \frac{1}{RePr}\frac{\partial}{\partial x_j}\left(\lambda\frac{\partial \theta}{\partial x_j}\right) - \frac{1}{RePrPl}Q^R\,, \tag{2.1d}$$

$$Q^R = \int_0^\infty \kappa_\nu \left[4I_{b\nu} - \frac{1}{\pi}\int_{4\pi} I_\nu d\Omega\right] d\nu\,, \tag{2.1e}$$

$$s_j \cdot \frac{\partial I_\nu}{\partial x_j} = \kappa_\nu (I_{b\nu} - I_\nu)\,. \tag{2.1f}$$

Here $\rho, \boldsymbol{u}, \theta, Q^R$ and I_λ are non-dimensional density, velocity vector, temperature, radiative heat source and spectral directional intensity, respectively, while $t, \boldsymbol{x}, \boldsymbol{s}, p, \theta, \mu, \lambda, c_p$ and κ_ν are non-dimensional time coordinate, spatial direction vector, propagation direction vector, pressure, temperature, viscosity, thermal conductivity, specific heat capacity and spectral absorption coefficient, respectively. The specific heat capacity c_p has been considered constant and incorporated into the Prandtl number. The thermophysical and radiative properties $(\rho, \mu, \lambda, \kappa_\nu)$ are varied between the cases and will be explicited later. The non-dimensional variables are defined as

$$t = \frac{t^*\delta^*}{U_b^*}, \quad \boldsymbol{x} = \frac{\boldsymbol{x}^*}{\delta^*}, \quad \rho = \frac{\rho^*}{\rho_c^*}, \quad \mu = \frac{\mu^*}{\mu_c^*}, \quad \lambda = \frac{\lambda^*}{\lambda_c^*},$$
$$\boldsymbol{u} = \frac{\boldsymbol{u}^*}{U_b^*}, \quad p = \frac{p^*}{\rho_c^* U_b^{*2}}, \quad \theta = \frac{T^* - T_c^*}{T_h^* - T_c^*},$$
$$I_\nu = \frac{I_\nu^*}{\sigma T_c^{*4}/\pi}, \quad \kappa_\nu = \kappa_\nu^* \delta^*, \quad Q^R = \frac{Q^{R*}}{\sigma T_c^{*4}/\delta^*}$$

Where δ^* is the half channel height, U_b^* is the bulk velocity and σ is the Stefan-Boltzmann constant. The asterisk identifies a dimensional value, while the subscripts h and c stand for values at the hot and cold wall, respectively. The non-dimensional parameters in the above equations are written as

Reynolds number $Re = \rho_c^* U_b^* L^* / \mu_c^*$

Prandtl number $Pr = c_{pc}^* \mu_c^* / \lambda_c^*$

Planck number $Pl = \lambda_c^* (T_h^* - T_c^*) / (\sigma {T_c^*}^4 \delta^*)$

Equations (2.1a-2.1d) (the fluid problem) are solved with a finite difference implementation, while equations (2.1e-2.1f), governing radiative heat transfer, are solved with two different methods based on the radiative properties of the medium. A Finite Volume Method (FVM) is used in case of a gray participating medium, while if the absorption coefficient varies with wavelength, a novel GPU optimized emission based quasi-Monte Carlo method is employed. All methods are described in the sections below with particular attention to the GPU Monte Carlo implementation.

2.3. FLUID FLOW SOLVER

The flow solver involves discretizations of the domain in both time and space. Spectral differentiation with Fourier expansion and periodic boundary conditions are used in space in the two homogeneous directions (spanwise and streamwise), while a sixth-order staggered compact finite difference [47, 48] is used to discretize the spatial derivatives in the wall-normal direction. To reduce aliasing errors when discretizing the advection terms, a skew-symmetric formulation based on the work of Feiereisen et al [49] is employed. The time advancement is performed with a second-order explicit Adams-Bashforth scheme formulated as

$$Y^{n+1} = Y^n + \Delta t \left(\frac{3}{2} \mathrm{RHS}^n - \frac{1}{2} \mathrm{RHS}^{n-1} \right) . \tag{2.2}$$

where Δt is the simulation time step and Y is a conserved variable. A pressure correction scheme is applied based on the projection method. First, the energy equation (2.1d) is advanced in time, providing a value for $(\rho\theta)^{n+1}$. An estimate of ρ at time $n+1$ calculated as

$$\rho^* = \rho^n + \Delta t \left(\frac{\partial \rho}{\partial t} \right)^n , \qquad \text{where} \qquad \left(\frac{\partial \rho}{\partial t} \right)^n = \frac{3\rho^n - 4\rho^{n-1} + \rho^{n-2}}{2\Delta t} , \tag{2.3}$$

is used to calculate $\theta^{n+1} = (\rho\theta)^{n+1} / \rho^*$. The thermodynamic and radiative properties at time step $n+1$ are then calculated from the temperature θ^{n+1}. Subsequently, the momentum equations (2.1b) are advanced employing the Adams-Bashfort scheme (eq. 2.2) without accounting for pressure to provide a momentum predictor $(\rho u_i)^*$. Mass conservation is ensured by imposing

$$(\rho u_i)^{n+1} = (\rho u_i)^* + \Delta t \frac{\partial p^{n+1}}{\partial x_i} , \qquad \text{with} \qquad \frac{\partial (\rho u_i)^{n+1}}{\partial x_i} = \left(\frac{\partial \rho}{\partial t} \right)^{n+1} . \tag{2.4}$$

Taking the divergence of the above equation yields a Poisson equation which is solved for pressure at time step $n+1$ using Fourier expansions in the homogeneous directions and a second order implicit scheme in wall-normal direction. A pressure gradient is applied in the streamwise direction that maintains a constant Reynolds number based on bulk velocity. For the validation of the DNS code, the reader is referred to Patel et al. [50].

2.4. MODELLING THERMAL RADIATION

Radiative heat transfer is fully described by the Radiative Transfer equation (eq. 2.1f) and by the radiative power source (eq. 2.1e). The coupling of radiative heat transfer with the energy equation is done through Q^R in equation 2.1d, therefore, the RTE has to be solved to obtain the value of the radiative heat source. As the RTE can be expressed in both in a differential form (as shown above) and in an integral form, the methods for the RTE solution can be divided into differential and integral methods.

Differential methods solve the differential formulation of the RTE by discretizing equation (2.1f) in a control volume formulation. Examples of these methods are the Spherical harmonics, discrete ordinates method and the finite volume method. Because of the formulation of these methods, they are more easily coupled with CFD simulations where a discrete spatial grid is required to obtain a solution. In the spherical harmonics approximation (P_N) method, the intensity is expressed by a series of spherical harmonics that divide the RTE into a set of first order Partial Differential Equations (PDE) [51] that can be solved with standard PDE solvers. The P_N approximation has been extensively used in its lowest-order approximation P_1 for one and two dimensional problems, but the complexity of P_N increases rapidly with higher order spherical harmonics required for three dimensional geometries. Furthermore, the P_N method performs poorly when compared to other methods for highly non isotropic radiation field and in optically thin limit [51]. One of the most popular method for modelling the RTE equation is the Discrete Ordinates method (DOM or S_N approximation). Akin to the P_N approximation, DOM is a tool to transform the RTE into a set of partial differential equations [34]. The discrete ordinates method is based on an angular discretization of the intensity propagation directions, discretizing the directional dependence of the RTE with a finite difference formulation. This method results in a fairly simple implementation and is particularly popular because of the easy coupling potential with CFD codes, but suffers of some severe drawbacks such as ray effect, false scattering and non conservation of radiative energy [34]. Moreover the set of discrete ordinates must satisfy the so called zero, first and second moments, a set of conditions on the ordinates and their weights that guarantee the correct implementation of the method.

Integral methods resolve the integral formulation of equation (2.1f). A commonly adopted method falling in this category is the Photon Monte Carlo method. A Monte Carlo photon transport simulation consists of launching a number of photon beams starting from a location in which a high energy density is encountered and tracing them until fully depleted. Monte Carlo methods can achieve a high degree of accuracy, being able to resolve exactly the RTE to an extent that is controllable by simulation parameters. A drawback of these methods is the high computational cost, having to trace several rays

(up to millions) in order to obtain a statistically significant result. Another example of an integral method is the zonal method, proposed by Hottel and Cohen [52]. In the zonal method, the volume and the surface of the enclosure are divided into several zones assuming constant temperature and radiation properties within the zone. Total Exchange factors are evaluated (surface-volume, volume-volume and surface-surface). Therefore, the RTE is reduced into a set of nonlinear algebraic equations solvable using various numerical matrix inversion techniques. The zonal method was popular in the past due to its simple implementation, but the need to invert full matrices causes high computational expenses when dealing with complex problems or optically thick cases.

2.5. FINITE VOLUME RADIATIVE SOLVER

The Finite Volume Method (FVM) was first developed from Briggs [53], as an alternative to the DOM in the field of neutron transport and further developed by Raithby and Chui [54] for thermal radiative transfer. Since the DOM does not necessarily guarantee energy conservation as it is based on a finite differencing scheme, a finite volume formulation was proposed to ensure conservation of radiant energy. Moreover, the FVM has been demonstrated to be unaffected by ray effects and to experience a reduced false scattering when compared to the DO method [34]. The finite volume discretized Radiative Transfer Equation (RTE) for a gray emitting- absorbing medium reads:

$$\sum_{k=w,e,s,n,t,b} I_{km}(\boldsymbol{n}_k \cdot \boldsymbol{s}_m) A_k = (\kappa I_{bi} - \kappa I_{im}) V_i \Omega_m \,, \tag{2.5}$$

where the subscript i stands for the cell-center value, subscript k denotes values at the faces of the computational cell, named w, e, s, n, t or b for west, east, north, south, bottom or top. The subscript m refers to the m_{th} direction and will be omitted in the following analysis at certain discussions. $\boldsymbol{s}_m$ is the propagation vector of direction m while $\boldsymbol{n}_k$ and A_k are the normal vector and area of face k, respectively. Finally I is the non-dimensional radiative intensity while κ, V and Ω are the non-dimensional absorption coefficient, the volume of cell i and the solid angle of direction m, respectively. For a complete derivation of equation (2.5) see ref. [34]. Figure 2.2 shows an example of the intensities required in equation (2.5) for an arbitrary direction m.

The center value (I_i) is to be calculated, hence a correlation between the facial (I_k) and the available cell-centered intensities must be found. The simplest scheme for spatial discretization, currently the most widely used, is the STEP scheme [34], which consists in assuming I_k equal to intensity at the center of the first cell in the upstream direction. Therefore $I_k = I_i$ where $(\boldsymbol{n}_k \cdot \boldsymbol{s}) > 0$ and $I_k = I_K$ where $(\boldsymbol{n}_k \cdot \boldsymbol{s}) < 0$. Subscript K stands for a value at the center of the neighbouring cell in k direction (takes the values W, E, S, N, T, B, see figure 2.2). The resulting equation is explicit in I_i and reads:

$$I_i = \frac{\kappa I_{bi} V \Omega - \sum_{(\boldsymbol{n}_k \cdot \boldsymbol{s})<0} I_K (\boldsymbol{n}_k \cdot \boldsymbol{s}) A_k}{\sum_{(\boldsymbol{n}_k \cdot \boldsymbol{s})<0} (\boldsymbol{n}_k \cdot \boldsymbol{s}) A_k + \kappa V \Omega} \,. \tag{2.6}$$

Since I_i depends only on upstream values (values for which $(\boldsymbol{n}_k \cdot \boldsymbol{s}) < 0$), a sweep approach through the whole domain is enough to obtain a converged solution (in case

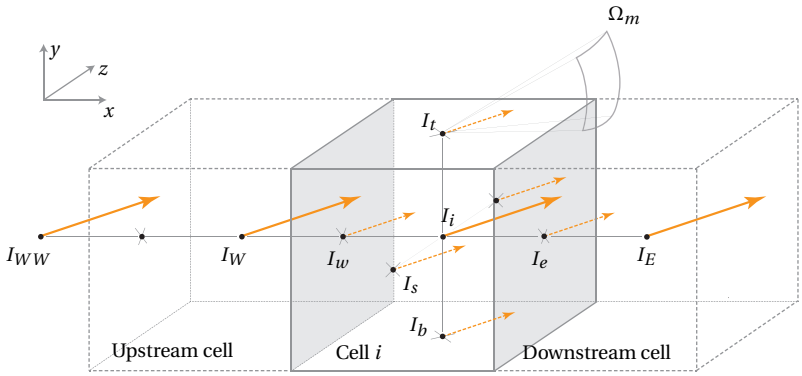

Figure 2.2: Schematic displaying the nomenclature of the finite volume solver for an arbitrary direction m corresponding to the solid angle Ω_m. All facial intensities are displayed with dashed arrows and defined by a lower case letter displaying the direction (b for bottom, s for south, w for west and so on). Intensities at the center of the neighbouring cells are defined by an upper case letter displaying the direction (T for top, N for north, E for east, etc). In this case, upstream cells are W in the $x-$direction, B in the $y-$direction and S in the $z-$direction. On the other hand, cells E, T and N are the downstream cells in the $x-$, $y-$ and $z-$direction, respectively.

of reflective walls an iterative procedure is necessary). The STEP scheme is proven to be stable and to avoid unphysical results, but has a high truncation error, that exacerbates increasing optical thickness [34]. Since the accuracy of the radiative solver would not match the high precision of the fluid solver, the STEP scheme is not suited to perform a DNS study on convection-radiation coupling, . The more accurate CLAM scheme [55] is a second order high resolution bounded scheme derived from fluid dynamics. It consists in discretizing the face intensity by including contributions from one downstream and two upstream values as:

$$\tilde{I}_k = \begin{cases} \dfrac{\tilde{x}_C^2 - \tilde{x}_k}{\tilde{x}_C(\tilde{x}_C - 1)}\tilde{I}_C + \dfrac{\tilde{x}_k - \tilde{x}_C}{\tilde{x}_C(\tilde{x}_C - 1)}\tilde{I}_C^2 & \text{if } 0 < \tilde{I}_C < 1\,, \\ \tilde{I}_C & \text{otherwise}\,, \end{cases} \tag{2.7}$$

where the subscript C stand for cell-center values upstream the considered face k in the propagation direction m and tilde denotes normalized values calculated as:

$$\tilde{I} = \frac{I - I_U}{I_D - I_U}\,, \quad \tilde{x} = \frac{x - x_U}{x_D - x_U}\,.$$

Subscript U and D stand for upstream and downstream cell-center values with regards to cell C in the propagation direction. Note that $\tilde{I}_k = \tilde{I}_C \Rightarrow I_k = I_C$ is the STEP scheme expressed in non-dimensional notation. An example of the CLAM scheme discretization can be shown using figure 2.2. For the considered direction m, the upstream cells are located west, south and bottom while the downstream cells are east, north and top. Therefore, in the specific case of the west facial intensity I_w, which is located upstream

the computational cell i in the $x-$direction, the CLAM scheme yields

$$\tilde{I}_w = \frac{I_w - I_{WW}}{I_i - I_{WW}} = \begin{cases} \dfrac{\tilde{x}_W^2 - \tilde{x}_w}{\tilde{x}_W(\tilde{x}_W - 1)}\tilde{I}_W + \dfrac{\tilde{x}_w - \tilde{x}_W}{\tilde{x}_W(\tilde{x}_W - 1)}\tilde{I}_W^2 & \text{if } 0 < \tilde{I}_W < 1\,, \\ \tilde{I}_W & \text{otherwise}\,, \end{cases} \tag{2.8}$$

where

$$\tilde{I}_W = \frac{I_W - I_{WW}}{I_i - I_{WW}}\,, \quad \tilde{x}_W = \frac{x_W - x_{WW}}{x_i - x_{WW}}\,, \quad \text{and} \quad \tilde{x}_w = \frac{x_w - x_{WW}}{x_i - x_{WW}}\,.$$

On the other hand, the facial intensity I_e, located downstream the computational cell, will be calculated from

$$\tilde{I}_e = \frac{I_e - I_W}{I_E - I_W} = \begin{cases} \dfrac{\tilde{x}_i^2 - \tilde{x}_e}{\tilde{x}_i(\tilde{x}_i - 1)}\tilde{I}_i + \dfrac{\tilde{x}_e - \tilde{x}_i}{\tilde{x}_i(\tilde{x}_i - 1)}\tilde{I}_i^2 & \text{if } 0 < \tilde{I}_i < 1\,, \\ \tilde{I}_i & \text{otherwise}\,, \end{cases} \tag{2.9}$$

where

$$\tilde{I}_i = \frac{I_i - I_W}{I_E - I_W}\,, \quad \tilde{x}_i = \frac{x_i - x_W}{x_E - x_W}\,, \quad \text{and} \quad \tilde{x}_e = \frac{x_e - x_W}{x_E - x_W}\,.$$

The CLAM scheme must satisfy the boundedness criterion which is violated if $\tilde{I}_k$ is not monotonic in the range $0 < \tilde{I}_C < 1$. In this case, there will be points for which $\tilde{I}_k > 1$. For a uniform mesh, $\tilde{x}_k = 0.75$ and $\tilde{x}_C = 0.5$ which leads to $\tilde{I}_k = \tilde{I}_C(2 - \tilde{I}_C)$ and ensures that the boundedness criterion is always satisfied. This is not necessarily the case for a non-uniform grid, where, if $\tilde{x}_k > \tilde{x}_C(2 - \tilde{x}_C)$, $\partial\tilde{I}_k/\partial\tilde{I}_C$ vanishes somewhere in the range $0 < \tilde{I}_C < 1$. Therefore, As described in [55], to avoid unbounded results that could arise in the non-uniform direction and near the walls, the functional relationship $\tilde{x}_k \leq \tilde{x}_C(2 - \tilde{x}_C)$ is monitored. Where it does not hold, boundness is enforced by setting $\tilde{I}_k = 1$.

The resulting equation is implicit in I_i since the value of intensity at the downstream faces is not readily available. To avoid the use of memory intensive implicit solvers, the iterative deferred correction approach is implemented, where downstream values are expressed as computed by the STEP scheme in the current iteration plus a correction resulting from the previous iteration:

$$I_{k,D}^{n+1} = I_{k,D_{STEP}}^{n+1} + \left(I_{k,D_{CLAM}}^{n} - I_{k,D_{STEP}}^{n}\right)\,. \tag{2.10}$$

On the other hand, intensities on the upstream faces are readily available within the current iteration thanks to the sweep approach. Finally, after the intensities I_i in all directions m have been calculated, the volumetric radiative source is given by

$$Q_i^R = \kappa\left(4I_{bi} - \frac{1}{\pi}\sum_m I_{im}\Omega_m\right) \tag{2.11}$$

2.6. QUASI-MONTE CARLO RADIATIVE SOLVER

Within a domain containing a non gray absorbing and emitting medium, the radiative power emitted by cell i and absorbed within cell j is expressed, as in Tesse et al. [18], by

$$Q^R_{i\to j} = \int_0^\infty \kappa_\nu(T_i) I_{b\nu}(T_i) \int_{V_i}\int_{4\pi} \sum_{m=1}^{N_c} t_\nu(i\to j,m)\cdot \cdot\left[\int_0^{l_{j,m}} \kappa_\nu(T_j) e^{-\kappa_\nu(T_j)s_{j,m}} ds_{j,m}\right] d\Omega dV_i d\nu, \tag{2.12}$$

where ν is the wavenumber, κ_ν is the spectral absorption coefficient, t_ν is the spectral transmissivity from cell i to the boundary of cell j following the path m, N_c is the number of paths that, from cell i, cross cell j, and $l_{j,m}$ is the distance travelled in cell j along the propagation direction. The volume integral V_j, as given in ref. [56] has been replaced by the integration over the solid angle Ω and the path length $s_{j,m}$ as done in ref. [18]. The integral in the square brackets represents the absorption within cell j, following path m. The analytical solution, considering cell j isothermal and homogeneous, is

$$\alpha_{\nu\, j,m} = 1 - e^{-\kappa_\nu(T_j) l_{j,m}}. \tag{2.13}$$

The spectral transmissivity $t_\nu(i\to j,m)$ is the result of the absorption by the finite volumes and surfaces crossed by path m, and can be calculated as

$$t_\nu(i\to j,m) = \prod_{k=i}^{j-1}(1-\alpha_{\nu\, k,m}) \times \prod_{c=1}^{N_r}(1-\varepsilon_w)\,, \tag{2.14}$$

where ε_w is the wall emissivity and N_r is the number of wall reflections that occurred for path m.

The Monte Carlo method consists in a statistical estimation of the integrals in equation (2.12) using a large number of samples that represent different paths and wavelengths. In particular, it is possible to develop probability distribution functions defined as

$$f_V = \frac{1}{V_i}\,, \quad f_\theta = \frac{\sin\theta}{2}\,, \quad f_\phi = \frac{1}{2\pi}\,, \quad f_\nu = \frac{\pi\kappa_\nu(T_i) I_{b\nu}(T_i)}{\kappa_p(T_i)\sigma T_i^4}\,, \tag{2.15}$$

where $\kappa_p(T_i)$ is the Planck mean absorption coefficient of cell i, while θ and ϕ are the polar and azimuthal angles, respectively, with $d\Omega = \sin\theta d\theta d\phi$. Substituting the probability distribution functions in equation (2.12) leads to

$$Q^R_{i\to j} = Q^{R,e}(T_i) \int_0^\infty f_\nu \int_{V_i} f_V \int_0^{2\pi} f_\phi \int_0^\pi f_\theta\, A_{\nu,m,i\to j}\, d\theta\, d\phi\, dV_i\, d\nu\,, \tag{2.16}$$

where $Q^{R,e}(T_i)$ and $A_{\nu,m,i\to j}$ are the total radiative power emitted by cell i and the spectral energy fraction emitted by cell i and absorbed in cell j through path m, respectively. These are calculated using

$$Q^{R,e}(T_i) = 4V_i\kappa_p(T_i)\sigma T_i^4, \tag{2.17}$$

$$A_{\nu,m,i\to j} = \sum_{m=1}^{N_c} t_\nu(i\to j,m)\alpha_{\nu\, j,m}. \tag{2.18}$$

A statistical estimation of the integrals in equation (2.16) involves launching several samples, referred hereafter as "rays" with properties sampled from the probability density functions given in (2.15).
The resulting discretized equation has then the form

$$\widetilde{Q^R_{i\to j}} = \frac{Q^{R,e}(T_i)}{N_r} \sum_{r=1}^{N_r} A_{r,i\to j} \,. \tag{2.19}$$

The tilde ~ denotes a statistical estimator and the subscript r indicates a ray, characterized by its wavenumber ν, and direction angles θ and ϕ (defining the path variable m), which are calculated inverting the following relations

$$\begin{aligned} R_\nu &= \int_0^\nu f_{\nu'}(T)d\nu' = \frac{\pi \int_0^\nu \kappa_{\nu'}(T) I_{b\nu'}(T)d\nu'}{\kappa_p(T)\sigma T^4} \,, \\ R_\theta &= \int_0^\theta f_{\theta'} d\theta' = \frac{1-\cos\theta}{2} \,, \\ R_\phi &= \int_0^\phi f_{\phi'} d\phi' = \frac{\phi}{2\pi} \,. \end{aligned} \tag{2.20}$$

R_ν, R_θ and R_ϕ are random numbers sampled from a uniform probability distribution function between 0 and 1.
In a reciprocal Monte Carlo formulation, both emitted and absorbed power are statistically estimated as

$$Q^R_{i,RM} = \underbrace{\sum_{j=1}^{N_v+N_s} \widetilde{Q^R_{i\to j}}}_{Q_i^{R,e}} - \underbrace{\sum_{j=1}^{N_v+N_s} \widetilde{Q^R_{j\to i}}}_{Q_i^{R,a}} \,, \tag{2.21}$$

where $N_v + N_s$ are the numbers of volume and surfaces that interact with cell i. The reciprocal formulation employes the following principle

$$\frac{Q^R_{i\to j,\nu}}{I_{b\nu}(T_i)} = \frac{Q^R_{j\to i,\nu}}{I_{b\nu}(T_j)} \,, \tag{2.22}$$

to automatically satisfy the reciprocity condition. As a consequence, the above formulation avoids problems of large variance in case of low temperature gradients (i.e. non reactive flows) or high optical thickness that are typical of a forward Monte Carlo method. Depending on the estimated quantity, it is possible to distinguish between two reciprocity Monte Carlo formulations [18]. These are, the Absorption-based Reciprocity Monte Carlo (ARMC) which connects the emission to the statistical estimation of the absorbed power, and, vice-versa, the Emission-based Reciprocity Monte Carlo (ERMC) which estimates absorption based on the calculation of emitted power. While ARMC results in a lower variance in low temperatures zones, characterized by relevant absorption, ERMC is more accurate in the high temperature regions that are dominated by emission. The advantage of ERMC is that Q^R in i is calculated by the emission of the cell, requiring only the computation of the rays leaving the cell itself. The corresponding

relation of an ERMC formulation is given as

$$Q^R_{i,ERMC} = \sum_{j=1}^{N_v+N_s} \widetilde{Q^R_{i\to j}} \cdot \left(1 - \frac{I_{bv}(T_j)}{I_{bv}(T_i)}\right) . \tag{2.23}$$

In addition, in the ERMC formulation the volumetric heat source [kW/m^3] is independent of the emitting cell volume. As a consequence, it is possible to emit all rays directly from the center of cell i, avoiding the sampling on f_V.

Recently, Zhang et al. [57] developed an optimized ERMC to reduce the variance in the low temperature regions. In the cold regions, Q^R is dominated by the absorption of radiation which originates from hot zones. Nevertheless, an ERMC entails the estimation of absorption based on the emission of the cell itself. Consequently, the wavelength of emission in colder regions will be higher than the actual wavelength of the absorbed radiation that follows Wien's displacement law. This leads to a large variance in cold spots, which is characteristic for an ERMC based method. Therefore, ref. [57] proposed to sample the wavenumber from the maximum temperature, which corresponds to a larger emission in the domain, using

$$f_v = \frac{\pi \kappa_v(T_{max}) I_{bv}(T_{max})}{\kappa_p(T_{max}) \sigma T^4_{max}} . \tag{2.24}$$

As a result, equation (2.19) has to be corrected with a prefactor R_I, resulting in

$$\widetilde{Q^R_{i\to j}} = \frac{Q^{R,e}(T_{max})}{N_r} \sum_{r=1}^{N_r} \Bigg(\underbrace{\frac{\kappa_v(T_i) I_{bv}(T_i)}{\kappa_v(T_{max}) I_{bv}(T_{max})}}_{R_I} \Bigg) A_{r,i\to j} . \tag{2.25}$$

2.6.1. SPECTRAL DISCRETIZATION

In general, gas absorption spectra are characterized by discrete absorption lines, leading to a strong dependency on wavelength. In order to store the absorption coefficients and the probabilities associated with a line-by-line spectrum, comprised of more than a million spectral points, an excessive amount of memory is required. In addition, the high variability of the spectra translates in a lower convergence rate of the Monte-Carlo method. For this reason, we chose a narrow-band correlated-k model to couple with the Monte Carlo solver [58]. The narrow-band method constitutes of an accurate spectral representation, comparable to a line-by-line description if enough pseudo-spectral points are considered, with significantly lower memory requirements. In addition it is naturally adaptable to a simple implementation of species transport and wavenumber-dependent scattering, in case multiphase flows are considered. The line-by-line spectrum of common gasses, for a wide range of temperatures and pressures, can be found in accurate online spectroscopy databases such as HITRAN 2012 [59] and HITEMP 2010 [14].

Since the narrow-band correlated-k model divides the spectrum into narrow bands with assigned quadrature points, the wavenumber probability function in equation (2.15) is discretized using two "discrete" probability functions, one for the narrow-band and the

other one for the quadrature point. The two variables associated with the wavenumber of the photon bundle are thus a narrow band index n and a quadrature point index g,

$$\int_0^{\nu} f_{\nu'} d\nu' \approx \sum_{n'=1}^{n-1} f_{n'} + f_n \cdot \sum_{g'=1}^{g-1} f_{g'}(n) \,, \tag{2.26}$$

where

$$f_n = \frac{\pi \Delta\nu_n I_{bn} \sum_{g'=1}^{Nq} \omega_{g'} k_{n,g'}}{\kappa_p \sigma T^4} \,, \quad f_g(n) = \frac{\omega_g k_{n,g}}{\sum_{g'=1}^{Nq} \omega_{g'} k_{n,g'}} \,, \tag{2.27}$$

and ω_g and N_q are the Gaussian weights associated with point g and the total number of quadrature points in a narrow-band, respectively. Since the quadrature points in a narrow-band all represent ideally the same wavenumber, the drawing of two independent random numbers is necessary in order to sample n and g,

$$R_n = \sum_{n'=1}^{n-1} f_{n'} \,, \quad R_g = \sum_{g'=1}^{g-1} f_{g'}(n). \tag{2.28}$$

2.6.2. ALGORITHM

To ease the understanding of the GPU ERMC implementation, we first describe a standard CPU implementation in algorithm 1. The first loop (line 1) is performed over all finite volumes in the computational domain. Each finite volume is described by its index (i,j,k), and coordinates of the center and the surrounding faces. For each finite volume, a predefined number of rays (`numberOfRays`) are launched. The variable `ray` is a data structure that contains the current position (`pos`) of the ray and the index of the corresponding cell (`ind`), as well as the direction vector (`dir`) and the current transmissivity (`transmissivity`). The MC method mainly consists of two routines, the initialization (line 4) and the marching of the ray (line 16). In the first routine, the necessary random numbers are drawn and the properties of the ray are initialized accordingly. To accommodate a narrow-band correlated-k description, two independent random numbers are drawn R_n and R_g, which lead to two different indices `n` and `g` that specify the narrow-band and the quadrature point within. To reduce the variance associated with the solution and fill the parameter space efficiently, the random numbers are sampled from a Sobol sequence. Therefore, technically, the following Monte Carlo is a "quasi Monte Carlo" solver since the random numbers are sampled from a quasi random and not from a pseudo random sequence. Marching the ray consists in finding the distances $\Delta p_x, \Delta p_y, \Delta p_z$, between the current location of the ray and the cell faces in direction `ray.dir`, specified by the angles ϕ and θ. The minimum distance, `ds`, determines which plane is crossed by the ray first. A schematic is displayed in figure 2.3, for which the ray intersects the x-normal plane first, such that the minimum distance `ds` will be equal to df_x. The radiative power of the initial cell (`QR`) is then calculated in a reciprocal fashion. Furthermore, the new ray position and cell index are updated accordingly. If the transmissivity drops under a certain tolerance `tol` (line 17), the ray is terminated and the remaining energy is dumped into the initial cell (line 29). The on-the-fly calculation of the blackbody intensity from Planck's law is prohibitive due to the excessive computations

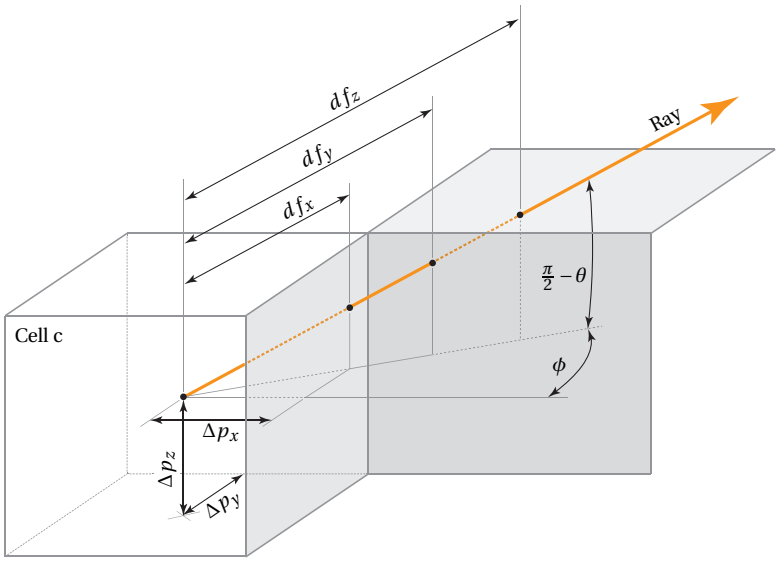

Figure 2.3: Schematic displaying the marching ray procedure.

Algorithm 1 ERMC CPU implementation

for cell **in** Cells **do** ▷ Loop over all finite volumes
  `QE` $\leftarrow 4\kappa_P(T_{max})\sigma T_{max}^4$ / `numberOfRays` ▷ Cell emission $Q^{R,e}$ in equation (2.19)
  for ray **in** Rays **do** ▷ Loop over rays
    procedure INITIALIZE
      $R_n, R_g \leftarrow$ `Rand`(Uniform distribution) ▷ Draw random numbers for indices n and g from a Uniform distribution
      $R_\theta, R_\phi \leftarrow$ `Rand`(Sobol distribution) ▷ Draw random numbers for angles from a Sobol distribution
      `ray.ind` $\leftarrow$ `cell.ind` ▷ Initialize the ray with the cell index i,j, and k
      `ray.pos` $\leftarrow$ `cell.center` ▷ Initialize ray starting coordinates with cell center coordintes x, y, and z
      `ray.dir` $\leftarrow$ direction(R_θ, R_ϕ) ▷ Find ray direction based on equation (2.20)
      `ray.transmissivity` $\leftarrow 1.0$
      `indDir` $\leftarrow$ sign(`ray.dir`) ▷ Ray direction in terms of index i,j, and k
      $n, g \leftarrow$ `findWavelength`(R_n, R_g) ▷ Binary search on CDF with R_n and CDF(n) with R_g
      $Ib1 \leftarrow$ `interpBlackbody`(n, temperature(`ray.ind`)) ▷ blackbody intensity of initial cell c
      $R_I \leftarrow Ib1 \times$ `interpAbsorpCoeff`(n, g, temperature(`ray.ind`)) ▷ R_I in equation (2.25)
      $R_I \leftarrow R_I$ / `interpBlackbody`(n, T_{max}) / `interpAbsorpCoeff`(n, g, T_{max})
    end procedure
    procedure MARCH
      while `ray.transmissivity` $> tol$ **do**
        $df \leftarrow \Delta p$/`ray.dir` ▷ Determine which face is crossed first (see figure 2.3)
        $ds \leftarrow min(df_x, df_y, df_z)$ ▷ Shortest distance is where ray crosses face
        $\kappa \leftarrow$ `interpAbsorpCoeff`(n, g, temperature(`ray.ind`))
        $\alpha \leftarrow 1 - \exp(-\kappa \times ds)$ ▷ equation (2.13)
        $Ib2 \leftarrow$ `interpBlackbody`(n, temperature(`ray.ind`))
        `Absorption` $\leftarrow$ `QE` $\times$ `ray.transmissivity` $\times\, \alpha \times (Ib2/Ib1 - 1) \times R_I$ ▷ equation (2.25)
        `QR(cell.ind)` $\leftarrow$ `QR(cell.ind)` $-$ `Absorption` ▷ radiative heat source of initial cell c
        `ray.pos` $\leftarrow$ `ray.pos` $+ ds \times$ `ray.dir` ▷ Update ray position
        `ray.ind` $\leftarrow$ `ray.ind` + `indDir` $\times (ds == [df_x, df_y, df_z])$ ▷ Update cell index depending on which face has been intersected
        `ray.transmissivity` $\leftarrow$ `ray.transmissivity` $\times (1 - \alpha)$ ▷ equation (2.14)
      end while
      `Absorption` $\leftarrow$ `QE` $\times$ `ray.transmissivity` $\times\, (Ib2/Ib1 - 1) \times R_I$
      `QR(cell.ind)` $\leftarrow$ `QR(cell.ind)` $-$ `Absorption` ▷ Dump the residual energy into the initial cell
    end procedure
  end for
end for

involved. To overcome this issue, the blackbody intensity is precomputed for the narrow band wavelengths and discrete points in the required temperature range and then stored in an suitable 2D table. The functions `interpBlackbody` and `interpAbsorptionCoeff` (lines 12-14, 20 and 22) perform linear interpolations of the spectral blackbody intensity and the absorption coefficient from the corresponding tables, respectively.

In the following sections, the 1D H_2O parallel slab case with parabolic temperature profile (case 10) will be used as a test case to compare the computational performances of the different implementations. As stated before, although the case is 1D in nature, it is calculated on a 3D grid with two periodic directions to mimic the computations for a DNS of a fully developed turbulent channel flow.

2.6.3. GPU IMPLEMENTATION

Graphical processing units have an architecture that, differently from CPUs, promote compute bound, highly parallelizable algorithms. The smallest parallel GPU units, called threads, run concurrently and are organized in thread blocks. All blocks can read and write into a global memory. The global memory is the "main" memory of the GPU, comparable to the heap in a C program, and has the slowest I/O access. Threads are grouped into groups of 32, termed "warps", which are executed by a single scheduling unit and thus follow a Single Instruction Multiple Thread (SIMT) execution model. Hence, all threads belonging to a particular warp execute the same instruction simultaneously. Due to these features, the objective of porting an application from CPU to GPU, is to increase parallelization to favour the SIMT execution. A further level of parallelization is obtained by using "streams". With this GPU feature, a device function, called "kernel" can be subdivided into parallel streams that run concurrently and independently, i.e. in a Multiple Instruction Multiple Data (MIMD) fashion, similar to multicore CPU computation (MPI parallelization). In compute bound problems, the use of streams is always recommended, since parallel MIMD execution is preferred to SIMT execution due to the absence of branch divergence (see section 2.6.4).

There are two main approaches to parallelize a radiative Monte Carlo algorithm on a GPU. Consider an example with a computational domain of five finite volumes (FV), each one sending five rays to march through the overall domain and five threads (Th) that can execute the marching of the rays. A schematic of this configuration is outlined in figure 2.4. The algorithm can then be parallelized by either ray parallelization or domain parallelization, which are outlined in more detail below.

In the first approach, each thread calculates one ray per finite volume. In this case, within each thread the finite volumes are executed in serial, while the rays per cell are parallelized. The solution will, therefore, be obtained by adding the partial results of each thread. The drawback of this approach is the continuous use of expensive atomic reductions (different threads have to read/write in the same memory location). On the other hand, if an ERMC formulation is employed, it is possible to use the second approach, which consists in having a single thread calculate all the rays belonging to an individual finite volume. This is possible due to the fact that, in a reciprocal formulation, the only information required to calculate the radiative source in a point are the rays leaving the latter. In the schematics of figure 2.4, the ray decomposition and the domain decomposition approaches are displayed on the left and on the right, respectively.

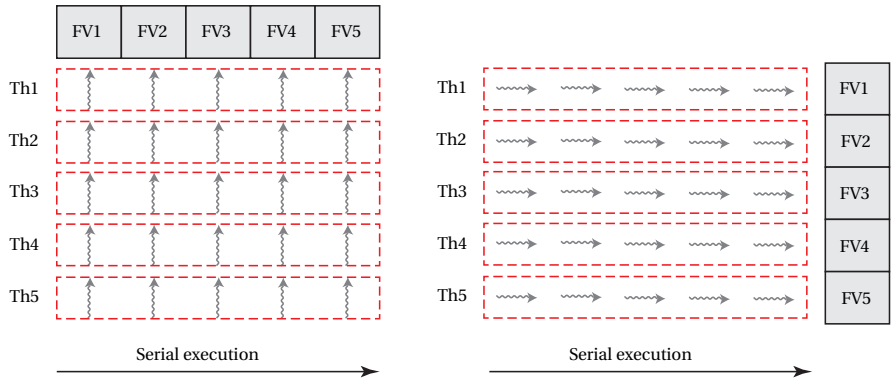

Figure 2.4: Schematic showing the concept of ray parallelization (left) and domain parallelization (right). This simple example is composed of five control volumes ($FV1-FV5$), five rays per cell (gray lines) and five threads working in parallel ($Th1-Th5$)

It is important to note that it is also possible to combine the two methods by exploiting the block/thread arrangement. Namely, divide the domain through different blocks and implement a ray parallelization for the finite volumes contained by the block. This configuration would speed up the necessary atomic reductions by enabling the use of shared memory that can be accessed by the whole block. However, shared memory is limited in size and for this reason this approach cannot scale efficiently to larger grids. Given these reasons, we conclude that the domain parallelization approach is more suitable for coupling a GPU Monte Carlo code with DNS.

Algorithm 2 displays the GPU implementation of the ERMC based on domain parallelization. The implementation closely resembles the one displayed in algorithm 1, with the difference that the routine now consists of two different GPU functions (or kernels) highlighted in light blue. The first one is in charge of initiating the calculation on the GPU, which immediately returns the control to the CPU, while the second routine retrieves the results. This approach enables a completely asynchronous computation of the GPU and allows to perform other tasks on the CPU (line 26) that would otherwise remain idle. Each kernel is executed `stream_max` times and computes (1/`stream_max`)th of the domain. The stream loops (lines 3 and 27) contain only non-blocking statements that enable a parallel stream execution. The core of the domain parallelization consists in mapping the thread index to a specific finite volume (lines 8-10). The for-loop over the computational cells is then replaced by a GPU-grid-stride loop that runs over the thread index (line 7) and covers all cells in the domain. The random number generation is performed on-the-fly by employing the CUDA library cuRand. The solution is stored in a global device variable `solution`, which is then retrieved by the second kernel once the computations are complete.

The GPU implementation is tested for case 10 (see table A.2, plane parallel slab of 1 [atm] H_2O with parabolic temperature profile) on a Tesla K40M. The execution speed is benchmarked against the CPU implementation executed on an Intel Xeon E5-2680 @ 2.40GHz. Table 2.1 shows the computational time required as a function of mesh size and number of rays per cell. In all the test cases, the maximum allowed number of

Algorithm 2 ERMC GPU implementation

```
1:  __device__ solution[stream_max][Ncell/stream_max]                          ▷ global device variable
2:  cudaMemcpyAsync(Temperature T, absCoeff κ, Grid, CopyFromCPUtoGPU)         ▷ memory copy to device (GPU)
3:  for s = 0; s<stream_max do                                                 ▷ loop over streams
4:      procedure KICKOFF(thread t, block b, stream s)                         ▷ First kernel for stream number s
5:          __Shared__ state = cuRandInit                                      ▷ cuRand variable in shared memory
6:          tid ← threadIdx.x + blockIdx.x × blockDim.x
7:          for idx = tid; idx < Ncells; idx = idx + blockDim.x × gridDim.x do  ▷ Grid-stride loop over the GPU grid
    structure
8:              cell.ind.i ← idx/(kmax × jmax) + 1 + s × imax/stream_max        ▷ Mapping thread index to mesh
9:              cell.ind.j ← idx/kmax + 1 − (cell.ind.i − 1 − s × imax/stream_max) × jmax
10:             cell.ind.k ← idx − kmax × (cell.ind.j − 1 + (cell.ind.i − 1 − s × imax/stream_max) × jmax + 1)
11:             QE ← 4κ_P(T_max)σT⁴_max/numberOfRays
12:             for ray in Rays do
13:                 procedure INITIALIZE
14:                     R_n, R_g ← cuRand(Uniform distribution, state)
15:                     R_θ, R_φ ← cuRand(Sobol distribution, state)           ▷ As in the CPU algorithm, but with cuRand instead
16:                     Lines 6 – 14 in Algorithm 1
17:                 end procedure
18:                 procedure MARCH
19:                     Lines 17 – 23 in Algorithm 1
20:                     solution[s][idx] ← solution[s][idx] − Absorption        ▷ device global variable that allows
    asynchronous computations
21:                     Lines 25 – 30 in Algorithm 1
22:                 end procedure
23:             end for
24:         end for
25:     end procedure
26: end for
27: Perform other tasks
28: for s = 0; s<stream_max do                                                 ▷ loop over streams
29:     procedure RETURN(thread t, block b, stream s)                          ▷ Second kernel for stream number s
30:         tid ← threadIdx.x + blockIdx.x × blockDim.x
31:         for idx = tid; idx < Ncells; idx = idx + blockDim.x × gridDim.x do
32:             QR[idx] ← solution[s][idx]
33:         end for
34:     end procedure
35:     cudaMemcpyAsync(Solution QR, CopyFromGPUtoCPU)                         ▷ memory copy to host (CPU)
36:     cudaDeviceReset()                                                      ▷ clear device memory allocations
37: end for
```

streams (16) is used, while the number of blocks and threads per block are calculated such that the GPU resources are fully utilized. The default values for the parameters that are not varied are a grid size of 64^3 and $6 \cdot 10^4$ rays per cell. The results in table 2.1 show that the speedup obtained with a straightforward GPU implementation, using domain decomposition, is already relatively high. Nonetheless, with the increase of problem size, the speedup does not show a satisfying improvement, reaching values of around $\sim 50\times$. This apparent limit is caused by the finite resources of the GPU. Being a compute bound algorithm, the scarce resource is the amount of registers per thread that sets the maximum number of threads running concurrently. If the number of registers is increased, the scheduling units serialize the execution of the exceeding warps. As a consequence, no further gain is observed when increasing the mesh size or the number of rays per cells. Note that the values in parenthesis for the CPU execution time in table 2.1 are extrapolated from the scaling of the other results and, as such represent an estimation only.

Table 2.1: Comparison between standard CPU and GPU implementation

grid size	16^3	32^3	48^3	64^3	96^3	128^3	160^3
CPU	269.4 s	2921.1 s	13182.7 s	39313.3 s	271844.4 s	(920183.3) s	(2452230.3) s
GPU	11.8 s	84.8 s	394.0 s	1169.5 s	6143 s	19623 s	47539 s
Speedup	22.8×	34.4×	33.5×	33.6×	44.3×	(46.9)×	(51.6)×
rays per cell	$6\cdot10^2$	$1.5\cdot10^3$	$6\cdot10^3$	$1.5\cdot10^4$	$3\cdot10^4$	$6\cdot10^4$	$1.5\cdot10^5$
CPU	369.7 s	961.7 s	3928.6 s	10432.2 s	19661.1 s	39313.3 s	132641.3 s
GPU	14.1 s	31.8 s	119.2 s	294.4 s	585.8 s	1170 s	2916 s
Speedup	26.2×	30.2×	33.0×	35.4×	33.6×	33.6×	45.5×

2.6.4. ALGORITHM ACCELERATION

A naive GPU implementation, as demonstrated in the section above, is usefull to provide a certain level of speedup, but is certainly not enough to address the computational requirements of a DNS simulation. In particular, the main problems and bottlenecks of such an algorithm are the slow memory access and the large inactivity of the threads due to the SIMT execution model. For this reason, we will address these issues by implementing acceleration techniques that will significantly reduce the execution time and thus enable a full coupling between DNS and the GPU Monte Carlo code.

TEXTURE MEMORY

Due to the GPU architecture, memory input and output is heavily affected by the access pattern of the threads. In particular, the global memory of a GPU is optimized for coalesced access. A coalesced memory transaction is one in which all of the threads in a half-warp access global memory at the same time. That is to say, consecutive threads should access consecutive memory addresses in the global memory to obtain efficient memory loads/stores. To avoid penalties associated with uncoalesced transactions, it is possible to store variables in registers (the memory associated with the single thread) or shared memory, which is fast-access memory common to all threads in a block. Unfortunately, these two memory types are severely limited in size (on a tesla K40M shared memory consists of only 49 kB per multiprocessor for a total of ~ 735 kB). Therefore, after all the fast memory resources have been depleted, it is necessary to store the bulk of the variables in the global memory. Since most memory fetches depend on the drawing of random numbers, it is not straightforward to predict which address consecutive threads might access. As a consequence, coalesced memory transactions are impossible to achieve in a Monte Carlo simulation. An easy way to optimize memory input and output is hence to employ texture memory. Texture memory is a type of read-only memory, which has been developed for graphical applications. Instead of storing variables linearly, as global memory does, texture memory is designed to optimize the spatial locality of memory access. In other words, each point is associated to a coordinate, and the most efficient memory fetch occurs when consecutive threads access adjacent coordinates in the texture memory instead of consecutive addresses. This scenario is much more likely in a domain parallelized Monte Carlo simulation. The input values to access a texure memory location are float coordinates, while the value returned from the memory is a linear (or trilinear in case of a 3D texture) interpolation of the adjacent

Table 2.2: Execution time with classical versus textured memory approach.

grid size	16^3	32^3	48^3	64^3	96^3	128^3	160^3
classic	11.8 *s*	84.8 *s*	394.0 *s*	1169.5 *s*	6143 *s*	19623 *s*	47539 *s*
texture	8.5 *s*	48.6 *s*	260.0 *s*	716.0 *s*	4381 *s*	12343 *s*	34047 *s*
Speedup	1.38×	1.74×	1.52×	1.64×	1.40×	1.59×	1.40×
rays per cell	$6\cdot10^2$	$1.5\cdot10^3$	$6\cdot10^3$	$1.5\cdot10^4$	$3\cdot10^4$	$6\cdot10^4$	$1.5\cdot10^5$
classic	14.1 *s*	31.8 *s*	119.2 *s*	294.4 *s*	585.7 *s*	1170 *s*	2916 *s*
texture	9.6 *s*	20.6 *s*	74.3 *s*	180.7 *s*	358.6 *s*	714.5 *s*	1784 *s*
Speedup	1.47×	1.54×	1.60×	1.63×	1.63×	1.64×	1.64×

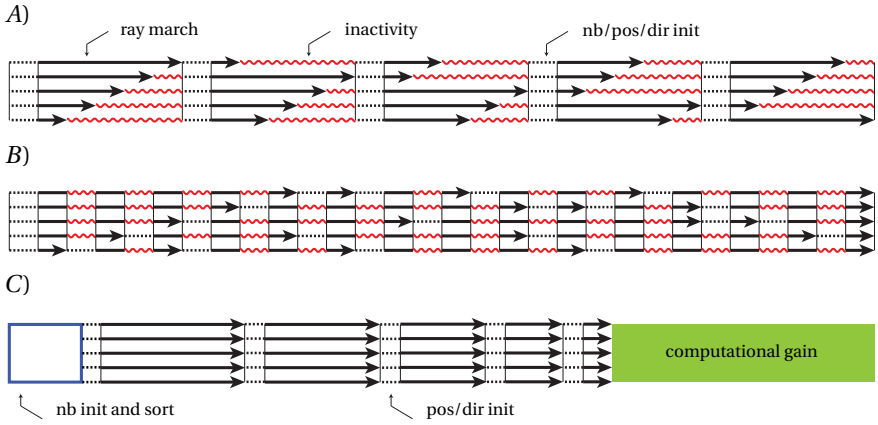

Figure 2.5: Example of a marching procedure for different GPU MC schemes. (*A*): standard MC implementation; (*B*): reinitialization MC; (*C*): sorting MC. The different rows represent the sequential execution of different threads in a warp. We show here only 5 threads and 5 rays to simplify the scheme, but in reality there are 32 threads in a warp and tens of thousand rays per thread. Note that the length of the arrows and the dashed lines (representing marching and initialization) are always preserved among the three schemes. On the other hand, the position and direction initialization time (dashed lines) is shorter in the last scheme (*C*), since the wavelength has already been chosen in the preprocessing step (blue box).

values. This feature is extremely useful as it provides fast linear interpolation, which is repeatedly required in a spectral MC code (lines 12, 13, 14, 20 and 22 in algorithm 1). Variables that were residing in the global memory (temperature, blackbody intensity and absorption coefficient), are therefore relocated to the texture memory. The results of the texture memory implementation are shown in table 2.2 in comparison to the standard GPU implementation. The use of texture memory results in a computational gain for all the different settings. Nonetheless, the speedup tends to decrease with mesh size. This behaviour could be caused by the reduced spatial locality of memory access for contiguous threads on a finer grid (i.e. the ray travels further, distancing itself from the aligned source cells). On the other hand, the speedup increases if more memory transactions are performed (i.e., increasing the numbers of rays per cell). While this implementation has been performed for a structured mesh, the benefits will be equivalent if the same warp behaviour is ensured on an unstructured grid (adjacent source point for consecutive threads).

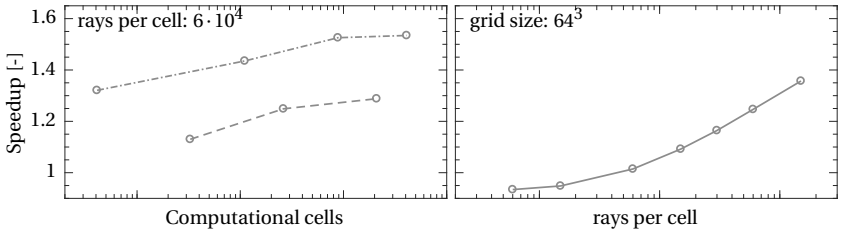

Figure 2.6: Speedup obtained with the narrow-band sorting technique. In the figure on the left, the dashed line connects the points characterized by a mesh which is 2^n·streams (16^3, 32^3 and 64^3), while the dashed dotted line all the other points

NARROW BAND SORTING

The SIMT execution model can lead to a severe performance loss, known as "branch divergence". A warp executes one common instruction at a time, so the threads must wait until the execution is terminated for the entire warp before proceeding. For this reason, full efficiency is realized when all 32 threads of a warp follow the same execution path (i.e., execute the same instruction at the same time). If threads of a warp diverge due to a data-dependent conditional branch (`if` or `while` statements), the warp executes all the paths entirely, disabling threads that are not on that path. For the purpose of correctness, the SIMT execution model can be essentially ignored. However, in terms of code efficiency, thread divergence is a serious issue and has to be addressed, particularly in the case of a MC simulation, where the abundant while loops and if conditions cause large thread inactivity.

A simple and straightforward approach to reduce inactivity, would be to re-initialize the ray whenever a marching is terminated within the warp. On the other hand, re-initializing the ray on a particular thread forces to temporarily disable the threads that have not yet completed the marching, serializing the initialization procedure. As a consequence, the execution time of multiple initializations might become longer than the benefit obtained by the lower inactivity during the marching procedure.

Taking into account the properties of the ray, leads to a more effective solution. For example, when two different threads in the same warp are marching rays with different wavelength, they handle different absorption coefficients. The ray with a higher κ_ν will complete the marching quicker than the one with lower κ_ν, due to the shorter path length. Since a Monte Carlo routine requires random draws of the wavelength based on a probability distribution function, it is a common scenario that threads are handling absorption coefficients of different order of magnitude. Due to the SIMT execution model, the time required for the warp to complete the current ray tracing is dictated by the thread with the lowest absorption coefficient. It is therefore beneficial to have threads handling absorption coefficient of similar value at all times, such that the tracing might complete simultaneously. To achieve this, it is necessary to precompute all wavelengths for each ray in each finite volume and sort them based on the magnitude of κ_ν. Consequently, threads will always march rays from the lowest to the highest κ_ν. While these values might be slightly different for different threads, the order of magni-

Table 2.3: Speedup using the narrow band sorting. The values of the speedup are referred to the textured execution times of table 2.2

grid size	16^3	32^3	48^3	64^3	96^3	128^3	160^3
Time	6.4 *s*	43.2 *s*	180.8 *s*	573.0 *s*	2866 *s*	9597 *s*	22189 *s*
Speedup	1.32×	1.13×	1.44×	1.25×	1.52×	1.29×	1.53×
rays per cell	$6\cdot10^2$	$1.5\cdot10^3$	$6\cdot10^3$	$1.5\cdot10^4$	$3\cdot10^4$	$6\cdot10^4$	$1.5\cdot10^5$
Time	10.3 *s*	21.7 *s*	73.2 *s*	165.5 *s*	308.0 *s*	573.2 *s*	1313 *s*
Speedup	0.93×	0.95×	1.01×	1.1×	1.16×	1.25×	1.36×

tude of κ_ν will be similar, thus significantly reducing the branch divergence of the warp.

The different configurations are outlined in figure 2.5. The first scheme is a standard MC that does not account for any branch divergence reduction technique. Scheme *B* shows a re-inizialization scheme in which, wherever a thread in the warp completes the marching, the ray is immediately re-initialized. It is clear that this scheme is successful only if the cost of initializing a ray is smaller than the tracing of the shortest ray. This is not the case in a medium with a high absorption, where rays can be terminated within 5 steps. Scheme *C* shows the advantage of reordering the rays based on their absorption coefficient which aligns the ray marching executions.

The results of the tests for a narrow-band sorting algorithm are shown in table 2.3 and figure 2.6. The speedup obtained with sorting the narrow bands is larger when the grid is not 2^n·streams (32, 64, 128). This is caused by an inefficient mapping of the grid onto the device resources, which in this case are powers of 2. Indeed, by sorting the narrow bands, it is possible to correct the penalties associated with an inadequate mapping. It is possible to notice that the speedup increases with increasing the number of mesh points, until it reaches a plateau for large mesh sizes. On the other hand, if the number of rays per cell are too small, the advantage of a lower warp inactivity is overshadowed by the cost of the sorting procedure. Contrarily, increasing the number of rays per cell leads to an linear growth of the speedup, since the warp inactivity is efficiently replaced by the ray marching computation.

It is interesting to notice the difference between the speedup of the narrow-band sorting scheme with respect to mesh size and the speedup using a texture memory approach only. While the first one increases, the latter decreases with grid size. This difference shows the interplay between memory transactions and computations as the mesh size increases, highlighting the larger relative importance of compute statements with increasing mesh size.

MULTIGRID

The radiative intensity is absorbed exponentially as function of the absorption coefficient and the travelled distance. Therefore, the intensity absorbed by traversing a cube of size Δx^3 will be roughly proportional to

$$I_{abs} \sim (1 - \exp(-\kappa_\nu C \Delta x)) \,. \tag{2.29}$$

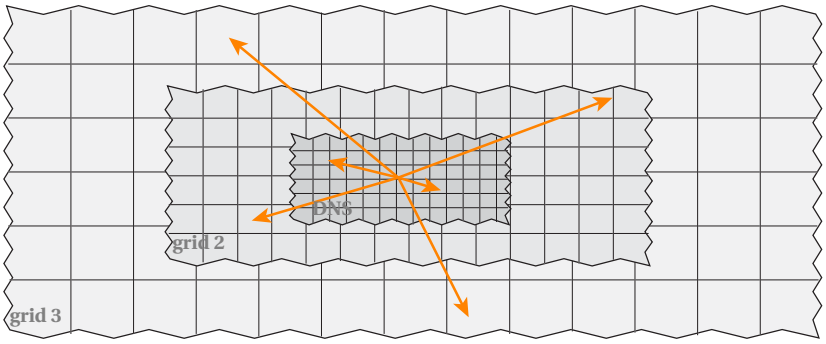

Figure 2.7: Schematic showing the concept of the mesh coarsening scheme. The orange lines symbolize the marched rays. Several grids are overlayed one on top of each other. The ray falls onto the coarsened mesh when it reaches the maximum number of steps in the current grid. The concept is shown here in two dimensions for simplicity.

with C a proportionality value depending on orientation. Consequently, the intensity of the ray leaving the cell is

$$I_{out} = I_{in} - I_{abs} \sim \exp\left(-\kappa_\nu C \Delta x\right), \tag{2.30}$$

which signifies that, for a low κ_ν, the intensity gradient of the propagating ray will be mild and the required cell size Δx can be relatively large. Vice versa, if κ_ν is large, a lower Δx is necessary to capture the steep intensity gradient. If an adequate Δx is chosen as a pre-processing step (as it could be done in a gray gas medium) the mesh will be over-resolved for the rays with low absorption, resulting in an inefficient ray tracing. Nevertheless, since a high κ_ν ray will be terminated fairly quickly, it requires a high resolution only on a small zone around the source point. On the contrary, a ray with low absorption will propagate far into the domain. By combining these two features of rays with different absorption coefficient, it is possible to construct a mesh strategy that optimizes the ray tracing, while retaining a high accuracy. The objective is to have a grid that is fine close to the starting cell and gradually coarser as the ray travels further away from the initial point. To obtain this effect, it is possible to overlay several meshes characterized by different cell sizes. The temperature values will be filtered on the coarser meshes from the DNS solution which represents the finest mesh level (radiative heat transfer does not introduce new spatial wavenumbers, so the smallest radiative length scales are as small as the Batchelor scales). For all finite volumes, the ray tracing commences on the DNS mesh and the ray is allowed to step onto the current mesh a fixed number of times. If the ray is not exhausted, it falls into a coarser mesh and so forth, until the last mesh is reached. The last (and coarsest) mesh will trace the ray until depletion. The only added overhead is the cost of the filtering onto coarser meshes, which is completely irrelevant compared to the gain in computational speed obtained. A similar method, involving patches of interest, was previously implemented by Humphrey et al. in two different occasions. Namely, in a parallel CPU Monte Carlo implementation [60] and in a gray gas GPU implementation [45]. They used this technique to reduce computation and communication time. On the other hand, we highlight the additional benefits

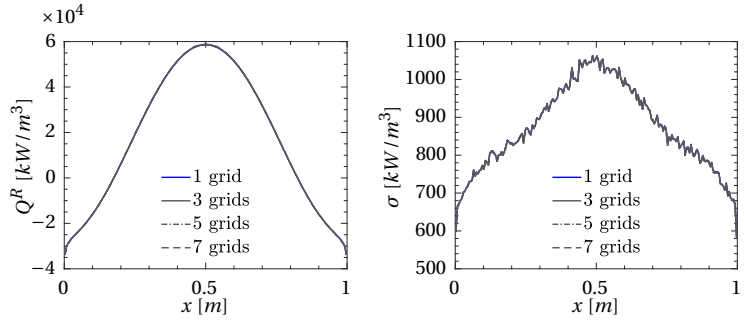

Figure 2.8: Comparison of the results for the parabolic H_2O case for different numbers of overlayed coarsened mesh used. 5 steps are allowed in each mesh. *a*): Radiative heat source, *b*): standard deviation

that such a method has in a non-gray GPU implementation, other than the reduction of computations. Here, due to the SIMT execution model, threads characterized by higher absorption rays will remain inactive, while waiting for the lower absorption rays to complete the computations. In this case, it is possible to tailor the method towards a pure reduction of thread inactivity by targeting the resolution of the higher impact, high absorption, rays. If this is done, the solution retains its accuracy and the parallel efficiency is greatly enhanced.

To optimize the number of steps in subsequent meshes, it is possible to rely on the transmissivity of the grids by specifying a fraction of intensity absorbed in the n$^{\text{th}}$ grid (p_n). As a consequence, the number of steps in the n$^{\text{th}}$ grid (s_n) will be

$$s_n = \texttt{int}\left(\frac{\ln\left(1-\sum_{m=1}^{n-1} p_m\right)}{\kappa_{\text{ref}}\Delta x_n} - \frac{\ln\left(1-\sum_{m=1}^{n} p_m\right)}{\kappa_{\text{ref}}\Delta x_n} \right). \tag{2.31}$$

Here, κ_{ref} is a reference absorption coefficient and can be specified in different ways. Using the Planck-mean absorption coefficient ($\kappa_{\text{ref}} = \kappa_p$) is the safest option to ensure unaltered accuracy. If execution speed has to be minimized, the largest average narrow-band absorption coefficient in the spectrum ($\kappa_{ref} = \overline{\kappa}_{max}$) can be employed. On the other hand, a more balanced choice is the average absorption coefficient of the most influential band ($\kappa_{ref} = \overline{\kappa}_n$) calculated as

$$\overline{\kappa}_n = \sum_{g=1}^{Nq} \omega_g k_{n,g}\,, \text{ where } n \text{ is the band containing } \overline{\nu} = \sum_{n'=1}^{N_b} \nu_{c,n'} \cdot f'_n\,, \tag{2.32}$$

and $\nu_{c,n'}$ is the central wavenumber of band n'. Since the wavenumber is sampled from the maximum temperature of the considered system, κ_p, $\overline{\kappa}_{max}$ and $\overline{\kappa}_n$ can be calculated from the maximum temperature spectrum only.

In practice, the correct fractions p_n that leave the results unaltered are not known a-priori. Therefore, to ensure an optimal number of steps, a trial and error procedure has to be employed until the results (both in terms of Q^R and σ) are method-independent. It is possible then to assess the implementation of the grid coarsening by calculating the fractions p_n from equation (2.31) and use these for future implementations. In addition,

more conservative settings (larger p_n in finer grids) have to be adopted in case of steeper temperature gradients and inhomogeneous cases.

Figure 2.7 shows a 2D representation of the mesh coarsening concept, while figure 2.8 shows the solutions of the test case employing the multigrid technique. In particular, the results shown in figure 2.8 have been obtained with a maximum of 7 overlayed grids corresponding to $192^3 \rightarrow 96^3 \rightarrow 48^3 \rightarrow 24^3 \rightarrow 12^3 \rightarrow 6^3 \rightarrow 3^3$. The rays were allowed to travel a maximum of 5 steps in each grid, while proceeding until termination on the last one. The absorbed fraction for different choices of κ_{ref}, based on equation (2.31), is shown in table 2.4. When using κ_p or $\overline{\kappa}_n$ as a reference, the largest absorption occurs in the third grid. On the other hand, the rays represented by $\overline{\kappa}_{max}$ are absorbed almost completely within the first grid.

Table 2.4: Absorbed fraction (p) in seven successive grids with 5 steps per grid. In case less than seven grids are used, the last grid absorbs the remaining intensity. For example, if three grids are used for $\kappa_{\text{ref}} = \kappa_p$, the first grid absorbs $p_1 = 12.4\%$, the second $p_2 = 20.3\%$, while the third the remaining intensity $p_3 = (100 - 12.4 - 20.3)\%$.

	κ_{ref}	p_1	p_2	p_3	p_4	p_5	p_6	p_7
κ_p	(5.07 [m^{-1}])	12.4%	20.3%	27.6%	25.9%	12.1%	1.6%	0.1%
$\overline{\kappa}_{max}$	(98.1 [m^{-1}])	92.22%	7.73%	0.05%	0.0%	0.0%	0.0%	0.0%
$\overline{\kappa}_n$	(8.80 [m^{-1}])	20.5%	29.2%	30.2%	16.9%	3.1%	0.09%	0.01%

As shown in figure 2.8, the results of the test case are unaffected by the grid coarsening technique, both in terms of radiative power source and its standard deviation. The speedup obtained, defined as t_1 / t_n, where t_1 is the time required for completing the calculation with one grid while t_n with using n grids, is shown in table 2.5. Despite the negligible influence in the results, by employing the multigrid technique, it is possible to reduce the computational cost by a factor that is roughly equal to the number of grids used. The reduction of thread inactivity using this method is clearly visible by comparing table 2.4 and table 2.5. By changing the implementation from 4 to 7 grids, the intensity fraction that is computed on the coarser grids is only 13.9%, 0.0% and 3.2% for κ_p, $\overline{\kappa}_{max}$ and $\overline{\kappa}_n$, respectively. Nonetheless, the speedup increases by almost a factor of 2.

Table 2.5: Speedup using multiple overlayed grids. 5 steps per grid

grid number	1	2	3	4	5	6	7
Speedup	1×	1.4×	2.6×	4.2×	5.8×	6.6×	7.1×

OVERALL PERFORMANCE INCREASE

An overview of the scaling performance using different acceleration techniques is given in figure 2.9 for varying problem sizes. Note that the implementations are additive (i.e., sorting employs texture memory allocations and multigrid performs also a narrow-band sorting). A coarsening ratio of 2 has been employed for successive grids in the multigrid implementation. The smallest allowed mesh had a size of 3^3, resulting in 3 grids for 16^3, 4 for 32^3, 5 for 48^3 and 64^3, and 6 grids for 96^3, 128^3 and 160^3. Again, only 5 steps were allowed in each level. The scaling of all implementations is well described by power

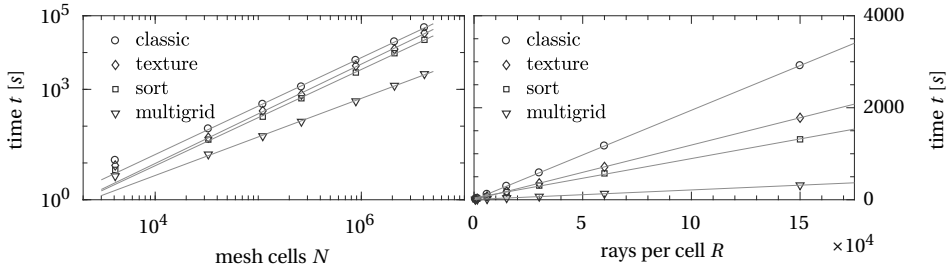

Figure 2.9: Scaling of the code with grid cells and rays per cell.

functions of mesh cells N and linear functions of the number of rays R. The gray lines depicted in figure 2.9 take the following form

- classic $t \propto N^{1.32}$, $t \propto 0.98R$,
- texture $t \propto N^{1.35}$, $t \propto 0.96R$,
- sorting $t \propto N^{1.31}$, $t \propto 0.7R$,
- multigrid $t \propto N^{1.05}$, $t \propto 0.7R$,

While a texture memory allocation has large benefits for the investigated cases, the computational gain is bound to decrease when the grid size increases (as seen in section 2.6.4) as given by the larger exponent when compared to the classic implementation ($1.35 > 1.32$). On the contrary, with a multigrid scheme it is possible to obtain a quasi-linear scaling Monte Carlo code with mesh size (exponent ≈ 1). Moreover, the narrow band sorting procedure allows a scaling greater than ideal with respect to the rays per cell ($0.7 \cdot R$). With more rays being launched, the drawn absorption coefficients fill the whole spectrum space efficiently, replacing the inactivity by aligning more effectively the thread marching.

It is demonstrated that, by employing these optimization techniques, it is possible not only to reduce the computational time, but also to significantly improve the scaling of the code with problem size. The performances of the optimized GPU Monte Carlo code, compared to a serial CPU Monte Carlo implementation executed on an Intel Xeon E5-2680 @ 2.40GHz, is shown in table 2.6. It has to be reminded that, while texture memory allocation and narrow band sorting only improve computational speed on a GPU, multigrid, although less effective, can be also implemented for a code that runs on a CPU, leading to an increase of code efficiency. The maximum speedup achieved was $570.4\times$ for a grid size of 96^3. For the largest problems, the CPU computational time was estimated from the scaling. Based on this estimation, we expect a impressive increase of speedup, differently from what is observed in table 2.1 (potentially we could achieve $938.8\times$ for a 160^3 grid).

Table 2.6: Comparison between standard CPU implementation and optimized GPU implementation

grid size	16^3	32^3	48^3	64^3	96^3	128^3	160^3
CPU	269.4 s	2921.1 s	13182.7 s	39313.3 s	271844.4 s	(920183.3) s	(2452230.3) s
GPU	4.4 s	17.1 s	53.7 s	132.8 s	476.6 s	1262 s	2612 s
Speedup	61.2×	170.8×	245.5×	296.0×	570.4×	(729.1)×	(938.8)×
rays per cell	$6\cdot10^2$	$1.5\cdot10^3$	$6\cdot10^3$	$1.5\cdot10^4$	$3\cdot10^4$	$6\cdot10^4$	$1.5\cdot10^5$
CPU	369.7 s	961.7 s	3928.6 s	10432.2 s	19661.1 s	39313.3 s	132641.3 s
GPU	4.1 s	6.3 s	17.1 s	37.5 s	69.9 s	132.4 s	316.0 s
Speedup	90.2×	152.7×	229.7×	278.2×	281.3×	296.9×	419.8×

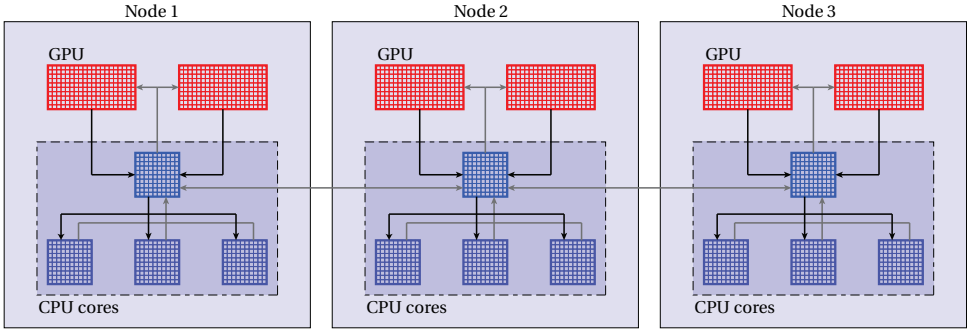

Figure 2.10: Schematic representing the multi GPU implementation. The domain is decomposed on different nodes. In each node one CPU core communicates to the GPUs the entire temperature domain and returns the computed radiative heat source to the CPUs within the node.

2.7. FLUID-RADIATION COUPLING

The two modules are coupled through the temperature field. As the full code is parallel, to ensure low execution time, care must be given to the linking of the two modules. The DNS code is implemented on CPUs and parallelized using MPI through the software library 2DECOMP&FFT http://www.2decomp.org, which is developed in the UK by NAG and freely available. The computational mesh is divided into `p_row*p_col` cores with the streamwise direction divided into `p_col` and the spanwise direction divided into `p_row` subdivisions. The communication of the flow variables between the cores is implemented with the use of ghost cells, whose values are updated using the `update_halo` routine in the `decomp_2d` library. Additionally, the fast Fourier transforms (FFT) require the use of the routines `transpose_x_to_y` and `transpose_y_to_z` from the same library.

FVM-DNS COUPLING

The finite volume radiative code is implemented on CPUs as the DNS code. As such, the parallelization is implemented in the same way, with the use of ghost cells to communicate intensity values between cores. The radiative heat source calculation is around 10 times slower than the fluid flow calculation. Nevertheless, radiative heat transfer is calculated, sequentially with the DNS solution, every fluid time step. As soon as the radiative solver reaches a converged result, it returns the radiative heat source Q^R to the

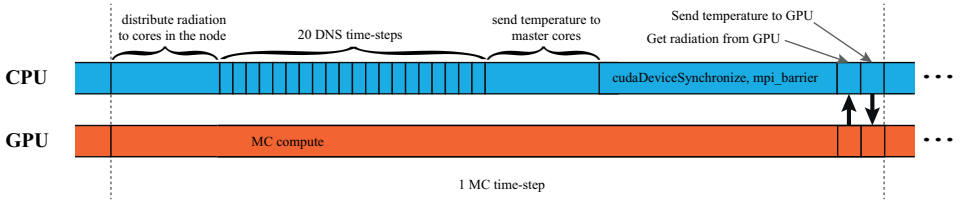

Figure 2.11: Schematic showing the layout of the asynchronous tasks for the CPU and the GPU. The length of the segments is not to scale. Here 20 DNS time-steps per MC time step are specified. On the other hand, for fully developed simulations, usually comprising of no more than 15 million mesh cells, 5 DNS time steps are sufficient to occupy efficiently the CPU compute time.

DNS solver with uses it in the energy equation for the calculation of $(\rho\theta)^{n+1}$. Only the radiative heat source at time step n is specified in the RHS of the energy equation.

MC-DNS COUPLING

The coupling between fluid flow and radiative heat transfer is implemented with the use of MPI libraries that handle communications between CPU cores. Each node has a master core which communicates with the available GPUs on the node. Thanks to the reciprocal formulation, the GPUs calculate the radiative source term only on the domain handled by the associated node. On the other hand, to perform ray tracing and to avoid boundary communication, all GPUs require the complete temperature field. A schematic of the multi GPU implementation is shown in figure 2.10. The gray arrows show the communication of the temperature field, while the black arrows show the path of the computed Q^R . The memory transfer to and from the GPU is completely asynchronous, such that the CPUs proceed to calculate additional fluid time steps, while the GPUs compute the radiative heat source. As a consequence the CPU computation is completely hidden by the radiative power calculation. Figure 2.11 shows the implementation of the CPU/GPU tasks and the synchronization between the two.

The code has been tested on the Cartesius' cluster located in Amsterdam, The Netherlands, on the accelerator island composed of 60 nodes containing 2 Tesla K40M each. The scaling of the code was examined up to 64 GPUs. The results are shown in figure 2.12. The strong scaling of the code is calculated by keeping the grid size constant (192^3 in this case) and increasing the number of GPUs. The quantity shown in figure 2.12(a) is the time required for one time step to complete on 1 GPU over the time required for N GPUs. As expected by the computational nature of the code, the scaling is almost ideal. Moreover, figure 2.12(b) shows the weak scaling efficiency, tested with and without the use of the multigrid scheme. In this case the grid size is increased proportionally to the number of GPUs used, with one GPU always computing on a 32^3 mesh. Since the problem size increases with the number of GPUs used, the code greatly benefits from the multigrid scheme, which improves the weak scaling efficiency from $\propto GPU^{-0.2}$ to $\propto GPU^{-0.08}$

To prove the level of accuracy achievable in an acceptable time span, the radiative power is calculated for a turbulent temperature field obtained from a DNS. The DNS represents a fully developed turbulent channel flow with a bulk Reynolds number of $Re = 3750$ and isothermal walls at 955 and 573 K at the bottom and top, respectively. The

flow is periodic in the streamwise and spanwise directions. The radiative properties of the medium are those of water vapour at 1 atm. The Planck mean absorption coefficient varies roughly from 5.5 m^{-1} near the hot wall to 15 [m^{-1}] near the cold wall and, therefore, can be considered optically thick. In such conditions, the turbulent radiative power spectrum is characterized by short length scales, comparable to the largest wavenumbers of the turbulent temperature spectrum. Therefore, the radiative heat source requires to be accurate on the full DNS mesh. The mesh is composed of 192^3 elements, while the box dimensions are 2, 2π and 4π m in the wall-normal (y), spanwise (z) and streamwise (x) directions, respectively. $6 \cdot 10^4$ rays per cells were used to calculate the radiative power. Snapshots of the radiative field are shown in figure 2.13. The left contours show the temperature field (in K), while the contours on the right are the calculated radiative power in kW/m^3. The top figures show the fields at a y location of 1.1 m (roughly at the center of the channel), while the bottom figures show a wall-normal plane located near the cold wall ($y \approx 1.97$ m). As seen from the figures, the radiative field is solved with a high accuracy, matching quite closely the turbulent structures of the temperature field as expected for a highly participating medium. In addition, as it will be demostrated later in chapter 3, in the center of the channel, the turbulent radiative field filters the large turbulent wavenumbers, due to the action of incident radiation acting on the isotropic temperature structures. As a result, the radiative field is composed primarily of smaller wavenumbers when compared to the corresponding temperature field.

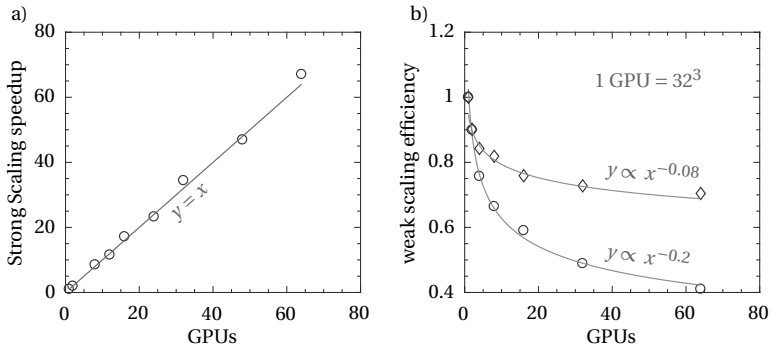

Figure 2.12: Performance of a multi GPU implementation. *a*): strong scaling speedup (t_1/t_n). *b*): weak scaling efficiency (t_1/t_n). Circles are results obtained without using multigrid and diamonds employing the multigrid technique. t_1 is the execution time on 1 GPU and t_n is the execution time on n GPUs

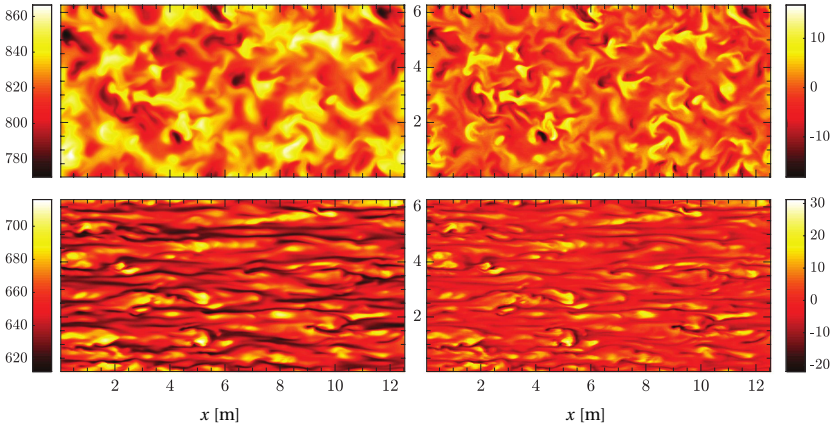

Figure 2.13: Instantaneous snapshots on a wall-parallel plane ($x-z$) at $y = 1.1$ (top) and $y = 1.97$ (bottom). Left: temperature T K. Right: Radiative power Q^R kW/m^3.

3

MODULATION OF TURBULENCE-RADIATION INTERACTION BY OPTICAL THICKNESS

It is well known that the radiative heat source has a non-monotonic dependency on the absorption coefficient due to the non-local nature of radiation [62]. As such, radiative heat transfer can be divided into three regimes: optically thin $\tau \ll 1$, optically intermediate $\tau \approx 1$ and optically thick $\tau \gg 1$, where optical thickness is defined as the ratio of geometrical to radiative length scales. In this chapter we extend this categorization to TRI by investigating the differences in radiative effects for optically thin, intermediate and thick turbulent flows. To simplify the analysis, the flow is assumed to behave as a gray gas with a constant absorption coefficient. We show that TRI changes drastically based on optical thickness, not only in magnitude, but in behaviour itself.

This chapter is based on the following publication, Silvestri, Patel, Roekaerts & Pecnik, Turbulence radiation interaction in channel flow with various optical depths, J. Fluid. Mech., **753** (2018), 360. [61]

3.1. INTRODUCTION

In a flow subjected to radiative heat transfer the most affected quantity is the temperature field. In particular, the long-range radiative heat transfer results in smoothing the gradients and a reduction of temperature fluctuations. In this context we can distinguish between an (1) indirect effect, whereby mean radiation reduces average temperature gradients and, therefore, reduces production of temperature fluctuations and a (2) direct effect. The latter is at the core of TRI and refers to the direct destruction of temperature fluctuations from the fluctuations of radiative power. This effect is more difficult to predict but it has a larger influence on radiative heat transfer [23], especially in those situations in which mean temperature gradients are not very high, e.g. in atmospheric flows [24, 25]. In this chapter we focus on the effect of radiation on the temperature field and investigate the dependency of TRI on the optical thickness.

To study the influence of radiation on the temperature field, the channel has been considered incompressible. In addition, to isolate the effect of optical thickness, the flow has been considered gray with a constant absorption coefficient κ^*. Therefore, equation (2.1e) becomes

$$Q^R = \kappa\Big(\underbrace{4I_b}_{E} - \underbrace{\frac{1}{\pi}\int_{4\pi} I d\Omega}_{G}\Big), \tag{3.1}$$

where emission (E) and absorption effects (through the incident radiation term G) can be investigated separately. Thanks to the normalization of temperature, it is possible to express explicitly E as a function of θ

$$E = 4\left(\frac{\theta}{T_0}+1\right)^4, \quad \text{where} \quad T_0 = \frac{T_c^*}{T_h^* - T_c^*}. \tag{3.2}$$

In this chapter we will discuss optical thickness effects where the optical thickness τ is defined as

$$\tau = \frac{1}{2}\int_0^{2\delta^*} \kappa^* dy = \kappa^* \delta^* = \kappa, \tag{3.3}$$

since κ^* is constant. Ultimately, in a emitting-absorbing gray channel flow with constant absorption coefficient, radiative heat source is expressed as

$$Q^R = \tau(E - G). \tag{3.4}$$

3.2. CASE DESCRIPTION

The flow domain consists of the periodic channel presented in figure 2.1. Reynolds number, Prandtl number and T_0 are constant for all the simulations with values of 2900, 1 and 1.5 (corresponding to $T_h^* = 955$ and $T_c^* = 573$ K), respectively. The Planck number is kept low, with a value of 0.03, to ensure a high relevance of radiative heat transfer. The walls are considered to be a black surface with emissivity $\epsilon_w = 1$. The optical thickness varies two orders of magnitude being 0.1, 1 and 10. The size of the computational domain in

Table 3.1: Description of the test cases

Cases	Re	Pr	Pl	T_0	τ
bench	2900	1	0.03	1.5	0 (transparent)
gray-01	2900	1	0.03	1.5	0.1
gray-1	2900	1	0.03	1.5	1
gray-10	2900	1	0.03	1.5	10

the streamwise and spanwise directions is $4\pi\delta$ and $3\pi\delta/2$, respectively. The computational grid is composed of $192\times168\times168$ cells in streamwise, spanwise and wall-normal direction for all cases. The grid resolution is $\Delta x^+ = 12.1$, $\Delta z^+ = 5.2$ and $\Delta y^+ = 0.85$ and 2.92 at the wall and in the center, respectively. This grid is considered fine enough to resolve the velocity field at the current Reynolds number [63], while temperature spectra that prove the grid adequacy for temperature scales, are shown in section 3.4. The directional dependency of intensity is discretized with the use of an angular grid of 8×12 elements in the polar and azimuthal direction on a unit sphere, respectively, resulting in a set of 96 independent directions. The results will be analysed by means of Reynolds averaging where a generic variable X can be decomposed in a sum of a mean component $\overline{X}$ and a fluctuating component X'. The averaging performed is a combination of spatial averaging (in the homogeneous directions) and ensemble averaging with a dataset of up to 300 independent realizations. The resulting averaged variables are one-dimensional as they only depend on the wall-normal coordinate.

3.3. MEAN FLOW STATISTICS

Before starting the quantitative analysis of the investigated cases, a qualitative view is given by means of instantaneous temperature fluctuation contours. Velocity is not shown, since temperature does not influence the momentum equation. For a detailed description of velocity statistics at the considered Reynolds number, the reader is referred to [64] and [63]. Wall-normal planes at $z/\delta = 3/4\pi$ are shown in figure 3.1, while figure 3.2 shows wall-parallel planes at $y/\delta = 1.4$. From top to bottom the contours show: No radiation, $\tau = 0.1$, $\tau = 1$ and $\tau = 10$. The snapshot contours clearly show the reduction of temperature fluctuations when moving from non radiative to radiative cases. For a high optical thickness ($\tau = 10$) small scale temperature fluctuations reduce in comparison with large scale fluctuations, and a large dissipation of temperature fluctuations near the walls occurs. These features of radiative flows will be explained in more detail in the next sections.

3.3.1. MEAN PROFILES

Figure 3.3(a-d) show the average profiles of non-dimensional temperature $\overline{\theta}$, divergence of radiative heat flux $\overline{Q}^R$ (the inlay shows a zoom on the y-axis), incident radiation $\overline{G}$ and

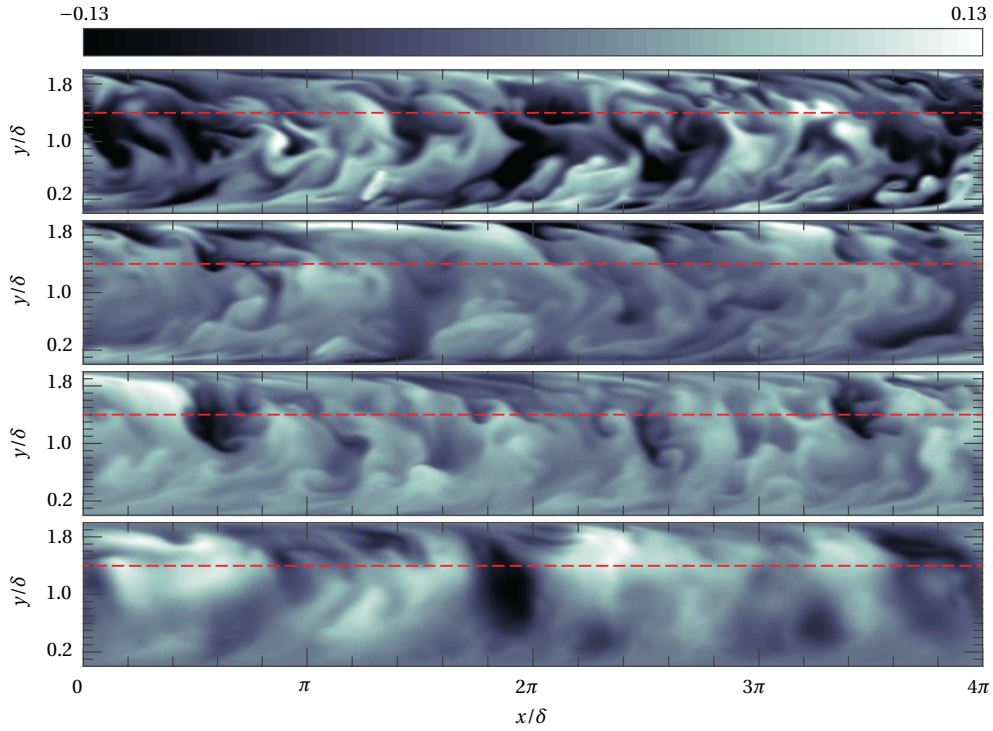

Figure 3.1: Snapshots of θ' on the wall-normal plane at $z/\delta = 3/4\pi$. From top to bottom: No radiation, $\tau = 0.1$, $\tau = 1$, $\tau = 10$. The red line highlights the position $y/\delta = 1.4$.

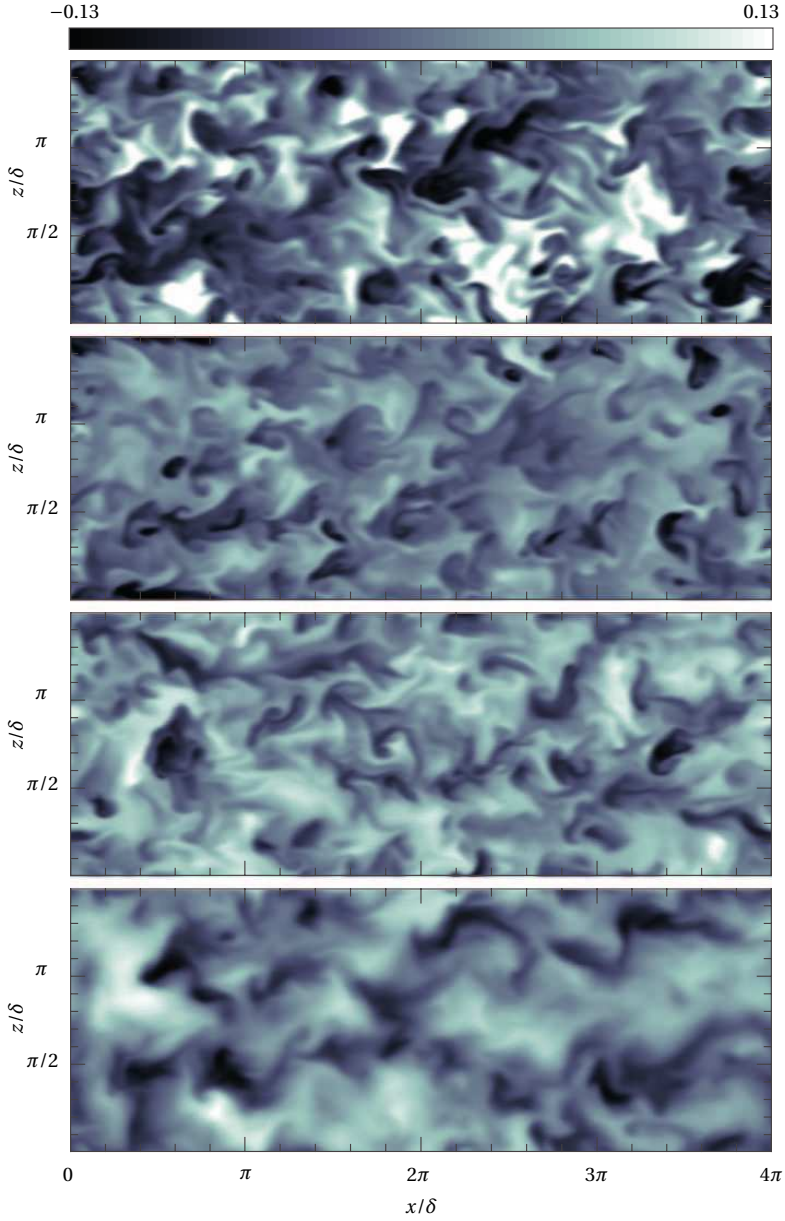

Figure 3.2: Snapshots of θ' on the wall-parallel plane at $y/\delta = 1.4$; From top to bottom: No radiation, $\tau = 0.1$, $\tau = 1.$, $\tau = 10$.

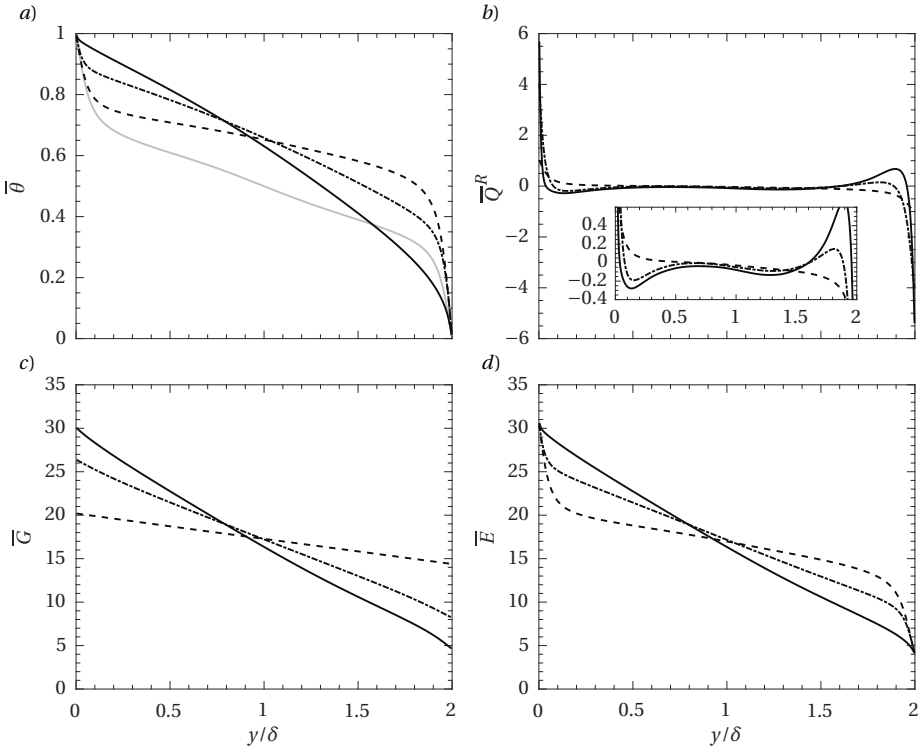

Figure 3.3: Averaged profiles, gray solid line: no radiation, dashed line: $\tau = 0.1$, dashed-dotted line: $\tau = 1$, black solid line: $\tau = 10$. (a): mean temperature; (b): mean emissive power; (c): mean incident radiation; (d): mean radiative heat source (the inlay shows a zoom on the y-axis around $\overline{Q}^R = 0$).

radiative emission $\overline{E}$, respectively. Note that $\overline{Q}^R$ represents the combined effect of an emission sink, $\tau\overline{E}$, and an absorption source, $\tau\overline{G}$, of energy. Radiative heat transfer has a strong influence on temperature profiles in all three cases. Boundary emissions remain constant as the temperature at the boundary is fixed and $\epsilon_w = 1$ (i.e. no reflection and transmission take place).

For a low optical thickness ($\tau = 0.1$), radiative heat transfer causes an increase in bulk temperature and a flattening of the temperature profile in the core of the channel. These results are caused by the long range of radiative heat transfer, which enables a direct heat exchange between the hot and the cold side. Due to the low absorption coefficient, the available energy source, $\tau\overline{G}$, as seen in figure 3.3(c), is fairly homogenous throughout the channel. On the hot side, as well as in the core of the channel, the temperature gradient reduces due to the increased bulk temperature, while it grows significantly on the cold side for the same reason.

Upon increasing the optical thickness ($\tau = 1$), the length scales of radiative heat transfer reduce due to larger absorption (i.e., intensity beams travel a shorter distance before being absorbed), shifting the radiative energy source, $\tau\overline{G}$, towards the hot side of the chan-

nel. This shift can be observed in figure 3.3(c) as the slope of incident radiation profile steepens. The temperature gradient increases in the channel core, while the gradients near the walls are reduced. A further increase of the optical thickness ($\tau = 10$) causes an additional steepening of the slope of the incident radiation profile, which results in a drastic decrease of temperature gradient near both walls. The result is an almost linear temperature profile. For $\tau = 0.1$, $\overline{Q}^R$ undergoes a monotonic transition from positive to negative values, resulting in a sink of energy on the hot side and a source on the cold side. Upon increasing the optical thickness, a local minimum and maximum appear close to the hot and cold wall, respectively, due to the shortening of radiative heat transfer length scales. Near the hot wall, due to incoming radiation from the boundary, absorption levels are higher than emission. The opposite occurs near the cold wall. The result is then the presence of local source/sink of energy and a subsequent reduction in temperature gradients near the walls at a high enough τ.

3.3.2. HEAT FLUXES

Reynolds averaging equation (2.1d) for a fully developed channel flow results in:

$$\frac{\partial}{\partial y}\left(\frac{1}{RePr}\frac{\partial\overline{\theta}}{\partial y} - \overline{v'\theta'}\right) - \frac{\overline{Q}^R}{RePrPl} = 0\,. \tag{3.5}$$

Integrating (3.5) in wall-normal direction yields:

$$\frac{1}{RePr}\frac{\partial\overline{\theta}}{\partial y} - \overline{v'\theta'} - \int_0^y \frac{\overline{Q}^R}{RePrPl}dy = C_1\,, \tag{3.6}$$

where $C_1 = \overline{q}_w - \overline{q}_{R,hw}$, with $\overline{q}_w$ the total heat flux and $\overline{q}_{R,hw}$ the radiative heat flux at the hot wall. The radiative heat source is identically equal to the divergence of the radiative heat flux $Q^R = \partial x_j q_{rj}$. The flow is statistically homogeneous in the spanwise and streamwise direction, hence it follows that:

$$\frac{\partial\overline{q}_{rx}}{\partial x} = \frac{\partial\overline{q}_{rz}}{\partial z} = 0\,. \tag{3.7}$$

This allows to state that:

$$\int_0^y \overline{Q}^R dy = \overline{q}_{ry} + C_2\,, \tag{3.8}$$

where $C_2 = \overline{q}_{R,hw}\cdot(RePrPl)$. Using (3.8) into (3.6) it is possible to define the three heat transfer mechanisms (conductive $\mathscr{D}$, convective $\mathscr{U}$ and radiative $\overline{q}_R$) as:

$$\overline{q}_w = \underbrace{-\frac{1}{RePr}\frac{\partial\overline{\theta}}{\partial y}}_{\mathscr{D}} \quad \underbrace{+\overline{v'\theta'}}_{\mathscr{U}} \quad \underbrace{+\frac{\overline{q}_{ry}}{RePrPl}}_{\overline{q}_R}. \tag{3.9}$$

Figure 3.4(a) shows the overall heat transfer in the channel $\mathscr{D} + \mathscr{U} + \overline{q}_R$, while figure 3.4(b-d) display the individual heat fluxes for $\tau = 0.1, 1, 10$. In figure 3.4(b) the radiative

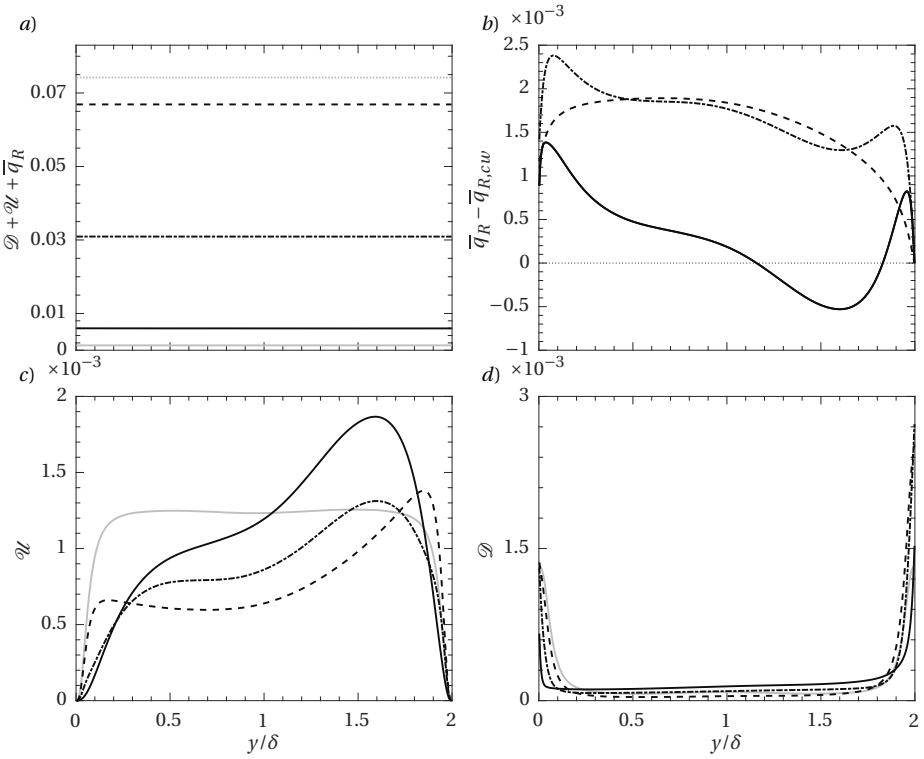

Figure 3.4: Contribution to heat flux by different heat transfer mechanisms, gray solid line: no radiation, gray dotted line: $\tau = 0$, dashed line: $\tau = 0.1$, dashed-dotted line: $\tau = 1$, black solid line: $\tau = 10$. (a): total heat flux; (b): mean radiative heat flux minus wall radiative flux on the cold side; (c): mean wall-normal turbulent heat flux; (d): mean conductive heat flux.

flux on the cold wall $\overline{q}_{R,cw}$ is subtracted from the radiative heat flux to improve the visibility and to highlight its gradient.

By inspecting figure 3.4(a) a drastic increase in the overall heat flux between non radiating and radiating cases is noticeable. Since the magnitudes of the turbulent and convective heat flux remain the same (figures 3.4(c) and 3.4(d)), the increment of the total heat flux shown is caused by radiative heat transfer. Furthermore, the heat flux tends to reduce significantly when the optical thickness is increased. Nevertheless, the rapid reduction in $\overline{q}_R$ with an increase of τ does not readily translate in a decrease of the contribution of radiation in the overall heat transfer to the fluid. A distinction must be made between wall-wall, fluid-wall and fluid-fluid radiative heat flux. As explained by [57], the wall-wall contribution refers to the constant flux between the walls, this contribution does not affect the fluid temperature. The fluid-wall flux includes both the heat flux that, emanating from the hot wall, is absorbed by the flow, and the heat flux generated by emission from the flow that reaches the cold wall. The former contribution increases the temperature of the fluid, while the latter decreases it. The fluid-fluid contribution refers to the heat flux originating within the fluid due to emission, and reabsorbed before reaching the cold wall. This contribution is responsible in shaping temperature profile and does not modify mean temperature within the channel. The correct magnitude of these three contributions cannot be estimated by the inspection of the total $\overline{q}_R$, but a qualitative explanation can be inferred considering the simple Beer-Lambert law. To show the extent of wall-wall radiative heat flux, a case with transparent medium and radiative wall has been added to figure 3.4(a) and (b) (gray dotted line). For this case, the radiative heat flux, entirely composed of wall-wall contribution, reaches the maximum possible value since it is not obstructed by the fluid. For $\tau = 0.1$, the thermal radiative waves can still travel relatively undisturbed from the hot to the cold wall since the transmissivity of the channel, $e^{-2\tau}$, is high (0.819). Therefore, wall-wall radiative heat flux comprises of the major share of $\overline{q}_R$. The consequence is a high heat transfer between hot and cold wall, but a relatively small share of thermal radiation that is effectively exchanged with the fluid. When the optical thickness increases, the radiative heat flux diminishes, but the wall/wall contribution decreases more rapidly, since the transmissivities for $\tau = 1$ and $\tau = 10$ are 0.135 and $2.1 \cdot 10^{-9}$, respectively. In other words, a higher share of thermal radiation travelling from hot to cold side is absorbed and redistributed within the media.

The shape of the radiative heat flux in figure 3.4(b), is determined by the action of emission and absorption. The increase of $\overline{q}_R$ near the hot wall is due to the effect of emission augmentation, while moving towards the cold boundary, thermal radiation is absorbed resulting in a reduction of $\overline{q}_R$. The peaks observed for $\tau = 1$ and 10 are related to the local near wall sink/source noticed in figure 3.3(b).

Figure 3.4(c) presents profiles of turbulent heat flux. In a non radiating case, the turbulent heat flux is symmetric and constant in the channel core. The symmetry of $\overline{v'\theta'}$ is lost for radiative cases, where a peak originates on the cold side. For a low optical thickness ($\tau = 0.1$) turbulent heat flux is suppressed near the hot wall, as well as in the rest of the channel due to the decrease in temperature gradient and a lower fluctuating thermal field. By increasing the optical thickness to $\tau = 1$ the peak at the cold side is reduced and shifted towards the core. In the center of the channel, turbulent heat transfer is en-

hanced by the increase of optical thickness. For a high optical thickness case ($\tau = 10$), turbulent heat flux is strongly intensified on the cold side and the peak is further shifted to the center.

SCALING OF TURBULENT HEAT FLUX IN RADIATIVE FLOWS

[29] analysed radiative flows to find a radiative scaling for turbulent heat transfer. This radiative-based scaling factor (γ) would ensure that

$$\frac{\overline{v'\theta'}_R}{\gamma_R} \approx \frac{\overline{v'\theta'}_0}{\gamma_0}\,, \tag{3.10}$$

where the subscripts R and 0 denote quantities for radiative and non radiative cases, respectively. If (3.10) holds, it is possible to obtain an expression for the turbulent heat diffusivity using the turbulent heat flux in a non radiative case as:

$$\alpha_t = \frac{1}{\rho c_p}\frac{\overline{v'\theta'}_R}{(\partial\overline{\theta}/\partial y)_R} = \frac{1}{\rho c_p}\frac{\gamma_R}{(\partial\overline{\theta}/\partial y)_R}\frac{\overline{v'\theta'}_0}{\gamma_0}\,. \tag{3.11}$$

This allows the calculation of the turbulent Prandtl number in a radiative turbulent flow by comparison with a non radiative flow, where models for Pr_t are well established. The resulting relation, see [29], is

$$Pr_{t\,R} = \frac{1}{RePr}\frac{(\partial\overline{\theta}/\partial y)_R}{\gamma_R}(Pr_{t0} + \nu_{t0}RePr)\,, \tag{3.12}$$

with the proposed scaling factor $\gamma_R(y) = \overline{q}_w - \overline{q}_R(y)$, where $\overline{q}_w$ is the wall heat flux while $\overline{q}_R(y)$ is the radiative heat flux within the channel. When no radiative heat transfer is involved, the scaling factor reduces to the conductive heat flux at the wall $\gamma_0 = \overline{q}_{w,0}$. Given equation (3.6), it is true that:

$$\gamma_R = \overline{q}_w - \overline{q}_R = \mathscr{U} + \mathscr{D}\,. \tag{3.13}$$

Using (3.13), equation (3.10) can be reformulated as:

$$\frac{\mathscr{U}_R}{\mathscr{U}_R + \mathscr{D}_R} \approx \frac{\mathscr{U}_0}{\mathscr{U}_0 + \mathscr{D}_0}\,, \tag{3.14}$$

and further rewritten as:

$$\frac{\mathscr{D}_R}{\mathscr{U}_R} \approx \frac{\mathscr{D}_0}{\mathscr{U}_0}\,, \tag{3.15}$$

i.e., the relative importance of turbulent heat transfer over conduction remains constant as radiation is introduced and optical thickness is increased.

This scaling can also be applied to temperature by using the friction temperature formulation, defined as

$$\theta_t = \frac{q_w}{\rho_w c p_w u_t}, \quad \text{where} \quad u_t = \sqrt{\frac{\mu_w}{\rho_w}\left(\frac{d\overline{u}}{dy}\right)_w}\,. \tag{3.16}$$

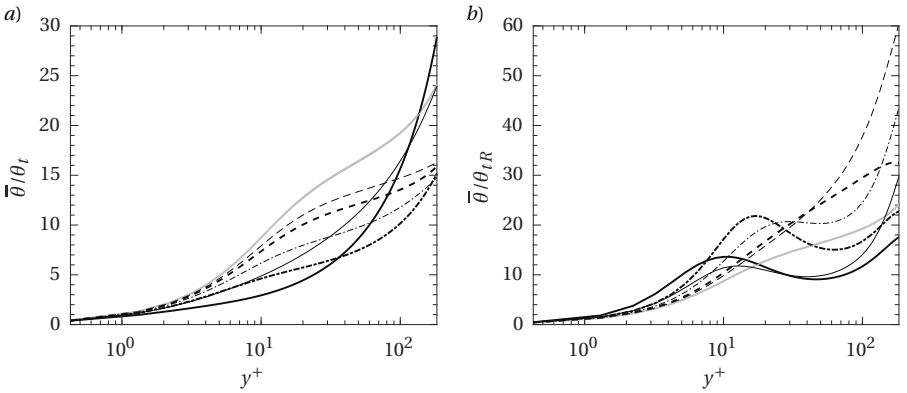

Figure 3.5: Average temperature scaled by θ_t (a) and θ_{tR} (b). Thick lines: hot side, thin lines: cold side. Gray solid line: no radiation, dashed line: $\tau = 0.1$, dashed-dotted line: $\tau = 1$, black solid line: $\tau = 10$. (b): turbulent Prandtl number calculated from DNS and modeled. Symbols: Pr_{t0}; black lines: DNS results; gray lines: modeled Pr_t. Dashed line: $\tau = 0.1$, dashed-dotted line: $\tau = 1$, solid line: $\tau = 10$.

By substituting γ_R to q_w it is possible to define a radiation-based friction temperature

$$\theta_{tR} = \frac{\gamma_R}{\rho_w c p_w u_t}. \tag{3.17}$$

The mean temperature is shown, averaged by wall values and by radiative scaling in figures 3.5 (a) and (b), respectively. As it is possible to notice in figure 3.5(a), the usual wall scaling completely fails in collapsing temperature profiles. Arguably, employing the radiative-based scaling results in a slightly improved agreement compared to the friction temperature normalization, despite being still very far from a collapse. Indeed, if normalized by θ_{tR}, the higher optical thicknesses ($\tau = 1$ and 10) show a local maximum around $y^+ = 15$ and $y^+ = 10$, respectively. These peaks are connected to the local maxima of the radiative heat flux in figure 3.4(b) and suggest that the effect of the TRI mechanism cannot be included in the mean temperature with a simple scaling procedure.

The resulting profiles of radiation-scaled $\mathscr{U}$ are shown in figure 3.6(a), while the modeled and the calculated turbulent Prandtl number from equation (3.12) are shown in figure 3.6(b). The value of non radiative turbulent Prandtl number and turbulent viscosity calculated from DNS, are used in equation (3.12).
The turbulent Prandtl number increases significantly when increasing the optical thickness, depicting the decrease in convective effects on mean temperature. The model developed by [29] performs exceptionally well with low optical thickness, being able to exactly reproduce Pr_{tR}. For intermediate values of optical thickness the model seems to deviate slightly from the calculated values, while showing a relevant deviation for higher values of optical thickness ($\tau = 10$).
In a constant property flow, condition (3.15) can be met identically only if Pr_t is independent of τ since turbulent Prandtl number is defined as:

$$Pr_t = -\frac{\mathscr{D}}{\mathscr{U}} \cdot \nu_t RePr\ , \tag{3.18}$$

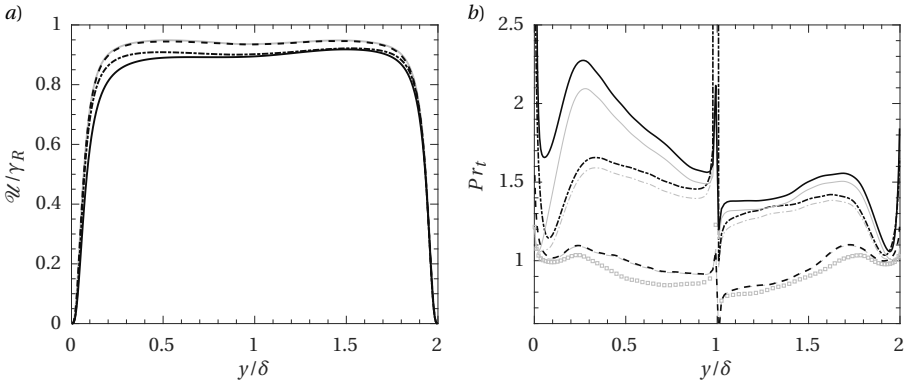

Figure 3.6: (a): Scaled turbulent heat transfer. Gray solid line: no radiation, dashed line: $\tau = 0.1$, dashed-dotted line: $\tau = 1$, black solid line: $\tau = 10$. (b): turbulent Prandtl number calculated from DNS and modeled. Symbols: Pr_{t0}; black lines: DNS results; gray lines: modeled Pr_t. Dashed line: $\tau = 0.1$, dashed-dotted line: $\tau = 1$, solid line: $\tau = 10$.

where ν_t is the turbulent viscosity, which is constant with respect to τ in an incompressible flow.

In order to better understand the disagreement between the model and DNS, it is necessary to point out the interplay between the energy equation, eq. (3.9), and the transport equation of turbulent heat flux $\mathscr{U}$ that, in an incompressible, absorbing-emitting, turbulent flow reads:

$$0 = \underbrace{-\overline{v'^2}\frac{\partial\overline{\theta}}{\partial y}}_{\mathscr{P}_{\mathscr{U}}} \underbrace{+\frac{\partial}{\partial y}\left(\frac{1}{RePr}\overline{v'\frac{\partial\theta'}{\partial y}} + \frac{1}{Re}\overline{\theta'\frac{\partial v'}{\partial y}} - \frac{1}{Re}\overline{v'^2\theta'}\right)}_{\phi_{\mathscr{U}}+\mathscr{T}_{\mathscr{U}}} + \underbrace{-\overline{\frac{\partial\theta'}{\partial x_j}\frac{\partial v'}{\partial x_j}}\frac{Pr+1}{RePr}}_{\epsilon_{\mathscr{U}}} \underbrace{-\overline{\theta'\frac{\partial p'}{\partial y}}}_{\Pi_{\mathscr{U}}} \underbrace{-\frac{1}{RePrPl}\overline{Q_r' v'}}_{\mathscr{R}_{\mathscr{U}}}. \tag{3.19}$$

$\mathscr{P}_{\mathscr{U}}$ is turbulent production, $\phi_{\mathscr{U}}$ is molecular and viscous diffusion, $\mathscr{T}_{\mathscr{U}}$ is turbulent transport, $\epsilon_{\mathscr{U}}$ is the molecular and viscous dissipation, $\Pi_{\mathscr{U}}$ is the pressure term (sum of pressure diffusion and pressure strain) and $\mathscr{R}_{\mathscr{U}}$ is the radiative term (sum of emissive and absorptive term). Figure 3.7(a) shows the production term for $\mathscr{U}$, while figure 3.7(b) presents the profiles of the radiation term. For $\tau = 0.1$, The introduction of the average radiative heat flux in eq. (3.9), causes the turbulent heat flux $\mathscr{U}$ to reduce in the channel core (figure 3.4(c)). As apparent, for a low optical thickness, the decrease of $\mathscr{U}$ is balanced by the decrease in temperature gradient, resulting in the validity of condition (3.15). This occurs since the direct effect of TRI on $\mathscr{U}$ (namely term $\overline{Q_r' v'}$ in equation (3.19)) has a negligible contribution. Therefore, a change in mean temperature gradient would readily reflect in a modification of $\mathscr{U}$ through the reduction of the turbulent production $\mathscr{P}_{\mathscr{U}}$, keeping the $\mathscr{D}/\mathscr{U}$ ratio constant. In other words, only mean radiative effects (i.e., $\overline{q}_R$ in equation (3.9)), play a role. Since direct radiative effects are negligi-

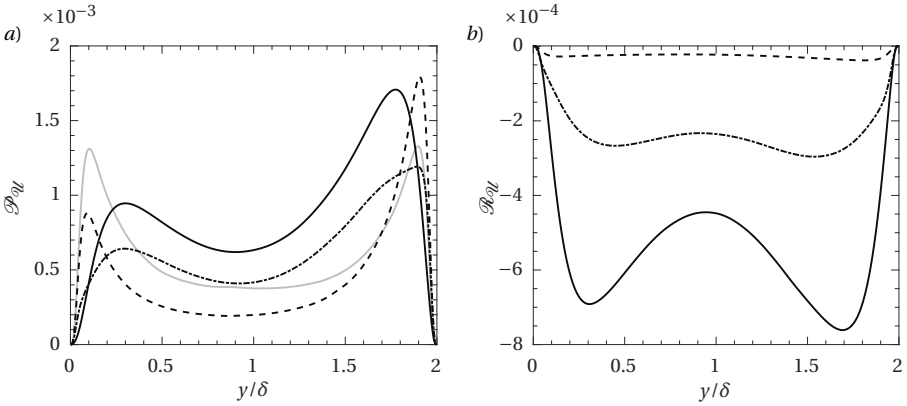

Figure 3.7: (a): Turbulent production of $\mathscr{U}$. (b): Radiative term. Gray solid line: no radiation, dashed line: $\tau = 0.1$, dashed-dotted line: $\tau = 1$, black solid line: $\tau = 10$.

ble, equation (3.19) keeps the balance between $\mathscr{U}$ and $\mathscr{D}$. Consequently, the modeled turbulent Prandtl number for a low optical thickness agrees with the value calculated from DNS. However, condition (3.15) is not a suitable approximation when increasing the optical thickness since the direct effect of TRI becomes relevant. It should be noted, that $\mathscr{P}_{\mathscr{U}}$ is representative of $\mathscr{D}$, since the term $\overline{v'^2}$ is not affected by temperature in the present case. Therefore, the increase in temperature gradient with the increase of τ is directly related to the rise in $\mathscr{R}_{\mathscr{U}}$, which represents the direct effect of radiative fluctuations on θ'. This increase in not reflected in the same fashion on the turbulent heat transfer $\mathscr{U}$. Namely, with the increase of radiative effects in the center of the channel (as it will be explained in details in the next sections), $\mathscr{P}_{\mathscr{U}}$ adapts to an increased $\mathscr{R}_{\mathscr{U}}$ leading to an increased $\mathscr{D}/\mathscr{U}$ ratio. This increase causes $\mathscr{U}_R/\gamma_R < \mathscr{U}_0/\gamma_0$, resulting in a deviation of the modeled turbulent Prandtl number. The deviation is larger on the hot side, since the model does not account for radiative field fluctuations (indeed, to consider a constant $\mathscr{D}/\mathscr{U}$ ratio implies that radiative fluctuations have no effect on θ'). As it will be shown in sections 3.3.3 and 3.4, the direct effect of radiation on thermal turbulence is directly proportional to the cube of the mean temperature, causing a larger deviation on the hot side.

This mechanism is confirmed by scaling $\mathscr{P}_{\mathscr{U}}$ and $\mathscr{R}_{\mathscr{U}}$ with γ_R, as shown in figure 3.8. As is evident from the $\tau = 0.1$ profile in figure 3.8(a), using the radiative-based scaling in the limit of low TRI effects causes the profiles of turbulent production to collapse. This is possible only because $\mathscr{R}_{\mathscr{U}} \to 0$ and all radiative effects on $\mathscr{U}$ are indirect, acting through the modification of $\mathscr{D}$, which is correctly taken into account dividing by γ_R. The collapse of $\mathscr{P}_{\mathscr{U}}$ cannot be achieved when the radiative term is significant. Note that $\mathscr{R}_{\mathscr{U}}$ is of the same magnitude of $\mathscr{P}_{\mathscr{U}}$ for larger optical thicknesses.

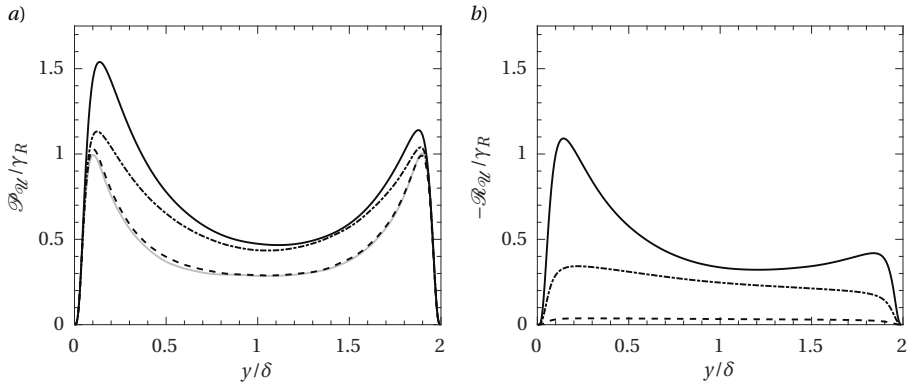

Figure 3.8: (a): Turbulent production of $\mathscr{U}$ normalized by γ_R. (b): Radiative term normalized by γ_R. Gray solid line: no radiation, dashed line: $\tau = 0.1$, dashed-dotted line: $\tau = 1$, black solid line: $\tau = 10$.

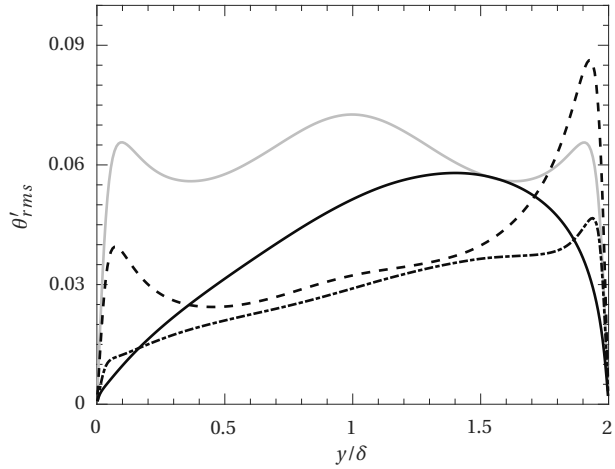

Figure 3.9: Turbulent intensity of temperature fluctuation, gray solid line: no radiation, dashed line: $\tau = 0.1$, dashed dotted line: $\tau = 1$, black solid line: $\tau = 10$.

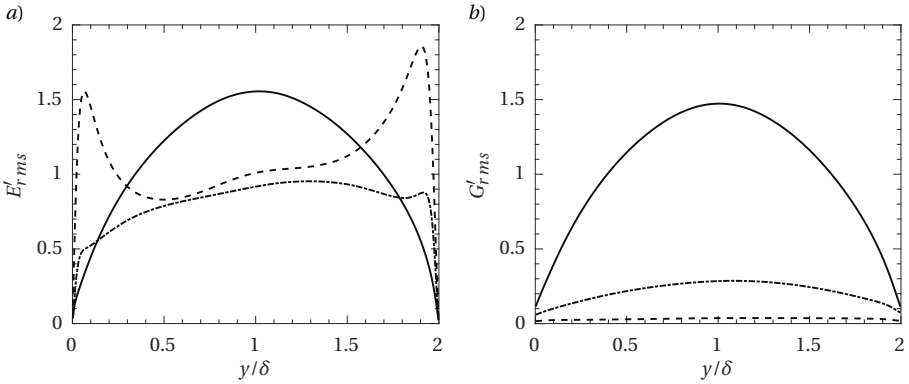

Figure 3.10: root mean square profiles of emission (a) and incident radiation (b), dashed line: $\tau = 0.1$, dashed dotted line: $\tau = 1$, black solid line: $\tau = 10$.

3.3.3. TEMPERATURE VARIANCE AND FLUCTUATIONS OF RADIATIVE QUANTITIES

Figure 3.9 shows temperature root mean square profiles for all cases. For the non radiating case the temperature root mean square profile is symmetric with peaks near the walls and a maximum in the center of the channel. The peaks near the walls are caused by a high correlation of temperature fluctuations with the streamwise velocity fluctuations [64]. The local maximum located in the channel core is generated by pockets of cold and hot fluid transported from the boundaries towards the center.

The influence of radiation on the turbulent temperature field can be analysed by means of the evolution equation for temperature fluctuations (resulting from the subtraction of the Reynolds averaged to the instantaneous energy equation):

$$\frac{\partial \theta'}{\partial t} + \overline{u_j}\frac{\partial \theta'}{\partial x_j} + v'\frac{\partial \overline{\theta}}{\partial y} + \frac{\partial u'_j \theta'}{\partial x_j} - \frac{\partial \overline{v'\theta'}}{\partial y} = \frac{1}{RePr}\frac{\partial^2 \theta'}{\partial x_j^2} - \tau\frac{E'}{RePrPl} + \tau\frac{G'}{RePrPl}\,. \tag{3.20}$$

G' is a source of temperature fluctuation, while E' acts as a sink. Note that E' is always positively correlated to θ', since

$$E' = 4\left[(\theta/T_0 + 1)^4\right]' \propto \overline{\theta}^3\theta'\,. \tag{3.21}$$

As a positive θ' fluctuation occurs a positive E' fluctuation follows, which increases emission and subsequently reduces temperature. The opposite is observed for negative θ'. Therefore, E' acts as a stabilization phenomenon towards the temperature field, reducing temperature fluctuations. In addition, emission fluctuations are proportional to the cube of the mean temperature, hence, in general, a higher temperature ensures higher levels of E'. On the other hand, G' counteracts the effects of E', and where fluctuations of G are high, the stabilizing effect of emission is weaker, allowing for higher θ' values. Also the effect of G' is enhanced with a larger $\overline{\theta}$, as it will be explained in section 3.4.

The near wall peak locations of $\overline{\theta'^2}$ are retained for the low optical thickness case ($\tau = 0.1$). The radiative power fluctuations are dominated by the emission fluctuations E' (figure 3.10(a)) and in conjunction with a lower temperature gradient, cause a mitigation of the temperature variance peak on the hot side. Indeed, G' (figure 3.10(b)) shows a negligible contribution to equation (3.20). On the other hand, the high temperature gradient occurring on the cold side increases the temperature variance near the cold wall beyond the non radiative case. This rise in fluctuation levels is not a direct effect of radiation, rather an effect of the increased production due to a higher temperature gradient (see the discussion on temperature variance budgets in section 3.3.4). The turbulent transport of hot and cold pockets towards the center of the channel is reduced, since turbulent structures, directed to the core, emit radiation causing the temperature to stabilize before the center is reached. As a result, the temperature variance in the channel core is strongly damped.

For an intermediate optical depth ($\tau = 1$), fluctuation levels are largely reduced both on the hot and cold side due to the direct action of radiative emission, which provides means of stabilization to temperature fluctuations. The turbulent transport of hot and cold temperature pockets is further decreased through emission of thermal radiation, which causes a reduction in temperature variance. In the core of the channel, near $y/\delta = 1.5$, incident radiation fluctuations G' grow larger and slightly counteract the sink produced by E' (see section 3.3.4).

Interestingly, we noticed that further increasing the optical thickness to $\tau = 10$ produces a higher level of temperature fluctuations than the previous radiative cases, since temperature variance partly recovers in the core of the channel. The small peak of $\overline{\theta'^2}$ at $y/\delta \approx 1.5$, noticed for $\tau = 1$, grows for $\tau = 10$ and shifts towards the center (at $y/\delta = 1.4$). Near-wall fluctuations are largely reduced both on the hot and cold side. This increase in temperature variance is caused by G' that reaches a magnitude comparable to E'.

In figure 3.10(b) it is possible to notice the drastic increase in incident radiation fluctuations upon increasing the optical thickness. This rise is caused by the reduction of radiative transfer length scales; incident radiation at a high optical thickness can be regarded mostly as a short range phenomenon, hence being heavily influenced by local temperature fluctuations. We noticed that the peak of incident radiation fluctuations is always located around the center of the channel. As it will be explained in section 3.4, incident radiation is mostly influenced by large temperature scales, while small thin structures mostly behave as a transparent media. For this reason G fluctuations are mostly concentrated near the channel center where temperature fluctuations are usually associated with larger and more isotropic scales of motion, while they decrease towards the walls where vortices are characterized by thin streaky structures.

Figure 3.11 shows the temperature fluctuations scaled with inner scaling using the friction temperature (a) and the radiation-based friction temperature (b). In the first case, the profiles do not show any collapse, proving that the different mechanism for temperature flucuation production is a result of a long-range effects that cannot be accounted for by using inner wall scaling. The radiation-based scaling of Vicquelin et al [29] shows an improvement, as all profiles show the same trend. On the other hand, as discussed in the previous section, the scaling does not account for direct effects of radiation and, therefore, large differences are still found among all the different cases.

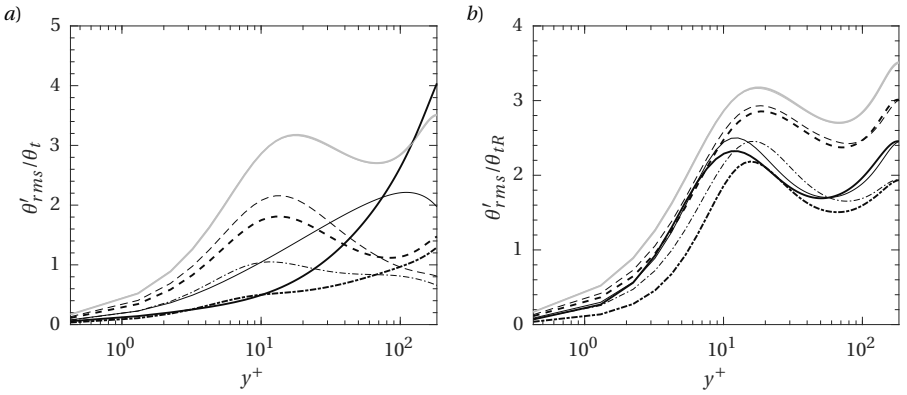

Figure 3.11: Temperature fluctuation scaled with friction temperature (a) and radiation-based friction temperature (b). Thick lines: hot side, thin lines: cold side. Gray solid line: no radiation, dashed line: $\tau = 0.1$, dashed dotted line: $\tau = 1$, black solid line: $\tau = 10$.

Despite the failure of this scaling, a better agreement between hot and cold side in the same case is retrieved, suggesting that this scaling can partly account for radiative heat transfer in cases with the same optical thickness. An additional explanation for the failure of the radiation-based scaling, which might explain deviations in $\theta'_{rms}/\theta_{tR}$ profiles, can be conjectured looking at scaled profiles of radiative quantity fluctuations. Figure 3.12 shows profiles of emission (a) and incident radiation (b) fluctuations normalized by γ_R (note that E and G have the dimensions of a heat flux). The emission profiles show an improved agreement when scaled by γ_R but have a worst collapse than $\theta'_{rms}/\theta_{tR}$, especially when comparing hot and cold side from the same case. This is probably caused by the fact that $E' \sim \overline{\theta}^3\theta'$ and, as seen in the previous section, $\overline{\theta}$ does not scale with θ_{tR}. On the other hand, scaled profiles of G'_{rms} pinpoint the reason of the failure of the radiative-based scaling. G'_{rms} seems to be completely unaccounted for by the radiative-based scaling as the growth with τ in the scaled profiles resemble very closely figure 3.10(b). We conclude that G fluctuations are most likely the reason for the growth of $\mathscr{R}_{\mathscr{U}}$ seen in figure 3.7. Consequently, G' can be assumed to be the cause of the failure of the radiative-based scaling. This is intuitive, as all the non-local effects of radiative heat transfer are encompassed in G, and the latter grows stronger with a higher optical thickness.

3.3.4. BUDGETS OF THE TEMPERATURE VARIANCE

Budgets of temperature variance are shown, to investigate the influence of radiation on the turbulent temperature field. The transport equation for temperature variance in the presence of radiative heat transfer reads:

$$0 = \underbrace{-2\overline{v'\theta'}\frac{\partial\overline{\theta}}{\partial y}}_{\mathscr{P}_\theta} \quad \underbrace{+\frac{\partial}{\partial y}\left(\frac{1}{RePr}\frac{\partial\overline{\theta'^2}}{\partial y} - \overline{v'\theta'^2}\right)}_{\phi_m+\mathscr{T}_\theta} \quad \underbrace{-\frac{2}{RePr}\overline{\left(\frac{\partial\theta'}{\partial x_j}\right)^2}}_{\epsilon_m} \quad \underbrace{-\frac{2}{RePrPl}\overline{Q^{R'}\theta'}}_{\mathscr{R}_\theta}, \tag{3.22}$$

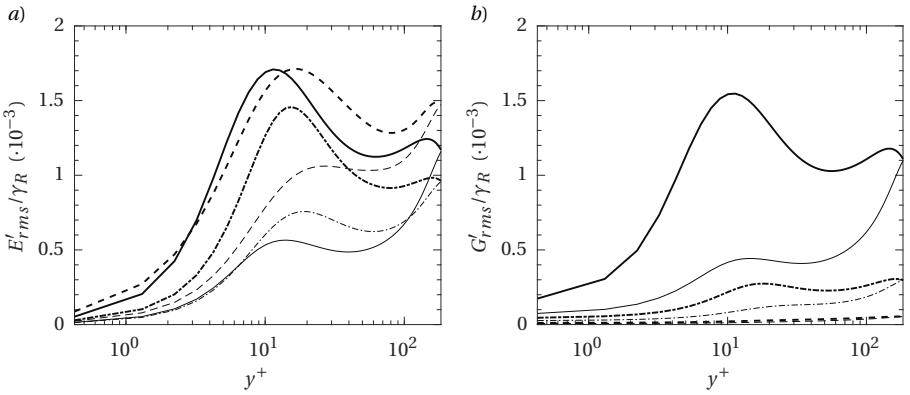

Figure 3.12: Root mean square profiles of emission (a) and incident radiation (b) normalized by radiation scaling γ_R. Thick lines: hot side, thin lines: cold side. Dashed line: $\tau = 0.1$, dashed dotted line: $\tau = 1$, black solid line: $\tau = 10$.

where $\mathscr{P}_\theta$ is the turbulent production, ϕ_m is the molecular diffusion, $\mathscr{T}_\theta$ is the turbulent transport, ϵ_m is the molecular dissipation and $\mathscr{R}_\theta$ is the radiation term. The radiation term, in analogy with the molecular terms (ϕ_m, ϵ_m), can be decomposed into a diffusion and a dissipation term:

$$\mathscr{R}_\theta = \underbrace{-\frac{2}{RePrPl}\overline{\frac{\partial q'_{ry}\theta'}{\partial y}}}_{\phi_r} \underbrace{+\frac{2}{RePrPl}\overline{\frac{\partial \theta'}{\partial x_j}q'_{rj}}}_{\epsilon_r}, \tag{3.23}$$

with ϕ_r radiative diffusion and ϵ_r radiative dissipation.

Figure 3.13(a-d) present the budgets of temperature variance of the non radiative and the radiative channel flows, where figure 3.13(a) corresponds to no radiation, 3.13(b) to $\tau = 0.1$, 3.13(c) to $\tau = 1$ and 3.13(d) to $\tau = 10$. Contrary to profiles in figure 3.13(a), budgets of temperature variance for the radiative flows in figures are non-symmetrical.

For the low optical thickness case, a noticeable rise in the production can be observed near the cold wall, due to the increase of the temperature gradient. In order to balance the larger production rate, molecular dissipation, molecular diffusion and turbulent transport increase when compared to a non radiative case. The opposite effect is experienced in the rest of the channel where the lower temperature gradient causes an overall reduction in the magnitude of the budgets. The radiation terms ($\mathscr{R}$, ϕ_r and ϵ_r) show a negligible contribution near the boundaries. A direct effect of radiation can be noticed in the core of the channel where radiative dissipation ϵ_r aids molecular dissipation in balancing production (inlay in figure 3.13(b)). Indeed, at a low optical thickness, radiation acts mainly through the modification of mean profiles as noticed by several previous studies [27, 30, 32], but in the center of the channel we noticed a non-negligible direct effect of radiative dissipation.

For an intermediate optical depth, figure 3.13(c), adjacent to the hot wall, the budgets reduce drastically, due to the lower turbulent production and the large effect of emission

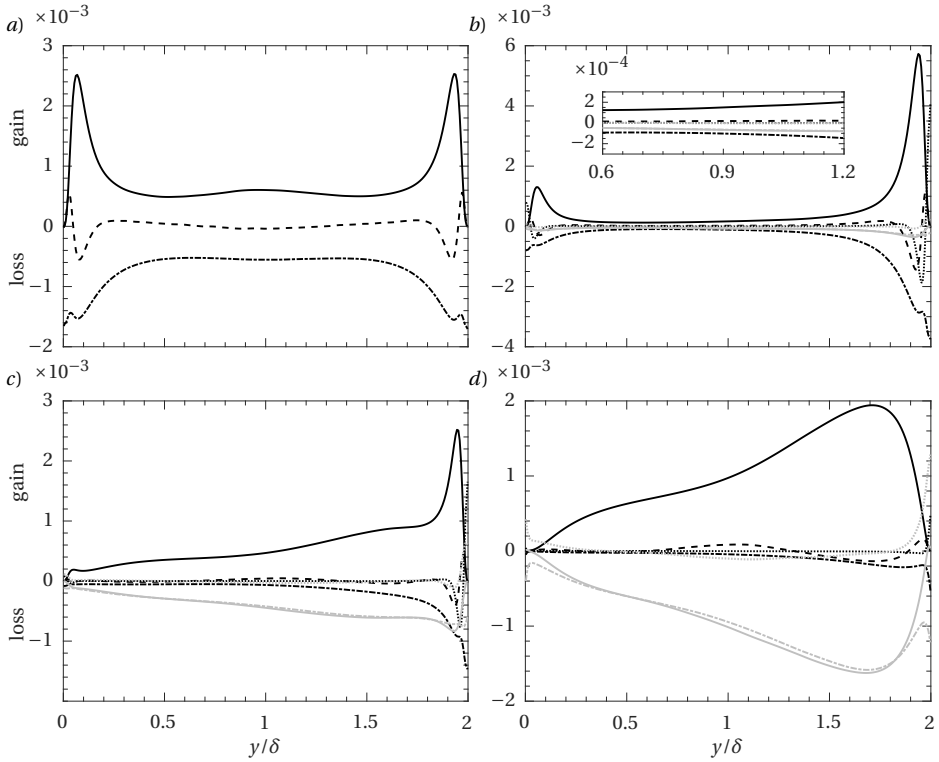

Figure 3.13: Budgets of temperature variance, 3.13(a): non radiative channel flow, 3.13(b): $\tau = 0.1$, inclusion highlights the core zone ($x/\delta = 0.4 - 1.2$), 3.13(c): $\tau = 1$, 3.13(d): $\tau = 10$. Black solid line: turbulent production $\mathscr{P}_\theta$, dashed line: turbulent transport $\mathscr{T}_\theta$, black dotted line: molecular diffusion ϕ_m, black dashed-dotted line: molecular dissipation ϵ_m, gray dotted line: radiative diffusion ϕ_r, gray dashed-dotted line: radiative dissipation ϵ_r, gray solid line: radiative term $\mathscr{R}_\theta$

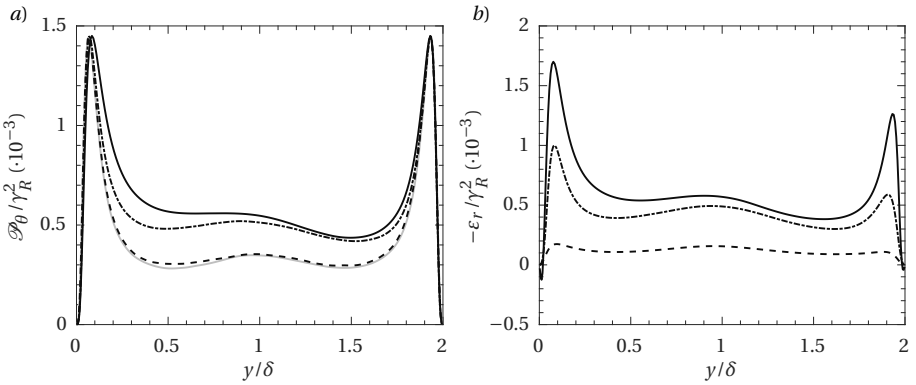

Figure 3.14: Turbulent production of temperature variance (a) and radiative dissipation (b) normalized by γ_R^2. gray solid lines: non-radiative channel flow, dashed: line $\tau = 0.1$, dashed-dotted line: $\tau = 1$, black solid line: $\tau = 10$

that results in lower θ'. On the cold side the same effect is observed, with an overall reduction in budgets of temperature variance. On the contrary, in the channel core, production rate increases. The combination of an increase in turbulent production, caused by the rise in temperature gradient, and the rise of G', is balanced by the strong growth of radiation dissipation. Molecular diffusion and dissipation experience a further reduction, being relevant on the cold side only. It will be shown that the appearance of a mildly fluctuating absorption field, shifts the temperature variance towards the core where larger structures are present (see the discussion on temperature length scales in radiative flows in section 3.4).

By further increasing the optical thickness, figure 3.13(d), an enhancement of the effects already noticed for $\tau = 1$ occurs. In the whole core of the channel, an overall increase in budgets' magnitude is noticed. The molecular terms fall off, showing the complete dominance of radiative terms. On the hot side, production is minimized due to the lower mean temperature gradient and the large effect of emission that reduces θ'. All the budgets near the hot wall reduce significantly, except for the radiative terms ϕ_r and ϵ_r that increase and balance each other. Indeed, by reducing the radiation length scales, radiative terms reduce to local quantities acting akin to molecular terms, as already noticed by [23]. The production is located further away from the wall, consistently with the shift of θ_{rms} towards the center of the channel, observed in section 3.3.3. Turbulent transport slightly grows in the core of the channel in order to redistribute fluctuations produced in the new peak location ($y/\delta \approx 1.7$). Therefore, with increasing the optical thickness, the relevance of molecular terms is reduced in favour of the radiative terms; the radiative dissipation and diffusion substitute the role of the molecular dissipation and diffusion in balancing the production. Hence, for a high enough optical thickness, the effect of radiation is not restricted to the modification of mean quantities, but acts directly on temperature statistics.

Figure 3.14 shows turbulent production and radiative dissipation profiles normalized by γ_R^2. For $\tau = 0.1$, production collapses with the transparent benchmark throughout the

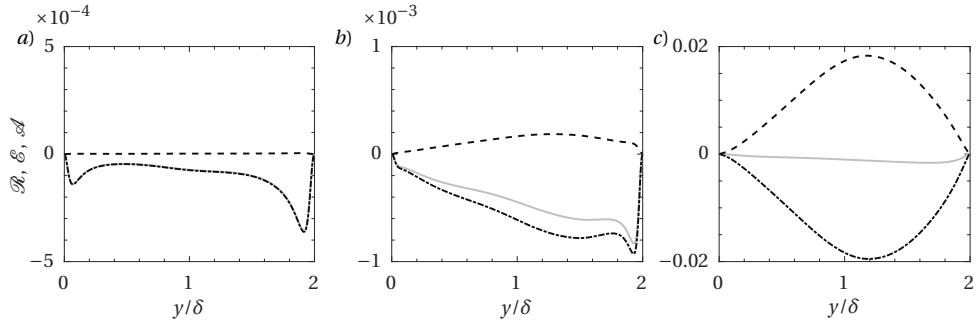

Figure 3.15: Radiation term $\mathscr{R}$ decomposed in absorption $\mathscr{R}_a$ and emission term $\mathscr{R}_e$. gray solid lines: $\mathscr{R}$, dashed-dotted lines: $\mathscr{R}_e$, dashed lines: $\mathscr{R}_a$. (a): $\tau = 0.1$, (b): $\tau = 1$, (c): $\tau = 10$

whole extent of the channel. In the other two cases, the peaks collapse nicely, especially near the cold wall where radiation effects are lower. However, in the center of the channel, the production profile deviates substantially. Despite ϵ_r growing with τ, we cannot directly connect the deviation of $\mathscr{P}_\theta/\gamma_R^2$ with ϵ_r/γ_R^2 as the latter shows a maximum at the location where the production's collapse is satisfactory. On the other hand, it is possible to connect the deviation of $\mathscr{P}_\theta$ in the channel center with G'_{rms}, which also reaches a maximum in the core of the channel and is minimal near the wall. This reinforces the observation that radiation fluctuations G' are the driving force of temperature field modification as well as the reason for the failure of a possible radiation-based scaling.

The evidence collected from the analysis of the temperature variance budgets, suggests that a further increase in the optical thickness would result in a further alignment of the production with the $\overline{G'^2}$ peak (figure 3.10(b)). Furthermore, the temperature fluctuations would recover and the radiative terms (ϕ_r and ϵ_r) would behave qualitatively similar to the molecular terms (ϕ_m and ϵ_m) in a transparent channel flow.

To highlight the effects of absorption and emission fluctuations, that act as a production and dissipation term for $\overline{\theta^{2\prime}}$, the radiative term $\mathscr{R}$ can also be decomposed as

$$\mathscr{R} = \mathscr{E} + \mathscr{A} \,, \tag{3.24}$$

where

$$\mathscr{E} = -\frac{2\tau}{RePrPl}\overline{E'\theta'}, \qquad \mathscr{A} = \frac{2\tau}{RePrPl}\overline{G'\theta'}. \tag{3.25}$$

Figure 3.15 shows the profiles of $\mathscr{R}$, $\mathscr{E}$ and $\mathscr{A}$. As the optical thickness increases the effect of the absorption production term grows drastically. Indeed G' is the cause of a modification of the thermal turbulence field, while emission fluctuations act as a dissipation of thermal fluctuations. It can also be noticed that $\mathscr{R}$,$\mathscr{A}$ and $\mathscr{E}$ increase substantially in magnitude upon increasing the optical thickness. The reason why $\mathscr{A}$ peaks always in the center of the channel, is motivated in the next section.

3.4. SPECTRAL ANALYSIS OF TRI

Before proceeding towards discussing the results obtained for turbulent channel flow it is useful to analytically investigate the effect of radiation on the turbulent temperature scales in homogeneous isotropic turbulence. A mathematical derivation of scale dependence of emission and absorption for a simple gray absorbing-emitting gas is outlined below [24, 58].

A three-dimensional Fourier transformation of the fluctuating RTE, obtained by subtracting the instantaneous and averaged form of equation 2.1f, presented in section 2.6, yields

$$\widehat{I'}(\boldsymbol{\omega}) = \left(\frac{\tau^2}{\tau^2 + (\boldsymbol{\omega}\cdot\boldsymbol{s})^2} - i\frac{\tau(\boldsymbol{\omega}\cdot\boldsymbol{s})}{\tau^2 + (\boldsymbol{\omega}\cdot\boldsymbol{s})^2} \right) \widehat{I'_b}(\boldsymbol{\omega}) \,, \tag{3.26}$$

Where $\boldsymbol{\omega}$ is the non dimensional wavenumber vector $(\omega_x, \omega_y, \omega_z)$. Since

$$\widehat{G'}(\boldsymbol{\omega}) = \frac{1}{\pi}\int_{4\pi} \widehat{I'}(\boldsymbol{\omega})\, d\Omega \,, \tag{3.27}$$

and $\widehat{I'_b}(\boldsymbol{\omega}) \neq f(\Omega)$ (isotropic emission), then

$$\widehat{G'}(\boldsymbol{\omega}) = \frac{\widehat{I'_b}(\boldsymbol{\omega})}{\pi}\int_{4\pi} \left(\frac{\tau^2}{\tau^2 + (\boldsymbol{\omega}\cdot\boldsymbol{s})^2} - i\frac{\tau(\boldsymbol{\omega}\cdot\boldsymbol{s})}{\tau^2 + (\boldsymbol{\omega}\cdot\boldsymbol{s})^2} \right) d\Omega \,. \tag{3.28}$$

An analytical solution to equation 3.28 exists, leading to the formulation of the Fourier transform of emission and absorption in homogeneous isotropic turbulence,

$$\widehat{E'}(\boldsymbol{\omega}) = 4\widehat{I'_b}(\boldsymbol{\omega}) \propto \overline{\theta}^3 \widehat{\theta'}(\boldsymbol{\omega}) \,, \tag{3.29}$$

$$\widehat{G'}(\boldsymbol{\omega}) = 4\widehat{I'_b}(\boldsymbol{\omega}) \cdot \frac{\tau}{\omega}\,\mathrm{atan}\left(\frac{\omega}{\tau}\right) = \widehat{E'} \cdot f(\omega,\tau) \propto \overline{\theta}^3 \widehat{\theta'}(\boldsymbol{\omega}) \cdot f(\omega,\kappa) \,. \tag{3.30}$$

Absorption is spectrally related to emission in a periodic domain by the function $f(\omega,\tau)$ where $\omega = ||\boldsymbol{\omega}||$. It is important to remember that, in gray gas, emission fluctuations always lead to a sink of temperature variance, while absorption fluctuations cause a source of temperature variance. This is not strictly true for non-gray gases, where κ' can modify the roles of emission and absorption. Since $0 < f(\omega,\tau) < 1$, the sink is always predominant and, in homogeneous isotropic turbulence, the spectral effect of radiation always leads to a dissipation of temperature spectrum. On the other hand, since $\widehat{G'}(\boldsymbol{\omega}) \propto f(\omega,\tau)$, this dissipation is heavily affected by both the wavenumber and the optical thickness. Emission scales are proportional to temperature scales at every k since, from a fourier transformation of $E' \propto \overline{\theta}^3\theta'$ (proportionality relation (3.21)), follows that $\widehat{E'}(\boldsymbol{\omega}) \propto \widehat{\theta'}(\boldsymbol{\omega})$. Therefore, emission leads to a sink on the temperature spectra that is proportional to the spectral energy at every wavenumber. On the other hand, $\widehat{G'}(\boldsymbol{\omega})$ heavily modifies the spectra, since absorption scales depend on the wavenumber as $f(\omega,\tau)$ (figure 3.16). In addition, radiative effects on the turbulent temperature spectrum, both of emission and absorption, increase with temperature since $\widehat{I_{b'}}(\boldsymbol{\omega}) \propto \overline{\theta}^3$, as anticipated in section 3.3.3.

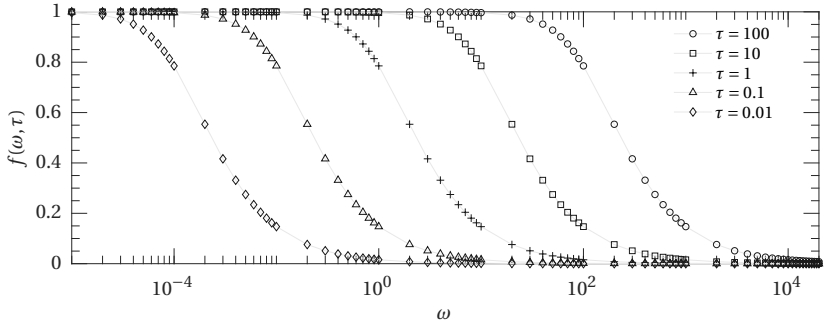

Figure 3.16: modification function $f(k,\tau)$ over wavenumber for different optical depths

The shape of $f(\omega,\tau)$ highlights the different behaviour of absorption when different temperature length scales are involved in the radiative heat transfer. If a turbulent temperature structure is large enough (i.e., ω is small enough), it can be considered "opaque", since it is able to capture the incoming radiation. Even though small scales are able to emit radiation, they are too thin to absorb and thus can be considered transparent to incoming radiation. This behaviour of temperature scales is dictated by the magnitude of the optical thickness. For a larger τ, the ability to absorb a greater quantity of incoming thermal radiation is extended to smaller scales. Therefore, increasing the optical thickness causes the "opaque wavenumber" threshold to increase and the $f(\omega,\tau)$ slope to diminish (figure 3.16). Additionally, the effects of absorption and emission are amplified by the optical thickness τ, since $\widehat{Q^{R\prime}} = \tau(\widehat{E}' - \widehat{G}')$.

From this analysis we conclude that: (1) the absorption reduces $\widehat{Q^{R\prime}}(\boldsymbol{\omega})$ resulting in a source of temperature variance, while emission increases $\widehat{Q^{R\prime}}(\boldsymbol{\omega})$, causing a dissipation of temperature fluctuations. (2) at a low optical thickness, a non-negligible effect of G is observed only on the larger scales, while the higher frequency fluctuations are still dominated by the effect of emission. (3) upon increasing the optical thickness, absorption length scales are reduced and are hence more correlated with temperature scales. Therefore, absorption is able to contrast emission effects up to larger wavenumbers. When the optically thick limit is reached $\widehat{G}'(\boldsymbol{\omega}) = \widehat{E}'(\boldsymbol{\omega})$ over all significant wavenumbers. (4) the combined effect of emission and absorption, for a κ large enough, results in a withdrawal of energy at a constant rate throughout the scales due to emission and a preferential accumulation of energy on the larger scales due to the effect of absorption. The temperature spectrum's slope steepens as a result. (5) modifying the significative wavenumbers of temperature in the system (i.e., increasing Re or Pr) results in a modification of the radiation effects over the turbulent temperature spectra due to the wavenumber dependency of $f(\omega,\tau)$. (6) a higher mean temperature results in an enhancement of both emission and absorption effects on the turbulent temperature spectrum.

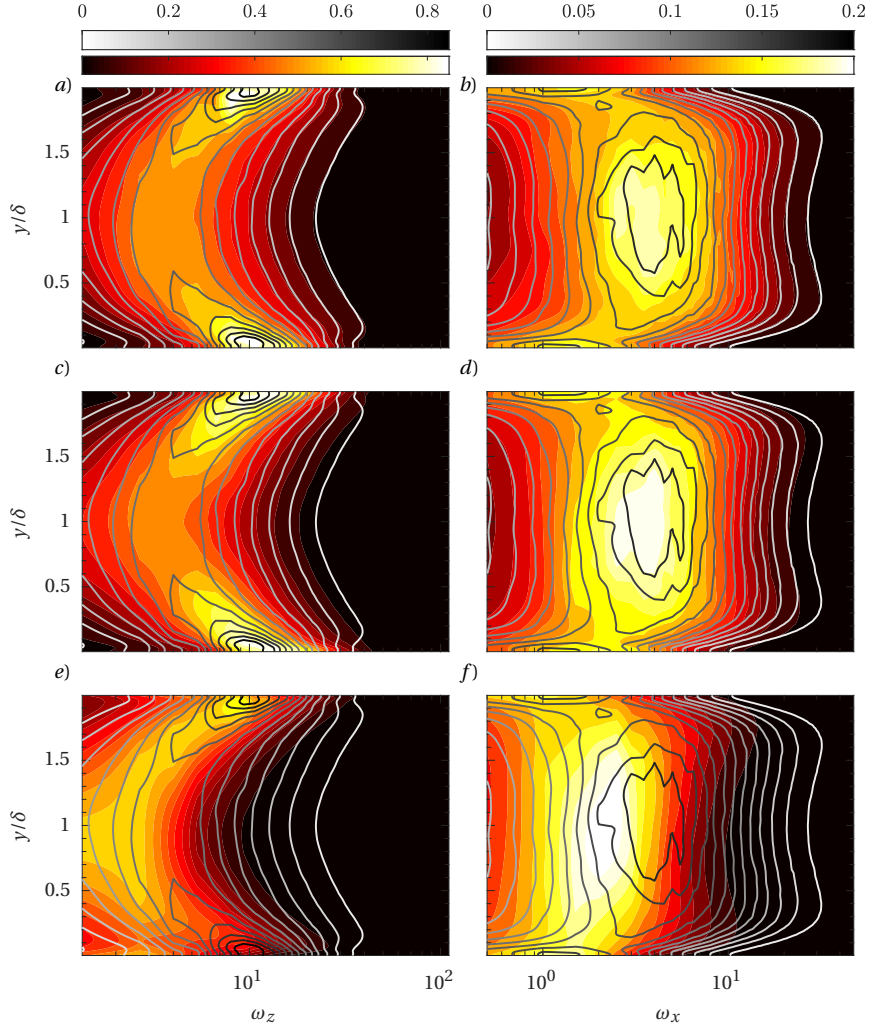

Figure 3.17: Pre-multiplied, normalized turbulent temperature spectra contours $k\mathscr{S}_{\theta\theta}(\omega)/\overline{\theta'^2}$. On the left hand side spanwise spectra are shown while streamwise spectra are on the right hand side. Lines correspond to non radiative case, while background contour correspond to: (a): $\tau = 0.1$; (b): $\tau = 0.1$; (c): $\tau = 1$; (d): $\tau = 1$; (e): $\tau = 10$; (f): $\tau = 10$

3.4.1. TEMPERATURE SPECTRA IN TURBULENT RADIATIVE CHANNEL FLOWS

In inhomogeneous anisotropic turbulence the turbulent temperature spectra will be different based on the location and the direction considered. In particular, in a turbulent channel flow with isothermal hot and cold walls, turbulent temperature structures are thin and streaky near the walls and somewhat larger and isotropic in the core (i.e, are characterized by a spectrum with energy concentrated at relatively small $||\boldsymbol{\omega}||$ while exhibiting the same trend in ω_z and ω_x).
Since temperature structures are not homogeneous, different radiative effects will apply in different zones. In particular where large and more isotropic structures are present, absorption will be more effective, retaining the emitted thermal energy, while where structures are thin and streaky (near the walls), emission will dominate, redistributing energy towards/from the walls and the center of the channel.

Figure 3.17 shows the comparison of the normalized pre-multiplied temperature spectra, in the spanwise and streamwise direction, between radiative cases (background contours) and the non radiative case (line contours). When $\tau = 0.1$, figures 3.17(a) and (b), the whole channel is optically thin, therefore emission dominates over absorption and no significant change in energy redistribution can be noticed. For $\tau = 1$, figures 3.17(c) and (d), a slight steepening of the spectra can be noticed in the core of the channel. Indeed, when increasing optical thickness to $\tau = 10$, figures 3.17(e) and (f), large structures located in the center of the channel become opaque. This causes the emitted radiation to be reabsorbed within the large scales. We therefore observe that, in the core of the channel, the large, isotropic temperature scales grow in size and intensity, due to the action of radiative absorption.

The spanwise turbulent temperature spectra at the location $y/\delta = 1.4$, $y/\delta = 1.93$ and $y/\delta = 0.054$ (location of temperature variance peaks) are shown in figures 3.18(a), 3.18(c), 3.18(e), respectively, while figures 3.18(b), 3.18(d), 3.18(f) show streamwise turbulent temperature spectra at the same locations. By analysing figures 3.18(a) and 3.18(b), it is possible to notice that for a low optical thickness, case $\tau = 0.1$, the thermal fluctuations are reduced proportionally throughout the whole spectrum and the slope is not significantly affected. This emphasizes that absorption does not play a significant role and that radiation affects the temperature spectrum through the emission TRI. A further decrease in overall thermal fluctuation intensity can be observed for $\tau = 1$, with a larger fluctuation reduction concentrated at large wavenumbers (i.e., within the small scales). The modification of the turbulent temperature spectrum for $\tau = 1$ proves that the increase of $\overline{G'^2}$ mostly affects large scales, while at small wavelength the stabilizing action of emission remains unaffected by absorption. Upon increasing the optical thickness ($\tau = 10$) the temperature fluctuations located in the low wavenumber region grow beyond the level of a non radiative case. We conclude that, due to the emission-absorption process, radiation energy emitted at small scales is absorbed by the low wavenumber range. The reduction of fluctuation due to emission is further amplified at high wavenumbers, confirming the previous observation of optically thin behaviour at the small scales.

Figures 3.18(c)-3.18(d) depict turbulent temperature spectra for all cases at $y/\delta = 1.93$. In the streamwise direction (figure 3.18(d)), due to the low level of incident radi-

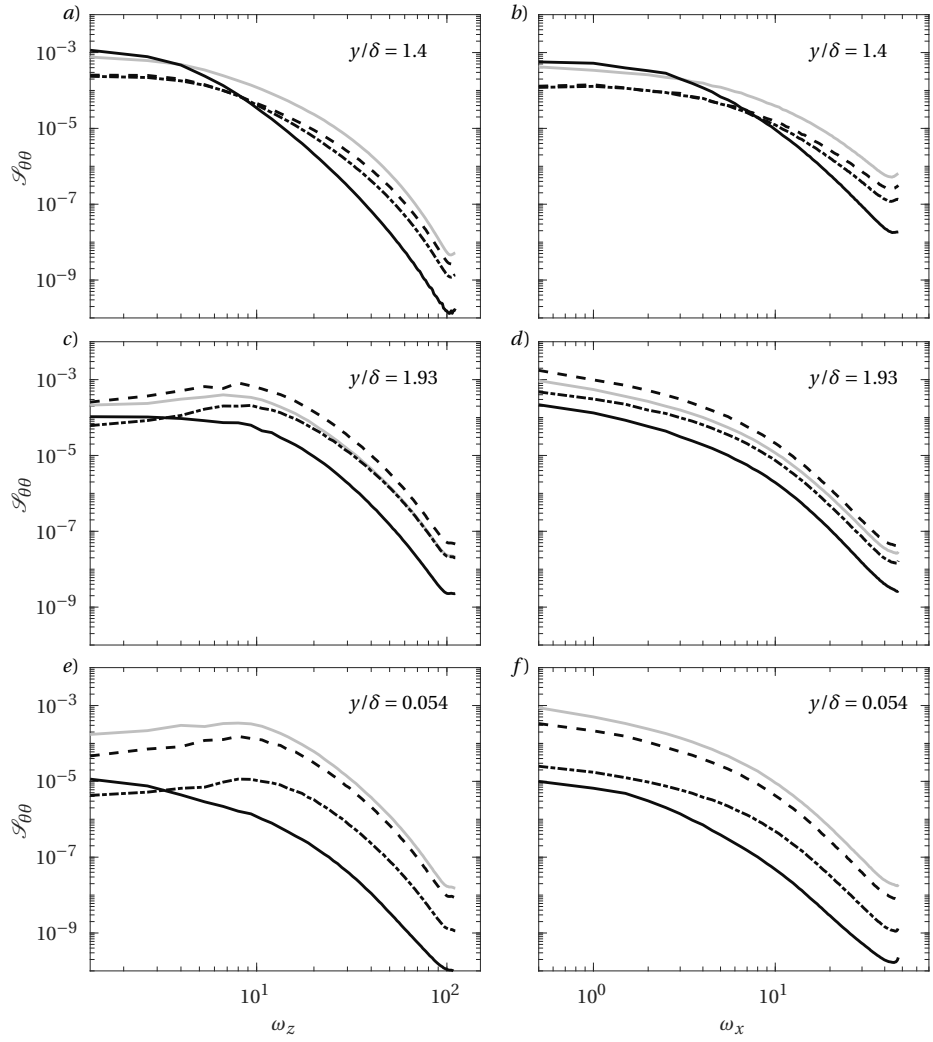

Figure 3.18: Turbulent temperature spectra $\mathscr{S}_{\theta\theta}$ for different locations; left hand side: spanwise spectra; right hand side: streamwise spectra. Gray solid line: no radiation, dashed line: $\tau = 0.1$, dashed dotted line: $\tau = 1$, black solid line: $\tau = 10$.

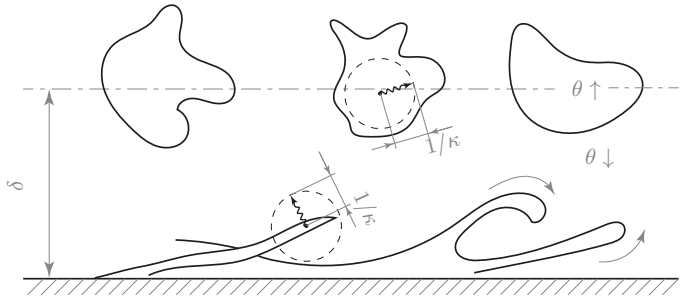

Figure 3.19: Schematic diagram of TRI in anisotropic turbulence. The solid lines show a qualitative representation of temperature structures (assuming positive temperature fluctuation for simplicity), while the dashed circles show the characteristic length scale of radiation. Radiative emission is isotropic (i.e., emission occurs similarly in every direction). The influence of dimension and anisotropy of temperature structures is highlighted. The more isotropic the structure (near the centerline), the more efficient it is in absorbing the radiation emitted within itself, whereas anisotropic structures (near the walls) will dissipate their energy towards the lower temperature surroundings. A larger τ would reduce the dimensions of the dashed circle that would eventually fit in smaller anisotropic scales.

ation fluctuations, we observe a constant rate dissipation throughout the whole spectrum, except for $\tau = 0.1$ where the higher temperature gradient produces higher θ' (see section 3.3.4). In the spanwise direction, the same behaviour as for the streamwise direction is noticed, with the exception of $\tau = 10$ where in the low wavenumber range absorption partly contrasts the dissipation effects of emission.

Finally, figures 3.18(e) and 3.18(f) show the spanwise and streamwise spectra at $y/\delta = 0.0545$, respectively. Qualitatively the slopes of the spectra are much similar to what is observed for $y/\delta = 1.93$, but all effects are enhanced by the higher mean temperature that increase radiative effects (as discussed in section 3.4). It is crucially important to point out that the results analysed in this section must be related to the observation of the impact of TRI discussed in section 3.3.4. There it is shown that the direct effect of radiation grows dramatically with an increase in τ, and therefore the impact of radiation on temperature at a low optical thickness ($\tau = 0.1$) is not only connected to direct effects, since also the modification of the mean temperature profile plays a large role.

Therefore, we summarize that: (1) for a low optical thickness the TRI effect mainly translates in a dissipation of thermal turbulence throughout the whole spectrum. For a higher optical thickness, besides dissipating fluctuations, TRI produces a withdrawal of energy from the small scales by the action of emission that is then deposited within the large scales through absorption. A steepening of the turbulent temperature spectrum thus occurs as a consequence of the accumulation of energy in the low frequency range. (2) Since radiative emission is isotropic, high anisotropy of temperature structures reduces absorption effects. (3) The accumulation of energy in large thermal eddies is noticed only in the core of the channel where large and isotropic structures are present. In the near wall region, where the growth of G' is inhibited by the presence of thin and highly anisotropic structures, a localized reduction of temperature fluctuation is observed for higher optical thicknesses, similarly to low optical thickness. (4) The higher mean temperature near the hot wall results in an enhancement of the radiative

effects.
A clear visualization of the features described above is obtained with instantaneous contours of temperature fluctuations shown in figures 3.1 and 3.2.

3.5. SUMMARY

In this chapter, a comprehensive study of turbulence radiation interactions in a radiative turbulent channel flow has been performed. The modification of the temperature field upon varying the optical thickness has been investigated with the aid of temperature variance budgets and turbulent temperature spectra. The results show different magnitudes and qualitative behaviours of turbulence-radiation interactions when different optical depths are considered, and highlight particularly the contrasting effects of radiative absorption and emission on TRI.

For a low optical thickness ($\tau = 0.1$) the role of absorption is limited to the modification of mean profiles since incident radiation (G) is not influenced by local thermal fluctuations. On the other hand, emission affects the whole temperature spectrum, stabilizing temperature and reducing thermal fluctuations mainly in the channel core. The direct effect of radiation on temperature variance is thus linked only to emission, and has a relatively small impact due to the low absorption coefficient. For an intermediate case ($\tau = 1$) the effects are amplified and a strong depletion of the thermal fluctuation field is noticed because of emission. When increasing the optical depth to moderately optically thick levels ($\tau = 10$), temperature variance shows a large influence on absorption due to a stronger local coupling between temperature and incident radiation. When $\tau = 10$, energy is withdrawn from the whole spectrum due to a tight coupling of emission and temperature fluctuations, and it is accumulated on the large scales that are more sensitive to absorption fluctuations. The effect of a larger absorption fluctuation field is then translated in a modification of TRI. Radiative fluctuations are not only restricted to dissipating temperature fluctuations, but also cause a redistribution of fluctuations over the temperature scales.

The effect of anisotropic turbulence results in a reduction of the aforementioned TRI transition near the boundaries where the thin streaky structures are not able to retain the emitted thermal radiation. In the center of the channel on the other hand, the larger isotropic structures can absorb and contain the redistributed energy.

Furthermore, a study of the budgets of temperature variance shows that with an increase in the optical thickness, the direct effect of radiation on temperature statistics grows drastically, replacing the role of molecular terms in dissipating and redistributing temperature variance. The radiative term ($\mathscr{R}_\theta$) has been investigated, in analogy with molecular terms, by decomposition in two quantities, namely radiative diffusion ϕ_r and radiative dissipation ϵ_r. As the optical thickness is increased, we observed a similarity between the behaviour of radiative and molecular terms.

Finally, we proved that, due to the non-local effect of long range heat transfer, encompassed in the incident radiation fluctuations, a collapsing of mean profiles via direct scaling is not possible, irrespective of the scaling chosen.

4

SCALING OF TURBULENCE-RADIATION INTERACTIONS

As demonstrated in the previous chapter, TRI plays a central role in shaping the temperature field in radiatively participating turbulent flows, but it is difficult to predict due to the unfeasibility of finding a direct temperature scaling in radiative environments. In this chapter we obviate to this problem by proposing a suitable approximation to the radiative field fluctuations which provides a quantitative assessment of the TRI phenomena. The mathematical model is developed for gray gas and validated with gray gas DNS cases.

Part of the contents of this chapter appeared in the following publications, Silvestri, Roekaerts and Pecnik, Assessing turbulence radiation interactions in turbulent flows of non-gray media, J. Quant. Spectr. Rad. Transf., **233** (2019), 134–148. [65]

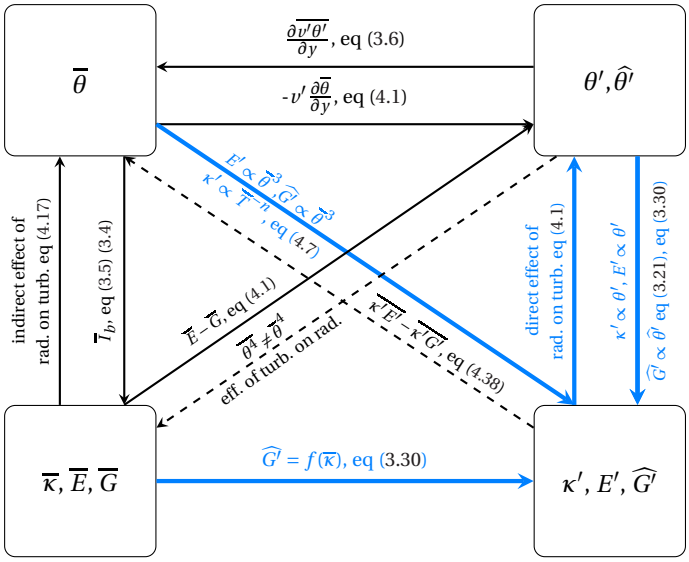

Figure 4.1: Schematic diagram of TRI in flow affected by radiative heat transfer. These relations will retain their validity in compressible turbulent flows. We did not investigate the effect of turbulence on radiation ($\theta' \rightarrow \overline{E}, \overline{G}$, shown as dashed) since it is reported to be negligible for non reactive flows [15, 22, 29, 32]. While E' is directly connected to $\overline{\theta}$ and θ', the connection between $\overline{\theta}$, θ' and G', occurs in a spectral domain, since G is a long-range variable, dependent on the whole temperature field.

4.1. INTRODUCTION

A simple diagram summarizing the effects of TRI on temperature fluctuations is shown in figure 4.1. Both mean and fluctuating radiative quantities have an effect on temperature statistics. While mean radiation indirectly affects θ' through the modification of $\overline{\theta}$, fluctuations of E and G have a direct effect on θ'.

In the previous chapter we have demonstrated that turbulence-radiation interactions prevent the scaling of the temperature field and heat fluxes due to the direct effect of radiative fluctuations. Since a direct scaling is impossible, predictive capabilities in flows affected by TRI are hampered. For this reason, in this chapter we provide a new approach to TRI scaling by directly estimating some TRI quantities. To generalize, figure 4.1 shows the pathways of TRI in presence of a variable absorption coefficient. In case of a variable κ, equation 3.20 yiels

$$\frac{\partial \theta'}{\partial t} + \overline{u_j}\frac{\partial \theta'}{\partial x_j} + v'\frac{\partial \overline{\theta}}{\partial y} + \frac{\partial u_j'\theta'}{\partial x_j} - \frac{\partial \overline{v'\theta'}}{\partial y} = \frac{1}{RePr}\frac{\partial^2 \theta'}{\partial x_j^2} - \frac{\overline{\kappa}}{RePrPl}\left(E' - G'\right) - \frac{\kappa'}{RePrPl}\left(\overline{E} - \overline{G}\right). \tag{4.1}$$

In the above equation second order quantities containing $\kappa' - E' - G'$ have been omitted. As demonstrated in the previous chapter, the largest effect of radiative fluctuations on $\overline{\theta}$ is due to the modification of θ' and the consequent change in turbulent heat transfer ($\overline{\theta} \rightarrow \kappa', E', G' \leftrightarrow \theta' \rightarrow \overline{\theta}$). In particular, the blue arrows in figure 4.1 highlight the dominant mechanism of TRI which prevents the possibility of scaling. In order to quan-

tify and model this TRI mechanism, it is necessary to provide approximations for the fluctuations of radiative quantities depicted in the bottom right block of figure 4.1. For this reason, this chapter focuses on quantitatively assessing the pathways highlighted in blue, which are qualitatively and mechanistically described in the previous chapter. This assessment is done here for gray gases and will be extended to non-gray gases in the next chapter.

4.2. APPROXIMATING RADIATIVE FIELD FLUCTUATIONS

TRI manifests in the appearance of a fluctuating radiative field. As such, in this section we will derive mathematical relations to express the fluctuations of radiative quantities. We will test these relation in the following sections using DNS data to prove the validity of the assumptions employed. Referring to equation (3.4) and the bottom left box of diagram 4.1, the quantities that require estimation are

$$E' \,, \quad \kappa' \,, \quad G' \,. \tag{4.2}$$

Since radiative field fluctuations appear as a consequence of temperature fluctuations, we propose a simple approach based on linear relations that takes the following form

$$E' \approx f_E \theta' \,, \quad \kappa' \approx f_\kappa \theta' \,, \quad G' \approx f_G \theta' \,, \tag{4.3}$$

where the coefficients of proportionality f_κ, f_E and f_G only depend on mean quantities and are independent of θ'.

4.2.1. APPROXIMATING E'

Given equation (3.2), emission fluctuations are defined as

$$E' = E - \overline{E} = 4\left(\frac{\theta}{T_0}+1\right)^4 - 4\overline{\left(\frac{\theta}{T_0}+1\right)^4} \,. \tag{4.4}$$

By substituting the definition of the Reynolds decomposition of $\theta = \theta' + \overline{\theta}$ and rearranging the terms with the same order of θ', it is possible to obtain

$$\begin{aligned} E' = &\left(\frac{16\overline{\theta}^3}{T_0^4} + \frac{48\overline{\theta}^2}{T_0^3} + \frac{48\overline{\theta}}{T_0^2} + \frac{16}{T_0}\right)\theta' + \\ &+ \left(\frac{24\overline{\theta}^2}{T_0^4} + \frac{48\overline{\theta}}{T_0^3} + \frac{24}{T_0^2}\right)(\theta'^2 - \overline{\theta'^2}) + \\ &+ \left(\frac{16\overline{\theta}}{T_0^4} + \frac{16}{T_0^3}\right)(\theta'^3 - \overline{\theta'^3}) + \\ &+ \left(\frac{4}{T_0^4}\right)(\theta'^4 - \overline{\theta'^4}) \,. \end{aligned} \tag{4.5}$$

Considering only the first order terms, θ', the first coefficient of proportionality f_E is defined as

$$f_E = \frac{16\overline{\theta}^3}{T_0^4} + \frac{48\overline{\theta}^2}{T_0^3} + \frac{48\overline{\theta}}{T_0^2} + \frac{16}{T_0}\,. \tag{4.6}$$

4.2.2. APPROXIMATING κ'

To develop the model, we take the Planck mean absorption coefficient as general representation of absorption coefficient variation for gray gases (the extension for non-gray gases will follow in the next chapter). Usually, κ is directly proportional to pressure and non-linearly related to temperature. Here (since we deal with an isobaric channel flow) we assume that κ depends only on temperature as a 5^{th} order polinomial function of T^{*-1} (as shown in [66]). It is important to point out that this fit is realistic and achievable also in case of a non-gray gas. Therefore,

$$\kappa = \delta^* \left(c_0 + \left(\frac{c_1}{T^*}\right) + \left(\frac{c_2}{T^{*2}}\right) + \left(\frac{c_3}{T^{*3}}\right) + \left(\frac{c_4}{T^{*4}}\right) + \left(\frac{c_5}{T^{*5}}\right)\right), \tag{4.7}$$

where $c_0 - c_5$ are the fitting constants. In order to derive f_κ, we will use the dimensional temperature T^*, with its mean $\overline{T^*} = T_c^* + \overline{\theta}\Delta T^*$ and its fluctuation as $T^{*\prime} = \theta' \Delta T^*$. The asterisk will be dropped hereafter for the sake of simplicity. By assuming low temperature fluctuations, $T'/\overline{T} \ll 1$ (invalid for reactive flows), and by performing a Taylor expansion (neglecting higher order terms), it is possible to show that $\overline{1/T^\alpha} \approx 1/\overline{T}^\alpha$. Therefore, the average of equation (4.7) can be approximated as

$$\overline{\kappa} \approx \delta^* \left(c_0 + \frac{c_1}{\overline{T}} + \frac{c_2}{\overline{T}^2} + \frac{c_3}{\overline{T}^3} + \frac{c_4}{\overline{T}^4} + \frac{c_5}{\overline{T}^5} \right). \tag{4.8}$$

Using the Reynolds decomposition for $\kappa' = \kappa - \overline{\kappa}$, it is possible to approximate κ' using (4.8). Starting with the terms containing T^{-1}, one obtains, by assuming that $T'\overline{T} \ll \overline{T}^2$,

$$c_1 \left(\frac{1}{T} - \frac{1}{\overline{T}} \right) = c_1 \left(\frac{\overline{T} - T}{T\overline{T}} \right) \approx -c_1 \frac{T'}{\overline{T}^2} = -c_1 \frac{\Delta T}{\overline{T}^2} \theta'. \tag{4.9}$$

Accordingly, the terms with T^{-2} can be expressed as

$$c_2 \left(\frac{1}{T^2} - \frac{1}{\overline{T}^2} \right) = c_2 \left(\frac{\overline{T'^2} - 2\overline{T}T' - T'^2}{(\overline{T}^2 + 2\overline{T}T' + T'^2)(\overline{T}^2 + \overline{T'^2})} \right). \tag{4.10}$$

Again, neglecting smaller terms in both the denominator ($\approx \overline{T}^4$) and the numerator ($2\overline{T}T' \gg \overline{T'^2} - T'^2$) yields

$$c_2 \left(\frac{1}{T^2} - \frac{1}{\overline{T}^2} \right) \approx -c_2 \frac{2\Delta T}{\overline{T}^3} \theta'\,. \tag{4.11}$$

In the same fashion it is possible to demonstrate that

$$\begin{aligned} c_3\left(\frac{1}{T^3}-\frac{1}{\overline{T}^3}\right) &\approx -c_3\frac{3\Delta T}{\overline{T}^4}\theta' \,, \\ c_4\left(\frac{1}{T^4}-\frac{1}{\overline{T}^4}\right) &\approx -c_4\frac{4\Delta T}{\overline{T}^5}\theta' \,, \\ c_5\left(\frac{1}{T^5}-\frac{1}{\overline{T}^5}\right) &\approx -c_5\frac{5\Delta T}{\overline{T}^6}\theta' \,. \end{aligned} \tag{4.12}$$

Combining the above expressions, the second function is given by

$$f_\kappa = -\delta^*\left(c_1\frac{\Delta T}{\overline{T}^2}+c_2\frac{2\Delta T}{\overline{T}^3}+c_3\frac{3\Delta T}{\overline{T}^4}+c_4\frac{4\Delta T}{\overline{T}^5}+c_5\frac{5\Delta T}{\overline{T}^6}\right) . \tag{4.13}$$

4.2.3. APPROXIMATING G'

Owing to the non-local nature of incident radiation G, and the conclusions of chapter 3, it is convenient to express the G' relation with the temperature field in the wavenumber domain (i.e., Fourier transformed), rather than in spatial domain. This derivation will follow very closely the one performed in section 3.4 for the case of a uniform κ and is similar to the approach taken by Soufiani in [26]. For the sake of simplicity, it is useful to first assume isotropic turbulence and then to generalize the relations for anisotropic cases. The derivation will be performed for a gray gas, and the extension for non-gray gases will follow in section 5.5.1. In the case of homogeneous isotropic turbulence with a gray gas, the Fourier transform of incident radiation fluctuations simply yields

$$\widehat{G'}(\boldsymbol{\omega}) = \frac{1}{\pi}\int_{4\pi}\widehat{I'}(\boldsymbol{\omega})\,d\Omega \,, \tag{4.14}$$

where the hat indicates a three dimensional, spatial Fourier transform of an underlying quantity, and $\boldsymbol{\omega}$ is the wavenumber vector. The RTE for the fluctuating component of the intensity ($I' = I - \overline{I}$) in spatial domain reads

$$s_j\frac{\partial I'}{\partial x_j} = \overline{\kappa}I'_b + \kappa'\overline{I}_b + \kappa' I'_b - \overline{\kappa}I' - \kappa'\overline{I} - \kappa' I' + (\overline{\kappa' I'_b} - \overline{\kappa' I'}) \,, \tag{4.15}$$

which after applying the Fourier transform gives

$$i(s_j\omega_j)\widehat{I'} = \overline{\kappa}\widehat{I'}_b + \widehat{\kappa'}\overline{I}_b - \overline{\kappa}\widehat{I'} - \widehat{\kappa'}\overline{I} \,. \tag{4.16}$$

Second order terms, $\kappa' I'_b$ and $\kappa' I'$, can be neglected in non-reactive turbulent flows, as demonstrated in Refs. [21, 22, 29, 31]. The Fourier transform of the intensity fluctuation $\widehat{I'}$ can then be expressed explicitly as

$$\widehat{I'} = \frac{\overline{\kappa}\widehat{I'}_b + \widehat{\kappa'}\overline{I}_b - \widehat{\kappa'}\overline{I}}{\overline{\kappa} + i(s_j\omega_j)} \,. \tag{4.17}$$

By substituting this relation back into (4.14), the Fourier transformed incident radiation fluctuations can be written as

$$\widehat{G'} = \underbrace{\frac{\overline{\kappa}\widehat{I'}_b}{\pi}\int_{4\pi}\frac{1}{\overline{\kappa}+i(s_j\omega_j)}d\Omega}_{\mathscr{G}_1} + \underbrace{\frac{\widehat{\kappa'}\overline{I}_b}{\pi}\int_{4\pi}\frac{1}{\overline{\kappa}+i(s_j\omega_j)}d\Omega}_{\mathscr{G}_2} - \underbrace{\frac{\widehat{\kappa'}}{\pi}\int_{4\pi}\frac{\overline{I}}{\overline{\kappa}+i(s_j\omega_j)}d\Omega}_{\mathscr{G}_3}\,. \tag{4.18}$$

In order to solve the integrals, it is convenient to split them into a real and an imaginary part as done in section 3.4. The integrand in both $\mathscr{G}_1$ and $\mathscr{G}_2$ can then be written as

$$\frac{1}{\overline{\kappa}+i(s_j\omega_j)} = \frac{\overline{\kappa}}{\overline{\kappa}^2+(s_j\omega_j)^2} - i\frac{(s_j\omega_j)}{\overline{\kappa}^2+(s_j\omega_j)^2}. \tag{4.19}$$

Using again a variable transformation $\mu = (s_j\omega_j)/\omega$, allows to integrate both terms to

$$\int_{4\pi}\frac{\overline{\kappa}}{\overline{\kappa}^2+(s_j\omega_j)^2}d\Omega = \frac{4\pi}{\omega}\text{atan}\left(\frac{\omega}{\overline{\kappa}}\right), \tag{4.20}$$

$$\int_{4\pi}\frac{(s_j\omega_j)}{\overline{\kappa}^2+(s_j\omega_j)^2}d\Omega = 0\,. \tag{4.21}$$

where $\omega = \|\boldsymbol{\omega}\|$. Note, the integral of the imaginary part is zero, such that the final expressions for $\mathscr{G}_1$ and $\mathscr{G}_2$ are

$$\mathscr{G}_1 = 4\overline{\kappa}\frac{\widehat{I'}_b}{\omega}\text{atan}\left(\frac{\omega}{\overline{\kappa}}\right), \tag{4.22}$$

$$\mathscr{G}_2 = 4\overline{I}_b\frac{\widehat{\kappa'}}{\omega}\text{atan}\left(\frac{\omega}{\overline{\kappa}}\right). \tag{4.23}$$

The term $\mathscr{G}_3$ requires a different treatment due to the presence of the non-isotropic quantity $\overline{I}$. As a crude approximation, let us assume an isotropic $\overline{I}$ field, i.e. $\overline{I}$ being independent of Ω. The implications of this approximation will be discussed in the following chapter. In this case, the integration gives an equivalent result as for $\mathscr{G}_1$ and $\mathscr{G}_2$ above, namely

$$\mathscr{G}_3 \approx 4\overline{I}\frac{\widehat{\kappa'}}{\omega}\text{atan}\left(\frac{\omega}{\overline{\kappa}}\right). \tag{4.24}$$

Since $\overline{I}$ has been assumed isotropic, the mean incident radiation reduces to $\overline{G} = 4\overline{I}$, such that

$$\mathscr{G}_3 \approx \overline{G}\frac{\widehat{\kappa'}}{\omega}\text{atan}\left(\frac{\omega}{\overline{\kappa}}\right). \tag{4.25}$$

Finally, the sum of the three individual terms gives the approximation of the incident radiation fluctuations in a Fourier transformed domain

$$\widehat{G'} \approx \overline{\kappa}\frac{\widehat{E'}}{\omega}\text{atan}\left(\frac{\omega}{\overline{\kappa}}\right) + \overline{E}\frac{\widehat{\kappa'}}{\omega}\text{atan}\left(\frac{\omega}{\overline{\kappa}}\right) - \overline{G}\frac{\widehat{\kappa'}}{\omega}\text{atan}\left(\frac{\omega}{\overline{\kappa}}\right), \tag{4.26}$$

where $4I_b$ has been replaced by E in the first and second term. Equation (4.26) relates the Fourier transform of G' to $\widehat{E'}$ and $\widehat{\kappa'}$. In particular, these are scaled by a real function of the wavenumber $(1/\omega \cdot \text{atan}(\omega/\overline{\kappa}))$. The lack of an imaginary part in the scaling

function implies that $\widehat{G'}$ has no direct phase shift when compared to $\widehat{E'}$ and $\widehat{\kappa'}$. The rotational phase shift produced by the presence of an imaginary part can only be caused by the long-range action of $\overline{I}$ in $\mathscr{G}_3$, which propagates local absorption coefficient fluctuations from other directions. However, by employing the isotropic assumption, the mean intensity ($\overline{I}$), which couples the local κ' to G', is considered equal coming from all directions.

To obtain a closed expression for $\widehat{G'}$ as a function of θ', it is necessary to replace ω with one characteristic value, namely ω_c. After collecting terms with κ' and replacing ω with ω_c, equation (4.26) can be written as

$$\widehat{G'} \approx \underbrace{\frac{\overline{\kappa}}{\omega_c}\operatorname{atan}\left(\frac{\omega_c}{\overline{\kappa}}\right)}_{\text{not } f(\omega)} \cdot \widehat{E'} + \underbrace{\frac{\overline{E}-\overline{G}}{\omega_c}\operatorname{atan}\left(\frac{\omega_c}{\overline{\kappa}}\right)}_{\text{not } f(\omega)} \cdot \widehat{\kappa'} \,. \tag{4.27}$$

This entails that the shape of the G spectrum is entirely defined by the E and κ spectra. We point out that, as seen in section 3.4, this is not necessarily true, but this model encompasses the different shape of the spectra in the parameter ω_c such that we preserve the integration over the wavenumbers. If this is done, an inverse Fourier transform of equation (4.27) yields

$$G' \approx \frac{\overline{\kappa}}{\omega_c}\operatorname{atan}\left(\frac{\omega_c}{\overline{\kappa}}\right) \cdot E' + \frac{\overline{E}-\overline{G}}{\omega_c}\operatorname{atan}\left(\frac{\omega_c}{\overline{\kappa}}\right) \cdot \kappa' \,. \tag{4.28}$$

Substituting $E' = f_E\theta'$ and $\kappa' = f_\kappa\theta'$ yields

$$G' \approx \left(\frac{\overline{\kappa}}{\omega_c}\operatorname{atan}\left(\frac{\omega_c}{\overline{\kappa}}\right) \cdot f_E + \frac{\overline{E}-\overline{G}}{\omega_c}\operatorname{atan}\left(\frac{\omega_c}{\overline{\kappa}}\right) \cdot f_\kappa\right) \cdot \theta' \,. \tag{4.29}$$

and finally the expression for the third and last coefficient of proportionalty f_G can be stated as follows

$$f_G = \left(\frac{f_E\overline{\kappa} + f_\kappa(\overline{E}-\overline{G})}{\omega_c}\right)\operatorname{atan}\left(\frac{\omega_c}{\overline{\kappa}}\right). \tag{4.30}$$

4.2.4. DETERMINING ω_c FOR ANISOTROPIC TURBULENCE

To obtain a formal expression for equation (4.28), the parameter ω_c, which represent the length scale of the average energy-containing temperature structure, requires a closure. In homogeneous isotropic turbulence it can be defined as the expected value of $\boldsymbol{\omega}$ based on the normalized turbulent temperature power density spectrum.

$$\omega_c = \left\| \int_0^\infty \frac{\boldsymbol{\omega}\mathscr{S}_{\theta\theta}(\boldsymbol{\omega})}{\overline{\theta'^2}} d\boldsymbol{\omega} \right\| \,, \tag{4.31}$$

where $\mathscr{S}_{\theta\theta}$ is the spectrum of temperature fluctuations. Note, temperature has been chosen since κ and E are fully defined by θ. The integrand in equation (4.31) represents the normalized distribution of temperature fluctuations over all scales (shown in figure

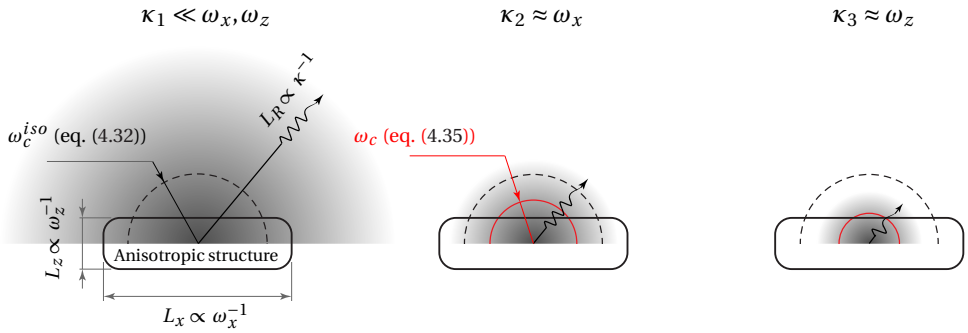

Figure 4.2: Illustration of radiative effects on anisotropic structures in media with different κ values. L_x, L_z and L_R are the length scales in the streamwise direction, in the spanwise direction and for radiative transfer, respectively. The dashed circle represents the model isotropic structure described by ω_c^{iso} (independent of κ). The red circle shows the correction to properly reflect the anisotropic structure.

3.17), and, as such, it is an appropriate choice to define the length scale of the energy containing eddies.

In a channel flow, however, temperature structures are anisotropic due to the presence of walls. In mathematical terms this means that the inhomogeneous wall-normal direction does not allow the application of the Fourier transform in equation (4.15) in all spatial directions. As such, $\partial_y \widehat{I'}$ would remain in equation (4.16), preventing the derivation of an analytic solution. To overcome this, we will only account for the anisotropic temperature structures in the turbulent flow and assume that the fluctuations of the incident radiation emerge from an unbounded domain without the presence of walls.

If we follow the same approach as in homogeneous isotropic turbulence, the dimension of the scales can be inferred from the one-dimensional temperature spectrum in span-wise and stream-wise directions. The resulting ω_c^{iso} is then obtained as

$$\omega_c^{iso} = \left[\left(\frac{\int_0^\infty \omega_x \mathcal{S}_{\theta\theta}(\omega_x) d\omega_x}{\overline{\theta'^2}} \right)^2 + \left(\frac{\int_0^\infty \omega_z \mathcal{S}_{\theta\theta}(\omega_z) d\omega_z}{\overline{\theta'^2}} \right)^2 \right]^{0.5}. \tag{4.32}$$

As described in section 3.4, anisotropic temperature structures are associated with an absorption penalty due to a "non-spherical surface to volume ratio" when compared to the isotropic nature of radiative emission. Figure 4.2 shows an example of an anisotropic structure immersed in flows of different absorption coefficients (increasing from left to right). L_R represents the mean-path length of radiative heat transfer which is inversely proportional to κ. If κ is much smaller than the structure's wavenumbers (figure 4.2, left), radiation escapes almost equally from all directions. It is clear that an isotropic structure with wavenumber ω_c^{iso} results in an equivalent behaviour, since the shape of the structure does not influence the absorption process. On the other hand, if κ^{-1} is comparable to the length scales of the temperature structure (center), radiation is allowed to escape in one direction, while being absorbed in another. However, the isotropic structure described by ω_c^{iso} (dashed circle in figure 4.2), results in a complete absorption in all directions. In this case, a more suitable approximation would be a smaller isotropic structure which allows for escaping radiation, as shown by the red circles in figure 4.2.

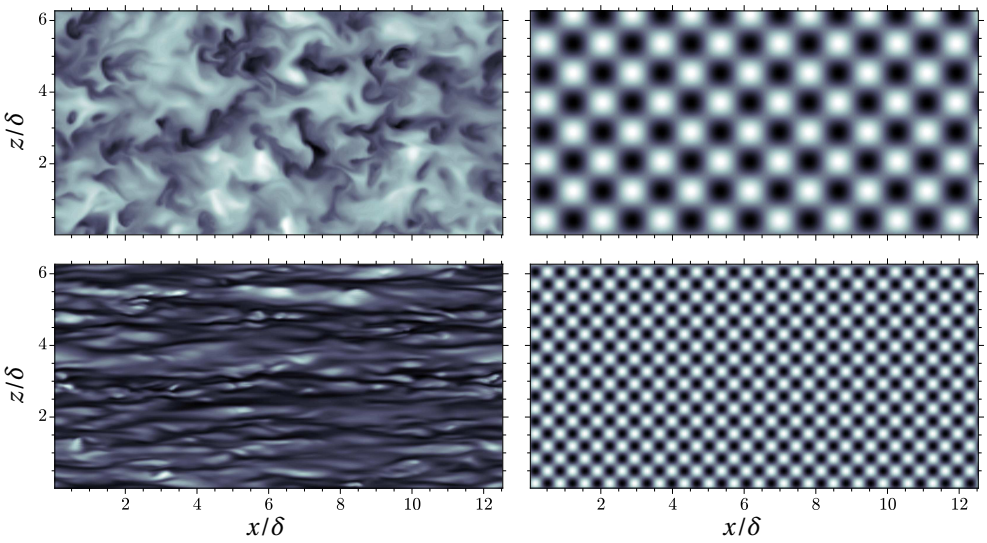

Figure 4.3: Visualization of the "collapsing" procedure that retrieves a characteristic ω_c to describe the radiative field. On the left: temperature fields at $y/\delta = 1.1$ (top) and $y/\delta = 1.97$ (bottom). On the right: corresponding single mode fields denoted by ω_c.

Therefore, it is necessary to increase ω_c^{iso} to account for this effect. It is crucial to notice that the correction of ω_c^{iso} must be larger as κ grows, as demonstrated in figure 4.2 by comparing the central and right image. As a first approximation, it is possible to correct for the structure's anisotropy by including the radiative length scale L_R in the definition of ω_c. By doing so, the increase of the absorption penalty with increasing κ is naturally included. Incorporating L_R in ω_c results in

$$\omega_c \propto \sqrt{{L_x}^{-2} + {L_z}^{-2} + {L_R}^{-2}} \ . \tag{4.33}$$

However, it yet has to be decided how much absorption to account for when defining the radiative length scale. From Beer's law, L_R can be expressed as

$$L_R = -\frac{\ln(X)}{\kappa} \ , \tag{4.34}$$

where X is the remaining radiative intensity after a certain distance L_R (in percentage). Mathematically speaking, complete absorption occurs at $L_R \to \infty$, which would result in $\omega_c = \omega_c^{iso}$. If 90% of absorbed radiation is accounted for, the corrected characteristic wavenumber can be expressed as

$$\omega_c = \left[\left(\frac{\int_0^\infty \omega_x \mathscr{S}_{\theta\theta}(\omega_x) d\omega_x}{\overline{\theta'^2}} \right)^2 + \left(\frac{\int_0^\infty \omega_z \mathscr{S}_{\theta\theta}(\omega_z) d\omega_z}{\overline{\theta'^2}} \right)^2 + \left(\frac{\overline{\kappa}}{\ln(10)} \right)^2 \right]^{0.5} \ . \tag{4.35}$$

An example of approximating all wavenumbers by one characteristic isotropic mode is visualized for the flow in a turbulent channel in figure 4.3. The contours on the left

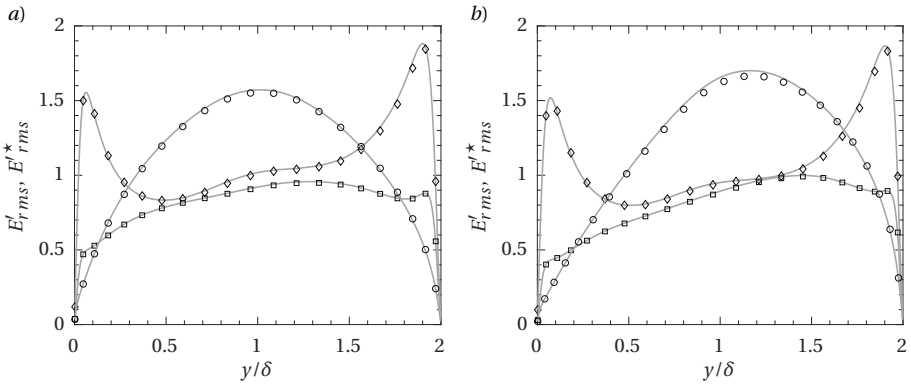

Figure 4.4: Comparison between emission fluctuations from DNS (symbols) and estimated using eq (4.36) (lines). *a*): constant absorption coefficient cases, *b*): variable absorption coefficient cases. Diamonds: $\tau = 0.1$. Squares: $\tau = 1$. Circles: $\tau = 10$.

show the temperature field at two wall parallel planes, namely at a plane close to a channel center (top) and a plane close to a wall (bottom). The contours on the right show the corresponding isotropic fields "seen" by the approximation of G'. These are characterized by a single mode described by ω_c as calculated by equation (4.35) (the amplitude of the field is completely irrelevant since ω_c provides only a scaling parameter). Consistent with the theory developed in the previous chapter, and the above reasoning, the dominant mode of anisotropic structures at $y/\delta = 1.97$ correspond to the largest wavenumber of the field.

4.3. VALIDATING THE LINEAR RELATIONS FOR GRAY GASES

The linear relations derived in the section above, are here validated with the three constant κ, gray cases discussed in chapter 3, as well as three additional gray cases with variable density and absorption coefficient, given in table 4.1.

Table 4.1: Description of the test cases

Cases	Re	Pr	Pl	T_0	ρ	κ	τ
gray-ρ01	3750	1	0.03	1.5	$T_0/(\theta + T_0)$	eq. (4.7)	0.1
gray-ρ1	3750	1	0.03	1.5	$T_0/(\theta + T_0)$	eq. (4.7)	1
gray-ρ10	3750	1	0.03	1.5	$T_0/(\theta + T_0)$	eq. (4.7)	10

The coefficients $c_0 - c_5$ for equation (4.7) are taken from the model of the Planck mean absorption coefficient of water vapour detailed by the Sandia laboratories [66]. These additional gray cases are used here only for validation purposes. An extensive description of the physics involved in these cases is presented in the next chapter while

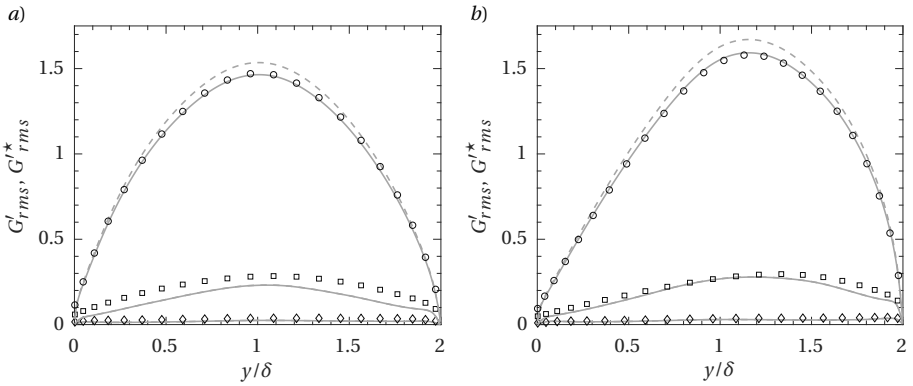

Figure 4.5: Comparison between incident radiation fluctuations from DNS (symbols) and estimated using eq (4.36) with ω_c^{iso} (eq. (4.32), dashed lines) and ω_c (eq. (4.35), solid line). *a*): constant absorption coefficient cases, *b*): variable absorption coefficient cases. Diamonds: $\tau = 0.1$. Squares: $\tau = 1$. Circles: $\tau = 10$.

discussing the effects of a variable absorption coefficient. Figures 4.4, 4.5 and 4.6 show the comparison between the radiative quantities (E'_{rms}, G'_{rms}, κ'_{rms}) and the estimations provided by the following

$$E'^{\star}_{rms} = f_E \theta'_{rms} \,, \quad G'^{\star}_{rms} = f_G \theta'_{rms} \,, \quad \kappa'^{\star}_{rms} = f_\kappa \theta'_{rms} \,. \tag{4.36}$$

The star superscript (here and in the following chapters) indicates an estimation. The right hand side of relations in (4.36) is calculated directly from DNS data. Emission fluctuations are shown in figure 4.4. As emission is independent of optical thickness, the accuracy of the approximation depends only on the magnitude of thermal fluctuations. From the results, it seems that in a non-reactive turbulent flow, emission fluctutions are very well predicted by their first order Taylor expansion. Figure 4.5 shows fluctuation of incident radiation. G' is the key quantity in TRI and the most difficult to predict as it depends both on turbulent structures and optical thickness. Figure 4.5 proves that the radiative field fluctuations are well represented by the derived relation. In particular, the accuracy of the approximation increases as the optical thickness grows. This is because the assumptions employed to obtain equations (4.28-4.35) neglect the presence of a wall. Indeed, if the optical thickness is large enough, the wall presence is less impactfull. Conveniently, G'_{rms} is larger (and more influent) at a larger optical thickness, requiring a more accurate approximation. G'_{rms} is estimated using both ω_c^{iso} (dashed line), and ω_c (gray solid line). Except for large optical thickness cases ($\tau = 10$), the two profiles collapse onto each other. This shows that it is necessary to correct for anisotropic structures only if $L_R \lesssim \omega_z^{-1}$, meaning if the optical thickness is large enough (see figure 4.2). Finally, κ'_{rms} are shown in figure 4.6 normalized by optical thickness for the variable absorption coefficient cases. As for emission fluctuations, κ' is not dependent on the radiative transfer process and is well represented by its first order approximation.

Figure 4.7 shows a comparison between the radiative terms that dominate TRI, ob-

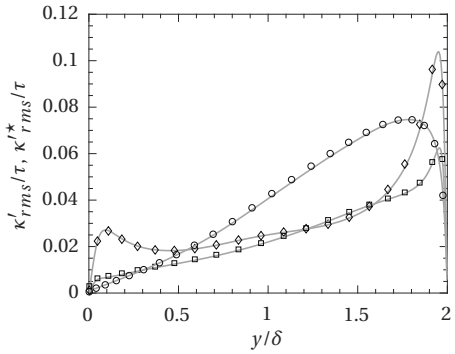

Figure 4.6: Comparison between absorption coefficient fluctuations from variable absorption coefficient DNS (symbols) and estimated using eq (4.36) (lines). Diamonds: $\tau = 0.1$. Squares: $\tau = 1$. Circles: $\tau = 10$.

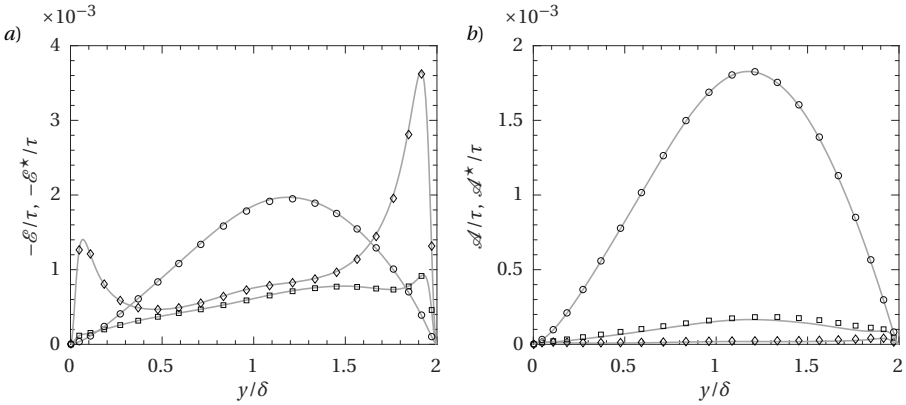

Figure 4.7: Comparison between radiative terms in the constant absorption coefficient cases from DNS (symbols) and estimated using eq. (4.37) (gray lines). Diamonds: $\tau = 0.1$. Squares: $\tau = 1$. Circles: $\tau = 10$.

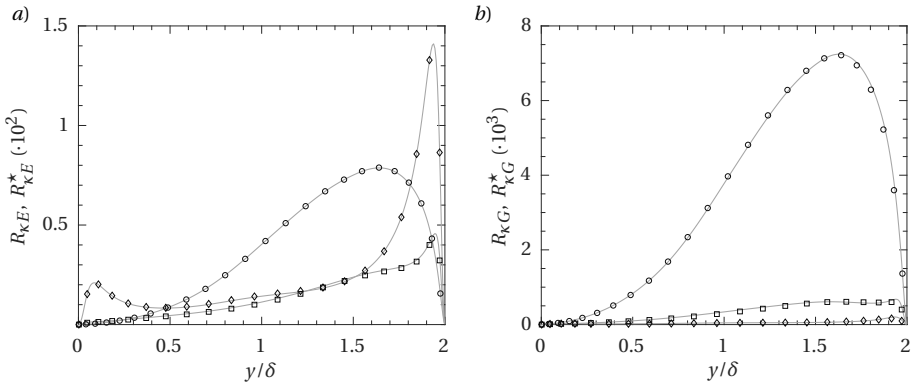

Figure 4.8: TRI correlations (symbols) and their approximations (lines) for the variable absorption coefficient, gray cases. Symbols: DNS results ($R_{\kappa E}$ and $R_{\kappa G}$). Lines: estimations ($R^{\star}_{\kappa E}$ and $R^{\star}_{\kappa G}$). Diamonds: $\tau = 0.1$. Squares: $\tau = 1$. Circles: $\tau = 10$.

tained by DNS and estimated from

$$\mathscr{E}^{\star} = -\frac{2\tau}{RePrPl} f_E \overline{\theta'^2}\,, \quad \mathscr{A}^{\star} = \frac{2\tau}{RePrPl} f_G \overline{\theta'^2}\,, \tag{4.37}$$

for the constant absorption coefficient cases. As proved by figure 4.7, the derived approximations provide good estimations also for temperature-radiation correlations.

Classically, TRI has been studied with the use of correlations that describe the influence of radiative field fluctuations. In particular, the focus has always been on identifying the deviation of the radiative heat source from the one obtained by mean quantities. This corresponds to investigating the $\kappa', E', G' \to \overline{\theta}$ path in figure 4.1. The definition of TRI correlations follows from the averaging of equation (3.4)

$$\overline{Q}^{R} = \overline{\kappa}\cdot\overline{E} - \overline{\kappa}\cdot\overline{G} + \underbrace{\overline{\kappa' E'}}_{\text{emission TRI}} - \underbrace{\overline{\kappa' G'}}_{\text{absorption TRI}}\,, \tag{4.38}$$

where the last two terms are the TRI contributions divided into emission and absorption TRI. The correlations, relate the magnitude of the TRI terms to the averaged terms, as done in [20]

$$R_{\kappa E} \equiv -\frac{\overline{\kappa' E'}}{\overline{\kappa}\cdot\overline{E}}\,, \quad R_{\kappa G} \equiv -\frac{\overline{\kappa' G'}}{\overline{\kappa}\cdot\overline{G}}\,. \tag{4.39}$$

These can be estimated using temperature variance and the derived linear relations as

$$R^{\star}_{\kappa E} = -\frac{f_\kappa f_E}{\overline{\kappa}\cdot\overline{E}}\overline{\theta'^2}\,, \quad R^{\star}_{\kappa G} = -\frac{f_\kappa f_G}{\overline{\kappa}\cdot\overline{G}}\overline{\theta'^2}\,. \tag{4.40}$$

Figure 4.8 shows the above defined TRI correlations obtained by DNS, in the variable absorption coefficient cases, compared to the modeled terms. The figures show an excellent agreement in all cases. Note that, indeed, the magnitude of the correlations

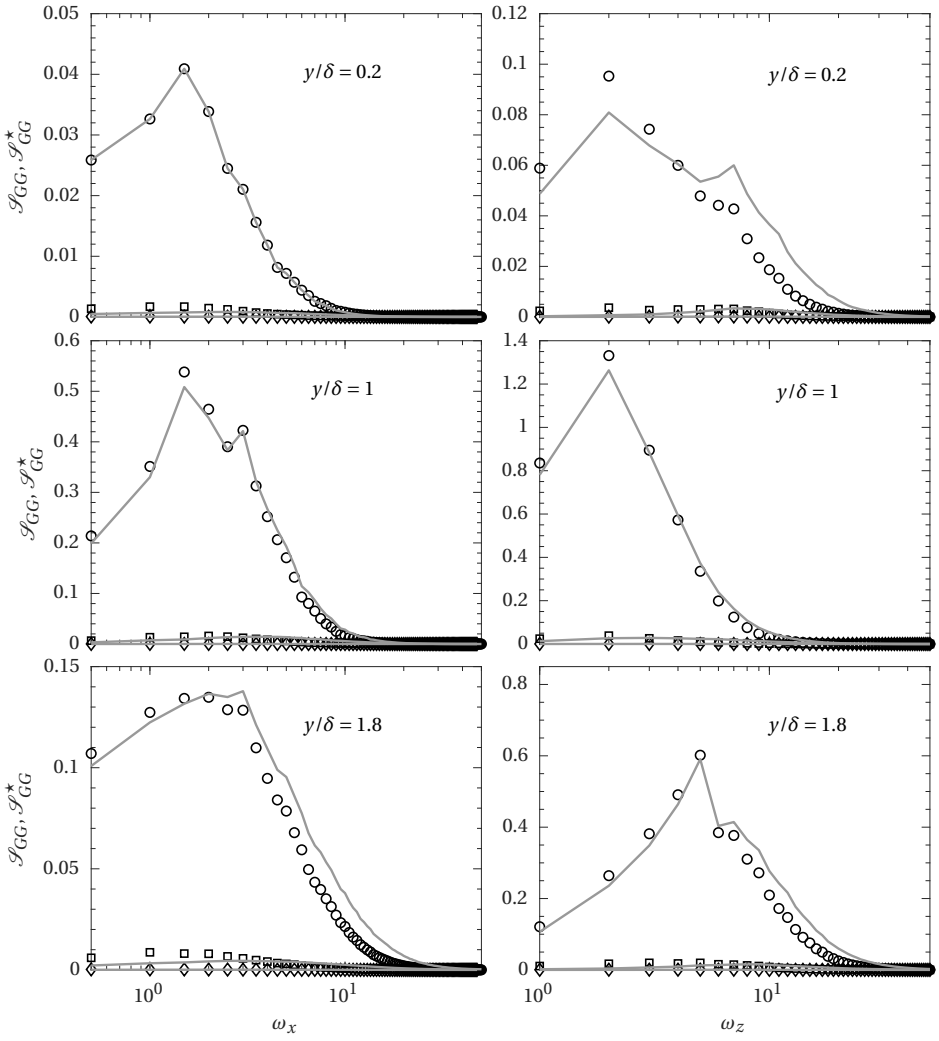

Figure 4.9: Profiles of streamwise and spanwise pre-multiplied incident radiation spectra for the different cases. Symbols represent DNS obtained profiles, $\mathscr{I}_{GG}$ approximated with formula (4.42). In particular, the diamonds are case gray-ρ01, the squares case gray-ρ1 while case gray-ρ10 is shown by the circles.

is relatively low $O(10^{-3}) - O(10^{2})$ confirming that the direct influence of radiative fluctuations on the mean temperature, as stated in chapter 3, is negligible in non-reactive turbulent flows.

Finally, the derivations performed in section 4.2.3 rely on a Fourier transformation of the incident radiation. In doing so, the modes of G are related to the E and κ modes. It is necessary, therefore, to verify if the derivations hold also in a Fourier transformed domain, before the inverse Fourier transform, equation (4.28), is performed. From equation (4.27), by neglecting the influence of absorption coefficient modes, we obtain

$$\widehat{G'} \approx \left(\frac{\overline{\kappa}}{\omega_c}\text{atan}\frac{\omega_c}{\overline{\kappa}}\right)\cdot\widehat{E'}\,. \tag{4.41}$$

The approximation of the incident radiation turbulent spectrum follows

$$\mathscr{S}_{GG} \approx \mathscr{S}^{\star}_{GG} = \left(\frac{\overline{\kappa}}{\omega_c}\text{atan}\frac{\omega_c}{\overline{\kappa}}\right)^{2}\cdot\mathscr{S}_{EE}\,, \tag{4.42}$$

where $\mathscr{S}^{\star}_{GG}$ is the model for the incident radiation spectra. Equation (4.42) entails that the shape of $\mathscr{S}_{GG}$ is the same as for the E spectrum. As explained in chapter 3 this is not necessarily true, but it is a more appropriate approximation as τ grows. Coincidentally, a relevant level of G' is found only at high τ. In general, as the G spectrum increases in value it approaches $\mathscr{S}_{EE}$, which is the limit in the case $\tau \to \infty$. Figure 4.9 shows the streamwise and spanwise pre-multiplied turbulent incident radiation spectra for the different cases, in the center of the channel ($y/\delta = 1$) and near the walls ($y/\delta = 0.2$, $y/\delta = 1.8$). As seen by figure 4.9, approximating the incident radiation spectra with $\mathscr{S}_{EE}$ is a reasonable assumption. Again, it is possible to notice that the approximation is more accurate near the center where the influence of the walls is lower. In addition, the predicted spectrum has a peak at larger wavenumbers as, following the discussion in section 3.4, G is more influencial on larger structures when compared to E which does not depend on scale size. Nevertheless, the integral of the spectrum is accurately predicted.

4.4. SUMMARY

In this chapter we derived analytical relations to predict TRI in non-reactive turbulent flows in the weak temperature fluctuation limit. For emission and absorption coefficient fluctuations, which are local quantites that do not depend on the radiative transfer process, the first order approximation is well suited and accurate to predict fluctuation levels. Incident radiation fluctuations are approximated by assuming that the temperature field is composed of only one characteristic length scale. This approximation works well for large enough optical thicknesses and is reasonably accurate for the whole optical thickness range, as it preserves the magnitude of incident radiative fluctuations.

5

VARIABLE AND SPECTRAL RADIATIVE PROPERTIES

Real gases are intrinsically non-gray, i.e., their absorption coefficient varies depending on the wavelength of incoming radiation. Therefore, gases are characterized by an absorption "spectrum" which is usually relatively complex and distinctive of the gas molecule (so much that it is used as a method for gas composition identification). This chapter deals with spectral radiation and its effect on TRI. While doing so, we derive a new spectral averaging that includes turbulence informations, which can simplify the TRI description in non-gray gases to the an ideal description comparable to gray gases.

This chapter is based on the following publication, Silvestri, Roekaerts and Pecnik, Assessing turbulence radiation interactions in turbulent flows of non-gray media, J. Quant. Spectr. Rad. Transf., **233** (2019), 134–148. [65]

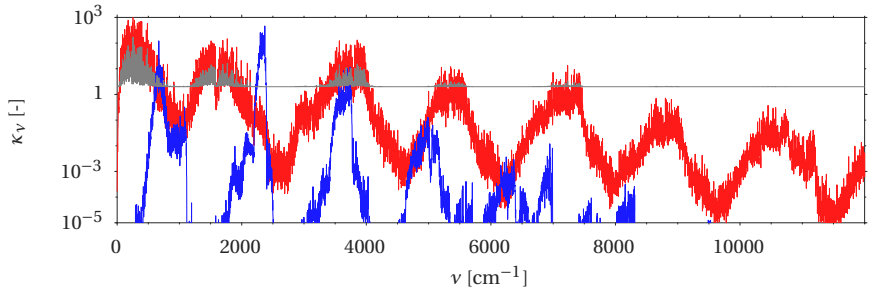

Figure 5.1: Absorption spectrum at 800 K and 1 atm for the non-gray cases: case spec-H_2O (red, H_2O), case spec-CO_2O (blue, CO_2) and case spec-Part (gray, QG).

5.1. INTRODUCTION

As we concluded in chapter 3, TRI is highly non-linear and hard to predict due to the counter intuitive dependency on the absorption coefficient. Traditionally, modelling efforts for TRI have accounted for the full radiative source, but, based on the results of the previous chapters, we highlight the necessity of separately accounting for emission and absorption. Moreover, till this point, only constant κ gray gas cases were discussed. While this is very useful to unveil the mechanics of TRI, the gray gas assumption is unrealistic, as all gases are intrinsically non-gray – i.e. have an absorption coefficient which varies based on the wavelength of the incoming radiation. A typical gas absorption spectrum is generally extremely complex (see figure 5.1), as it is composed of millon lines which correspond to specific quantum molecular transition (vibrational, rotational, electronic...). As a consequence, a variable spectrum causes a steep increase in TRI non-linearity and poses a daunting challenge in terms of predicting TRI. The scope of this chapter, is, therefore, to provide a universal understanding of TRI, including, first, the effect of a variable absorption coefficient, decomposed in a mean and fluctuating part, and, second, the impact of a spectrally varying absorption coefficient. As this last effect significantly raises the complexity of the analysis, an additional objective of this chapter is to derive a new spectral averaged parameter, a priori calculated, which allows a leading order comparison between gray and non-gray gases.

5.2. CASES DESCRIPTION AND PROPERTY VARIATION

The simulated cases are seven in total, three gray cases described in table 4.1 and four cases with spectral absorption coefficient, summarized in table 5.1. Also for the non-gray cases, the same setup as for the previous cases is used (turbulent channel flow, see chapter 2).

The first three cases in table 5.1 differ only in the description of radiative heat transfer, while the last case (highRe-H_2O) is a higher Reynolds number case with variable thermodynamic transport properties (μ and λ) and a larger temperature difference between hot and cold wall ($T_c^* = 600$, $T_h^* = 1800$, K). For each radiative case a transparent

Table 5.1: Description of the spectrally varying cases

Cases	Re	Pr	T_0	ρ	μ	λ
spec-H_2O	3750	1	1.5	$T_0/(\theta+T_0)$	const	const
spec-CO_2	3750	1	1.5	$T_0/(\theta+T_0)$	const	const
spec-Part	3750	1	1.5	$T_0/(\theta+T_0)$	const	const
highRe-H_2O	16700	0.93	0.5	$T_0/(\theta+T_0)$	$\rho^{-1.15}$	$\rho^{-1.35}$

benchmark is performed with $\kappa = 0$. The employed grid consists of $192\times192\times192$ for all cases except for the higher Reynolds number case which is discretized on $768\times416\times512$ mesh points in the streamwise, wall-normal and spanwise direction, respectively. The radiative properties and numerical details for the radiation model are summarized in table 5.2. Since a higher optical thickness requires a finer discretization, a larger number of directions was used for case gray-ρ10 and more rays per cell were employed for case spec-H_2O. For the gray, variable κ cases, equation (4.7) has been multiplied by a constant C_κ to achieve the desired optical thickness value. The constants $c_0 - c_5$ are taken from the model of Planck mean absorption coefficient of water vapour described in [66]. For the spectral cases, the optical thickness value in table 5.2 refers to the optical thickness obtained with the Planck mean absorption coefficient calculated as

$$\tau = \frac{1}{2}\int_0^2 \kappa_p dy\,, \quad \text{where} \quad \kappa_p = \frac{1}{I_b}\int_0^\infty \kappa_\nu I_{b\nu} d\nu\,. \tag{5.1}$$

Figure 5.1 shows a reference spectrum for the spectral cases at 800 K and 1 atm. Note that the absorption coefficient varies also with temperature. These spectra are obtained from a high resolution spectral database [59] and are (1) the spectra of water vapour named H_2O, (2) the spectra of 10% carbon dioxide and 90% nitrogen, labelled CO_2 and (3) a synthetic spectra which mimics a multiphase medium, obtained by summing a constant to 10% H_2O spectrum, called QG for quasi-gray. These absorption spectra are specifically designed to compare TRI in flows with different spectral variability going from high (CO_2), to medium (H_2O) and low (QG).

To maintain consistency and allow a comparison between the gray and non-gray cases, we define a reference incidence radiation such that also in cases with spectrally varying absorption coefficient

$$Q^R = \kappa_p(E-G)\,. \tag{5.2}$$

Therefore, the definition of E does not change, while G reads

$$G = \frac{1}{\kappa_p}\int_0^\infty \kappa_\nu \frac{1}{\pi}\int_{4\pi} I_\nu d\nu\,. \tag{5.3}$$

Note that if κ is not a function of ν, we retrieve the gray gas definition of G, equation (3.1). Figure 5.2 shows profiles of average density (a) and absorption coefficient normalized by optical thickness (b). Here, and in the rest of the chapter, if not otherwise specified, κ and τ for non-gray cases refer to Planck mean absorption coefficient and optical thickness, respectively. In figure 5.2 as well as in the following figures, among the

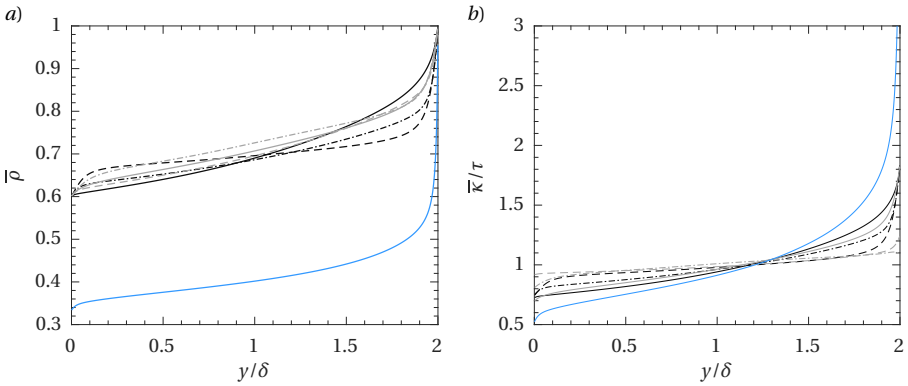

Figure 5.2: Profiles of averaged density (a) and absorption coefficient normalized by the optical thickness (b). Black lines: dashed gray-ρ01, dashed-dotted: gray-ρ1, solid: gray-ρ10. Gray lines: dashed: spec-Part, dashed-dotted: spec-CO_2, solid: spec-H_2O. Light blue line: highRe-H_2O.

Table 5.2: Parameters for the numerical modelling of radiative heat transfer

Cases	Pl	κ	τ	Method	discretization
gray-ρ01	0.03	gray, eq (4.7)	0.1	FVM	96 angles
gray-ρ1	0.03	gray, eq (4.7)	1	FVM	96 angles
gray-ρ10	0.03	gray, eq (4.7)	10	FVM	384 angles
spec-H_2O	0.03	H_2O spectra	8.02	QMC	$15{\cdot}10^3$ rays/cell
spec-CO_2	0.03	CO_2 spectra	2.99	QMC	$9\cdot10^3$ rays/cell
spec-Part	0.03	QG spectra	2.79	QMC	$9\cdot10^3$ rays/cell
highRe-H_2O	0.03	H_2O spectra	2.12	QMC	$10{\cdot}10^3$ rays/cell

two distinct groups (gray and spectral) the dashed, dashed-dotted and solid lines will represent, in order, the lowest to the highest optical thickness, respectively. Figure 5.2 shows that density change is rather moderate except for the highest Reynolds number case where density varies of a factor three. In terms of absorption coefficient, the gray cases have a factor two variation from the hot to the cold wall, while, except for case spec-H_2O which also has a factor two variation, the spectral cases have a more moderate κ gradient. Finally, $\overline{\kappa}$ varies quite extensively in case highRe-H_2O owing to the large temperature difference between hot and cold wall. Figure 5.3 shows velocity profiles on the cold side, where (a) shows $\overline{u}^+ = \overline{u}/u_t$ plotted against $y^+ = y\cdot Re_t$, while (b) shows the extended Van Driest transformed velocity $\overline{u}^\star$ plotted against the semi-local coordinate $y^\star = y\cdot Re_t^\star$ with $\overline{u}^\star$ defined as in [50]

$$d\overline{u}^\star = \left(1+\frac{y}{Re_t^\star}\frac{dRe_t^\star}{dy}\right)\sqrt{\frac{\overline{\rho}}{\rho_w}}d\left(\frac{\overline{u}}{u_t}\right), \tag{5.4}$$

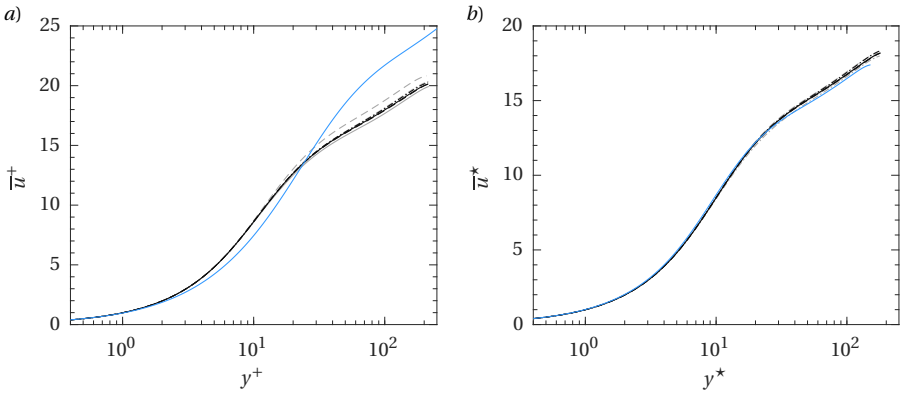

Figure 5.3: Profiles of $\overline{u}^+$ (a) and $\overline{u}^\star$ (b). Black lines: dashed gray-ρ01, dashed-dotted: gray-ρ1, solid: gray-ρ10. Gray lines: dashed: spec-Part, dashed-dotted: spec-CO_2, solid: spec-H_2O. Light blue line: highRe-H_2O.

$$\text{where} \quad Re_t^\star = Re_t \sqrt{\frac{\overline{\rho}}{\rho_w}} \frac{\mu_w}{\overline{\mu}}, \quad \text{and} \quad Re_t = \frac{\rho_w u_t \delta}{\mu_w}.$$

It is possible to notice that $\overline{u}^+$ is very similar for all the lower Reynolds number cases. In a participating turbulent flow, velocity profiles and velocity statistics are not directly connected to radiative heat transfer but are indirectly affected by the modification of the density profiles. Since density variations are relatively small (40% between the hot and the cold wall), the effects of radiation on velocity are very small. On the other hand, the highest Reynolds number case has a different $\overline{u}^+$ profile owing to the large density variation and the transport property gradients, which is corrected by employing the extended Van Driest transformation. Indeed, as shown by [67, 68], the extended Van Driest transformation results in a satisfactory collapse of channel flows velocity profiles for cases with different property gradients and $\overline{u}^+$ profiles.

The same normalization procedure can be implemented for the temperature field [50]. Figure 5.4 shows the temperature field normalized using different methods. Figures 5.4(a) and (c) show the incompressible scaling used in chapter 3, where (a) is the classical friction temperature scaling, while (c) is the radiation-based scaling introduced by [29]. Figures 5.4(b) is the extended Van Driest transformed temperature calculated as

$$d\overline{\theta}^\star = \left(1 + \frac{y}{Re_t^\star} \frac{dRe_t^\star}{dy}\right) \sqrt{\frac{\overline{\rho}}{\rho_w}} d\left(\frac{\overline{\theta}}{\theta_t}\right) \tag{5.5}$$

Finally, figure 5.4(d) has been obtained by substituting θ_{tR} to θ_t in the above expression to account for radiative heat transfer. As a confirmation of what has been concluded in chapter 3, the collapse of temperature profiles is virtually non-existent even when using semi-local scaling or radiation-based scaling. This is expected since the requisite for the above defined semi-local scaling to work is that both Prandtl and turbulent Prandtl number have a value of 1. In these cases, despite $Pr = 1$, the turbulent Prandtl number is largely modified by the presence of radiative heat transfer (see figure 3.6). Therefore,

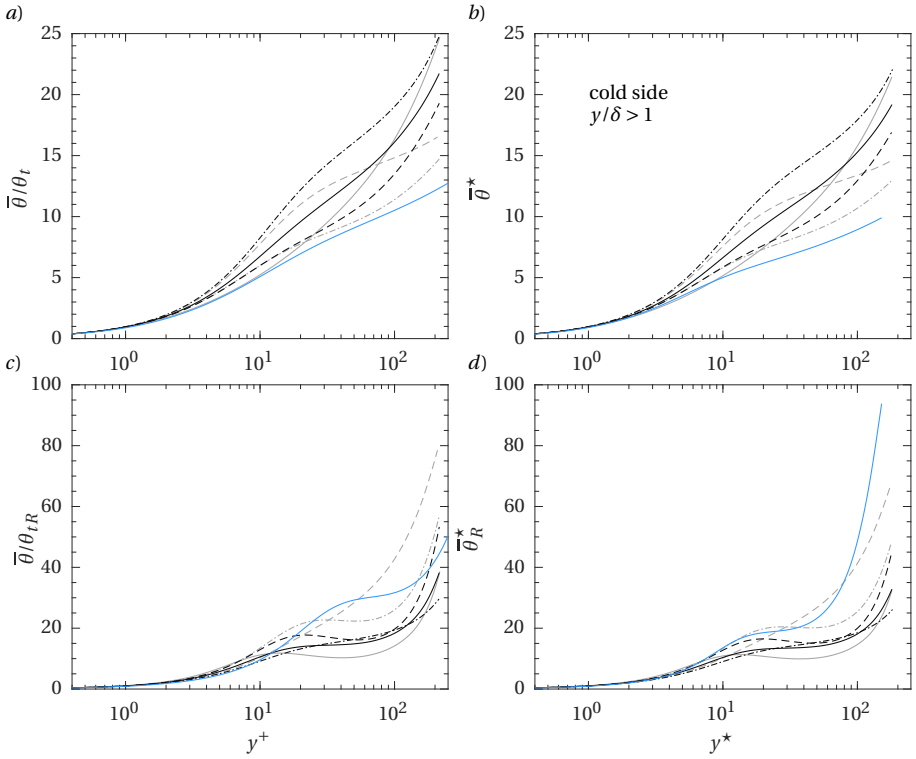

Figure 5.4: Normalized temperature field. Black lines: dashed gray-ρ01, dashed-dotted: gray-ρ1, solid: gray-ρ10. Gray lines: dashed: spec-Part, dashed-dotted: spec-CO_2, solid: spec-H_2O. Light blue line: highRe-H_2O.

the semi-local scaling would have not worked also in radiatively participating flows for which TRI can be neglected. We noticed that using the radiative-based scaling, the same local maxima for large enough optical thickness are retrieved. This suggests the appearance of local maxima in the radiative flux for most of the cases. Despite the failure of all the scalings, the use of the semi-local coordinate $y^\star$ allows an alignment of the the local maxima around $y^\star \approx 12$.

5.3. GRAY GAS CASES

In this section we investigate the effect of a variable absorption coefficient in terms of a mean ($\overline{\kappa}$) and a fluctuating value (κ'). Figure 5.5 shows a comparison between the temperature profile of the variable absorption coefficient cases and their constant absorption coefficient counterparts. Figure 5.5(a) shows unscaled temperature profiles while 5.5(b) shows the radiative-based extended Van Driest temperature transformation. For the variable absorption coefficient cases an overall increase in mean temperature is noticed. This is caused by the absorption coefficient increasing near the cold

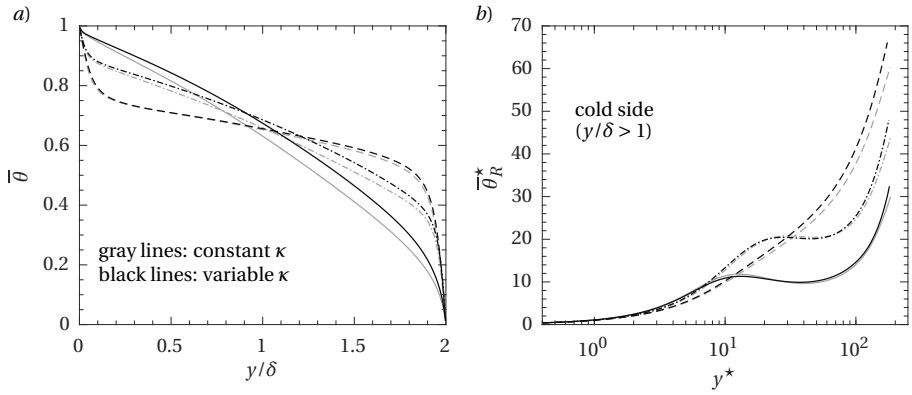

Figure 5.5: Comparison of mean temperature between variable κ cases (black lines) and constant κ cases (gray lines). Dashed lines: $\tau = 0.1$, dashed-dotted lines: $\tau = 1$, solid lines: $\tau = 10$

side $\kappa_c > \tau$, decreasing substantially the range of radiative heat transfer towards the cold wall. Contrarily, the lower absorption coefficient near the hot side $\kappa_h < \tau$ allows the high-temperature emitted energy from the hot wall to travel further in the channel, causing an increase in the mean temperature. This cannot be deemed a local effect but stems from the long-range nature of radiative heat transfer. On the other hand, if normalized with radiative-based semi-local scaling, the difference between the variable and constant κ cases decreases significantly, especially for $\tau = 10$ which had the highest deviation in $\overline{\theta}$. To understand the reason, it is useful to recall figure 4.8, which proved that

$$\overline{\kappa' E'} \ll \overline{\kappa} \cdot \overline{E}\,, \quad \text{and} \quad \overline{\kappa' G'} \ll \overline{\kappa} \cdot \overline{G}\,. \tag{5.6}$$

Therefore, we can express the average radiative heat source as

$$\overline{Q}^R \approx \overline{\kappa}(\overline{E} - \overline{G})\,. \tag{5.7}$$

This expression allows to formulate two different observations. (1) The fluctuations of absorption coefficient κ' do not directly affect the mean temperature field. (2) The radiative-based normalization, which follows

$$\gamma_R = \overline{q}_w - \int_0^y \overline{\kappa}(\overline{E} - \overline{G})\, dy \tag{5.8}$$

accounts for moderate deviations of the mean absorption coefficient ($\overline{\kappa}$) from the optical thickness value τ as it includes non-local long-range effects with the integral of the absorption coefficient. Finally, figure 5.6 shows profiles of θ'_{rms} (a) and θ'_{rms} scaled by the semi-local friction temperature (b) defined as

$$\theta^\star_{tR} = \frac{\gamma_R}{\overline{\rho} c_p u^\star_t}\,, \quad \text{where} \quad u^\star_t = \sqrt{\frac{\mu_w}{\overline{\rho}} \left(\frac{d\overline{u}}{dy}\right)_w}\,. \tag{5.9}$$

Since the analysis performed in the chapter 3 well suits the trend observed for θ'_{rms}, we are going to use it to explain the difference between variable absorption coefficient case

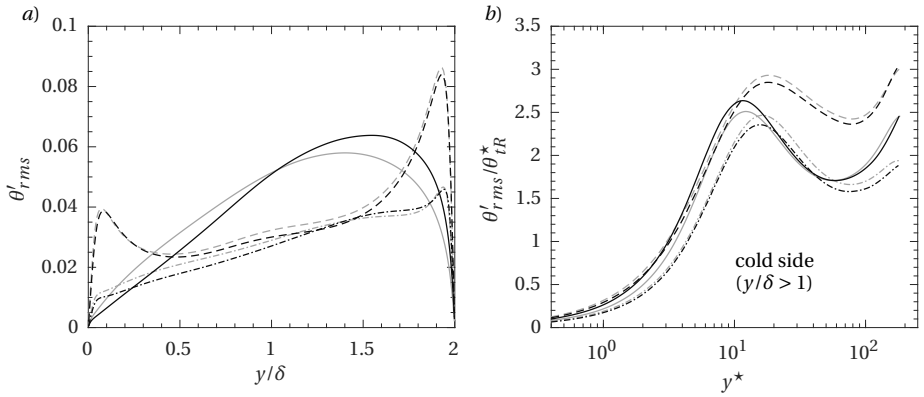

Figure 5.6: Comparison of temperature fluctuations between variable κ cases (black lines) and constant κ cases (gray lines) (a) normalized by $\theta^{\star}_{tR}$ in (b). Dashed lines: $\tau = 0.1$, dashed-dotted lines: $\tau = 1$, solid lines: $\tau = 10$.

and constant κ case. It is possible to notice that $\theta'_{rms,\upsilon} - \theta'_{rms,c}$ (where the subscript υ stands for variable properties and c for constant properties), has a different behaviour for $\tau = 0.1$ with respect to $\tau = 1$ and $\tau = 10$, despite $\overline{\kappa}/\tau$ following the same trend. While for $\tau = 0.1$ the difference between variable and constant κ is negative across the whole extent of the channel, for $\tau = 1$ and $\tau = 10$ is negative on the hot side, positive on the cold side, and shows an increment with an increase in τ. This discrepancy, if we assume that the variability of κ manifests only in a change of TRI (and not in indirect effects through the change of temperature gradients), follows closely the mechanism described in chapter 3. If the absorption coefficient is below a certain threshold, absorption fluctuations are low, and cannot counteract emission fluctuations. Therefore, the effect of a fluctuating radiative field translates in a sink that is directly proportional to the temperature and $\overline{\kappa}$. In this case κ varies within the channel, therefore, for gray-ρ01, the emission sink will be stronger on the cold side where $\overline{\kappa}$ is larger. On the other hand, with an increase in τ beyond a certain threshold, the effect of absorption starts to play a role, and, as described in chapter 3, a higher τ leads to higher θ' due to the larger source term connected to G'. This is confirmed in figure 5.6 where, to a $\overline{\kappa}/\tau > 1$ corresponds $\theta'_{rms,\upsilon} > \theta'_{rms,c}$, and viceversa for $\overline{\kappa}/\tau < 1$. This difference increases with τ due to the larger multiplicative factor κ, and a larger absolute deviation of κ from τ. From this analysis it seems that a variable absorption coefficient modifies the temperature fluctuations only in virtue of a higher/lower average absorption coefficient $\overline{\kappa}$ which impacts locally the interplay of E' and G'. No visible effect of κ' is recognized. A substantiation of this claim comes from scaled profile in figure 5.6(b) as the radiative-based scaling (which accounts only for the average absorption coefficient) results in an improved collapse of θ'_{rms} (at constant τ). To confirm this claim, in the next section we investigate the effects of κ' on θ'

5.3.1. IMPACT OF κ' ON TEMPERATURE VARIANCE

We have demonstrated that, in non-reactive flows, κ' has a negligible contribution to equation 4.38 and thus, cannot directly impact $\overline{\theta}$. Therefore, the only possible influence

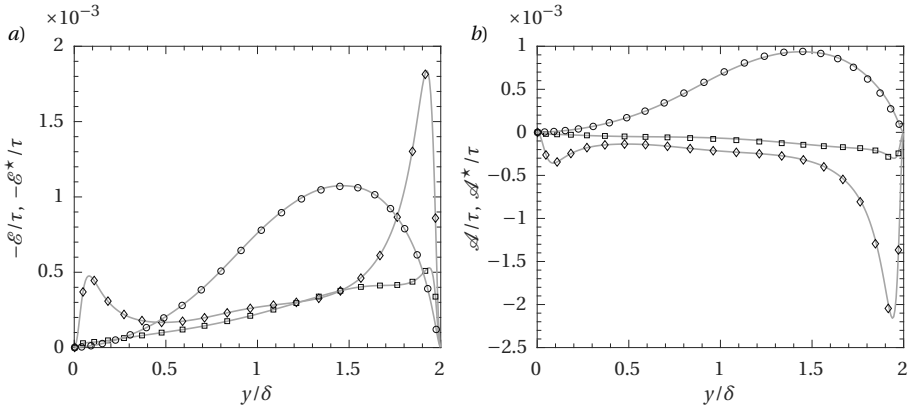

Figure 5.7: Emission (a) and absorption terms (b) for the variable absorption coefficient cases. Diamonds: $\tau = 0.1$, squares: $\tau = 1$, circles: $\tau = 10$. Gray lines are $\mathscr{E}^\star$ and $\mathscr{A}^\star$ estimated from equation (4.37).

of κ' on $\overline{\theta}$, is through the modification of θ'. The effect of radiative heat transfer on the turbulent temperature field manifests through the radiation term $\mathscr{R}_\theta$, which, in the Favre averaged temperature variance equation (neglecting terms containing $\overline{\theta''}$), reads

$$\overline{\rho}\frac{D\widetilde{\theta''^2}}{Dt} = -2\overline{\rho}\widetilde{u_j''\theta''}\frac{\partial\widetilde{\theta}}{\partial x_j} - \frac{\partial\overline{\rho}\widetilde{u_j''\theta''^2}}{\partial x_j} + \frac{2}{RePr}\left[\frac{1}{2}\frac{\partial^2\overline{\theta'^2}}{\partial x_j^2} - \overline{\left(\frac{\partial\theta'}{\partial x_j}\right)^2}\right] \underbrace{-\frac{2}{RePrPl}\overline{Q^{R'}\theta'}}_{\mathscr{R}_\theta}. \quad (5.10)$$

As seen in chapter 3, the magnitude of the radiation term depends on the optical thickness of the medium. As τ tends to zero the radiative terms disappears. The same occurs when $\tau \to \infty$. Around $\tau = 10$, the radiative term is dominant and balances turbulent production. The radiation term $\mathscr{R}_\theta$ can be decomposed, once again, in an emission term $\mathscr{E}$ and an absorption term $\mathscr{A}$ as

$$\mathscr{R}_\theta = \underbrace{-\frac{2}{RePrPl}\overline{(\kappa E)'\theta'}}_{\mathscr{E}} + \underbrace{\frac{2}{RePrPl}\overline{(\kappa G)'\theta'}}_{\mathscr{A}}. \quad (5.11)$$

$\mathscr{E}$ and $\mathscr{A}$ can be expanded, neglecting third order correlations, into terms depending on $\overline{\kappa}$ and on κ' to highlight the different influence of the mean and the fluctuating part of the absorption coefficient.

$$\mathscr{E} = \underbrace{-\frac{2}{RePrPl}\overline{E}\cdot\overline{\kappa'\theta'}}_{\mathscr{E}_{\kappa'}} \underbrace{-\frac{2}{RePrPl}\overline{\kappa E'\theta'}}_{\mathscr{E}_{\overline{\kappa}}}, \quad \mathscr{A} = \underbrace{\frac{2}{RePrPl}\overline{G}\cdot\overline{\kappa'\theta'}}_{\mathscr{A}_{\kappa'}} + \underbrace{\frac{2}{RePrPl}\overline{\kappa G'\theta'}}_{\mathscr{A}_{\overline{\kappa}}}. \quad (5.12)$$

Here the subscripts $\overline{\kappa}$ and κ' indicate which term $\mathscr{E}$ and $\mathscr{A}$ are dependent on. To expand the derivations of chapter 4, it is possible to substitute relations (4.3) to the RHS of equations (5.12) and obtain estimations for $\mathscr{E}$ and $\mathscr{A}$ in variable absorption coefficient

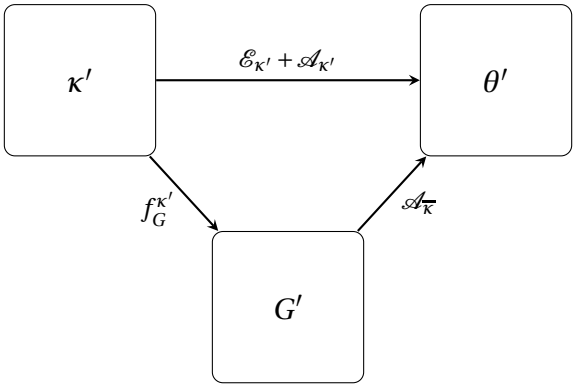

Figure 5.8: Effect of κ' on θ'.

flows

$$\mathscr{E} \approx \mathscr{E}^\star = \underbrace{-\frac{2}{RePrPl}\overline{E} f_\kappa \overline{\theta'^2}}_{\mathscr{E}^\star_{\kappa'}} \underbrace{-\frac{2}{RePrPl}\overline{\kappa} f_E \overline{\theta'^2}}_{\mathscr{E}^\star_{\overline{\kappa}}}, \tag{5.13}$$

$$\mathscr{A} \approx \mathscr{A}^\star = \underbrace{\frac{2}{RePrPl}\overline{G} f_\kappa \overline{\theta'^2}}_{\mathscr{A}^\star_{\kappa'}} + \underbrace{\frac{2}{RePrPl}\overline{\kappa} f_G \overline{\theta'^2}}_{\mathscr{A}^\star_{\overline{\kappa}}}. \tag{5.14}$$

Figure 5.7 shows the emission and absorption terms for the variable κ cases. While $\mathscr{E}$ is very similar to the results obtained for constant κ (as it does not depend directly on the radiative transfer process), $\mathscr{A}$ switches sign for the lower optical thickness cases. This is a consequence of the $\overline{\kappa'\theta'}$ correlation which is negative as κ (in these cases and in most practical situations) is a decreasing function of T. While $\mathscr{E}_{\overline{\kappa}}$ is always dominant such that $\mathscr{E}$ maintains the same sign, for lower optical thicknesses, $\mathscr{A}_{\overline{\kappa}}$ is smaller than $\mathscr{A}_{\kappa'}$. Heuristically speaking, in a low optical thickness flow, a positive temperature fluctuation causes a negative absorption coefficient fluctuation which, as a consequence, decreases the energy absorbed within the structure and tends to decrease θ'. The opposite occurs for a negative θ'. Nevertheless, the approximations provided are able to express correctly the variation of the radiative terms.

Nonetheless, the impact of κ' on θ' is not felt through the individual terms $\mathscr{E}_{\kappa'}$ and $\mathscr{A}'_\kappa$ but through their sum. In addition, the presence of an absorption coefficient fluctuation can modify θ' by impacting the incident radiation fluctuations G'. The relation derived in chapter 4 becomes helpful to study this interaction, as it is possible to decompose f_G into a $\overline{\kappa}$ and a κ' dependent term as

$$f_{G,\overline{\kappa}} = \frac{f_E \overline{\kappa}}{\omega_c} \text{atan}\left(\frac{\omega_c}{\overline{\kappa}}\right) \quad , \quad f_{G,\kappa'} = \frac{f_\kappa(\overline{E} - \overline{G})}{\omega_c} \text{atan}\left(\frac{\omega_c}{\overline{\kappa}}\right) , \tag{5.15}$$

with $f_G = f_{G,\overline{\kappa}} + f_{G,\kappa'}$. Figure 5.8 summarizes the coupling described above: κ' can influence θ' directly, through $\mathscr{E}_{\kappa'} + \mathscr{A}_{\kappa'}$, or indirectly through the modification of G'.

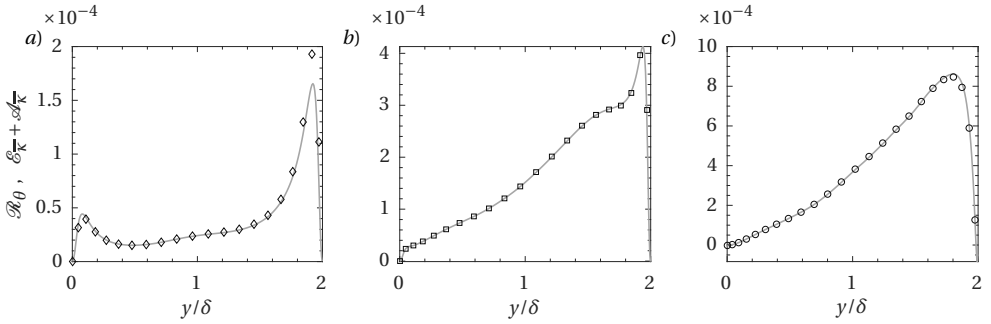

Figure 5.9: Comparison between full radiative term $\mathscr{R}_\theta$ (symbols) and using only the terms which depend on the mean absorption coefficient $\mathscr{E}_{\overline{\kappa}} + \mathscr{A}_{\overline{\kappa}}$ (lines). (a): $\tau = 0.1$, (b): $\tau = 1$, (c): $\tau = 10$

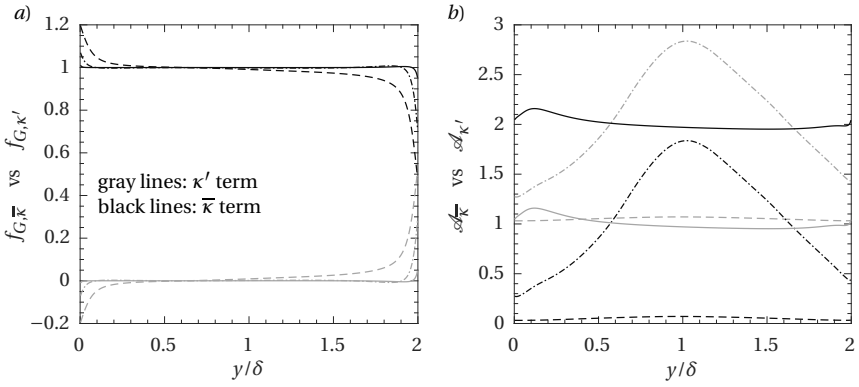

Figure 5.10: Influence of κ' on G'. (*a*): comparison between $f_{G,\overline{\kappa}}$ (black) and $f_{G,\kappa'}$ (gray) normalized by f_G. (*b*): comparison between $\mathscr{A}_{\overline{\kappa}}$ (black) and $\mathscr{A}_{\kappa'}$ (gray) normalized by $\mathscr{A}$. Dashed lines: $\tau = 0.1$, dashed-dotted lines: $\tau = 1$, solid lines: $\tau = 10$.

The direct impact of κ' on θ' can be visualized by comparing $(\mathscr{E}_{\overline{\kappa}} + \mathscr{A}_{\overline{\kappa}})$ to $(\mathscr{E}_{\kappa'} + \mathscr{A}_{\kappa'})$. This comparison is displayed in figure 5.9 for cases gray-ρ01 (a), gray-ρ1 (b) and gray-ρ10 (b). The symbols show the full radiation term $\mathscr{R}_\theta$, while the lines are the radiation term calculated accounting for $\overline{\kappa}$ contributions only. Assuming that $\kappa \approx \overline{\kappa}$ is enough to retrieve the full radiation term, thereby demonstrating that κ' has a negligible direct influence on temperature fluctuations. This occurs for two different reasons depending on different values of the optical thickness. (1) If τ is small, $\mathscr{E}_{\kappa'}$ and $\mathscr{A}_{\kappa'}$ are individually small compared to $\mathscr{E}_{\overline{\kappa}}$, which is the dominant term. (2) If τ is large $\mathscr{E}_{\kappa'}$ and $\mathscr{A}_{\kappa'}$ are not negligible, but their sum tends to zero more rapidly than $(\mathscr{E}_{\overline{\kappa}} + \mathscr{A}_{\overline{\kappa}})$ as $\overline{G} \to \overline{E}$ quicker than $G' \to E'$ when $\tau \to \infty$.

Moreover, the comparison between $f_{G,\overline{\kappa}}$ and $f_{G,\kappa'}$ is shown in figure 5.10(a). The two terms are normalized by the total f_G to highlight their relative magnitude. The results prove that $f_{G,\overline{\kappa}}$ is always dominant over the κ' term. The relative difference between the two terms increases with a larger optical thickness as a consequence of $\overline{G} \to \overline{E}$ for increasing τ. A small, but non-negligible influence of $f_{G,\kappa'}$ can be detected in the lower

optical thickness case (gray-ρ01). To quantify the indirect effect of κ' on θ', it is necessary to verify the impact of the absorptive term $\mathscr{A}_{\overline{\kappa}}$, which connects G' to θ' (see figure 5.8). Figure 5.10(b) shows the comparison between the absorptive term depending on κ' (in gray) and $\mathscr{A}_{\overline{\kappa}}$ (in black). For a low optical thickness the latter tends to zero, which indirectly proves that $G' = 0$ in the limit of $\tau \to 0$. As a consequence, despite $f_{G,\kappa'}$ having a non negligible value in the low optical thickness regime, the low magnitude of $\mathscr{A}_{\overline{\kappa}}$ nullifies any possible influence of κ'.

In conclusion, it has been demonstrated that in high-temperature non-reacting flows, TRI can be accounted for by the variation of the mean absorption coefficient alone. The presence of κ' can be neglected completely, independently from the value of the optical thickness.

5.4. NON-GRAY GAS CASES

This section is intended to investigate how a wavelength dependent absorption coefficient modifies TRI. The absorption spectra of cases spec-H_2O, spec-CO_2 and spec-Part, as defined in table 6.2, are specifically designed to compare TRI in flows with different spectral variability. The spectrally averaged parameters for the three cases are shown in table 5.3, where τ is the Planck mean optical thickness while t is the global transmissivity, defined as

$$t = \frac{1}{I_b|_{y/\delta=1}} \int_0^\infty I_{b\nu}|_{y/\delta=1} \exp\left(-\kappa_\nu|_{y/\delta=1}\right) d\nu \,. \tag{5.16}$$

Global transmissivity provides an opposite measure of optical thickness as it measures the transparency of the media with 1 being a transparent medium and 0 a completely opaque one.

Table 5.3: Optical thickness and global transmissivity for the non-gray cases.

Case	spec-H_2O	spec-CO_2	spec-Part	highRe-H_2O
τ	8.02	2.99	2.79	2.12
t	0.51	0.88	0.10	0.64

The categorization of TRI in non-gray gases results problematic. Based on the optical thickness of the channel, one has $\tau_H > \tau_C \gtrsim \tau_P > \tau_R$, were subscripts H, C, P and R indicate cases spec-H_2O, spec-CO_2, spec-Part and highRe-H_2O, repsectively. This suggests that TRI in spec-H_2O is characterized by an optically thicker behaviour when compared to spec-CO_2, spec-Part and highRe-H_2O. Contrarily, the transmissivity (equation 5.16) for these cases satisfies $t_P < t_H < t_R < t_C$, implying that case spec-CO_2 is the most transparent but spec-Part is the most opaque. As these two parameters contradict each other, it is already possible to state that either of these two parameters fail to describe how the TRI mechanism manifests itself.

Figure 5.11 shows several quantities of interest for the four investigated cases. The figures present plots of Favre-averaged temperature and temperature rms on the left and right, respectively. The largest Reynolds number case, with a higher wall temperature difference, will be discussed separately later. Looking at the lower Reynolds number cases,

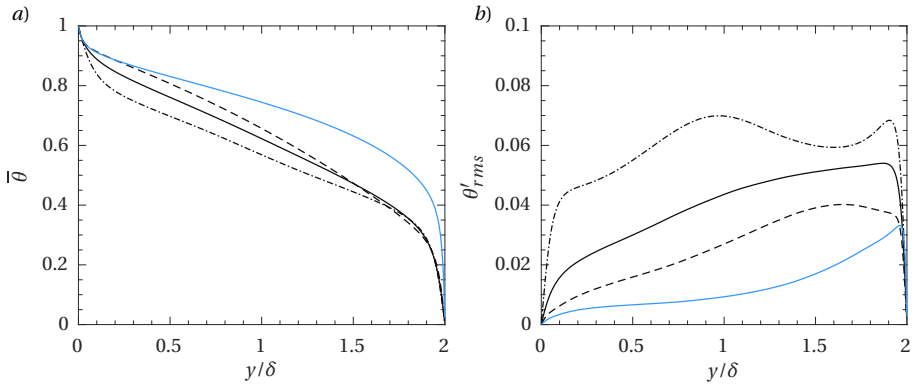

Figure 5.11: Temperature field for non-gray gas cases. (a): average temperature profile. (b): temperature rms profiles. Dashed black line: spec-Part, dashed-dotted line: spec-CO_2, solid black line: spec-H_2O, solid light blue line: highRe-H_2O.

contrarily to what could be expected, profiles of spec-H_2O are enclosed in between those of spec-CO_2 and spec-Part. Moreover, case spec-Part and spec-CO_2 show very different profiles, despite having similar average absorption coefficients. Global transmissivity seems to order correctly the mean temperature profiles but fails to completely capture the physics occurring. For example, the bulk temperature is lower for case spec-CO_2 than for case spec-Part, signifying a lower radiative heat flux from the hot wall, and therefore a lower bulk Q^R in case spec-CO_2. By taking into account equation (5.7), this could be the effect of two contrasting causes: (1) a lower $\overline{\kappa}$ (more transparent case), (2) a lower $\overline{E}-\overline{G}$, which is typical of a higher optical thickness fluid. Since spec-CO_2 and spec-Part have very similar $\overline{\kappa}$ (see figure 5.2), it is clear that the correct option is the second.

This is corroborated by the fact that also TRI in case spec-CO_2 is akin to an optical thick case, as can be noticed by the larger temperature gradient near the walls. This indicates that the highly anisotropic temperature structures close to the boundaries are sensitive to G', enabling a higher turbulent heat transfer from the near wall region to the core of the channel. Evidence can be found by inspecting the θ_{rms} profile in figure 5.11(b), which indeed is as high as for a non-radiative case. As a consequence, a larger turbulent heat transfer is observed when compared to the other radiative cases, especially near the hot wall. The results for case spec-CO_2 appear more similar to a gray gas case with $\tau > 10$ than what can be predicted using τ or t.

On the other hand, case spec-Part shows optically thinner TRI when compared to the other low Reynolds number non-gray cases. This is substantiated by the lower θ'_{rms} which are a proof of lower G fluctuations. A confirmation of the above reasoning is found by inspecting the radiation terms $\mathscr{E}$ and $\mathscr{A}$, shown in figure 5.12. The left plot corresponds to profiles of case spec-H_2O, while center and right plots show values for case spec-CO_2 and spec-Part, respectively. The magnitude of $\mathscr{E}$ and $\mathscr{A}$ are highest for case spec-CO_2, followed by spec-H_2O and spec-Part. In particular, it is possible to notice that for case spec-CO_2, $\mathscr{A} \approx \mathscr{E}$, proving that the incident fluctuation field is tightly correlated to the temperature field. This is typical of an optically thick flow, as it will be explained in

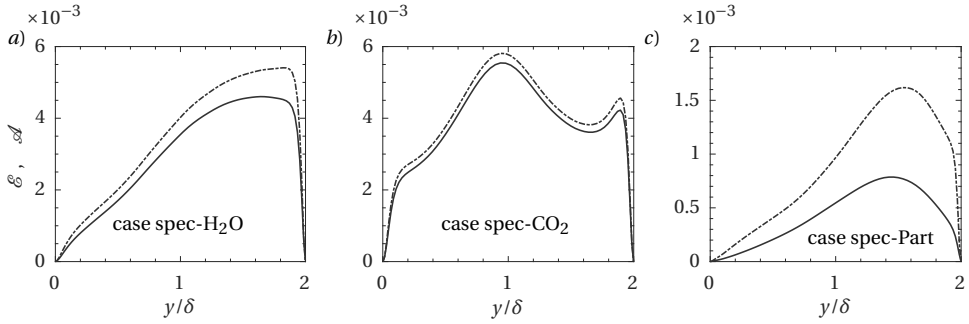

Figure 5.12: Radiation terms $\mathscr{E}$ (dashed-dotted line) and $\mathscr{A}$ (solid line). Left: case spec-$_2$OH. Center: case spec-CO_2. Right: case spec-Part.

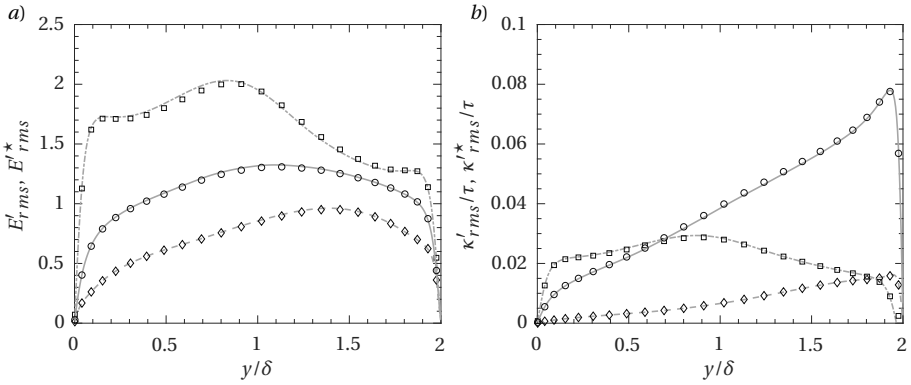

Figure 5.13: Comparison between (a) E'_{rms} and κ'_{rms} obtained by DNS (symbols) and calculated with equation (4.3) (lines). Diamonds and dashed line: spec-Part, Squares and dashed-dotted line: spec-CO_2, Circles and solid line: spec-H_2O

the next section. Following the analysis of the DNS results, the categorization of TRI in the non-gray cases suggest that the three cases effectively behave as decreasing in optical thickness when going from spec-CO_2 to spec-H_2O and then to spec-Part.

An additional verification comes from the linear relations developed in chapter 4. Figure 5.13 shows κ'_{rms} and E'_{rms} for the non-gray cases compared to the linear approximations derived in chapter 4. It is clear that, since all effects connected to a spectral absorption coefficient are linear (integrated in κ and not appearing in E), κ'_{rms} and E'_{rms} are well represented by the linear approximations derived for gray gas. On the other hand, G'_{rms} is shown in figure 5.14. Firstly, it is possible to notice that G'_{rms} is larger for case spec-CO_2 when compared to spec-H_2O. This is completely counterintuitive given the theory developed in chapter 3 and the respective optical thicknesses (2.99 and 8.02). Also global transmissivity fails to explain this behaviour as, based on t, spec-CO_2 is more transparent than spec-H_2O. Indeed, the estimation based on θ'_{rms} and f_G predicts a lower level of G'_{rms} for spec-CO_2, confirming that spec-CO_2 behaves as a larger optical thickness case. For case spec-Part, on the other hand, the estimation provides a rela-

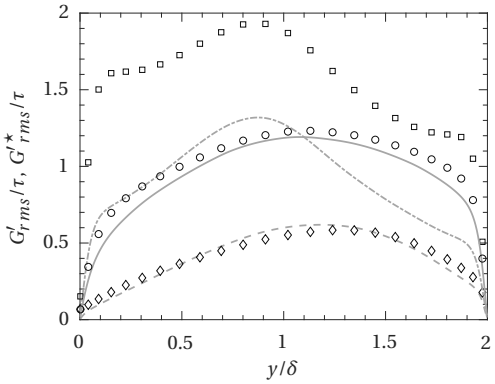

Figure 5.14: Comparison between G'_{rms} obtained by DNS (symbols) and calculated with equation (4.3) (lines). Diamonds and dashed line: spec-Part, Squares and dashed-dotted line: spec-CO_2, Circles and solid line: spec-H_2O

tively accurate prediction. The deviation of $G'^{\star}_{rms}$, especially in spec-CO_2, suggests that TRI follows a different parameter in non-gray gases which might include the variability of the absorption spectra. In the next section we will provide an effective parameter to assess TRI and compare gray gas cases to non-gray gas cases.

5.5. HOW TO CATEGORIZE TRI IN NON-GRAY GASES?

Due to the high variability of the absorption spectra of a non-gray gas, using τ or t to categorize TRI is ambiguous and may even lead to wrong conclusions, as clearly demonstrated in section 5.4. For this reason, it is necessary to identify a new parameter to clearly characterize TRI for a wide range of optical thicknesses, which is not trivial due to the non-monotonic behaviour of most variables and their complex non-linear interactions. Starting from the gray gas cases, it is possible to observe a consistent trend, which will help identifying the unique mechanisms of TRI. Taking into account the two extremes of an optically thin and thick gas, it can be stated that

$$E' \gg G' \to 0, \qquad \text{if } \tau \to 0\,, \tag{5.17}$$

$$E' - G' \ll G' \to E', \quad \text{if } \tau \to \infty\,. \tag{5.18}$$

In the optically thin limit, only emission produces fluctuations, while in the optically thick limit, emission and absorption fluctuations balance. We claim that, for a gray gas, increasing or decreasing τ can be linked to approaching either limiting behaviour, without the necessity of analyzing any other quantity or parameter to characterize TRI. As a consequence, if two flows have substantially different τ values, for example $\tau_1 > \tau_2$, it follows that $(E'_1 - G'_1)/G'_1 < (E'_2 - G'_2)/G'_2$. This means that incident radiation fluctuations approach emission fluctuations since radiation is absorbed closer to the emission point. More generally, using the decomposition of the radiation term $\mathscr{R}_\theta$, equation (5.12), this

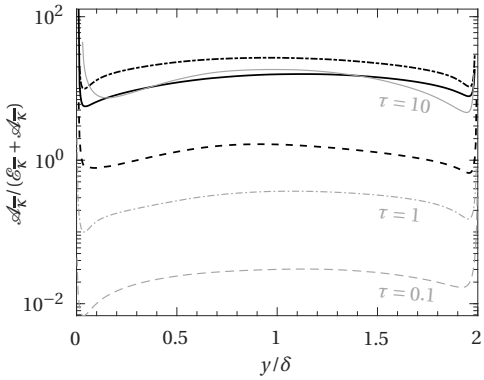

Figure 5.15: Profiles of $\mathscr{A}_{\overline{\kappa}}/(\mathscr{E}_{\overline{\kappa}}+\mathscr{A}_{\overline{\kappa}})$ for the different gray (gray lines) and non-gray gas cases (black line). dashed lines: case spec-Part and gray-ρ01, dashed dotted line: case spec-CO_2 and gray-ρ1, solid line: case spec-H_2O and gray-ρ10.

can be approximated by the following inequality

$$\left.\frac{\mathscr{A}_{\overline{\kappa}}}{\mathscr{E}_{\overline{\kappa}}+\mathscr{A}_{\overline{\kappa}}}\right|_{\tau_1} \gtrsim \left.\frac{\mathscr{A}_{\overline{\kappa}}}{\mathscr{E}_{\overline{\kappa}}+\mathscr{A}_{\overline{\kappa}}}\right|_{\tau_2<\tau_1} . \tag{5.19}$$

Indeed, figure 5.15 confirms that for gray gas turbulence, the quantity in the above equation is monotonically associated to τ (see the gray lines). The definition of large and small optical thickness TRI can be related to the expressions in (5.17-5.18). Consequently, comparing optical depths, with regards to TRI, is interchangeable with comparing the quantities in expression (5.19).

On the other hand, for a non-gray gas this is not the case. Figure 5.15 indeed confirms that the non-gray gas cases behave as if $\tau_C > \tau_H > \tau_P$. Neither the Planck-mean optical thickness τ nor the global transmissivity t can reflect this behaviour. Hence, it is necessary to derive a new spectrally integrated parameter to categorize TRI, which can allow a leading order comparison between non-gray and gray gas cases.

5.5.1. DERIVATION OF A TRI BASED SPECTRAL AVERAGING

Since the new parameter must be connected to TRI, it is useful to employ the three correlations derived in section 4.2 and adapt them when necessary for non-gray gases. As seen in the previous section, f_κ and f_E do not require any modifications to account for spectrally varying absorption coefficients, since κ and E are spectrally integrated quantities. This is exemplified by figure 5.13, which proves the validity of f_E and f_κ in non-gray gases. On the other hand, due to the dependency of G_ν on κ_ν (eq. 5.3), f_G must be modified to account for non-gray gases. If we assume that κ' (and κ'_ν) have a negligible influence on G, as demonstrated previously in this chapter, we can write

$$G' \approx \frac{1}{\overline{\kappa}} \int_0^\infty \overline{\kappa}_\nu G'_\nu d\nu \,, \quad \text{where} \quad G'_\nu = \frac{1}{\pi} \int_{4\pi} I'_\nu d\Omega \,. \tag{5.20}$$

Since, in the absence of anelastic scattering, a single wavelength can be described by a gray gas with absorption coefficient κ_ν, G'_ν is properly predicted by

$$G'_\nu \approx 4\overline{\kappa}_\nu \frac{I'_{b\nu}}{\omega_c} \mathrm{atan}\left(\frac{\omega_c}{\overline{\kappa}_\nu}\right). \tag{5.21}$$

Additionally, since G' is a spectrally integrated quantity, it can be approximated with a gray gas having a fictitious absorption coefficient κ_g. As a consequence, the combination of equations (5.20) and (5.21) yields a constitutive relation for κ_g,

$$4I'_b \frac{\kappa_g}{\omega_c} \mathrm{atan}\frac{\omega_c}{\kappa_g} \approx \frac{1}{\overline{\overline{\kappa}}} \int_0^\infty \overline{\kappa}_\nu^2 \frac{4I'_{b\nu}}{\omega_c} \mathrm{atan}\left(\frac{\omega_c}{\overline{\kappa}_\nu}\right) d\nu\,. \tag{5.22}$$

Equation (5.22) provides a mathematical framework to define a new spectral averaging which results in a mean absorption coefficient that controls TRI. The new turbulence mean absorption coefficient can be calculated, in a first approximation, by dropping the averages and primes. By performing this procedure it is assumed that κ'_λ and κ' are negligible, which has been already substantiated, and that the ratio of the fluctuation of blackbody intensity to the mean is independent of wavelength $I'_{b\nu}/I_{b\nu}(T) \neq f(\nu)$.

$$\frac{\kappa_g(T)}{\omega_c} \mathrm{atan}\frac{\omega_c}{\kappa_g(T)} \equiv \frac{1}{\kappa_p(T) I_b(T)} \int_0^\infty \kappa_\nu^2(T) \frac{I_{b,\nu}(T)}{\omega_c} \mathrm{atan}\left(\frac{\omega_c}{\kappa_\nu(T)}\right) d\nu\,, \tag{5.23}$$

As the $\overline{\kappa}$ in equation (4.35) for the calculation of ω_c refers to the penalty from isotropic emission, the Planck mean absorption coefficient $\overline{\kappa}$ is retained for ω_c both on the LHS and RHS of equation (5.23). The newly defined κ_g can be used to substitute $\overline{\kappa}$ in the coupling function f_G, such that the linear relation between G_{rms} and θ_{rms} can be written as

$$G'^{\star}_{rms}(\kappa_g) = \frac{f_E \cdot \kappa_g(\overline{T}) + f_{\kappa_g}(\overline{E} - \overline{G})}{\omega_c} \mathrm{atan}\left(\frac{\omega_c}{\kappa_g(\overline{T})}\right) \cdot \theta_{rms}\,. \tag{5.24}$$

Figure 5.16 shows profiles of κ_g compared to the Planck mean absorption coefficient κ as functions of temperature and the predicted $G'^{\star}_{rms}$ profiles, both obtained from DNS and predicted by κ_g. From top to bottom, figure 5.16 displays profiles for cases spec-H_2O, spec-CO_2 and spec-Part, respectively. For all non-gray gas cases, using κ_g in the definition of f_G, leads to an accurate prediction of incident radiation fluctuations. Contrarily, employing $\overline{\kappa}$ (figure 5.14) always results in an under-prediction of G'. As already noticed, the disagreement is lowest for case spec-Part and largest for case spec-CO_2. This discrepancy can be related to the difference between κ_g and $\overline{\kappa}$. While for case spec-Part, $\kappa_g < 1.4\kappa$, for case spec-H_2O, $1.45\kappa < \kappa_g < 2\kappa$ and for case spec-CO_2 $3\kappa < \kappa_g < 8\kappa$. As can be noted, for all the cases considered herein $\kappa_g > \overline{\kappa}$. Yet, there is no proof to claim that this must be always the case. Nevertheless, it is apparent that the difference is related to the variability of the absorption spectrum. For example, if the absorption coefficient is independent of the wavelength (i.e., gray gas), then $\kappa_g = \overline{\kappa}$. On the other hand, if the absorption coefficient shows a large variability, the weighting function $(\kappa_\nu/\omega_c)\mathrm{atan}(\omega_c/\kappa_\nu)$ within the integrand in equation (5.23) filters out the lowest, while retaining the largest spectral absorption coefficients. Physically speaking, only the spectral lines with a large

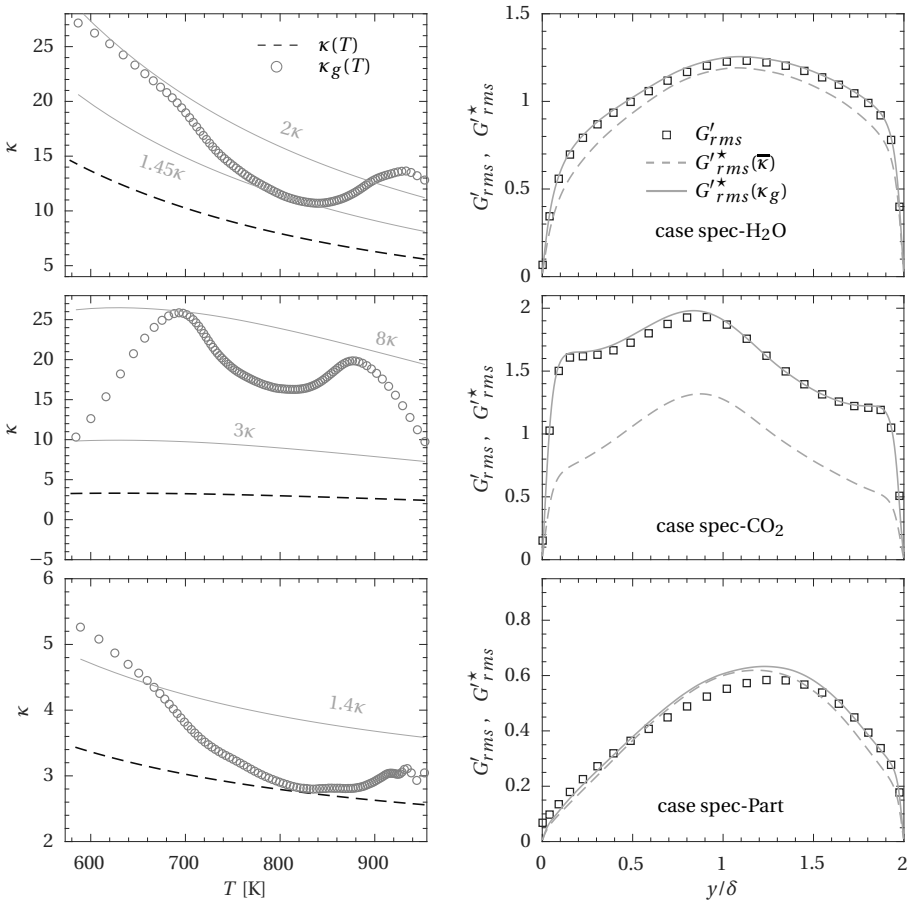

Figure 5.16: Left: Planck mean absorption coefficient and TRI mean absorption coefficient for cases spec-H_2O (top), spec-CO_2 (center) and spec-Part (bottom) as a function of the temperature. These profiles are contingent to a turbulent fully developed channel flow. Lines of constant multiples of κ are added as reference in gray. Right: Comparison between G'_{rms} obtained by DNS (symbols) and $G'^{\star}_{rms}$ obtained from equations (4.30) and (5.24) for the same cases.

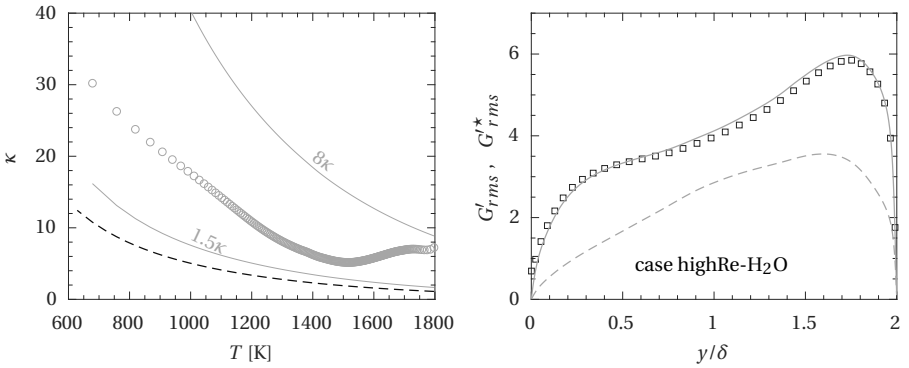

Figure 5.17: (a): Planck mean absorption coefficient and TRI mean absorption coefficient for highRe-H_2O as a function of the temperature. Lines of constant multiples of κ are added as reference in gray. Right: Comparison between G'_{rms} obtained by DNS (symbols) and $G'^{\star}_{rms}$ obtained from equations (4.30) and (5.24) for the same case. Lines and symbols as in figure 5.16

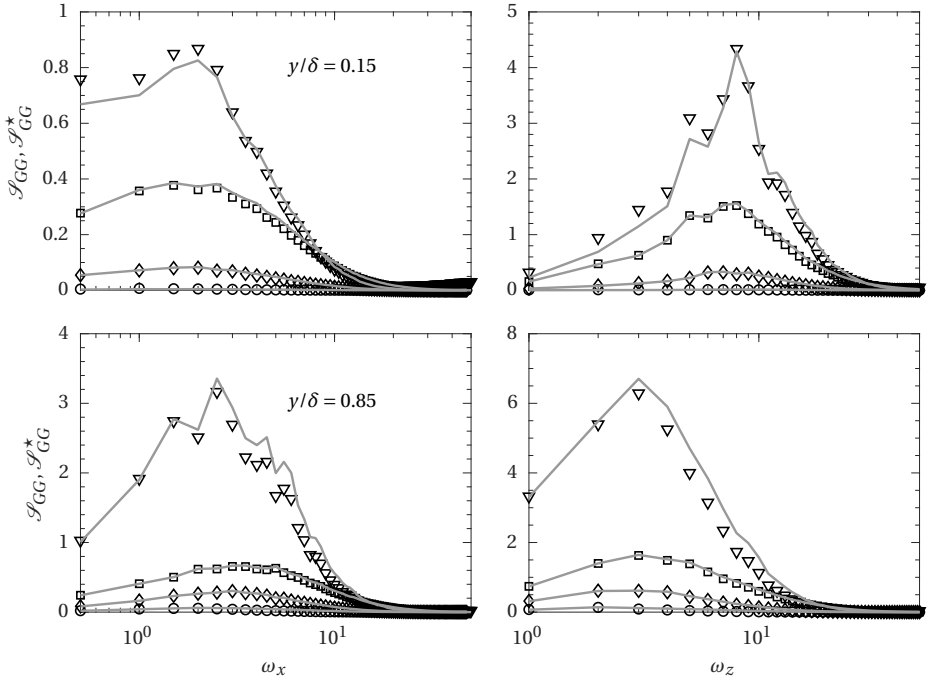

Figure 5.18: Profiles of streamwise and spanwise pre-multiplied incident radiation spectra for the different cases. Symbols represent DNS obtained profiles, $\mathscr{I}_{GG}$ approximated using κ_g in formula (4.42). In particular, the circles are case spec-Part, the diamonds case spec-H_2O while case spec-CO_2 is shown by the squares and case highRe-H_2O by the triangles.

enough absorption coefficient will produce a noticeable G'_ν and contribute to the integrated effect. To verify the derivation, figure 5.17 shows the same profiles of figure 5.16 for case highRe-H_2O. Again, the predicted values are very accurate. It is interesting to notice how G'_{rms} are much higher for this case than for the others (absolute value of around 5) despite the temperature fluctuations being lower (see figure 5.11). As κ_g is well predicted, this is not an effect of larger absorption but is caused the larger energy available for emission due to the higher temperature. Mathematically speaking, term f_E is larger due to its T_0 dependency (eq. 4.6) and this influence trickles down on G'. It is not, therefore, an optical thickness effect. Nevertheless, all the different effects are captured in the approximation f_G. A substantiation of the approximation is shown in figure 5.18 which presents incident radiation spectra near the wall ($y/h = 0.15$) and near the center of the channel ($y/h = 0.85$). It is clear that using the temperature spectra and only one characteristic wavenumber is suitable to approximate the incident radiation spectra. We also point out that the larger the κ_g, the better $\mathscr{S}^\star_{GG}$ approximates $\mathscr{S}_{GG}$ as the incident radiation spectrum approaches the turbulent emission spectrum. As described in chapter 4 this was the case for increasing κ in gray gas. Therefore, it is possible to notice the behavioural similarity of non-gray flows and gray flows with $\kappa \approx \kappa_g$.

Based on this analysis, it is now possible to define a new effective optical thickness τ_g by spatially averaging κ_g in wall-normal direction, as follows

$$\tau_g = \frac{1}{2}\int_0^2 \kappa_g(\overline{T})dy\,. \tag{5.25}$$

The obtained values of τ_g compared to τ are summarized for the non-gray gas cases in table 5.4. In contrast to τ, the new parameter for the optical thickness τ_g is able to characterize TRI. Based on τ_g, case spec-CO_2 has the highest optical thickness, followed by case spec-H_2O and spec-Part, consistently with what has been observed in the DNS results. It is possible to conclude, that κ_g is not only a convenient quantity useful to predict the fluctuations of incident radiation but also the parameter which unambiguously characterizes TRI in a non-gray turbulent flow.

Table 5.4: Comparison between τ and τ_g.

Case	spec-H_2O	spec-CO_2	spec-Part	highRe-H_2O
τ	8.02	2.99	2.79	2.12
τ_g	13.4	18.9	3.1	7.1

Hereafter, we provide a physical interpretation for the reason why τ_g is able to properly characterize TRI, where the other spectrally integrated parameters fail. The spectral transmissivity t_ν and normalized emission i_ν are defined as

$$t_\nu = e^{-\kappa_\nu}\,, \quad i_\nu = \frac{\kappa_\nu I_{b\nu}}{\max(\kappa_\nu I_{b\nu})}\,. \tag{5.26}$$

While t_ν is a measure of absorption and, if integrated, leads to the global transmissivity t, i_ν shows the redistribution of emission over the wavelength and forms the basis of τ's definition.

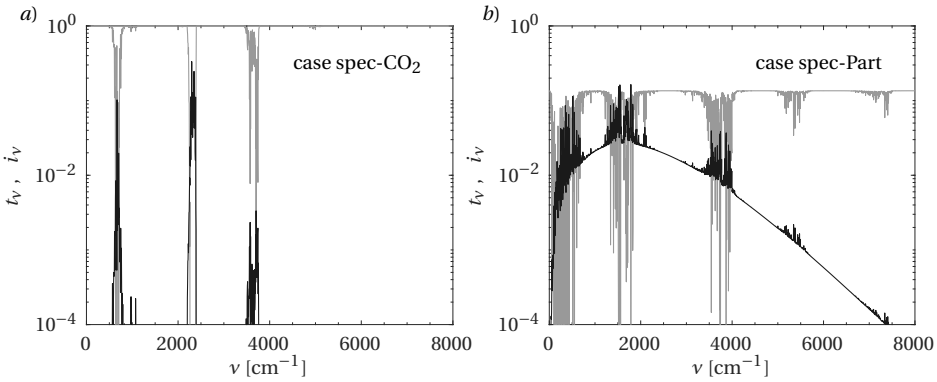

Figure 5.19: Spectral transmissivity (gray lines) and normalized emission (black lines) for non-gray cases spec-CO_2 (a) and spec-Part (b) at 800 K.

The comparison between cases spec-Part and spec-CO_2, shown in figure 5.19, displays quite effectively why neither τ or t can be used for characterizing TRI. If the t_ν is considered, case spec-Part appears the optically thickest case ($t = 0.10$ see table 5.3), while case spec-CO_2, due to the limited width of the absorption bands is in average relatively transparent ($t = 0.88$). If the combination of t_ν and i_ν is taken into account on a spectral basis, it is possible to show why τ and t fail. While i_ν is significant throughout the whole spectrum for case spec-Part, for case spec-CO_2 the emission is confined in regions where $t_\nu \to 0$ resulting in an optically thick behaviour. It is not possible to categorize TRI if one of the two effects is neglected (i.e., using τ or t) since TRI is driven by the dual effect of emission and absorption on a spectral basis. On the other hand, deriving the definition of a new parameter based on G', as done in equation (5.23), allows to take into account the dual effect of spectral emission and absorption, since G' is necessarily produced by local E', see equation (4.28). The connection of i_ν and t_ν on a ν basis is intrinsically included in the definition of τ_g which is, therefore, the appropriate parameter to characterize TRI.

Thanks to this characteristic we can claim that, despite derived in the framework of TRI, τ_g and the new spectral averaging is not relegated to turbulent flows. τ_g can be though of as an integral representation of the spectral balance between emission and re-absorption in a non-gray gas column of length $L = \omega_c^{-1}$ at rest. A higher τ_g signifies a medium which is optically thicker to self-emitted radiation.

5.6. SUMMARY

In the chapter we performed a comprehensive study of the effect of variable κ on TRI in a turbulent channel flow. We employed the relations derived in the previous chapter to identify the impact of $\overline{\kappa}$ and κ' on the modification of the temperature field. It was demonstrated that TRI is fully accounted for by the variations of the mean absorption coefficient alone. For all purposes, in a non-reactive turbulent flow, κ' can be neglected,

independently from the value of τ.

Moreover, we defined a diagnostic quantity $\mathscr{A}_{\overline{\kappa}}/(\mathscr{E}_{\overline{\kappa}}+\mathscr{A}_{\overline{\kappa}})$ that allows a monotonic comparison between TRI for flows of different τ values. With this quantity, the influence of TRI for four different non-gray gas cases was assessed. The results show that the behaviour of a non-gray gas is decoupled from the value of the Planck-mean optical thickness. In particular, the variability of the absorption spectrum impacts the interactions between temperature and radiative field. Therefore, from the approximation of incident radiation fluctuations (which are responsible of the behavioural changes in TRI effects), a new definition of spectrally averaged absorption coefficient has been derived. This new turbulence based mean absorption coefficient κ_g proves to effectively predict TRI in non-gray gas turbulent flows. In addition, κ_g provides the base for the definition of a new optical thickness τ_g which allows a conclusive comparison among gray and non-gray cases. This τ_g is not useful only in the context of turbulent flows but allows additional insight in media at rest also.

6

MODELLING TRI IN TURBULENT FLOWS

This chapter focusses on modelling the physical phenomenon investigated throughout the thesis. As a physical description of TRI has been provided in chapters 3 to 5, we propose here a model which allows a coupling of radiative heat transfer and turbulence in a Reynolds averaged Navier-Stokes (RANS) framework. The model is tested with the setup described in chapter 2 and validated with the available DNS cases.

The contents of this chapter appear in the following publication, Silvestri, Roekaerts and Pecnik, Modeling turbulent heat transfer accounting for turbulence-radiation interactions, Int. J. Heat Fluid Flow **89**, 108728 (2021), [69] .

6.1. INTRODUCTION

In the previous chapters we gathered understanding on the TRI mechanism and the coupling of convective and radiative heat transfer in high-temperature turbulent flows. This chapter focusses on converting this knowledge in predictive capabilities in the form of a RANS model. When solving the Reynolds averaged Navier-Stokes (RANS) equations it is necessary to model the unclosed terms. Modelling of TRI is usually accounted for employing the Optically Thin Fluctuation Approximation (OTFA) [70–73]. This approximation assumes that turbulent eddies are optically thin and, as a consequence, incident radiation fluctuations can be neglected when compared to mean incident radiation. Nevertheless, in optically thick flows (and non-gray gas with large τ_g), the OTFA is conceptually wrong as $G' \rightarrow E'$ [74]. To ovviate this problem, Coelho [75] developed a closure for the time averaged RTE which involves the calculation of additional equations for intensity fluctuations. Using this closure it is possible to account for the direct interactions of fluctuating temperature with mean radiative quantities ($\theta' \rightarrow Q^R$) and fluctuating radiation with mean temperature ($Q^{R'} \rightarrow \overline{\theta}$), represented by the dashed lines in figure 4.1. While these pathways have been demonstrated to be relevant in combustion processes and reactive flows, in chapters 4 and 5 we have shown that in non-reactive flows, they are trumped by the effect of radiation on the fluctuating temperature field (blue lines in figure 4.1). As a consequence, we have extensively proven that TRI modifies severely the value of the turbulent heat transfer, which is one of the variable requiring a proper closure model. This closure has never been provided in the presence of radiative heat transfer leading to the failure of all the developed models in high temperature, participating turbulent flows. Here we provide the inclusion of TRI in the modelling of the turbulent heat transfer following a rigorous mathematical procedure. We construct the model on the base of the knowledge gathered in the previous chapters, especially the relations derived in chapter 4 and extended in chapter 5. The derived "TRI" closure is applied to a standard two equation model for turbulent heat flux and tested against various DNS cases to demonstrate both its necessity and validity.

6.2. GOVERNING EQUATIONS

Favre averaging the Navier-Stokes equations for an emitting absorbing turbulent medium (eq. 2.1a-2.1d), yields

$$\frac{\partial \overline{\rho}}{\partial t} + \frac{\partial \overline{\rho} \widetilde{u}_i}{\partial x_i} = 0 \,, \tag{6.1}$$

$$\frac{\partial \overline{\rho} \widetilde{u}_i}{\partial t} + \frac{\partial \overline{\rho} \widetilde{u}_i \widetilde{u}_j}{\partial x_j} = -\frac{\partial \overline{p}}{\partial x_i} + \frac{\partial}{\partial x_j}\left(\overline{\tau}_{ij} - \overline{\rho u_i'' u_j''}\right) \,, \tag{6.2}$$

$$\frac{\partial \overline{\rho} \widetilde{\theta}}{\partial t} + \frac{\partial \overline{\rho} \widetilde{\theta} \widetilde{u}_j}{\partial x_j} = \frac{\partial}{\partial x_j}\left(\overline{q}_{cj} - \overline{\rho u_j'' \theta''}\right) - \frac{\overline{Q^R}}{Rd} \,, \tag{6.3}$$

where

$$\tau_{ij} = \frac{\mu}{Re}\left(\frac{\partial u_j}{\partial x_i} + \frac{\partial u_i}{\partial x_j} - \frac{2}{3}\delta_{ij}\frac{\partial u_k}{\partial x_k}\right) \,, \quad q_{cj} = \frac{\lambda}{Pe}\frac{\partial \theta}{\partial x_j} \,, \quad Q^R = \kappa(E-G)$$

The non-dimensional parameters appearing in equations (6.1-6.3) are the Peclet number $Pe = RePr$ and the Radiation number $Rd = RePrPl$. The Reynolds stress $\overline{\rho u_i'' u_j''}$ and the turbulent heat flux $\overline{\rho u_j'' \theta''}$ in equations (6.2) and (6.3), respectively, are unclosed terms that require a closure. The modelling of the Reynolds stress is well established and, since radiative heat transfer does not directly affect velocity (as shown in chapter 5), it is not a topic of this study. On the other hand, the turbulent heat flux $\overline{\rho u_j'' \theta''}$ is greatly affected by radiative heat transfer and, therefore, its effect has to be accounted to ensure correct temperature predictions.

The specific novelty of this chapter consists in the modelling of all the relevant TRI pathways (blue lines in figure 4.1) and the inclusion of these effects into a general turbulent heat transfer closure model ($\overline{\rho u_j'' \theta''}$). To avoid errors in modelling the radiative heat source, we employ the averaged radiative quantities ($\overline{E}$, $\overline{G}$, $\overline{\kappa}$) directly from the reference DNS simulations. In order to model TRI, it is necessary to approximate the fluctuations of radiative quantities corresponding to the bottom right block in figure 4.1. For this purpose, we use the linear expressions derived in chapter 4 which relate the fluctuations of the radiative quantities (κ', E' and G') to the temperature fluctuations θ'. Namely,

$$\kappa' \approx f_\kappa \theta' \,, \quad E' \approx f_E \theta' \,, \quad G' \approx f_G \theta' \,. \tag{6.4}$$

where f_κ, f_E and f_G are the coefficients of proportionality, functions of averaged quantities only. We will perform the derivation of the TRI model in a general geometry and then apply it to the specific problem at hand (a high-temperature turbulent channel flow).

6.3. TWO EQUATION CLOSURE MODEL

Most of the turbulent heat transfer closure models used in a RANS framework are based on the gradient-diffusion hypothesis which states that

$$\overline{\rho u_j'' \theta''} = -\alpha_t \frac{\partial \overline{\theta}}{\partial x_j} \,, \tag{6.5}$$

where α_t is the flow dependent "eddy diffusivity". This quantity can be approximated in several ways. The most common is to relate it to the eddy viscosity μ_t as $\alpha_t = \mu_t / Pr_t$, with Pr_t as the "turbulent Prandtl number", usually taken as costant equal to 0.9 [76]. This is a quite crude approximation which works in the limit of high Reynolds number flows when $Pr \approx 1$. We have already demonstrated in chapter 3 that Pr_t is largely modified by radiative heat transfer and cannot be used if the flow is able to emit and absorb radiation. The two equation model, on the other hand, does not rely on the turbulent Prandtl number, and estimates the turbulent diffusivity α_t by relating it to a mixed time scale τ_m, which incorporates both the velocity field and the temperature field information as

$$\tau_m = \tau_u^m \tau_s^n \,, \quad \text{with} \quad \tau_u = \frac{k}{\varepsilon} \,, \quad \tau_s = \frac{\overline{\theta'^2}}{\varepsilon_\theta} \,, \quad \text{and} \quad m + n = 1 \,, \tag{6.6}$$

where τ_u is a time scale characteristic of the velocity field, while τ_s represents the time scale of the thermal field. Usually, the contribution of these two time scales to the mixed

time scale is considered equal (i.e., the exponents m and n are taken as $m = n = 0.5$) [77–80]. In this work we followed the same approach. The expression for the eddy diffusivity then becomes

$$\alpha_t = \overline{\rho} C_m f_m k \tau_m \,, \tag{6.7}$$

where $f_m k$ is a damping function that accounts for low Reynolds number effects. This model has been developed and tested, with different details, in [77–80]. In this work we follow the model version developed by Deng et al. [77]. The model functions and constants involved are summarized later in section 6.5. In order to assess the thermal time scale τ_s, two additional non-dimensional transport equations, for temperature variance $\overline{\theta'^2}$ and dissipation of temperature variance ε_θ, respectively, are solved (from here the name of the closure model). In contrast to previous works, we have here derived these equations for a radiatively participating flow, to account for the effect of radiative heat transfer. Both additional equations are displayed and discussed in the sections below.

6.3.1. TEMPERATURE VARIANCE TRANSPORT EQUATION

The exact transport equation for the temperature variance reads:

$$\begin{aligned}
&\underbrace{\frac{\partial \overline{\rho\theta''^2}}{\partial t} + \frac{\partial \widetilde{u_j}\,\overline{\rho\theta''^2}}{\partial x_j}}_{\mathscr{C}_\theta} = \underbrace{-2\,\overline{\rho u_j''\theta''}\frac{\partial \widetilde{\theta}}{\partial x_j}}_{\mathscr{P}_\theta} + \underbrace{\frac{\partial \overline{\rho u_j''\theta''^2}}{\partial x_j}}_{\mathscr{T}_\theta} \\
&+ \underbrace{\frac{\partial}{\partial x_j}\left(\overline{\frac{\lambda}{Pe}\frac{\partial \theta'^2}{\partial x_j}}\right)}_{\phi_\theta} - 2\underbrace{\overline{\frac{\lambda}{Pe}\left(\frac{\partial \theta'}{\partial x_j}\right)^2}}_{\overline{\rho}\varepsilon_\theta} \\
&\underbrace{-\frac{2}{Rd}\overline{Q^{R\prime}\theta''}}_{\mathscr{R}_\theta} + \underbrace{\overline{\theta''}\left[\frac{\partial}{\partial x_j}\left(\frac{\overline{\lambda}}{Pe}\frac{\partial \overline{\theta'^2}}{\partial x_j}\right) + \frac{2}{Rd}\overline{Q^R}\right]}_{\mathscr{D}_\theta} .
\end{aligned} \tag{6.8}$$

In order to obtain a closed form of the above equation, several assumptions and approximations have to be applied. A first approximation consists in neglecting the terms containing $\overline{\theta''}$ ($\mathscr{D}_\theta$ in the above equation). This is exact in an incompressible flow, and, given the Morkovin hypothesis [81], which states that compressibility can be accounted for by considering mean density variations alone, it is an accurate approximation in low Mach number flows as well. This approximation implies that

$$\begin{aligned}
&\widetilde{\theta} \approx \overline{\theta}\,, \quad \text{since} \quad \widetilde{\theta} = \overline{\theta} - \overline{\theta''} \\
&\widetilde{\theta''^2} \approx \overline{\theta'^2}\,, \quad \text{since} \quad \widetilde{\theta''^2} = \overline{\theta'^2} + \frac{\overline{\rho'\theta'^2}}{\overline{\rho}} - \overline{\theta''}^2
\end{aligned} \tag{6.9}$$

The validity of this assumption for the investigated cases is demonstrated by showing profiles of $\overline{\theta}$ and $\widetilde{\theta}$ in figure 6.1(a), and $\overline{\theta'^2}$ and $\widetilde{\theta''^2}$ in figure 6.1(b). In addition, it is common practice to assume that thermal conductivity fluctuations are low compared to

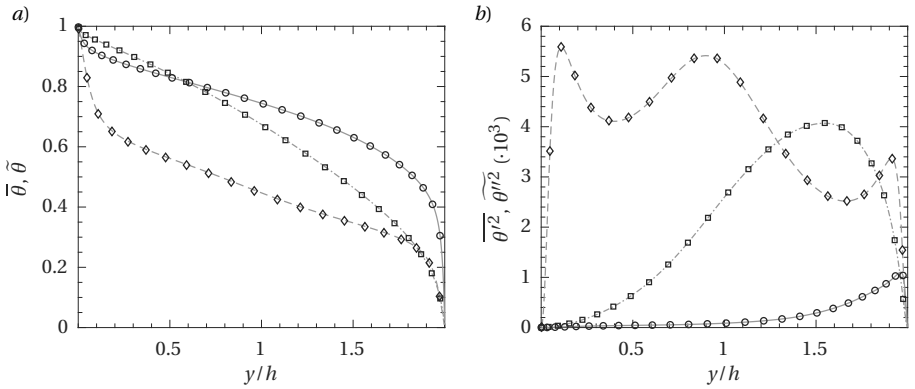

Figure 6.1: Reynolds (lines) and Favre (symbols) averaged temperature and temperature variance for three representative cases with different temperature and density gradients. Diamonds and dashed lines: case bench-ρ, squares and dashed-dotted lines: case gray-ρ10, circles and solid lines: case highRe-H−2O.

its mean value (i.e., $\lambda \approx \overline{\lambda}$). Finally, the transport term is commonly modelled using a gradient-diffusion hypothesis employing the eddy diffusivity α_t scaled by a coefficient σ_θ. All these approximations lead to

$$\begin{aligned}\frac{\partial \overline{\rho}\overline{\theta''^2}}{\partial t} + \frac{\partial \widetilde{u_j}\overline{\rho}\overline{\theta''^2}}{\partial x_j} = \frac{\partial}{\partial x_j}\left[\left(\frac{\overline{\lambda}}{Pe} + \frac{\alpha_t}{\sigma_\theta}\right)\frac{\partial \overline{\theta'^2}}{\partial x_j}\right] + 2P_\theta \\ - 2\overline{\rho}\varepsilon_\theta - \underbrace{\frac{2}{Rd}\overline{Q^{R'}\theta'}}_{\mathscr{R}_\theta},\end{aligned} \tag{6.10}$$

where P_θ is the production of temperature variance, estimated, consistently with the turbulent heat flux, as

$$P_\theta = \alpha_t\left(\frac{\partial \overline{\theta}}{\partial x_j}\right)^2, \tag{6.11}$$

and ε_θ is the scalar dissipation calculated by its own transport equation. The remaining unclosed term in this equation is the new radiative term $\mathscr{R}_\theta$.

6.3.2. SCALAR DISSIPATION TRANSPORT EQUATION

The additional transport equation for ε_θ has been derived for constant property flow and applied also to variable density flow keeping in mind that density fluctuations are low compared to the average density. For a transparent, constant property case, the fol-

lowing formulation is equivalent to one derived in [77]

$$\begin{aligned}\overline{\rho}\frac{D\varepsilon_\theta}{Dt} = &\frac{\partial}{\partial x_j}\left[\left(\frac{\overline{\lambda}}{Pe}+\frac{\alpha_t}{\sigma_{\varepsilon_\theta}}\right)\frac{\partial\varepsilon_\theta}{\partial x_j}\right] \\ &\underbrace{+\frac{C_p f_p}{\tau_m}\overline{\rho}P_\theta}_{\mathscr{P}_{\varepsilon_\theta}}\underbrace{-\frac{C_{d1}f_{d1}}{\tau_s}\overline{\rho}\varepsilon_\theta-\frac{C_{d2}f_{d2}}{\tau_u}\overline{\rho}\varepsilon_\theta}_{\varepsilon_{\varepsilon_\theta}} \\ &\underbrace{-\frac{2\overline{\lambda}}{PeRd}\overline{\frac{\partial Q^{R'}}{\partial x_j}\frac{\partial\theta''}{\partial x_j}}}_{\mathscr{R}_{\varepsilon_\theta}}.\end{aligned} \tag{6.12}$$

Again, the turbulent transport term has been modelled by employing the gradient-diffusion approximation as for the temperature variance transport equation. In equation (6.12) the terms $\mathscr{P}_{\varepsilon_\theta}$ and $\varepsilon_{\varepsilon_\theta}$ are the production and the dissipation term, respectively. The first is modeled with the use of the mixed time scale, while the latter is divided into two different parts, one that accounts for velocity time scale and one which accounts for temperature time scale. Constants C_p, C_{d1} and C_{d2} and model functions f_p, f_{d1}, f_{d2} are taken as in [77] and shown in section 6.5. A new unclosed radiative term $\mathscr{R}_{\varepsilon_\theta}$ appears. The rationale for the derivation of this new term follows the procedure which leads to the ε_θ budget equation. Starting from an incompressible, constant viscosity formulation,

$$\varepsilon_\theta = \frac{1}{Pe}\overline{\left(\frac{\partial\theta'}{\partial x_j}\right)^2}. \tag{6.13}$$

In this case, $\partial_t\varepsilon_\theta$ is equivalent to

$$\frac{\partial\varepsilon_\theta}{\partial t} = \overline{\frac{2}{Pe}\frac{\partial\theta'}{\partial x_j}\frac{\partial}{\partial x_j}\left(\frac{\partial\theta}{\partial t}-\frac{\partial\overline{\theta}}{\partial t}\right)}. \tag{6.14}$$

Therefore, the procedure to obtain the radiative term in the scalar dissipation budget equation follows these steps: (1) subtract the mean radiative heat source to then instantaneous radiative source, (2) derive the result in x_j, (3) multiply by $2Pe^{-1}\partial_{x_j}\theta'$, (4) Reynolds average the resulting term. If stemming from the compressible low Mach number Navier-Stokes equations (expressed in a non-conservative form), $\partial_t\theta$ requires a division by ρ on the RHS. The first step of the procedure would then yield

$$\frac{1}{Rd}\left(\frac{Q^R}{\rho}-\frac{\overline{Q^R}}{\overline{\rho}}\right). \tag{6.15}$$

On the other hand, to account for variable density, it is common practice to multiply the scalar dissipation equation with $\overline{\rho}$ [79]. Therefore, by assuming that, in this context,

$$\left(\frac{1}{\rho}\right)\cdot\overline{\rho}\approx\overline{\left(\frac{1}{\rho}\right)}\cdot\overline{\rho}\approx 1\,, \tag{6.16}$$

the radiative terms obtained following the incompressible procedure is assumed to be valid also in a variable density framework. It has to be reminded that this assumption is valid only under the Morkovin hypothesis of weak density fluctuations and, therefore, it cannot be directly applied to high Mach number flows. To account for variable thermal conductivity, $\mathscr{R}_{\varepsilon_\theta}$ is further multiplied by $\overline{\lambda}$ by assuming weak thermal conductivity fluctuations (as in this case $\varepsilon_\theta \approx \overline{\lambda} Pe^{-1}\overline{(\partial x_j \theta')'}$). The final radiative term, as anticipated in equation (6.12) reads

$$\mathscr{R}_{\varepsilon_\theta} = \frac{2\overline{\lambda}}{PeRd}\overline{\frac{\partial Q^{R'}}{\partial x_j}\frac{\partial \theta''}{\partial x_j}} \tag{6.17}$$

6.4. TRI MODELLING

By following the approach presented in chapter 4, it is possible to find a closure for the additional radiative terms in equations (6.10) and (6.12) by using the model functions. The radiative term in equation (6.10) can be rewritten in terms of emission and incident radiation by substituting $Q = \kappa(E - G)$. Additionally, a Reynolds decomposition of κ, E and G yields

$$\begin{aligned}\mathscr{R}_\theta = &\frac{2}{Rd}\left(\overline{\kappa}(\overline{E'\theta'} - \overline{G'\theta'}) + (\overline{E} - \overline{G})\overline{\kappa'\theta'}\right) \\ &+ \frac{2}{Rd}\left(\overline{\kappa' E'\theta'} - \overline{\kappa' G'\theta'}\right).\end{aligned} \tag{6.18}$$

From the modelling of radiative fluctuations as given in equations (6.4)

$$\begin{aligned}\mathscr{R}_\theta \approx &\frac{2}{Rd}\left(\overline{\kappa}(f_E - f_G) + (\overline{E} - \overline{G}) f_\kappa\right)\overline{\theta'^2} \\ &+ \frac{2}{Rd} f_\kappa (f_E - f_G)\overline{\theta'^3}.\end{aligned} \tag{6.19}$$

Since $f_\kappa \ll \overline{\kappa}$ (absorption coefficient fluctuations are generally negligible, see chapter 5) and $\overline{\theta'^3} \ll \overline{\theta'^2}$, it is possible to safely neglect the last term on the RHS. The final model for the radiative term in the temperature variance budget equation reads

$$\mathscr{R}_\theta = \frac{2}{Rd}\left(\overline{\kappa}(f_E - f_G) + (\overline{E} - \overline{G}) f_\kappa\right)\overline{\theta'^2}. \tag{6.20}$$

The above equation is closed, as it depends on quantities readily available in a RANS framework (provided $\overline{\theta'^2}$ is modeled).

The radiative term $\mathscr{R}_{\varepsilon_\theta}$ in equation (6.12) can be expanded, by performing a Reynolds

decomposition of κ and Q^R, as

$$\begin{aligned}\mathscr{R}_{\varepsilon_\theta} = 2\frac{\overline{\lambda}}{PeRd}\underbrace{\left(\overline{\frac{\partial\kappa'(\overline{E}-\overline{G})}{\partial x_j}\frac{\partial\theta'}{\partial x_j}}+\overline{\frac{\partial\kappa'(E'-G')}{\partial x_j}\frac{\partial\theta'}{\partial x_j}}\right)}_{\text{fluctuating }\kappa} \\ +2\frac{\overline{\lambda}}{PeRd}\underbrace{\left(\overline{\frac{\partial\overline{\kappa}(E'-G')}{\partial x_j}\frac{\partial\theta'}{\partial x_j}}\right)}_{\text{average }\kappa}.\end{aligned} \tag{6.21}$$

As already done for equation (6.3), we neglect the higher order term containing $\kappa'(E'-G')$. This is substantiated by the low impact of absorption coefficient fluctuations, demonstrated in chapter 5. By further splitting the derivatives,

$$\begin{aligned}\mathscr{R}_{\varepsilon_\theta} = 2\frac{\overline{\lambda}}{PeRd}\left(\overline{\frac{\partial\kappa'}{\partial x_j}\frac{\partial\theta'}{\partial x_j}}(\overline{E}-\overline{G})+\overline{\kappa'\frac{\partial\theta'}{\partial x_j}\frac{\partial(\overline{E}-\overline{G})}{\partial x_j}}\right) \\ +2\frac{\overline{\lambda}}{PeRd}\left(\overline{(E'-G')\frac{\partial\theta'}{\partial x_j}\frac{\partial\overline{\kappa}}{\partial x_j}}+\overline{\frac{\partial(E'-G')}{\partial x_j}\frac{\partial\theta'}{\partial x_j}\overline{\kappa}}\right).\end{aligned} \tag{6.22}$$

Substituting the linear relations and rearranging, yields the model for the radiative term in the ε_θ transport equation

$$\begin{aligned}\mathscr{R}_{\varepsilon_\theta} = \frac{2}{Rd}\left[\overline{\kappa}_p(f_E-f_G)+(\overline{E}-\overline{G})f_\kappa\right]\varepsilon_\theta \\ +\frac{\overline{\lambda}}{PeRd}\frac{\partial}{\partial x_j}\left[\overline{\kappa}_p(f_E-f_G)\right]\frac{\partial\overline{\theta'^2}}{\partial x_j} \\ +\frac{\overline{\lambda}}{PeRd}\frac{\partial}{\partial x_j}\left[f_\kappa(\overline{E}-\overline{G})\right]\frac{\partial\overline{\theta'^2}}{\partial x_j}.\end{aligned} \tag{6.23}$$

Also the above expression, provided $\overline{\theta'^2}$ and ε_θ are modeled, depends on quantities readily availbale and can be directly implemented in the turbulent heat transfer model. Note that $\overline{\kappa}$, $\overline{E}$ aand $\overline{G}$ are taken from the respective DNS simulations. However, chapter 5 demonstrated that the terms involving $\overline{E}$ and $\overline{G}$ in equations (6.20) and (6.23) are negligible irrespective of the optical thickness value.

6.4.1. MODIFIED TEMPERATURE TIME SCALE

The definition of τ_s to be used in the expression of the eddy diffusivity (6.7) accounts only for conductive dissipation of temperature variance (ε_θ). However, TRI acts as an additional "radiative dissipation" ε_r which reduces drastically the temperature time scale [23]. Therefore, to include TRI in the definition of α_t, we must define a "modified" temperature time scale τ_s^R which accounts for ε_r

$$\tau_s^R = \frac{\overline{\theta'^2}}{\varepsilon_\theta + C_r\varepsilon_r}, \tag{6.24}$$

where C_r is a model constant, here taken as $C_r = 0.5$. Radiative dissipation ε_r, in a strict sense, is the dissipative part of the radiative term $\mathscr{R}_\theta$ which can be retreived by expressing the radiative heat source in terms of divergence of radiative heat flux, By employing this definition it is possible to decompose the radiative term $\mathscr{R}_\theta$ into a dissipation ε_r and a transport term ϕ_r as done in chapter 3,

$$\frac{\mathscr{R}_\theta}{2} = \underbrace{\frac{1}{Rd}\frac{\partial \overline{q'_{rj}\theta'}}{\partial x_j}}_{\phi_r} - \underbrace{\frac{1}{Rd}\overline{q'_{rj}\frac{\partial \theta'}{\partial x_j}}}_{\varepsilon_r} \tag{6.25}$$

On the other hand, we can assume that, away from the walls, the dissipation term is much larger than the transport term $\left(\varepsilon_r \gg \phi_r\right)$ as shown in chapter 3. Therefore, it is possible to assume that $\varepsilon_r \approx 0.5\mathscr{R}_\theta$. From this definition, the eddy diffusivity can then be corrected as follows

$$\alpha_t = \overline{\rho} C_m f_m k \tau_m^R \quad \text{where} \quad \tau_m^R = \left(\tau_u \tau_s^R\right)^{0.5}, \quad \text{with} \quad \tau_s^R = \frac{\overline{\theta'^2}}{\varepsilon_\theta + 0.5 C_r \mathscr{R}_\theta}. \tag{6.26}$$

It has to be pointed out that τ_s is present also in the scalar dissipation transport equation (6.12) to model the dissipation and the production term ($\varepsilon_{\varepsilon_\theta}$ and $\mathscr{P}_{\varepsilon_\theta}$, respectively). Here, the original definition of τ_s is maintained, as the influence of radiation is directly modeled through the term $\mathscr{R}_{\varepsilon_\theta}$.

6.4.2. CHARACTERISTIC WAVENUMBER

The model employed for incident radiation fluctuations ($G' \approx f_G \theta'$) requires the estimation of the "characteristic wavenumber" ω_c, which represents the length scale of the average energy-containing temperature structure. In chapter 4 we defined it, such that anisotropy due to wall turbulence is accounted for, using the one-dimensional temperature power spectrum (eq. 4.35). Since the power spectrum is not available in a RANS simulation, the integral length scale of temperature is used, calculated as in ref. [24]

$$l_\theta = C_{\varepsilon 2} C_m \frac{\overline{\theta'^2} k^{1/2}}{\varepsilon_\theta} \approx \omega_c^{-1}. \tag{6.27}$$

In non-gray gas cases, κ_g depends on ω_c. An iterative procedure is, therefore necessary: κ_g is initialized with $\overline{\kappa}$ and, as the solution is iterated, κ_g is updated as a function of the integral length scale and the mean dimensional temperature

$$\kappa_g l_\theta \cdot \operatorname{atan}\left(\frac{1}{\kappa_g l_\theta}\right) = \frac{1}{\kappa_p(\overline{T}^*) I_b(\overline{T}^*)} \int_0^\infty \kappa_\nu^2(\overline{T}^*) I_{b\nu}(\overline{T}^*) l_\theta \cdot \operatorname{atan}\left(\frac{1}{\kappa_\nu\left(\overline{T}^*\right) l_\theta}\right) d\nu, \tag{6.28}$$

by integrating over line-by-line spectra retrieved from a high resolution, accurate spectral database [59].

6.5. SUMMARY OF THE MODEL EQUATIONS

In this section, the radiative modification is tested on the different DNS cases analysed in the previous chapters. Since the DNS data is statistically steady and homogeneous in the streamwise and spanwise direction, the model equations simplify to a one-dimensional problem (only the gradients in the wall-normal direction remain). Below, we summarize the model equations as well as the values for all the constants involved. It is reminded that we neglect fluctuation of transport properties ($\lambda \approx \overline{\lambda}$, $\mu \approx \overline{\mu}$) and make use of the gradient-diffusion hypothesis

$$\overline{\rho u'' v''} = -\mu_t \frac{\partial \overline{u}}{\partial y} \quad \text{and} \quad \overline{\rho v'' \theta''} = -\alpha_t \frac{\partial \overline{\theta}}{\partial y} \,. \tag{6.29}$$

the model RANS equations for a statistically fully developed turbulent channel flow reduce to,

$$\frac{\partial}{\partial y}\left[\left(\frac{\overline{\mu}}{Re} + \mu_t\right)\frac{\partial \overline{u}}{\partial y}\right] = \frac{\partial \overline{p}}{\partial x} \,, \tag{6.30}$$

$$\frac{\partial}{\partial y}\left[\left(\frac{\overline{\lambda}}{Pe} + \alpha_t\right)\frac{\partial \overline{\theta}}{\partial y}\right] = \overline{\frac{\kappa_p Q}{Rd}} \,. \tag{6.31}$$

Given the moderate Reynolds number of the test cases, turbulent viscosity is calculated using the $v^2 - f$ model of Durbin [82] which is able to correctly predict wall damping by introducing ad-hoc damping relations. The model is not shown here, for more details the reader is referred to ref. [82]. In particular, for variable density cases, the variable property formulation of Otero et al [83] is implemented, as it slighlty improves the turbulent stress predictions (proof in section 6.6.1). The turbulent heat flux model equations are summarized below

$$\alpha_t = \overline{\rho} C_m f_m k \left(\frac{k}{\varepsilon} \cdot \frac{\overline{\theta'^2}}{\varepsilon_\theta + C_r \varepsilon_r}\right)^{0.5} \,, \tag{6.32}$$

$$-\frac{\partial}{\partial y}\left[\left(\frac{\overline{\lambda}}{Pe} + \frac{\alpha_t}{\sigma_\theta}\right)\frac{\partial \overline{\theta'^2}}{\partial y}\right] = 2P_\theta - 2\overline{\rho}\varepsilon_\theta - \mathscr{R}_\theta \,, \tag{6.33}$$

$$-\frac{\partial}{\partial y}\left[\left(\frac{\overline{\lambda}}{Pe} + \frac{\alpha_t}{\sigma_{\varepsilon_\theta}}\right)\frac{\partial \varepsilon_\theta}{\partial y}\right] = \frac{C_p f_p}{\tau_m} P_\theta - \left[\frac{C_{d1} f_{d1}}{\tau_s} + \frac{C_{d2} f_{d2}}{\tau_u}\right]\overline{\rho}\varepsilon_\theta - \mathscr{R}_{\varepsilon_\theta} \,, \tag{6.34}$$

with the model functions and constants (as in Deng et al. [77]) shown in table 6.1, and below

Table 6.1: Model constants as in Deng et al. [77]

C_m	C_r	C_p	C_{d1}	C_{d2}	$C_{\varepsilon 2}$	σ_θ	$\sigma_{\varepsilon_\theta}$
0.1	0.5	2.34	2.0	0.9	1.9	1.0	1.0

$$f_m = \left[1-\exp\left(-\frac{Re_\varepsilon}{16}\right)\right]^2\left(1+\frac{3}{Re_t^{3/4}}\right), \quad f_p = 1\,,$$

$$f_{d1} = 1-\exp\left(-\frac{Re_\varepsilon}{1.7}\right)^2, \quad f_\varepsilon = \left(1-0.3\exp\left[-\left(\frac{Re_\varepsilon}{6.5}\right)^2\right]\right)\left[1-\exp\left(-\frac{Re_\varepsilon}{3.1}\right)\right]^2,$$

$$f_{d2} = \frac{1}{C_{d2}}\left(C_{\varepsilon 2}f_\varepsilon - 1\right)\left[1-\exp\left(-\frac{Re_\varepsilon}{5.8}\right)^2\right], \quad Re_\varepsilon = \frac{\rho^{3/4}\varepsilon^{1/4}y}{\mu^{3/4}}, \quad Re_t = \frac{\rho}{\mu}\frac{k^2}{\varepsilon}.$$

6.5.1. TEST CASES

The investigated cases are the ones discussed in the previous chapters as well as additional cases with different parameters, all summarized in table 6.2. All cases are forced convection in a periodic channel bounded by an isothermal hot and cold wall. Both walls are black ($\epsilon_w = 1$). In terms of thermal boundary conditions, the first 14 cases have $T_h^* = 955$ K and $T_c^* = 573$ K corresponding to $T_0 = 1.5$, while the last two have $T_h^* = 1800$ K and $T_c^* = 600$ K ($T_0 = 0.5$). All cases have a constant Planck number equal to 0.03. The

Table 6.2: Description of the test cases

Cases	Re	Pr	T_0	ρ	μ	λ	κ	τ
bench	2900	1	1.5	const	const	const	0	0
gray-01	2900	1	1.5	const	const	const	0.1	0.1
gray-1	2900	1	1.5	const	const	const	1	1
gray-5	2900	1	1.5	const	const	const	5	5
gray-10	2900	1	1.5	const	const	const	10	10
gray-20	2900	1	1.5	const	const	const	20	20
gray-10p	2900	0.7	1.5	const	const	const	10	10
bench-ρ	3750	1	1.5	$T_0/(\theta+T_0)$	const	const	0	0
gray-ρ01	3750	1	1.5	$T_0/(\theta+T_0)$	const	const	(eq. 4.7)	0.1
gray-ρ1	3750	1	1.5	$T_0/(\theta+T_0)$	const	const	(eq. 4.7)	1
gray-ρ10	3750	1	1.5	$T_0/(\theta+T_0)$	const	const	(eq. 4.7)	10
spec-H_2O	3750	1	1.5	$T_0/(\theta+T_0)$	const	const	H_2O spectra	8.023
spec-CO_2	3750	1	1.5	$T_0/(\theta+T_0)$	const	const	CO_2 spectra	2.99
spec-Part	3750	1	1.5	$T_0/(\theta+T_0)$	const	const	QG spectra	2.79
bench-highRe	16700	0.93	0.5	$T_0/(\theta+T_0)$	$\rho^{-1.15}$	$\rho^{-1.35}$	0	0
highRe-H_2O	16700	0.93	0.5	$T_0/(\theta+T_0)$	$\rho^{-1.15}$	$\rho^{-1.35}$	H_2O spectra	2.12

DNS database includes constant and variable properties as well as gray and non-gray cases. In particular, the first seven cases are constant property, constant absorption coefficient and gray. They differ only in the magnitude of κ and, therefore, optical thickness (τ). These DNS cases are presented and discussed in chapter 3.

The next four cases, designated by a ρ in the name, are still gray, but with temperature-dependent density and absorption coefficient. In particular the absorption coefficient is a 5^{th} order polinomial of T^{*-1} (eq. 4.7). Finally, the last five cases have a spectrally

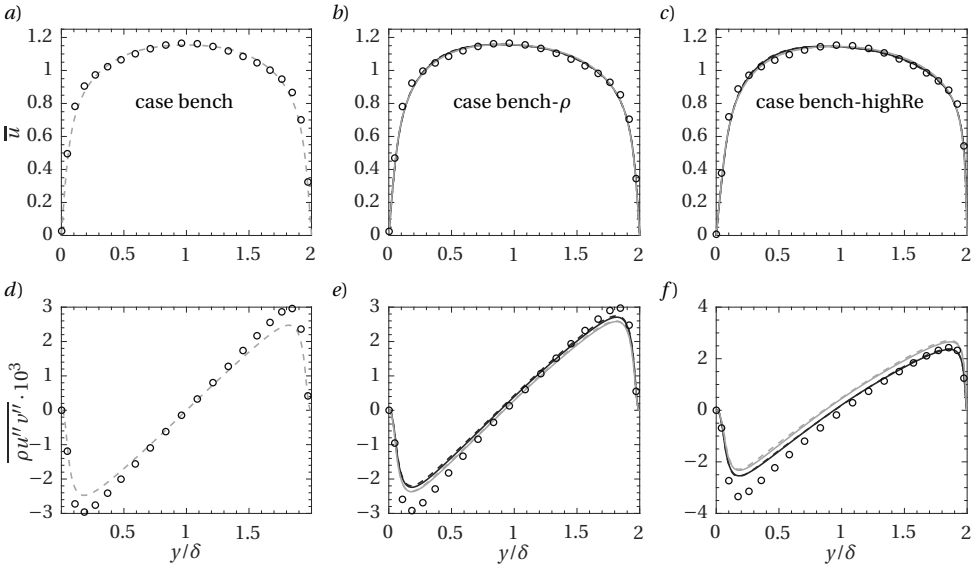

Figure 6.2: Profiles of mean velocity and turbulent stress for the transparent cases compared to DNS data. The black line shows results obtained with a classical scaling, while the gray lines show the improved semi-local $v^2 - f$ formulation which relies on semi-local scaling and semi-local Reynolds number. In terms of turbulent heat flux models, a dashed line represents the $Pr_t = 0.9$ model, while a solid line shows the two-equation model.

varying, temperature dependent absorption coefficient and variable density. The employed spectra are described in section 5.2. The last two cases in table 6.2 have a higher Reynolds number and variable viscosity and thermal conductivity.

Among all these cases, three transparent benchmarks (bench, bench-ρ and bench-highRe) are used to test the employed RANS models. In the rest of the section the following RANS model combinations will be compared:

- $v^2 - f$ for μ_t with $\alpha_t = \mu_t / 0.9$
- $v^2 - f$ for μ_t and $\overline{\theta'^2} - \varepsilon_\theta$ for α_t with no TRI model ($\mathscr{R}_\theta = \mathscr{R}_{\varepsilon_\theta} = 0$)
- $v^2 - f$ for μ_t and $\overline{\theta'^2} - \varepsilon_\theta$ for α_t with TRI model

We remind that, since the focus of this report is the modelling of turbulent heat transfer in presence of radiation, to avoid errors in the calculation of the radiative sources, the profiles of the average radiative quantities ($\overline{\kappa}$, $\overline{E}$ and $\overline{G}$) are taken directly from DNS calculations. This ensures that, even if negligible, the $\theta' \rightarrow \overline{\kappa}, \overline{E}, \overline{G}$ pathway is still accounted for (figure 4.1).

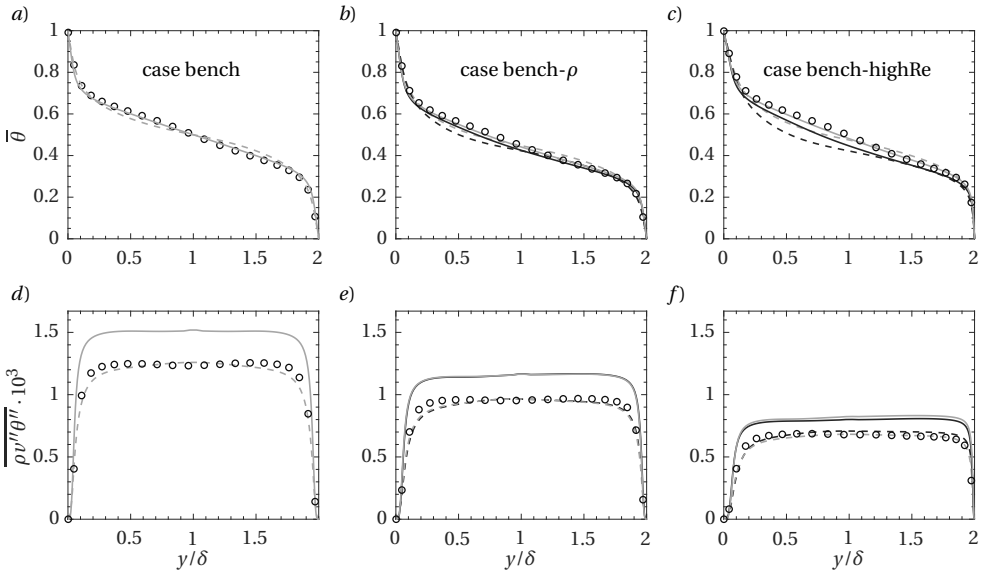

Figure 6.3: Profiles of mean temperature and turbulent heat flux for the transparent cases compared to DNS data. The black line shows results obtained with a classical scaling, while the gray lines show the improved semi-local $v^2 - f$ formulation which relies on semi-local scaling and semi-local Reynolds number. In terms of turbulent heat flux models, a dashed line represents the $Pr_t = 0.9$ model, while a solid line shows the two-equation model.

6.6. RESULTS

6.6.1. TRANSPARENT CASES

The models are first tested on the transparent benchmarks to ensure correct implementation. Figure 6.2 shows mean velocity results (top row) and Reynolds stress (bottom row). Here, the dashed lines show results obtained with a simple constant turbulent Prandtl number, while the solid lines are the calculations obtained using the two equation turbulent heat flux model. In particular, the black lines shows the results obtained using a classical implementation, based on wall scaling, while the gray lines are obtained using an improved $v^2 - f$ model, which accounts for variable properties, developed on the basis of semi-local scaling [84] and implemented in Otero et al. [83]. In the bench case, the turbulent heat flux model does not affect the velocity field, as temperature is a passive scalar. Therefore – as all the results would collapse on a single line – only one RANS result for the velocity field is shown. It is possible to notice that the $v^2 - f$ model slightly underpredicts the turbulent stress. For the bench-ρ and the bench-highRe cases, the classical and improved $v^2 - f$ formulations for μ_t are compared. It is possible to notice that, again, the choice of the turbulent heat flux model does not affect the velocity field (constant turbulent Prandtl number yields same results as the-two equation model), but the $v^2 - f$ formulation does, with slightly improved results using the "semi-

local scaling" implementation described in Otero et al. [83] when large property variations are present (case bench-highRe). In the latter case, the turbulent stress is largely underpredicted on the hot side. The reason might be the very low density and high viscosity on the hot side that cause local low Reynolds number effects which are known to reduce the accuracy of a $k-\varepsilon$ based turbulence model.

In constrast, the turbulent heat flux and mean temperature profiles (presented in figure 6.3) show differences between the models used. If the constant turbulent Prandtl model is used, the turbulent heat flux is mispredicted in the center of the channel, leading to improved mixing and a mean temperature profile which is lower on the hot side and higher on the cold side of the channel. On the other hand, the two equation model leads to an overprediction of the turbulent heat flux in the core of the channel. This is caused by a slight overprediction of the turbulent heat transfer (derivative of $\overline{\rho v'' \theta''}$) in the thermal conductive layer. Despite this overprediction, the important quantity is the derivative of the turbulent heat flux, which is better predicted with the two-equation model compared to the constant turbulent Prandtl number approach. This is clearly proven by the better agreement of the mean temperature profile. Note that, as shown by equation (6.31, the mean temperature profile is completely determined by α_t (in a transparent case) and, therefore, reflects the real performance of the turbulent heat flux model. Therefore, the two-equation model leads to a smaller "thermal boundary layer" than the actual DNS data but an overall good performance in terms of average temperature profile in the core of the channel. Again, it is possible to notice that the variable properties v^2-f model yields slightly improved results in case of large property variations (case bench-highRe). For this reason, the improved variable property v^2-f formulation is used for all the following simulations.

6.6.2. CONSTANT PROPERTY, GRAY CASES

Figure 6.4 shows the results obtained for constant properties, low to intermediate optical thickness cases. As already demonstrated in several previous studies [20, 21, 29, 57, 61] if the channel is optically thin, the influence of TRI is negligible. Indeed, it is possible to notice that, since TRI is negligible, the differences between the models, for case gray-01, closely resemble the transparent cases. In particular, by assuming a constant turbulent Prandtl number, turbulent heat transfer is mispredicted in the center of the channel leading to a higher mean temperature on the cold side of the channel. The two equation model overpredicts the turbulent heat flux as in benchmark case, while the addition of a TRI model improves slightly the predictions. This does not translate in a visible improvement in the mean temperature profile as TRI impact is still very low. On the other hand, at an intermediate optical thickness TRI starts to play an important role, strongly affecting the turbulent temperature field. This influence is reflected in the failure of the standard models in predicting both the turbulent heat transfer and the average temperature field. In particular, turbulent heat flux is always severely over-predicted leading to an increased temperature mixing when compared to the DNS results. This is caused by the fact that standard models do not take into account the additional dissipative effect of radiative heat transfer on temperature fluctuations and, therefore, predict much higher thermal turbulence levels. In reality, TRI decouples the connection between turbulent velocity and temperature field, and severely reduce temperature fluctuations thanks to

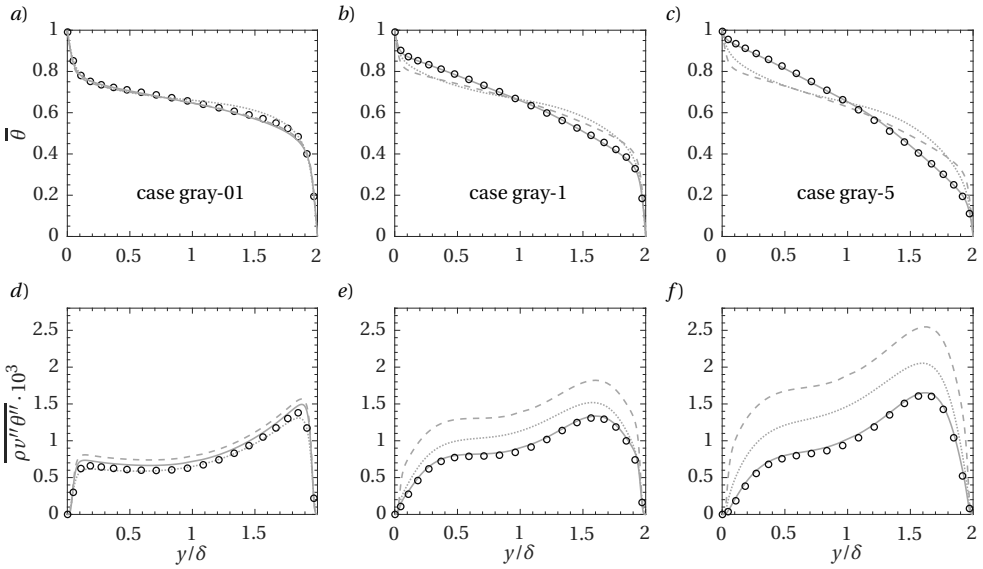

Figure 6.4: Profiles of mean temperature (top row) and turbulent heat flux (bottom row) for the low/intermediate optical thickness, constant absorption coefficient cases. DNS results are shown with circles. The dotted lines are results from setting $Pr_t = 0.9$, while the dashed and solid lines show result from the two equation model, without and with including TRI, respectively.

a long-range heat transfer mechanism. This results in a much lower turbulent heat flux compared to a non-radiative case with the same mean temperature gradient and velocity fluctuations. Contrarily, including a TRI model allows to predict the reduction in turbulent heat flux leading to accurate results in terms of mean temperature profile. It is possible to notice that increasing optical thickness (case gray-5) leads to a more severe misprediction of temperature by the standard models due to a higher TRI influence.

Figure 6.5 shows the optical thicker cases (gray-10, gray-20 and gray-10p). Again, since the impact of TRI on the turbulent temperature field is very high, the use of the proposed model is necessary to achieve an accurate prediction. Nonetheless, we imagine that substantially increasing the optical thickness ($\tau \gg 1$) would decrease the necessity of the TRI model. This is caused by the fact that the strength of TRI is not a monotonic function of τ, it is zero at $\tau = 0$, reaches a maximum and returns to zero at $\tau \to \infty$. Case gray-10p shows the results obtained for a lower Prandtl number ($Pr = 0.7$). The TRI model performs still exceptionally. We did not test Prandtl numbers larger than unity because of the unavailability of DNS data. Nevertheless, since the relative influence of the radiative heat transfer (and TRI) is reduced with an increase in Prandtl number, we believe that the results will still be accurate without any modification. It is possible to imagine that for a higher Prandtl number ($Pr > 1$) temperature structures will be significantly different, and this change will have to be taken into account with a Prandtl number dependency of the characteristic wavenumber ω_c (approximated by l_θ). Nonetheless, the strength of TRI, which scales with Pr^{-1}, will reduce in intensity. Therefore, it is straight-

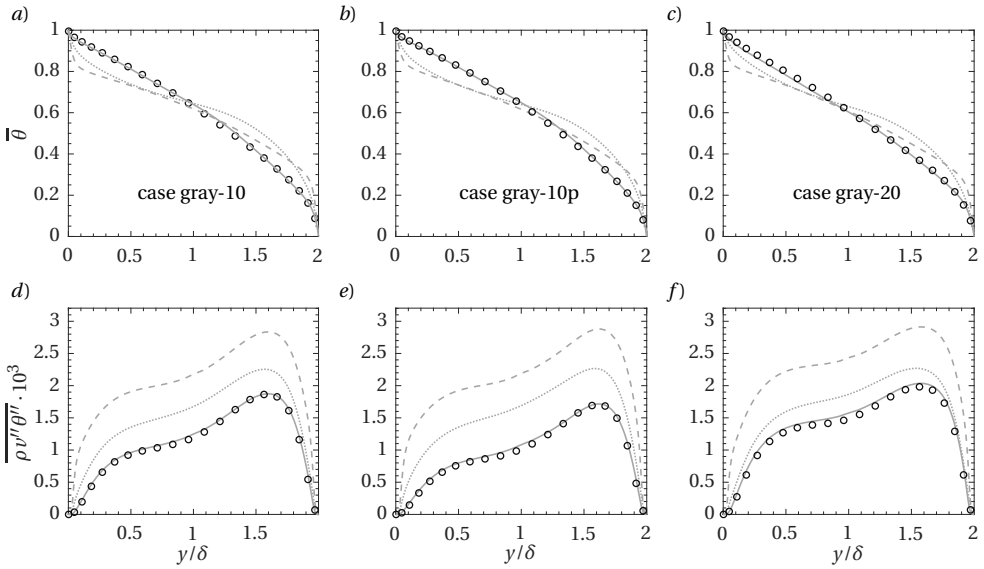

Figure 6.5: Profiles of mean temperature (top row) and turbulent heat flux (bottom row) for the high optical thickness, constant absorption coefficient cases. DNS results are shown with circles. The dotted lines are results from setting $Pr_t = 0.9$, while the dashed and solid lines show result from the two equation model, without and with including TRI, respectively.

forward to show that also for an increased Prandtl number, no significant modification of the proposed model would be required.

Finally, it is important to notice how, in both figures 6.4 and 6.5, the two equation model without TRI performs very poorly in terms of turbulent heat transfer. We already showed that the two equation model results in an over-estimation of turbulent heat transfer near the walls (figure 6.2). In case of radiative heat transfer, where turbulent heat transfer is largely suppressed near the boundaries, this over-estimation becomes unacceptable. TRI, especially in case of an intermediate to high optical thickness, is the dominant mechanism. Thus, by including a closure model for TRI we are able to correct the mispredictions and obtain excellent results. The constant turbulent Prandtl number model (red dashed lines) did not necessarily over-predict the turbulent heat flux near the walls in the benchmark cases, but is still a very crude approximation which connects tightly the velocity and the temperature field. This connection is partly severed by TRI leading also to unacceptable results as optical thickness (and radiative heat transfer strength) increases.

6.6.3. VARIABLE PROPERTY, GRAY CASES

Figure 6.6 shows results for the variable property, gray cases compared to DNS. As explained in [65] the fluctuation of absorption coefficient do not impact TRI significantly as much as E and G fluctuations. As a consequence, the results for these cases follow very

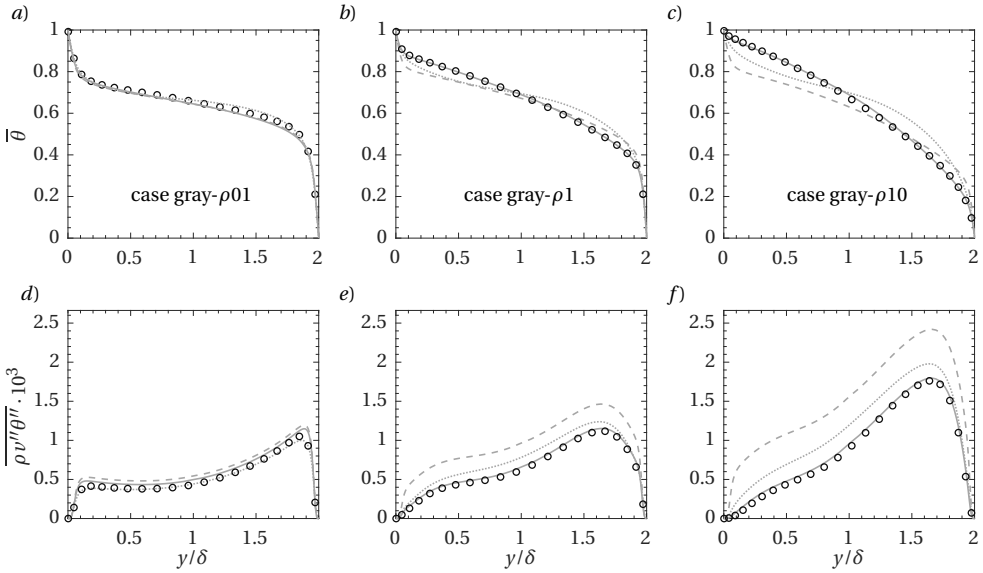

Figure 6.6: Profiles of mean temperature (top row) and turbulent heat flux (bottom row) for the variable absorption coefficient, gray cases. DNS results are shown with circles. The dotted lines are results from setting $Pr_t = 0.9$, while the dashed and solid lines show result from the two equation model, without and with including TRI, respectively.

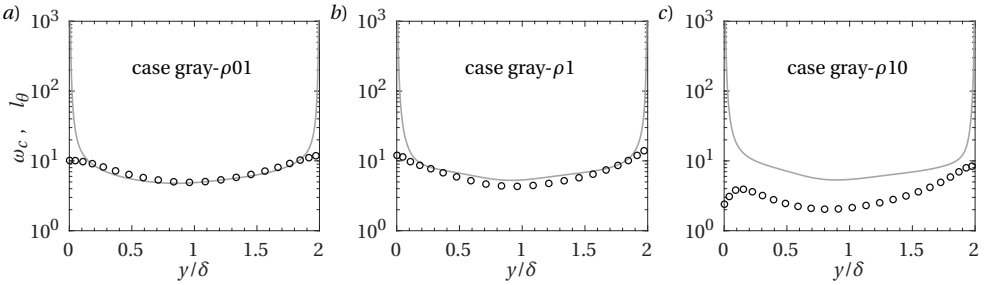

Figure 6.7: Characteristic wavenumber ω_c from DNS (circles), calculated with equation (4.35) compared to the characteristic length scale (solid lines) obtained in the RANS simulations using equation (6.27)

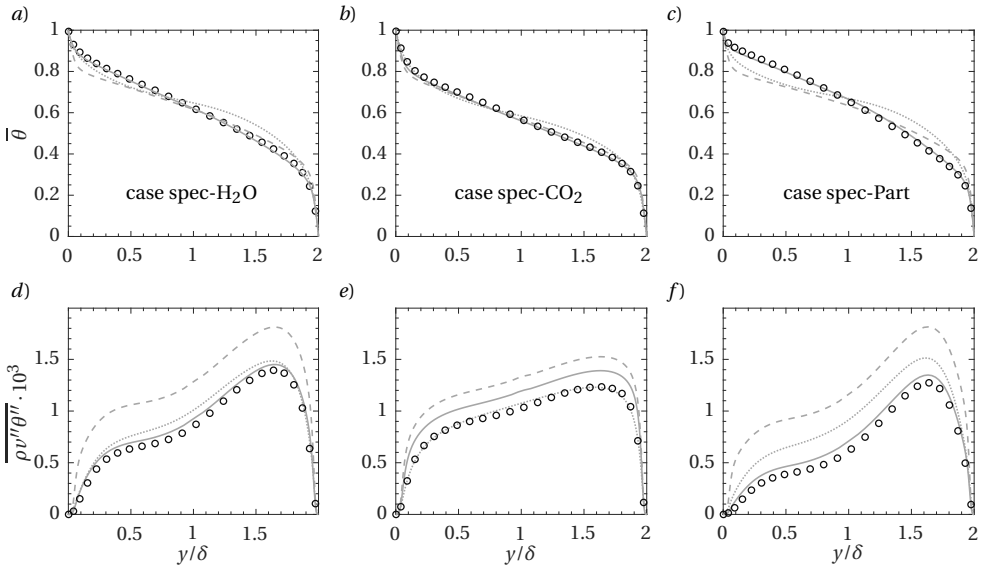

Figure 6.8: Profiles of mean temperature (top row) and turbulent heat flux (bottom row) for the non-gray cases. DNS results are shown with circles. The dotted lines are results from setting $Pr_t = 0.9$, while the dashed and solid lines show result from the two equation model, without and with including TRI, respectively.

closely what observed in figures 6.4 and 6.5. In particular, the low optical thickness case does not feel the impact of a fluctuating radiative field and adding a TRI closure model does not change significantly the results. Contrarily, a large improvement is found when including TRI for intermediate and large optical thickness cases (gray-ρ1 and gray-ρ10). To show the accuracy of the length scale approximation, figure 6.7 shows profiles of ω_c as calculated from DNS data with equation (4.35) and l_θ^{-1} approximated with equation (6.27) in the RANS simulations. It can be noticed that near the walls l_θ^{-1} has an unphysical spike which is not seen in the DNS data. While ω_c has a fixed value at a boundary, l_θ tends to zero as k goes to zero, which means that, following expression (6.27), the integral length scale of temperature structures tends to zero as a fixed boundary is approached. This caused the characteristic wavenumber calculated by the RANS model to tend to infinity. Another misprediction is seen in the value of ω_c for the optically thickest case gray-ρ10. This is attributed to the fact that equation (6.27) is not able to predict thermal structure's enlargement caused by the dual absorption-emission process at high absorption rates [61] as it does not include any radiative quantity. Nonetheless, both of these deviations from DNS values (which will be addressed later in section 6.6.5 while discussing second order statistics) do not impact the predictions of both turbulent heat transfer and mean temperature.

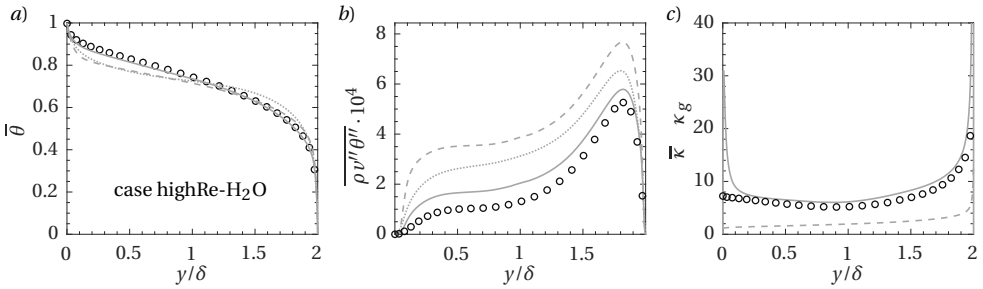

Figure 6.9: Profiles of (a) mean temperature, (b) turbulent heat flux and (c) κ_g for the non-gray, high Reynolds number case. DNS results are shown with circles. In (a) and (b), the dotted lines are results from setting P_{rt} = 0.9, while the dashed and solid lines show result from the two equation model, without and with including TRI, respectively. In subfigure (c) the solid line shows the profile of κ_g obtained iteratively with equation (36) compared to the DNS results. The Planck mean absorption coefficient is shown (dashed line) as a reference.

6.6.4. NON-GRAY CASES

Figures 6.8 and 6.9 presents the results for the non-gray cases with a spectrally varying absorption coefficient. For the non-gray cases, the failure of the standard models is not connected to the optical thickness (shown in table 6.2) as for the previously analysed gray cases (i.e., for gray-gas cases higher τ leads to larger misprediction if the TRI model is not included). In particular, case spec-Part (with $\tau_p = 2.79$) shows the worst performance in terms of both turbulent heat flux and mean temperature. On the other hand, case spec-CO_2, with a comparable optical thickness (2.99) seems to be relatively unaffected by TRI.

This is because, as we explain in chapter 5, two different parameters control TRI in a non-gray gas: τ_p which is the Planck-mean optical thickness, and τ_g, which is the TRI-equivalent optical thickness, based on the parameter κ_g. These two parameters are defined as follows

$$\tau_p = 0.5\int_0^2 \overline{\kappa}_p dy\,, \quad \text{and} \quad \tau_g = 0.5\int_0^2 \kappa_g(\overline{\theta},\omega_c)dy\,. \tag{6.35}$$

In gray gas cases $\tau = \tau_g = \tau_p$, meaning that TRI depends only on the Planck-mean optical thickness. This is not the case in non-gray gases. The two optical thicknesses are shown, for the different cases, in the table 6.3, together with the gray-equivalent optical thickness (τ_{eq}) described below.

Table 6.3: TRI-governing parameters for the different non-gray cases.

case	spec-H_2O	spec-CO_2	spec-Part	highRe-H_2O
τ_p	8.023	2.99	2.79	2.12
τ_g	13.4	18.9	3.1	7.09
τ_{eq}	0.736	0.118	2.391	0.384

Since the impact of κ' is negligible, TRI scales with

$$\mathscr{R}_\theta/\overline{\theta'^2} \approx \kappa_p(f_E - f_G) \propto \kappa_p \cdot (1 - \kappa_g \cdot f(\kappa_g))\,, \tag{6.36}$$

where $\kappa_g \cdot f(\kappa_g)$ is bounded between 0 and 1 and increases with κ_g. The RHS of the above proportionality relation has been obtained dividing $\mathscr{R}_\theta$ by $(\overline{\theta'^2} f_E)$. Therefore, the impact of radiation increases with τ_p and decreases with τ_g. To compare the results shown in figure 6.8 with the gray gas cases it is possible to define a new optical thickness (we call it here gray-equivalent), which is a combination of these two parameters. If we assume that only one absorption coefficient (here denoted κ_{eq} is responsible for TRI (as in gray gases), the "gray-equivalent" optical thickness can be defined as

$$\tau_{eq} = 0.5 \int_0^2 \kappa_{eq} dy\,, \quad \text{where} \quad \kappa_{eq}\left(1 - \frac{\kappa_{eq}}{\omega_c}\text{atan}\frac{\omega_c}{\kappa_{eq}}\right) \equiv \kappa_p\left(1 - \frac{\kappa_g}{\omega_c}\text{atan}\frac{\omega_c}{\kappa_g}\right). \tag{6.37}$$

The values of τ_{eq} for each case, calculated with DNS data and ω_c as in equation (4.35), are given in table 6.3. Given these values, it is possible to compare the predictions obtained for the non-gray cases with the gray gas cases.

For spec-H_2O, ($\tau_{eq} = 0.74$) neglecting TRI results in slightly better prediction than for the gray cases with $\tau = 1$ (gray-1 and gray-ρ1), but still unacceptable if compared to the optically thin gray cases (gray-01 and gray-ρ01). In this case, the inclusion of a TRI model is necessary to obtain satisfactory results. Moreover, spec-CO_2, despite the seemingly high τ_p, is very similar to the optically thin cases (gray-01 and gray-ρ01) given that τ_{eq} is equal to 0.118. Therefore, the two equation model is improved only slightly when including the TRI closure. On the other hand, since spec-Part has very similar τ_p and τ_g (the absorption spectrum has a really low variability), the result is similar to an optically intermediate gray case with optical thickness between 1 and 5 and hence largely impacted by TRI. Finally, case highRe-H_2O, which is shown in figure 6.9, has a τ_{eq} lower than case spec-H_2O, but is more affected by TRI (i.e., the deviations of the standard models are larger). This is caused by the fact that, in this case, there is more emitted energy that can dissipate thermal fluctuations. In simple terms, the average dimensional temperature is higher or, mathematically,

$$\mathscr{R}_\theta / \overline{\theta'^2} \propto f_E\,, \quad \text{where} \quad f_E \propto \overline{\theta}^3 T_0^{-4}, \tag{6.38}$$

meaning that $\mathscr{R}_\theta$ increases with mean non-dimensional temperature ($\overline{\theta}$) and with the non-dimensional temperature difference $T_0^{-1} = (T_h^* - T_c^*)/T_c^*$. As for case highRe-$H_2O$, the temperature difference is three times larger than for the other cases, TRI strength is magnified by a factor of 3^4.

Indeed, the TRI closure model seems to yield remarkable results independently of the mean temperature or the Planck-mean, TRI-equivalent and gray-equivalent optical thicknesses of the case. Figure 6.10 shown the comparison between the integral thermal length scales (top) and the TRI-equivalent absorption coefficient (bottom), calculated with DNS data and obtained with the RANS simulations. The dashed lines are the Planck-mean absorption coefficient profiles, plotted for reference. As seen previously for the variable property cases, the integral length scale l_θ tends to zero while approaching the boundary, causing a spike in the characteristic wavenumber l_θ^{-1}. This is reflected in the calculation of the TRI-equivalent absorption coefficient which also spikes near the walls. Fortunately, the relevant function which approximates the incident radiation fluctuation is dependent on the ratio κ_g/ω_c. Therefore, the misprediction of ω_c is corrected

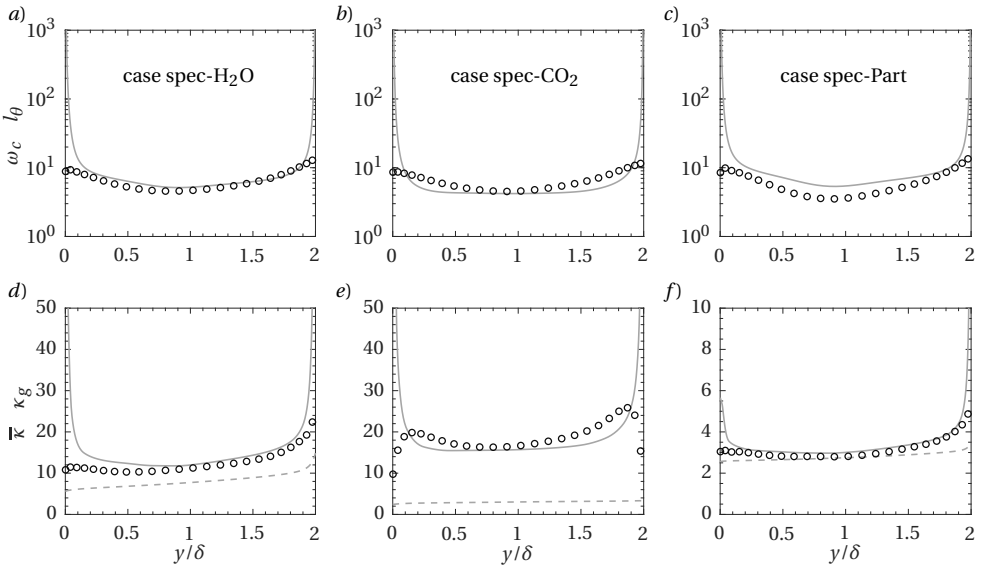

Figure 6.10: Top row: characteristic wavenumber ω_c from DNS (circles), calculated with equation (4.35) compared to the characteristic length scale (solid lines) calculated with equation (6.27). Bottom row: comparison between the actual κ_g calculated from DNS data (circles) and the one obtained iteratively with equation (6.28) (blue dashed-dotted line). The Planck-mean absorption coefficient (dashed line) is shown as a reference.

by the calculation of the TRI-equivalent absorption coefficient. The TRI-equivalent absorption coefficient for case highRe-H_2O is shown in figure 6.9(c). Aside the problems close to the boundaries, the model (and iterative approach) employed seems to yield fairly correct values, especially for the calculation of κ_g, which, due to its dependency on both temperature and thermal length scales, is the most complex quantity to assess.

6.6.5. SECOND ORDER STATISTICS

In this section we present the quantities calculated by the two equation model ($\overline{\theta'^2}$ and ε_θ) and the radiative dissipation assessed by the additional TRI closure model ($\mathscr{R}_\theta$). Since, in case of an eddy diffusivity calculated using a constant turbulent Prandtl number these quantities are not available, only the two equation model is shown in comparison to DNS data. Figure 6.11 shows the results obtained for the constant property gray cases. It is possible to notice that for a low to intermediate optical thickness (gray-01, gray-1, gray-5), the TRI model predicts very accurately radiative dissipation, leading to a satisfactory calculation of temperature variance and molecular dissipation. Already for $\tau = 1$, not accounting for TRI causes temperature variance and molecular dissipation to be unphysically high. This is caused by the large mean temperature gradient which develops in the center of the channel that translates in a high temperature variance turbulent production rate. The high production rate, coupled to absence of a radiative dissipation model results in a large overprediction of temperature variance. Increasing the

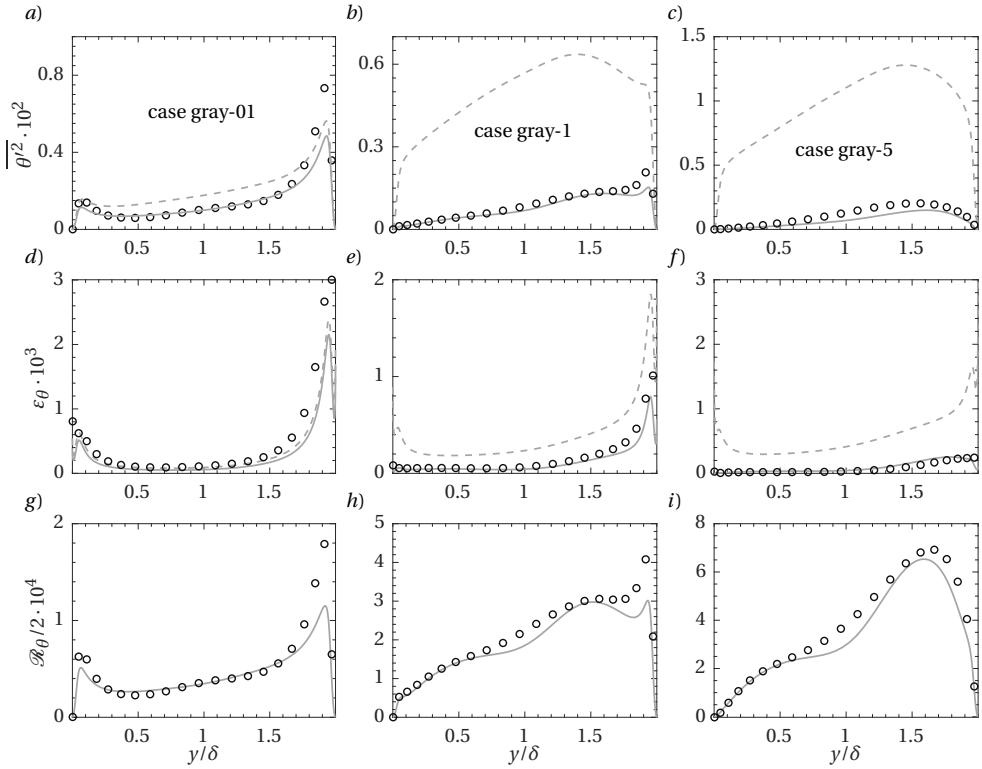

Figure 6.11: Profile of second order statistics calculated using the two equation turbulent heat flux model for the constant absorption coefficient cases. The top row shows temperature variance, while middle and bottom row display molecular and radiative dissipation, respectively. The symbols show DNS data while the red and blue lines show the results obtained using the two equation model without and with the addition of a TRI model, respectively

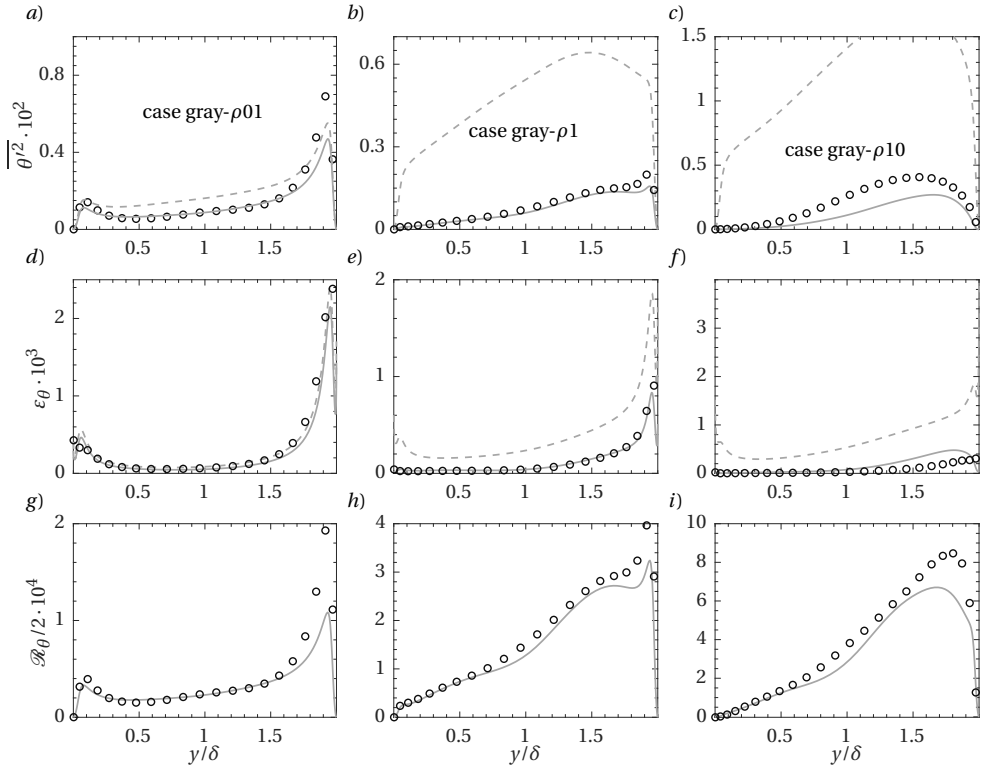

Figure 6.12: Profile of second order statistics calculated using the two equation turbulent heat flux model for the constant absorption coefficient cases. The top row shows temperature variance, while middle and bottom row display scalar and radiative dissipation, respectively. The symbols show DNS data while the dashed and solid lines show the results obtained using the two equation model without and with the addition of a TRI model, respectively

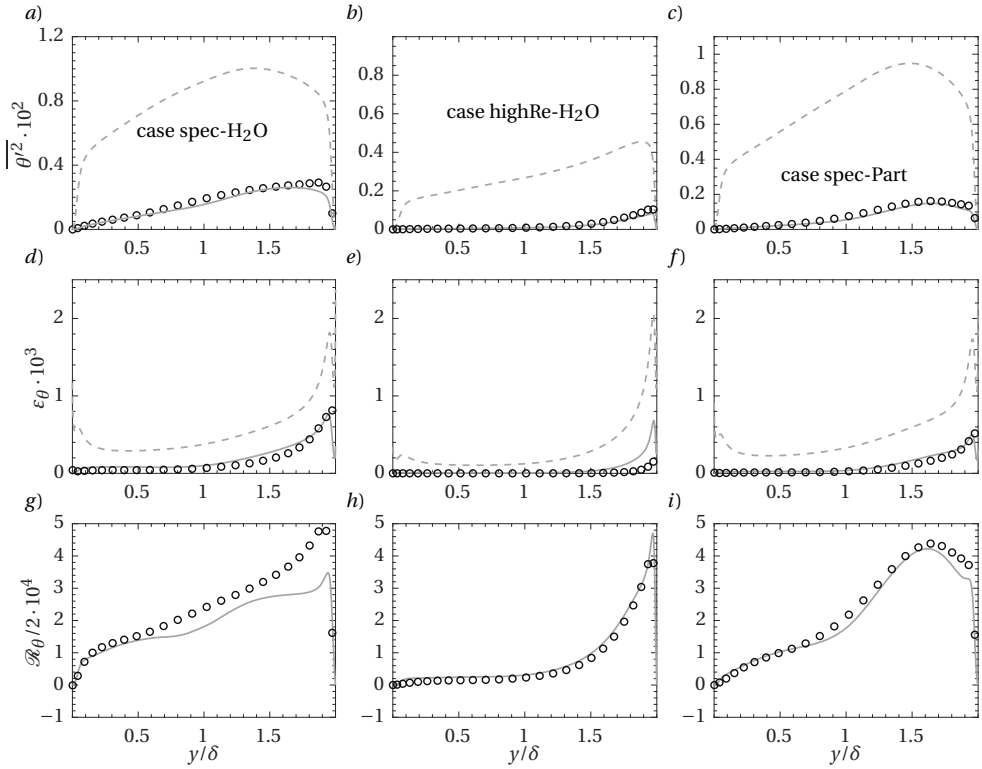

Figure 6.13: Profile of second order statistics calculated using the two equation turbulent heat flux model for the variable absorption coefficient cases. The top row shows temperature variance, while middle and bottom row display scalar and radiative dissipation, respectively. The symbols show DNS data while the dashed and solid lines show the results obtained using the two equation model without and with the addition of a TRI model, respectively

optical thickness further (gray-10, gray-20) leads to a lower accuracy in terms of radiative dissipation. This is most likely caused by the overprediction of the characteristic wavenumber. Since, for these cases, the characteristic wavenumber is effectively higher than the actual value obtained from the DNS simulations (figure 6.7), predicted incident radiation fluctuations (G') are lower, see eq. (4.28), which result in a higher absolute value of radiative dissipation, see equation (6.19). Physically speaking, the model is predicting smaller thermal structures which are optically thinner and not capable of re-absorbing emitted radiation. This will lead to a decreased temperature variance (and ultimately a lower equilibrium $\mathscr{R}_\theta$). Therefore, the cause for having a lower $\mathscr{R}_\theta$ in figure 6.11 (for high optical thickness cases) is, counter-intuitively, an overprediction of radiative dissipation. Nevertheless, the temperature variance obtained by neglecting TRI is progressively worse as the optical thickness increases due to the larger mean temperature gradient. Therefore, despite slight inaccuracies in the second order statistics, including TRI leads to excellent results also for higher optical thickness cases.

Figures 6.12 and 6.12 show the performance of the RANS simulations in terms of second order statistics for variable properties and non-gray cases. As for the average profiles, the conclusions drawn for constant property cases are suitable for the variable property gray cases with the same optical thickness. It is interesting to notice the high accuracy of the TRI model in an intermediate optical thickness scenario, as for gray-ρ1 and all the non-gray cases. Also for highRe-H_2O, which has variable transport properties and a significantly larger ΔT^* and Re, the TRI model approximates very accurately radiative dissipation, allowing a correct prediction of temperature variance and molecular dissipation.

6.7. SUMMARY

We developed a general radiative modification which can be applied to most turbulent heat transfer models. The modification consists of a first order approximation of the fluctuating radiative field which is expressed as a linear function of temperature fluctuations. This TRI closure model is then applied to a two-equation turbulent heat flux model which evaluates temperature variance and scalar dissipation rate. The improved model has been tested on several cases in comparison with the available DNS data to prove its validity. The results show that in case of a radiative flow, the proposed model is always capable to improve the results when compared to the standard models available.

7

CONCLUSION

The simulations performed in the course of this research work were aimed at developing a thorough understanding of turbulence-radiation coupling. To do this, an innovative approach has been developed, wherein the Navier-Stokes equations are solved with a DNS formulation on CPUs and the Radiative Transfer equation is solved on GPUs. Particularly, The GPU Monte Carlo implementation has been optimized for thermal radiation simulations achieving a significative speedup compared to a CPU Monte Carlo implementation. This new approach allows a full one-to-one coupling of turbulence and radiative heat transfer, granting the access to a complete description of TRI. Following the simulation of radiatively participating turbulent channel flows with different optical depths and variable radiative properties, the following conclusions can be made:

- Radiative heat transfer causes a decrease of temperature fluctuations due to a direct dissipation effect.
- In gray gases, the radiative dissipation of temperature is behaviourally different depending on the optical thickness of the flow. To account for the behavioural difference, it is necessary to separate the impact of emission from the one of absorption.
- For a low optical thickness, the role of absorption is limited to the modification of the mean temperature field through the mean incident radiation. As a consequence, the only direct effect of radiative heat transfer on temperature fluctuation is felt through emission fluctuations, which act as a damping effect for the temperature field.
- In higher optical thickness flows, absorption tends to occur more close to the emission point, causing an interplay between emission and absorption fluctuations. In particular, energy is dissipated from small temperature structures which are relatively optically thin, and deposited in larger temperature structure where absorption is more relevant. The temperature spectra show a steepened gradient as a consequence.

- Due to the low "surface-to-volume" ratio, streaky anisotropic temperature structures, typically found near solid boundaries, have an enhanced radiative dissipation.

- The non-local nature of radiative heat transfer causes the impossibility of any direct scaling of the temperature field, especially for larger optical depths where incident radiation fluctuations dominate the production of temperature structures.

- In non-reactive flows, emission and absorption coefficient fluctuations are well described by first order functions of temperature fluctuations. On the other hand, in gray gases, it is possible to connect incident radiation fluctuations to the absorption coefficient and a characteristic wavenumber which represents the inverse of the length scale of the most energetic temperature scale of the flow.

- In non-reactive flows, turbulence-radiation coupling is fully accounted for by the variations of the mean absoption coefficient alone. For any purpose, κ' can be neglected, independently from the value of the optical thickness.

- In non-gray gases, the behaviour of TRI cannot be characterized by either the optical thickness or the global transmissivity, due to the interaction of emission and absorption at a spectral level. For this reason, we derived a new spectral averaging which accounts for the length scale of turbulent structures. This averaging provides a framework to define a new TRI-equivalent optical thickness τ_g which allows a comparison between flows with different spectral properties. τ_g also allows insight into quiescent media as it quantifies the optical depth related to absorption of self-emitted radiation.

- Based on the results obtained, a new TRI closure has been developed. This closure can be applied to simple turbulent heat flux models in a RANS framework to significantly improve the predictions of the temperature field.

It has to be reminded that all the results are obtained in the framework of non-reactive turbulent flows, where temperature fluctuations can be considered weak. In reactive flows, where temperature fluctuation are much higher, emission and absorption coefficient fluctuations are not expected to be well represented by their first order linear approximations. On the other hand, as radiative heat transfer dissipates temperature fluctuations, it is possible that the derived model will be valid and produce improved results also in a turbulent combustion case. All the other theoretical conclusions are believed to apply correcly also to combustion cases. In particular the model for G' which is not dependent on the weak temperature fluctuation approximation. As a suggestion for future studies we recommend to validate the proposed model also for combustion cases. The validation can be performed with experiments for both low optical thickness flames with a large participating medium volume fraction (as example the ones found in MILD combustion [85, 86]) and high optical thickness (sooting) flames. Additional future outlooks include observing the effect of TRI on temperature in multispecies mixtures, where radiation and turbulence interact with species transport. If the effect of species transport can be included in the variation of the absorption coefficient only, it might be possible

to incorporate in the theory developed in this thesis. In particular, we recommend to investigate the impact of absorption coefficient fluctuations κ' on the temperature field in a combusting and a multispecies flows. If this is large, τ_g might have to be redefined accordingly.

A

VALIDATION AND VERIFICATION

Table A.1: Test cases

cases	$1D_1$	$1D_2$	$1D_3$	$1D_4$	$1D_5$	$3D_1$	$3D_2$	$3D_3$
κ	5	50	50	200	200	0.1	1	20
τ	0.5	5	5	20	20	0.1	1	20
ϵ	1	1	0.6	1	0.6	1	1	1
T_w	500	500	500	500	500	0	0	0
dimensions	1	1	1	1	1	3	3	3

A.0.1. FINITE VOLUME RADIATIVE SOLVER

The implemented scheme is tested in various one dimensional and three dimensional cases, while comparing the performance of STEP and CLAM scheme for different optical thicknesses. Table A.1 shows the details of the validation cases. All tests were performed on a 100^3 grid with 96 propagation directions, as in the performed simulations. For 1D cases, temperature profile is parabolic with a value of 500 K at the walls and 2500 K in the center. Periodic boundary conditions were implemented in two directions. For the 3D cases, the benchmark developed by Sakurai et al [87] is tested. The temperature profile in the 3D cases is:

$$T(x,y,z) = \left(\frac{\sin(x\pi)}{Lx} \cdot \frac{\sin(y\pi)}{Ly} \cdot \frac{\sin(z\pi)}{Lz} \cdot \frac{\pi}{\sigma} \right)^{1/4}, \tag{A.1}$$

while the walls are black and cold (0 K).
Figures A.1 and A.2 show the one dimensional and three dimensional test cases, respectively. STEP and CLAM scheme are both suitable when low optical thickness is considered, since, at the level of a cell, the system is optically thin, while when increasing τ the crude approximation of the STEP scheme produces inaccurate results. This is due to the fact that the cell is not necessarily optically thin (already at $\tau = 5$) and intensity in the cell center is, therefore, different from the upstream face value. CLAM scheme, on the other hand, is able to reproduce all the analytical results up to $\tau \sim 20$ (cases $3D_3$, $1D_4$ and $1D_5$).

A.0.2. GPU MONTE CARLO SOLVER

To ensure a correct implementation the algorithm is verified and validated using a combination of gray and non-gray gases in 1D and 3D. In total, 14 cases are used which are summarized in table A.2. All the cases, 1D and 3D alike, are calculated on a 3D grid. To mimic the one-dimensionality, two periodic directions are employed in the 1D cases, over which the results are then averaged. Beside the case names in column 1, the second column shows values of the absorption coefficient κ for the gray gas cases (cases 1 to 4), and the names of the non-gray gases (H_2O, CO_2 or mix) for cases 5 to 14. The entry "mix", found in cases 12 and 13, refers to a mixture of 11.6% CO_2 and 15.5% H_2O at 1 atm. All other cases are enclosures filled with a pure substance (molar fraction of 1) at 1 atm. The other columns indicate the prescribed temperature distribution (linear, parabolic, etc.), the spatial inhomogeneous dimensions (1D or 3D), the wall emissivities

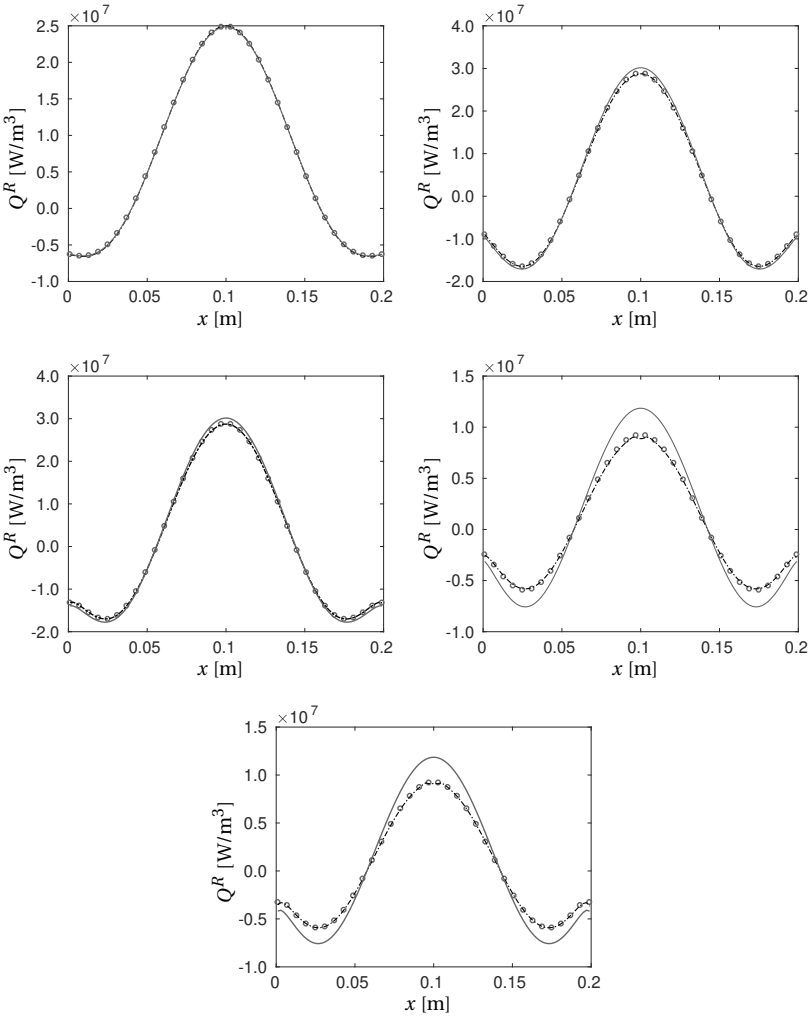

Figure A.1: comparison between solution from FVM and analytical solution for 1D gray slab. Figure A.1(a): case $1D_1$, figure A.1(b): case $1D_2$, figure A.1(c): case $1D_3$, figure A.1(d): case $1D_4$, figure A.1(e): case $1D_5$. Circles: exact solution, dashed-dotted line: CLAM scheme, solid line: STEP scheme.

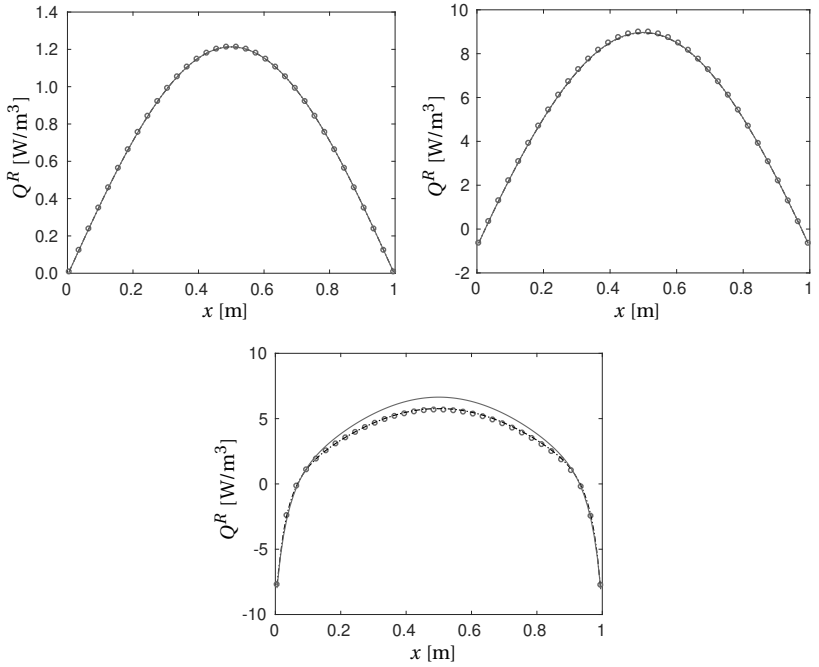

Figure A.2: comparison between solution from FVM and analytical solution for 3D cubic enclosure. Solution is shown at $y = 0.5$ and $z = 0.5$. Figure A.2(a): case $3D_1$, figure A.2(b): case $3D_2$, figure A.2(c): case $3D_3$. Circles: exact solution, dashed-dotted line: CLAM scheme, solid line: STEP scheme.

Table A.2: Description of validation cases

Case	κ	Temp.	Dimensions	Domain	ε_w	τ / t	Comparison
Case 1	1 [m^{-1}]	lin1	1D	1 [m]	1 (all walls)	1 / 0.368	analytical solution
Case 2	1 [m^{-1}]	parab1	1D	1 [m]	1 (all walls)	1 / 0.368	analytical solution
Case 3	0.5 [m^{-1}]	sin	3D	1 [m^3]	1 (all walls)	0.5 / 0.607	analytical solution [87]
Case 4	5 [m^{-1}]	sin	3D	1 [m^3]	1 (all walls)	5 / 0.007	analytical solution [87]
Case 5	H_2O	1000 [K]	1D	0.1 [m]	1 (all walls)	0.51 / 0.81	Kim et al. [88]
Case 6	H_2O	1000 [K]	1D	1 [m]	1 (all walls)	5.1 / 0.54	Kim et al. [88]
Case 7	CO_2	lin2	1D	1 [m]	1 (all walls)	25.5 / 0.82	Cherkaoui et al. [56]
Case 8	CO_2	lin2	1D	1 [m]	0, 1	25.5 / 0.82	Cherkaoui et al. [56]
Case 9	CO_2	lin2	1D	1 [m]	0.1, 0.1	25.5 / 0.82	Cherkaoui et al. [56]
Case 10	H_2O	parab1	1D	1 [m]	1 (all walls)	4.98 / 0.49	Line-by-Line MC
Case 11	CO_2	parab1	1D	1 [m]	1 (all walls)	22.11 / 0.821	Line-by-Line MC
Case 12	mix	parab2	1D	0.2 [m]	1 (all walls)	0.30/ 0.76	Tesse et al. [18]
Case 13	mix	parab2	1D	4 [m]	1 (all walls)	5.93 / 0.036	Tesse et al. [18]
Case 14	H_2O	3dimens	3D	1 [m^3]	1 (all walls)	4.98 / 0.49	Line-by-Line MC

ε_w, the global optical thickness and global transmissivity (τ / t), and the source used for the verification or the validation. Further details are given in the subsequent discussions of the individual cases.

The gray gas cases 1, 2, 3 and 4 are used to verify the correctness of the ray marching procedure and are compared to existing analytical solutions. Although $\kappa \neq f(\nu)$, the spectral (narrow-band) description shown in algorithm 1 is retained with precomputed probability functions based on a gray gas absorption coefficient. Two different geometries are examined, namely a 1 m parallel slab (1D) and a 1 m^3 cube (3D). The walls are considered black with $\varepsilon_w = 1$. For the 1D cases, two different temperature profiles (lin1 and parab) are considered, given as

$$\text{lin1:} \quad T_m = 500 + 1000x \text{ [K]}, \;\; T_{w1} = 500 \text{ [}K\text{]}, \;\; T_{w2} = 1500 \text{ [K]}, \tag{A.2}$$

$$\text{parab1:} \quad T_m = 500 - 2000x^2 + 2000x \text{ [K]}, \;\; T_{w1} = T_{w2} = 500 \text{ [K]}, \tag{A.3}$$

where T_m is the temperature of the medium and T_{w1} and T_{w2} are the temperatures at the left and right wall, respectively. For the 3D cases, the walls are cold (0 [K]), and the

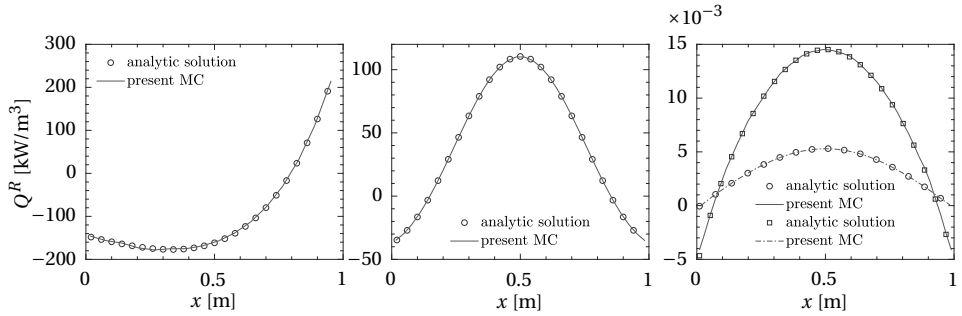

Figure A.3: Verification of the present MC code (lines) for a gray gas in comparison with analytic solution (symbols). Left: case 1, center: case 2, right: circles and dashed dotted line case 3, squares and solid line case 4 (both at $y = z = 0.5$ [m]).

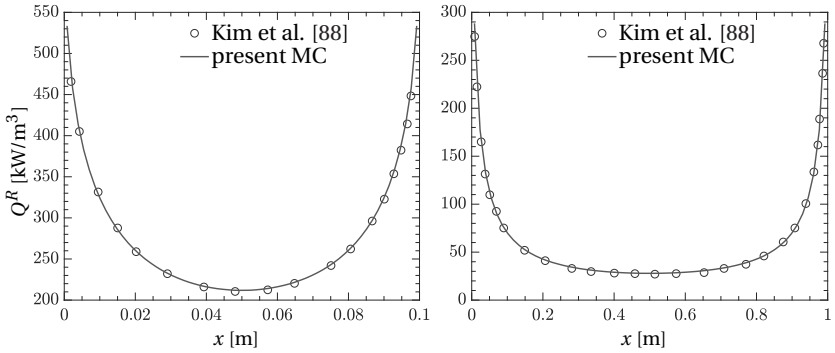

Figure A.4: Validation of the present MC code (lines) for H_2O in the isothermal case in comparison with values from [88] (circles). Left: case 5, right: case 6.

temperature profile is given as

$$\text{sin: } T_m = \left(\sin\pi x \cdot \sin\pi y \cdot \sin\pi z \cdot \pi/\sigma\right)^{0.25} \text{ [K]}, \tag{A.4}$$

in order to compare the results with the quasi-analytic solution derived by Sakurai et al. [87]. The absorption coefficient for the 1D slab has a value of 1 m^{-1}, while for the 3D domain the two cases have different absorption coefficients of $\kappa = 0.5$ and 5 m^{-1} (case 3 and 4, respectively). For these four cases, the results are obtained on a 32^3 grid with 2000 rays per cell. Note that for the 1D cases, an averaging was performed along the periodic directions. As can be seen in figure A.3, the MC implementation is accurately able to reproduce the analytic solutions with adequate precision.

To validate the spectral discretization, a combination of isothermal and non-isothermal cases with H_2O and CO_2 have been used. 119 and 139 narrow bands were selected for H_2O and CO_2, respectively, with each band containing 16 quadrature points. The radiative power of a 1D slab filled with water vapour at 1 atm and 1000 K, bounded by two cold black walls at a distance of 0.1 (case 5) and 1 m (case 6), has been compared with data presented in Kim et al. [88] as shown in figure A.4. The results for the 1D slab filled

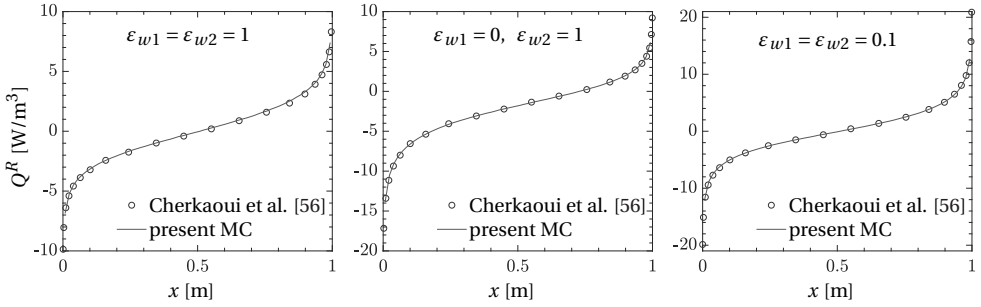

Figure A.5: Validation of the present MC code for CO_2 at 1 [atm] in comparison with results from [56]. Linear temperature profile $T = 295 + 10x$ [K]. $T_{w1} = 295$ [K] (lin2). $T_{w2} = 305$ [K]. Cases 7, 8 and 9 at the left, right and center, respectively.

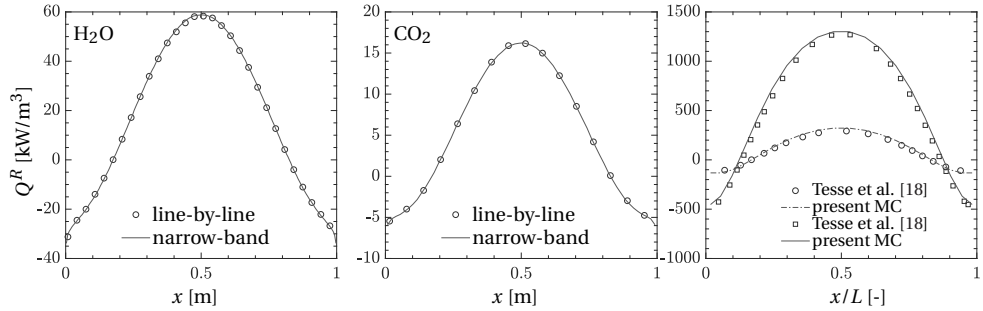

Figure A.6: left and right show the comparison of MC implementation with the line-by-line solution for H20 (left) and CO2 (center) at 1 [atm] with a parabolic temperature profile, equation (A.3). The right figure shows the comparison of the H_2O-CO_2 mixture with results from Tesse et al. [18]. circles and dashed dotted line case 13, squares and solid line case 12.

with CO_2 at 1 atm and three different wall emissivities (cases 7, 8 and 9) are shown in figure A.5. The temperature profiles for the CO_2 cases are linear with the left wall at 295 K and the right wall at 305 K (lin2). The radiative power is compared to data presented in Cherkaoui et al. [56]. In all cases (cases 5-9) the comparison clearly demonstrates the high accuracy of the spectral discretization.

Two additional cases (case 10 and 11) are proposed to validate the spectral discretization and the MC implementation with a line-by-line version of the present MC code. The radiative power is calculated for H_2O and CO_2 at 1 [atm] with parabolic temperature profiles (equation (A.3)). The results obtained with the narrow-band correlated-k MC, shown in figure A.6, are in close agreement with the line-by-line benchmark to again prove the correct implementation. Figure A.6 also shows the results for the H_2O-CO_2 mixture (cases 12 and 13) in comparison with the results from Tesse et al. [18]. For these cases the temperature profile was set to

$$\text{parab2: } T_m = 500 - 8000(x/L)^2 + 8000(x/L) \text{ [K]}, \quad T_{w1} = T_{w2} = 500 \text{ [K]}, \tag{A.5}$$

with L the length of the domain. Due to the high temperatures involved ($T_c = 2500$ K),

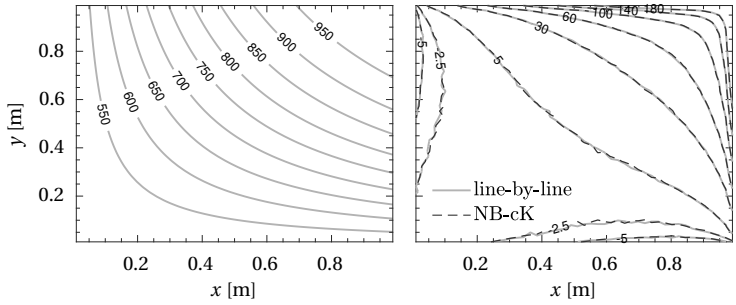

Figure A.7: 3D non gray case. Left: temperature profile at $z = 0.5$ [m] in [K]. Right: radiative power at $z = 0.5$ [m] in [kW/m^3].

the spectrum for the mixture was retrieved using the HITEMP 2010 database [14]. The spectra between 0 and 25000 cm^{-1} were then divided into 999 narrow-bands and 16 quadrature points per band for a total of 15984 pseudo-spectral points. As demonstrated in figure A.6, also in case of a mixture, the present MC shows satisfactory agreement with the published literature.

The last validation case (14) consists of 1 m^3 cube with black walls filled with H_2O. The temperature profile is given by

$$\text{3dimens: } T_m = 500 - 2000 \cdot (x \cdot y \cdot z)^2 + 2000 \cdot x \cdot y \cdot z \text{ [K]}, \quad T_w = 500 \text{ [K]}. \tag{A.6}$$

Figure A.7 shows the results of the 3D non-gray case compared to a line-by-line version of the current MC. The left contour shows the temperature at $z = 0.5$ m, while the right plot shows the comparison of the results obtained with the narrow-band correlated-k method and the line-by-line benchmark at the same location (shown in kW/m^3). The solution is again in excellent agreement with the line-by-line benchmark case.

BIBLIOGRAPHY

[1] S. Londerville and C. B. Jr., *The Coen & Hamworthy Combustion Handbook*, 1st ed. (CRC press, 2013).

[2] P. Coelho, *Radiative transfer in combustion systems,* in *Handbook of Thermal Science and Engineering*, edited by F. Kulacki (Springer, 2017).

[3] R. Viskanta and M. Mengüç, *Radiation heat transfer in combustion science,* Progress in Energy and Combustion science , 97 (1987).

[4] T. Ren, M. Modest, and S. Roy, *Monte Carlo simulation for radiative heat transfer in a high-pressure industrial gas turbine combustion chamber,* in *Proc. of the ASME 2017 Heat Transfer Conference*, HT2017 (Bellevue, Washington, USA, 2017).

[5] H. Willit, *Fog and haze,* Monthly Weather Review **56**, 435 (1928).

[6] H. Byers, *General Meteorology*, 1st ed. (McGraw-Hill, New York, 1959).

[7] J. Jiusto, *Fog structure,* Invited Review Paper, Symposium workshop clouds (1980).

[8] W. Cotton, G. Bryan, and S. van den Heever, *Fogs and stratocumulus clouds,* International Geophysics **99**, 179 (2011).

[9] J. Ren, X. Li, and H. Jiang, *Conjugate heat transfer characteristics in a highly thermally loaded film cooling configuration with tbc in syngas,* Aerospace **16** (2019), i10.3390/aerospace6020016.

[10] *SORCE: SOlar Radiation & Climate Experiment,* Laboratory for Atmospheric and Space Physics, University of Colorado Boulder.

[11] W. Jeong, J. Lee, and Y. Jeong, *Potential improvements of supercritical recompression CO_2 Brayton cycle by mixing other gases for power conversion system of a SFR,* Nuclear Engineering and Design **241**, 2128 (2011).

[12] Y. Ahn, S. Bae, M. Kim, S. Cho, S. Baik, J. Lee, and J. Cha, *Review of supercritical CO_2 power cycle technology and current status of research and development,* Nuclear Engineering and Technology **47**, 647 (2015).

[13] V. Cheang, R. Hedderwick, and C. McGregor, *Benchmarking supercritical carbon dioxide cycles against steam Rankine cycles for concentrated solar power,* Solar Energy **113**, 199 (2015).

[14] L. Rothman, I. Gordon, R. Barber, H. Dothe, R. Gamache, A. Goldman, V. Perevalov, S. Tashkun, and J. Tennyson, *HITEMP, the high-temperature molecular spectroscopic database,* Journal of Quantitative Spectroscopy & Radiative Transfer **111**, 2139 (2010).

[15] P. Coelho, *Turbulence radiation interaction: From theory to application in numerical simulations,* Journal of heat transfer **134** (2012).

[16] H. Pourasani and A. Mani, *Effects of preferential concentration on heat transfer in particle-based solar receivers,* Journal of Solar Energy Engineering **139**, 021008 (2017).

[17] P. Coelho, O. Teerling, and D. Roekaerts, *Spectral radiative effects and turbulence/radiation interaction in a non-luminous turbulent jet diffusion flame,* Combustion and flame **133**, 75 (2003).

[18] L. Tesse, F. Dupoirieux, and J. Taine, *Monte Carlo modeling of radiative transfer in a turbulent sooty flame,* International Journal of Heat and Mass Transfer **47**, 555 (2004).

[19] P. Coelho, *Numerical simulation of the interaction between turbulence and radiation in reactive flows,* Progress in Energy and Combustion Science **33**, 311 (2007).

[20] K. Deshmukh, M. Modest, and D. Haworth, *Direct numerical simulation of turbulence-radiation interactions in a statistically one-dimensional nonpremixed system,* Journal of Quantitative Spectroscopy and Radiative Transfer **109**, 2391 (2008).

[21] A. Gupta, M. Modest, and D. Haworth, *Large-eddy simulation of turbulence-radiation interactions in a turbulent planar channel flow,* Journal of Heat transfer **131** (2009), 10.1115/1.3085875.

[22] M. Roger, P. Coelho, and C. da Silva, *Relevance of the subgrid-scales for large eddy simulations of turbulence-radiation interactions in a turbulent plane jet,* Journal of Quantitative Spectroscopy and Radiative Transfer **112**, 1250 (2011).

[23] A. Townsend, *The effects of radiative transfer on turbulent flow of a stratified fluid,* Journal of Fluid Mechanics **4**, 361 (1958).

[24] M. Coantic and O. Simonin, *Radiative effects on turbulent temperature spectra and budgets in the planetary boundary layer,* Journal of the Atmospheric Sciences **41**, 2629 (1984).

[25] D. Schertzer and O. Simonin, *A theoretical study of radiative cooling in homogeneous and isotropic turbulence,* in *Turbulent Shear Flows 3, September 9–11, 1981* (Springer Berlin Heidelberg, Berlin, Heidelberg, 1982) pp. 262–274.

[26] A. Soufiani, *Temperature turbulence spectrum for high-temperature radiating gases,* Journal of Thermophysics **5**, 489 (1991).

[27] A. Sakurai, K. Matsubara, K. Takakuwa, and R. Kanbayashi, *Radiation effects on mixed turbulent natural and forced convection in a horizontal channel using direct numerical simulation,* International journal of Heat and Mass Transfer **55**, 2539 (2012).

[28] Y. Zhang, R. Vicquelin, O. Gicquel, and J. Taine, *Physical study of radiation effects on the boundary layer structure in a turbulent channel flow,* International journal of Heat and Mass Transfer **61**, 654 (2013).

[29] R. Vicquelin, Y. Zhang, O. Gicquel, and J. Taine, *Effects of radiation in turbulent channel flow: analysis of coupled direct numerical simulations,* Journal of Fluid Mechanics **753**, 360 (2014).

[30] S. Ghosh, R. Friedrich, M. Pfitzner, C. Stemmer, B. Cuenot, and M. E. Hafi, *Effects of radiative heat transfer on the structure of turbulence supersonic channel flow,* Journal of fluid mechanics **677**, 417 (2011).

[31] S. Ghosh, R. Friedrich, and C. Stemmer, *Contrasting turbulence-radiation interaction in supersonic channel and pipe flow,* International journal of Heat and fluid flow **48**, 24 (2014).

[32] S. Ghosh and R. Friedrich, *Effects of radiative heat transfer on the turbulence structure in inert and reacting mixing layers,* Physics of Fluids **27** (2015), 10.1063/1.4920990.

[33] S. Silvestri and R. Pecnik, *A fast gpu monte carlo radiative heat transfer implementation for coupling with direct numerical simulation,* J. Comp. Phys. X **3**, 100032 (2019).

[34] M. F. Modest, *Radiative Heat Transfer*, Academic Press (2013).

[35] H. Pourasani, H. Kolla, J. Chen, and A. Mani, *Spectral analysis of energy transfer in variable density, radiatively heated particle-laden flows,* Proceedings of the Summer Program, Center for Turbulence Research, Stanford University , 27 (2014).

[36] J. Owens, D. Luebke, N. Govindaraju, M. Harris, J. Krüger, A. Lefohn, and T. Purcell, *A survey of general-purpose computation on graphics hardware,* Eurographics, State of the Art Report , 21 (2005).

[37] *NVIDIA CUDA C Programming Guide*, NVIDIA Corporation (2011).

[38] *Gpu machine learning,* `http://www.nvidia.com/object/machine-learning.html`.

[39] *Gpu medical imaging,* `http://www.nvidia.com/object/medical_imaging.html`.

[40] M. Nobile, P. Cazzaniga, A. Tangherloni, and D. Besozzi, *Graphics processing units in bioinformatics, computational biology and systems biology,* Briefings in Bioinformatics **18**, 870 (2016).

[41] A. Khajeh-Saeed and J. Perot, *Direct numerical simulation of turbulence using gpu accelerated supercomputers,* Journal of Computational Physics **235**, 241 (2013).

[42] F. Salvadore, M. Bernardini, and M. Botti, *Gpu accelerated flow solver for direct numerical simulation of turbulent flows,* Journal of Computational Physics **235**, 129 (2013).

[43] V. Cvetanoska and T. Stojanovski, *Using high performance computing and monte carlo simulation for pricing american options,* The 9th Conference for Informatics and Information Technology (2012).

[44] Y. Liang, X. Xing, and Y. Li, *A gpu-based large-scale monte carlo simulation method for systems with long-range interactions,* Journal of Computational Physics **338**, 252 (2017).

[45] A. Humphrey, D. Sunderland, T. Harman, and M. Berzins, *Radiative heat transfer calculation on 16384 gpus using a reverse monte carlo ray tracing approach with adaptive mesh refinement,* 2016 IEEE International Parallel and Distributed Processing Symposium Workshops , 1222 (2016).

[46] F. Heymann and R. Siebenmorgen, *GPU-based Monte Carlo dust radiative transfer scheme applied to active galactic nuclei,* The Astrophysical Journal **751** (2012).

[47] S. Lele, *Compact finite difference schemes with spectral-like resolution,* Journal of computational physics , 16 (1992).

[48] B. Boersma, *A 6th order staggered compact finite difference method for the incompressible Navier Stokes and scalar transport equations,* Journal of computational physics , 4940 (2011).

[49] W. Feiereisen, *Numerical simulation of a compressible homogeneous, turbulent shear flow,* Ph.D. thesis, Thermoscience Division, Department of Mechanical Engineering, Stanford University, Standford (1989).

[50] A. Patel, J. Peeters, B. Boersma, and R. Pecnik, *Semi-local scaling and turbulence modulation in variable property turbulent channel flows,* Physics of Fluids **27** (2015), 10.1063/1.4929813.

[51] K. Deshmukh, M. Modest, and D. Haworth, *Higher-order spherical harmonics to model radiation in direct numerical simulation of turbulent reactive flows,* Journal of Computational Thermal Sciences **1** (2009).

[52] H. Hottel and E. Cohen, *Radiant heat exchange in a gas-filled enclosure: Allowance for nonuniformity of gas temperature,* A.l.Ch.E Journal **4** (1958).

[53] L. Briggs, W. M. Jr., and E. Lewis, *Ray-effect mitigation in discrete ordinate-like angular finite element approximations in neutron transport,* Nuclear Science and Engineering **57**, 205 (1975).

[54] G. Raithby and E. Chui, *A finite-volume method for predicting a radiant heat transfer enclosures with participating media,* Journal of Computational Physics **112**, 415 (1990).

[55] P. Coelho, *Bounded skew high-order resolution schemes for the discrete ordinates method,* Journal of Computational Physics **175**, 412 (2002).

[56] M. Cherkaoui, J. Dufresne, R. Fournier, J. Grandpeix, and A. Lahellec, *Monte Carlo simulation of radiation in gases with narrow-band model and a net-exchange formulation,* Journal of Heat Transfer **118**, 401 (1996).

[57] Y. Zhang, O. Gicquel, and J. Taine, *Optimized emission-based reciprocity monte carlo method to speed up computation in complex systems,* International Journal of Heat and Mass Transfer **55**, 8172 (2012).

[58] A. Soufiani and J. Taine, *High temperature gas radiative property parameters of statistical narrow-band model for H_2O, CO_2 and co, and correlated-k model for H_2O and CO_2,* International Journal of Heat and Mass Transfer **40**, 987 (1996).

[59] L. Rothman, I. Gordon, A. Barbe, D. Benner, P. Bernath, and M. Birk, *The HITRAN 2012 molecular spectroscopic database,* Journal of Quantitative Spectroscopy & Radiative Transfer **130**, 4 (2013).

[60] A. Humphrey, T. Harman, M. Berzins, and P. Smith, *A scalable algorithm for radiative heat transfer using reverse Monte Carlo ray tracing,* International Conference on High Performance Computing , 212 (2015).

[61] S. Silvestri, A. Patel, D. Roekaerts, and R. Pecnik, *Turbulence radiation interaction in channel flow with various optical depths,* Journal of Fluid Mechanics **834**, 359 (2018).

[62] J. Howell, M. P. Mengüç, and R. Siegel, *Thermal Radiation Heat Transfer*, 6th ed. (CRC Press, 2016).

[63] J. Kim, P. Moin, and R. Moser, *Turbulence statistics in fully developed channel flow at low Reynolds number,* Journal of fluid mechanics **177**, 133 (1987).

[64] J. Kim and P. Moin, *Transport of passive scalars in turbulent channel flow,* NASA Ames Research Center, Presented at the Sixth Symposium on Turbulent Sheet Flows (1987).

[65] S. Silvestri, D. Roekaerts, and R. Pecnik, *Assessing turbulence radiation interactions in turbulent flows of non-gray media.* Journal of Quantitative Spectroscopy and Radiative Transfer **233**, 134 (2019).

[66] W. Grosshandler, *RADCAL: A Narrow-Band model for Radiation calculations in a combustion environment*, Tech. Rep. (NIST technical note, 1993).

[67] A. Patel, B. Boersma, and R. Pecnik, *The influence of near-wall density and viscosity gradients on turbulence in channel flows,* Journal of Fluid Mechanics **809**, 793–820 (2016).

[68] A. Trettel and J. Larsson, *Mean velocity scaling for compressible wall turbulence with heat transfer,* Physics of Fluids **28**, 026102 (2016).

[69] S. Silvestri, D. Roekaerts, and R. Pecnik, *Modelling turbulent heat flux accounting for turbulence-radiation interactions,* Internaltional Journal of Heat and Fluid Flow **89**, 108728 (2021).

[70] F. Eiberger, P. Habisreuther, N. Zarzalis, and F. Turrini, *Evaluation of the turbulence radiation interaction and the validity of the optically thin fluid approximation in a high turbulent premixed methane flame,* Proceedings of ASME Turbo Expo 2015: Turbine Technical Conference and Exposition (2015).

[71] P. Coelho, *Assessment of a presumed joint pdf for the simulation of turbulent-radiation interaction in turbulent reactive flows,* Applied Thermal Engineering **49**, 22 (2012).

[72] J. Consalvi and F. Nmira, *Effects of soot absorption coefficient-planck function correlation on radiative heat transfer in oxygen-enriched propane turbulent diffusion flame,* Journal of Quantitative Spectroscopy and Radiative Transfer **172**, 50 (2016).

[73] F. Nmira, Y. Liu, J. Consalvi, F.Andre, and F. Liu, *Pressure effects on radiative heat transfer in sooting turbulent diffusion flames,* Journal of Quantitative Spectroscopy and Radiative Transfer **245**, 50 (2020).

[74] R. Mehta, *Detailed modeling of soot formation and turbulence-radiatino interaction in turbulent jet flames*, Ph.D. thesis, The Pennsylvania State University (2008).

[75] P. Coelho, *A general closure model for the time-averaged radiative transfer equation in turbulent flows,* Proceedings of the 14th International Heat Transfer Conference , 1 (2010).

[76] R. Antonia and J. Kim, *Turbulent prandtl number in the near-wall region of a turbulent channel flow,* Int. Journal of Heat and Mass Transfer **34**, 1905 (1991).

[77] B. Deng, W. Wu, and S. Xi, *A near-wall two-equation heat transfer model for wall turbulent flows,* Int. Journal of Heat and Mass Transfer **44**, 691 (2001).

[78] Y. Nagano and C. Kim, *A two-equation model for heat transport in wall turbulent shear flows,* Journal of Heat Transfer **110**, 583 (1988).

[79] J. Sanders and I. Gokalp, *Scalar dissipation rate modelling in variable density turbulent axisymmetric jets and diffusion flames,* Physics of Fluids **10**, 938 (1998).

[80] R. So, *Near-wall modeling of turbulent heat transfer with different prandtl numbers,* Proceedings of Symposium on Energy Engineering in the 21st Century **1** (2000).

[81] M. Morkovin, *Effects of Compressibility on Turbulent Flows*, edited by A. Favre (Gordon and Breach, New York, 1962) pp. 367–380.

[82] P. Durbin, *Separated flow computations with the k-epsilon-v-squared model,* AIAA **33**, 659 (1995).

[83] G. Otero, A. Patel, R. Diez, and R. Pecnik, *Turbulence modelling for flows with strong variatyions in thermo-physical properties,* International Journal of Heat and Fluid Flow **73**, 114 (2018).

[84] R. Pecnik and A. Patel, *Scaling and modelling of turbulence in variable property channel flows,* Journal of Fluid Mechanics **823** (2017).

[85] P. Li, J. Mi, B. Dally, F. Wang, L. Wang, Z. Liu, S. Chen, and C. Zheng, *Progress and recent trend in mild combustion,* Science China, Technological Sciences **52**, 255 (2011).

[86] S. Xu, Y. Tu, P. Huang, C. Luang, Z. Wang, B. Shi, H. Liu, and Z. Liu, *Effect of wall temperature on methane mild combustion and heat transfer behaviours with non-preheated air,* Applied thermal engineering **174**, 115282 (2020).

[87] A. Sakurai, T. Song, S. Maruyama, and H. Kim, *Comparison of radiation element method and discrete ordinates interpolation method applied to three-dimensional radiative heat transfer,* Numerical Heat Transfer **48**, 259 (2005).

[88] T. Kim, J. Menart, and H. Lee, *Nongrey radiative gas analyses using the S-N discrete ordinates method,* Journal of Heat Transfer **113**, 946 (1991).

ACKNOWLEDGEMENTS

A fantastic chapter of my life is closing with the defense of this dissertation. It has been a lot of work, a lot of fun, a lot full of unforgettable experiences, and, as such, a lot of people to thank. First and foremost, I would like to thank my promotors, prof.dr. Dirk Roekaerts and dr. Rene Pecnik. Thank you for having faith in me and allowing me the freedom to pursue my research. Thank you for all the contributions to my work, for the enlightening discussions and the helpful feedback. Without your guidance and support my Ph.D. research would not have been possible.

I would particularly like to thank dr. Rene Pecnik for helping me grow professionally as a researcher but also on a personal level as an individual. Thank you for always being available to discuss anything and being committed to making me succeed. I benefitted greatly from your knowledge and your passion. I would additionally like to thank the committee members to taking their time to evaluate my dissertation.

Speaking of the colleagues, P&E is not a typical work environment! For this reason, I was lucky to have the best group of colleagues (slash friends), you can ask for. To the ones that lasted till the very end, Stephan, Rishabh, Gustavo, Rumen, Noura, Fatma thanks for making me feel at home at the workplace, not only because of amazing lunch discussions about science (and not only), but also because of the follow-ups consisting in nights of dinners, games, and beers that lasted till early morning. I would also like to thank the new collegues and the ones that long finished, but contributed to making my Ph.D. an amazing experience. An honorable mention goes to Johan (Man you made Monday mornings look fun, and that says it all!) and to my friend Uttiya, companion of many laughs and nights out.

I also had the privilege to have amazing friends from the beginning to the end of my Ph.D. journey. A great thanks to my first friends, Enrico and Giamma that despite moving out, never felt really away. I would also like to thank Francesco and Francesca, my favorite southern couple and fitness companions, my “Bouwpub colleagues” Luis and Ursa, all the old friends with which I started this journey in the Netherlands, and the new friends which shared with me these wacky Corona times. Thanks to you week days were interesting and weekends were fun. How to not mention my flatmate Manas. I greatly enjoyed living with you in van Embdenstraat and will surely miss it. Thanks for putting up with (and sharing) a lot of craziness. I would also like to thank my Rotterdam friends Edo, Alex, and Marci. Inbetween laughs, jokes and coversations you made me grow into a better person. Finally, I would like to thank Carlos and Anna for truly everything. I will miss you both greatly, but I know we will never be truly apart.

To conclude, I would like to thank my family: my sister Alice, my mother Fiorenza and my father Marco. I feel very grateful for your love, patience and support. This dissertation is dedicated to you.

LIST OF PUBLICATIONS

JOURNAL PUBLICATIONS

1. **S. Silvestri**, D.J.E.M. Roekaerts, and R. Pecnik, *Modeling turbulent heat transfer accounting for turbulence-radiation interactions*, Int. J. Heat Fluid Flow **89**, 108728 (2021) (chapter 6).

2. **S. Silvestri**, D.J.E.M. Roekaerts, and R. Pecnik, *Assessing turbulence-radiation interactions in turbulent flows of non-gray media*, J. Quant. Spectr. Rad. Transf. **233**, 134–148 (2019) (chapter 4 & 5).

3. **S. Silvestri**, and R. Pecnik, *A fast gpu monte carlo radiative heat transfer implementation for coupling with direct numerical simulation*, J. Comp. Phys. X **3**, 100032 (2019) (chapter 2).

4. **S. Silvestri**, A. Patel, D.J.E.M. Roekaerts, and R. Pecnik, *Turbulence radiation interaction in channel flow with various optical depths*, J. Fluid Mech. **753**, 360 (2018) (chapter 3).

BOOK CHAPTERS

1. **S. Silvestri** and D.J.E.M. Roekaerts, *Mixed convection and radiation heat transfer in porous media for solar thermal applications* (Y. Mahmoudi, K. Hooman, & K. Vafai, Eds) in Covective heat transfer in porous media, CRC press (2020). (not included in this thesis)

CONFERENCE PUBLICATIONS AND PRESENTATIONS

1. **S. Silvestri**, D.J.E.M. Roekaerts, and R. Pecnik, *Coupled convective and radiative heat transfer in turbulent flows*, In Physics at Veldhoven, Veldhoven, the Netherlands (2020).

2. **S. Silvestri**, D.J.E.M. Roekaerts, and R. Pecnik, *Coupled turbulence and radiation calculations on heterogeneous computing architectures*, In APS, division of fluid dynamics, Seattle, United States (2019).

3. **S. Silvestri**, D.J.E.M. Roekaerts, and R. Pecnik, *Simulation of coupled convection and radiation on heterogeneous computing architectures*, In Grand opening DHPC center, Delft, the Netherlands (2019).

4. **S. Silvestri**, D.J.E.M. Roekaerts, and R. Pecnik, *Coupling of convection and radiation in turbulent flows*, In APS, division of fluid dynamics, Atlanta, United States (2018).

5. **S. Silvestri**, D.J.E.M. Roekaerts, and R. Pecnik, *DNS of turbulence-radiation interactions in non-gray media: influence of variable absorption coefficient and real spectra*, In Computational thermal radiation in participating media, Cascais, Portugal (2018).

6. **S. Silvestri**, A. Patel, D.J.E.M. Roekaerts, and R. Pecnik, *Turbulence radiation interaction in channel flow with various optical depths*, In European turbulence conference, Stockholm, Sweden (2017).

7. **S. Silvestri**, D.J.E.M. Roekaerts, and R. Pecnik, *Particle size influence in high temperature volumetric absorption of sunlight*, In CHAINS, Veldhoven, the Netherlands (2017).